DOUBLE OPTICAL GATING

by

STEVE GILBERTSON

B.S., Kansas State University, 2005

AN ABSTRACT OF A DISSERTATION

submitted in partial fulfillment of the requirements for the degree

DOCTOR OF PHILOSOPHY

Department of Physics
College of Arts and Sciences

KANSAS STATE UNIVERSITY
Manhattan, Kansas

2010

Abstract

The observation and control of dynamics in atomic and molecular targets requires the use of laser pulses with duration less than the characteristic timescale of the process which is to be manipulated. For electron dynamics, this time scale is on the order of attoseconds where 1 attosecond = 10^{-18} seconds. In order to generate pulses on this time scale, different gating methods have been proposed. The idea is to extract or "gate" a single pulse from an attosecond pulse train and switch off all the other pulses. While previous methods have had some success, they are very difficult to implement and so far very few labs have access to these unique light sources. The purpose of this work is to introduce a new method, called double optical gating (DOG), and to demonstrate its effectiveness at generating high contrast single isolated attosecond pulses from multi-cycle lasers. First, the method is described in detail and is investigated in the spectral domain. The resulting attosecond pulses produced are then temporally characterized through attosecond streaking. A second method of gating, called generalized double optical gating (GDOG), is also introduced. This method allows attosecond pulse generation directly from a carrier-envelope phase un-stabilized laser system for the first time. Next the methods of DOG and GDOG are implemented in attosecond applications like high flux pulses and extreme broadband spectrum generation. Finally, the attosecond pulses themselves are used in experiments. First, an attosecond/femtosecond cross correlation is used for characterization of spatial and temporal properties of femtosecond pulses. Then, an attosecond pump, femtosecond probe experiment is conducted to observe and control electron dynamics in helium for the first time.

DOUBLE OPTICAL GATING

by

STEVEN GILBERTSON

B.S., Kansas State University, 2005

A DISSERTATION

submitted in partial fulfillment of the requirements for the degree

DOCTOR OF PHILOSOPHY

Department of Physics
College of Arts and Sciences

KANSAS STATE UNIVERSITY
Manhattan, Kansas

2010

Approved by:

Major Professor
Dr. Zenghu Chang

Copyright

Abstract

The observation and control of dynamics in atomic and molecular targets requires the use of laser pulses with duration less than the characteristic timescale of the process which is to be manipulated. For electron dynamics, this time scale is on the order of attoseconds where 1 attosecond = 10^{-18} seconds. In order to generate pulses on this time scale, different gating methods have been proposed. The idea is to extract or "gate" a single pulse from an attosecond pulse train and switch off all the other pulses. While previous methods have had some success, they are very difficult to implement and so far very few labs have access to these unique light sources. The purpose of this work is to introduce a new method, called double optical gating (DOG), and to demonstrate its effectiveness at generating high contrast single isolated attosecond pulses from multi-cycle lasers. First, the method is described in detail and is investigated in the spectral domain. The resulting attosecond pulses produced are then temporally characterized through attosecond streaking. A second method of gating, called generalized double optical gating (GDOG), is also introduced. This method allows attosecond pulse generation directly from a carrier-envelope phase un-stabilized laser system for the first time. Next the methods of DOG and GDOG are implemented in attosecond applications like high flux pulses and extreme broadband spectrum generation. Finally, the attosecond pulses themselves are used in experiments. First, an attosecond/femtosecond cross correlation is used for characterization of spatial and temporal properties of femtosecond pulses. Then, an attosecond pump, femtosecond probe experiment is conducted to observe and control electron dynamics in helium for the first time.

Table of Contents

List of Figures viii
List of Tables xviii
Acknowledgements xix
CHAPTER 1 - Introduction 1
1.1 Attosecond Pulse Trains 1
1.1.1 The Principle of High-order Harmonic Generation 2
1.2.1 Experimental setup 6
1.3.1 Hints of Isolated Sub-femtosecond Pulses 9
1.4.1 Overview of this Thesis 10
CHAPTER 2 - Attosecond Pulse Generation 11
2.1 Principle of Double Optical Gating 11
2.1.1 Two Color Gating 11
2.1.2 Polarization Gating 16
2.1.3 Double Optical Gating 23
2.1.3a Interferometric DOG 27
2.1.3b Collinear DOG 38
2.1.3c Generalized Double Optical Gating (GDOG) 50
2.2 Phase Matching Considerations with DOG 62
2.2.1 Theoretical Considerations 62
2.2.2 Experimental results 67
CHAPTER 3 - Temporal Characterization of Attosecond Pulses 74
3.1 Principle of Attosecond Streaking 74
3.1.1 Reconstructing Attosecond Pulses 78
3.1.2 The Attosecond Streak Camera 80
3.1.2 Streak Camera Electronics and Resolution 84
3.1.2a Alignment procedure for the streak camera 92
3.2 Two Color Streaking 95
3.3 Attosecond Pulses with DOG 98

3.3.1 Intrinsic Chirp of Attosecond Pulses 103
3.4 Attosecond Pulses with GDOG 107
CHAPTER 4 - Applications of DOG and GDOG 110
4.1 Extreme Broadband Attosecond Pulses 110
4.2 Attosecond Pulses from any Laser 116
4.2.1 Attosecond Pulses Directly from an Amplifier 116
4.2.2 Attosecond Pulses from Carrier Envelope Phase Unstabilized Lasers 124
4.3 High Energy Attosecond Pulses 132
CHAPTER 5 - Applications of Attosecond Pulses 135
5.1 Attosecond / Femtosecond Cross Correlations 135
5.1.1 Temporally Varying Electric Fields 135
5.1.2 Spatially Varying Electric Fields 142
5.2 Attosecond / Femtosecond Pump Probe Experiments 148
5.2.1 Temporal Measurements and Control of Electron Dynamics 148
CHAPTER 6 - Conclusions and Outlook 159
Publications 161
References 166
Appendix A - ADK Calculation 175
Appendix B - Quartz Plates Calculations 177
Appendix C - BBO Crystal Selection for DOG 184
Appendix D - Interferometer Locking Method 193
Appendix E - Pulse Energy Measurement 196
Appendix F - The Kansas Light Source Amplifier 198

List of Figures

Figure 1.1 The 3 Step Model for HHG (adapted from [1]). 2
Figure 1.2 (a)Return phase versus release phase (b) Electron Returning Kinetic Energy..... 4
Figure 1.3 (a) Possible trajectories from an electron in a laser field. (b) The return kinetic energy versus return time. The long (green) and short (red) trajectories are indicated. 5
Figure 1.4 (a) XUV Spectrometer (b) Attosecond pulse train from a gas target 7
Figure 1.5 Long Pulse Spectra (a) and ADK Calculations (b) 8
Figure 1.6 Long Pulse versus Short Pulse Spectrum (a) and representation of the attosecond pulse trains in each case (b). 9
Figure 2.1 Two-Color Electric Field Distributions (a). Individual fields (b). Combined fields with $\phi_{rel}=0$ (c) Combined fields with $\phi_{rel}=0.64\pi$. 12
Figure 2.2 (a) Return phase versus release phase for $\phi=0$ (black) and for a one color field (red). (b) Electron Returning Kinetic Energy in a Two-Color Field with $\phi=0$ (black) and a one color field (red). (c) Return phase versus release phase for $\phi=\pi$ (green) and for $\phi=1.6\pi$ (blue). (d) Electron Returning Kinetic Energy in a Two-Color Field with $\phi=\pi$ (green) and for $\phi=1.6\pi$ (blue). 13
Figure 2.3 Interferometer for Generating a Two-Color Field..... 14
Figure 2.4 (a) Spectrum of a 9 fs pulse (b) FROG trace for a 9 fs laser pulse (c) reconstructed temporal profile and phase. 15
Figure 2.5 Two-Color Linear Spectra. 16
Figure 2.6 (a) Total Electric Field Components for Polarization Gating (b) Driving field (red line) and Gating field (green line). 18
Figure 2.7 Time Dependent Ellipticity for Polarization Gating. 19
Figure 2.8 Optical Components for Polarization Gating 20
Figure 2.9 Ionization Probability versus Pulse Duration for Polarization Gating. 22
Figure 2.10 Attosecond Pulses trains in PG (a) and DOG (b). 23
Figure 2.11 (a) Total field components for DOG. (b) SHG field (purple line), Driving field alone (black line), Driving field with SHG (red line), and Gating field (green line). 24

Figure 2.12 The Gate Width Equation (a) and Ionization Probability for DOG (b) PG results are also displayed for reference. 25
Figure 2.13 The Peak Intensity within the Gate Width for DOG and PG. 26
Figure 2.14 Interferometric DOG setup. 27
Figure 2.15 Spectra from Interferometric DOG. 29
Figure 2.16 Lineout Plots from Interferometric DOG. 30
Figure 2.17 Cross Correlation Scan of IR and SHG. 32
Figure 2.18 Fine Relative Phase Scan between SHG and IR. 33
Figure 2.19 Temporal Profiles of DOG (a) and PG (b) Spectrum from an Argon Target. 34
Figure 2.20 (a) Spectral image of a neon spectrum. (b) Lineout plot of (a). (c) Temporal Profile of DOG Spectrum. 34
Figure 2.21 CEP Effect on DOG pulse. 35
Figure 2.22 HHG Spectra as a Function of CEP from DOG. 36
Figure 2.23 Comparison of CEP Effects in DOG (a) and PG (b). 37
Figure 2.24 Experimental Setup for Collinear DOG. 38
Figure 2.25 Field Components for Collinear DOG (a) After the 1st Quartz Plate, (b) After the 2nd Quartz Plate, and (c) after the BBO. 40
Figure 2.26 Phase Delay versus Angle for BBO (a) and Quartz (b). 41
Figure 2.27 Quartz Plate Thickness versus Pulse Duration for Collinear DOG. 42
Figure 2.28 Field Components from Different Quartz Plates (a) and the Ratio of the Linear Contribution to the Circular Contribution of the DOG Field (b). 43
Figure 2.29 CEP Effect on (a) Collinear DOG and (b) Interferometric DOG. 44
Figure 2.30 XUV Spectrometer with Collinear DOG Optics. 45
Figure 2.31 Group and Phase Delay between 800 nm and 400 nm in Fused Silica. 45
Figure 2.32 (a) Spectra in argon from Collinear DOG. (b) Lineout plots of (a). (c) CEP scans for each input laser pulse duration used. 47
Figure 2.33 (a) Spectra in neon from Collinear DOG. (b) Lineout plots of (a). (c) CEP scans for each input laser pulse duration used. 48
Figure 2.34 (a) Spectra in helium from Collinear DOG. (b) Lineout plots of (a). (c) CEP scans for each input laser pulse duration used. 49

Figure 2.35 GDOG field components (a) Driving field (b) Gating field. (c) The time dependent ellipticity for GDOG. 52
Figure 2.36 (a) GDOG optics. QP=quartz plate, BW = Brewster window. (b) the gating and driving field without the BW in place. (c) the same fields but after passing through the BW. 53
Figure 2.37 Reflectivity versus incident angle for fused silica. 53
Figure 2.38 ADK calculation for GDOG (green line) as a function of input pulse duration. 54
Figure 2.39 (a) Ratio of linear to maximum elliptically polarized portion for PG (red line), DOG (blue line), and GDOG (green line). (b) The calculated peak intensity in the center of the pulse for each method assuming identical input power. 55
Figure 2.40 (a) DOG driving field (red line) and gating field (blue line) for 48 fs delay. (b) GDOG driving field (red line) and gating field (blue line) for 24 fs delay..... 56
Figure 2.41 The saturation intensity as a function of pulse duration for neon (red line) and argon (blue line). 57
Figure 2.42 Typical FROG traces for 10 fs and 20 fs laser pulses. The left figures are the FROG images and the right figures are the reconstructed temporal profiles (red lines) and temporal phases (blue lines). 57
Figure 2.43 (a) Typical spectra from GDOG without and with the Brewster window installed. (b) Lineout plots of the spectra in (a). (c) Fourier transforms of the plots in (b)..... 58
Figure 2.44 (a) Spectra from GDOG (red), DOG (blue) and PG (green) in an argon target for a 10 fs (upper figure) and 20 fs (lower figure) pulse. (b) Spectra from GDOG (red), DOG (blue) and PG (green) in an neon target for a 10 fs (upper figure) and 20 fs (lower figure) pulse. 59
Figure 2.45 (a) CE phase scans for GDOG in an argon target for 10 fs (upper figure) and 20 fs (lower figure) pulses. (b) The same as (a) but from a neon target. 61
Figure 2.46 Gouy phase (green line) and atomic dipole phase for the short (red line) and long (blue line) trajectories. The sum of Gouy and atomic dipole phases are given for the short (magenta line) and long (cyan line) trajectories. The rectangular areas represent ~1mm long interaction regions that may be used in an experiment. 65
Figure 2.47 Output photon flux versus medium Pressure/length product for different values of pressure/coherence length products. 67

Figure 2.48 (a) Spectra dependence on gas cell position for HHG from argon. (b) The measured pulse energy for each position. (c) Spectra dependence on gas cell position for HHG from neon. (d) The measured pulse energy for each position. 68
Figure 2.49 (a) Spectra dependence on gas cell pressure for HHG from argon. (b) The measured pulse energy for each position. (c) Spectra dependence on gas cell pressure for HHG from neon. (d) The measured pulse energy for each position. 69
Figure 2.50 CE phase scans in (a) argon and (b) neon for several values of gas pressure. 71
Figure 2.51 Pressure-length product versus Energy for neon (black) and argon (red). 72
Figure 2.52 Experimental (triangles) and calculated (solid line) values for output photon flux in (a) argon and (b) neon. 72
Figure 3.1 Photoionization cross sections for (a) helium (b) neon (c) argon and (d) krypton..... 75
Figure 3.2 (a) Photoelectron burst in an oscillating laser field. The red line represents the vector potential of the laser field and the vertical arrows indicate the momentum shift the photoelectrons receive at each point. (b) A simulated streaked spectrogram for a ~200 as TL pulse in a 9 fs laser field..... 76
Figure 3.3 Simulated streaked spectrograms of a 6 fs pulse with 5 x 10^{12} W/cm^2 intensity streaking a 200 as pulse with (a) no chirp added, (b) -50 as^2 chirp, and (c) 50 as^2 chirp. 77
Figure 3.4 (a) and (b) Energy domain representation of temporal pulse with positive chirp at two different delays. (c) and (d) The same delays in (a) and (b) but with a TL pulse. 78
Figure 3.5 Experimental setup of the streak camera. 80
Figure 3.6 Reflectivity (blue) and phase (red) of the Mo/Si XUV mirror. 82
Figure 3.7 Focused spot profiles for the (a) outer mirror and (b) inner mirror..... 83
Figure 3.8 Schematic of streak camera position sensitive TOF detector. 85
Figure 3.9 Electronics diagram for the streak camera. 86
Figure 3.10 Wiggle pattern calculated from equation 3.5. 88
Figure 3.11 Helium spectra for different values of retarding potential. 89
Figure 3.12 (a) Experimental data (circles), Pearson fitting (red line) and cubic background (dashed line). (b) Resolution vs. kinetic energy for experimental data (red circles), and calculated resolution for two different time resolutions (green and blue lines)..... 90
Figure 3.13 CE phase effect form a spectrum generated in argon and used to produce photoelectrons in neon. 92

Figure 3.14 Sideband ratio vs. (a) delay, (b) x-position, (c) y-position, and (d) z-position. In all cases, the black squares represent experimental data points and the red lines are Gaussian fits to the data. 94
Figure 3.15 (a) Photoelectron spectrum from a linear one color laser field. (b) Photoelectron spectrum including sidebands after an IR laser field is added to the spectrum in (a). 96
Figure 3.16 (a) Simulated streaked image for a half cycle attosecond pulse train and (b) full cycle pulse train. 96
Figure 3.17 (a) Experimental and (b) simulated streaked spectrogram for two-color streaking. . 97
Figure 3.18 (a) Experimental and (b) retrieved streaked spectrograms from a 9 fs laser with DOG in argon and with neon as the detection gas. (c) The extracted temporal profile (black line) and phase (red dotted line). The inset shows the temporal profile over a longer delay. (d) The unstreaked spectrum (blue dotted line) and retrieved spectrum (black line) and phase (red dotted line). 99
Figure 3.19 (a) Experimental and (b) retrieved streaked spectrograms from a 9 fs laser with DOG in argon and with krypton as the detection gas. (c) The extracted temporal profile (black line) and phase (red dotted line). The inset shows the temporal profile over a longer delay. (d) The unstreaked spectrum (blue dotted line) and retrieved spectrum (black line) and phase (red dotted line). 100
Figure 3.20 (a) Experimental and (b) retrieved streaked spectrograms from a 9 fs laser with DOG in neon and with neon as the detection gas. (c) The extracted temporal profile (black line) and phase (red dotted line). The inset shows the temporal profile over a longer delay. (d) The unstreaked spectrum (blue dotted line) and retrieved spectrum (black line) and phase (red dotted line). 102
Figure 3.21 Streaked spectrograms generated from argon with the detection gas as (a) krypton, (b) argon, (c) and neon. (d) Neon as the generation gas and detection gas. 103
Figure 3.22 Returning phase as a function of energy. The red line is a linear fit of the short trajectory contribution. 104
Figure 3.23 (a) Al filter transmission, (b) total phase, (c) group delay, and (d) group delay dispersion for 200 nm (black line) and 300 nm (red line) filter thickness. 106
Figure 3.24 Spectrograms generated with argon and krypton as the detection gas with phase compensation from a (a) 200 nm and (b) 300 nm aluminum filter. 107

Figure 3.25 (a) Experimental and (b) retrieved streaked spectrograms from a 20 fs laser with GDOG in argon and with neon as the detection gas. (c) The extracted temporal profile (black line) and phase (red dotted line). The inset shows the temporal profile over a longer delay. (d) The unstreaked spectrum (blue dotted line) and retrieved spectrum (black line) and phase (red dotted line). 108
Figure 4.1 XUV spectrometer for measuring broad spectra. 111
Figure 4.2 XUV spectra from DOG (upper figure) and a linear pulse (lower figure). 112
Figure 4.3 Lineout plot of the DOG spectrum (a) and the TL pulse duration (b). 113
Figure 4.4 (a) Spectrum images without (upper) and with (lower) the filter in place. (b) The lineout plots of the spectra in (a) for the case without (red) and with (blue) the filter in place. The green dashed line is the filter transmission (figure taken from ref. [87]). 113
Figure 4.5 CE phase scan of DOG pulse for water window photons. 114
Figure 4.6 (a) Experimental and (b) retrieved streaked spectrograms from a 9 fs laser from neon. (c) The extracted temporal profile (black line) and phase (red dotted line). (d) The unstreaked (blue dotted line) and retrieved spectrum (black line) and phase (red line). 115
Figure 4.7 The experimental spectrum (red line) as compared with the reflectance of the Mo/Si mirror in the streak camera. 116
Figure 4.8 The KLS laser system. G = grating, PC = Pockels cell, BS = beamsplitter. 117
Figure 4.9 The KLS spectrum before (solid line) and after (dashed line) the spectral filter. 118
Figure 4.10 FROG trace of a 25 fs laser pulse. (a) Experimental trace, (b) retrieved trace, (c) temporal profile (black solid line) and phase (blue dashed line). 118
Figure 4.11 (a) CE phase scan from an argon target generated with a 25 fs pulse. (b) Integrated signal showing the modulation depth and periodicity. 119
Figure 4.12 (a) Streaked spectrogram from 25 fs laser pulse (b) zoomed in portion as indicated in (a). 120
Figure 4.13 (a) Experimental and (b) retrieved streaked spectrograms from a 25 fs laser with argon as the generation gas. (c) The extracted temporal profile (black line) and phase (red dotted line). (d) The unstreaked (blue dotted line) and retrieved spectrum (black line) and phase (red line). 121
Figure 4.14 (a) Comparison of temporal profiles and phases for 60 s (red line) and 1 s (blue line) integration times. (b) Temporal profiles on an extended time scale. (c) Reconstructed

spectra and phases for the pulses in (a). (d) Comparison of the retrieved pulse duration for different integration times. 123
Figure 4.15 CE phase effect on an attosecond pulse when the gate width is less than one optical cycle. In (a), the CE phase is 0 and in (b) the phase is π/2. 124
Figure 4.16 Experimental CE phase effect on an attosecond pulse when the gate width is less than one optical cycle. The upper plot shows the energy vs. CE phase and the lower plot shows the total signal integrated along the energy axis. 125
Figure 4.17 Streaked spectrograms for four different values of the input CE phase. Figure (a) is π, (b) is π/2, (c) is 0, and (d) is 3π/2. 126
Figure 4.18 Streaked spectrograms (upper figures) and f-2f interference fringes (lower figures) for four different values of the input CE phase. Figure (a) is π, (b) is π/2, (c) is 0, and (d) is 3π/2. 127
Figure 4.19 Lineout plots of the CE phase fringe patterns of the lower plots in figure 4.18. 127
Figure 4.20 (a) streaked spectrogram from a CE phase unlocked pulse. (b) The reconstructed temporal profile (solid line) and phase (dashed line). 128
Figure 4.21 (a) The XUV only spectrum for the spectrograms in figure 4.17. (b) the electric fields of the spectrograms extracted through Fourier filtering. 129
Figure 4.22 The temporal profiles for (a) 0 and π and (b) π/2 and 3π/2..... 130
Figure 4.23 Streaked spectrograms from GDOG for CE phases of (a) π and (b) 0..... 130
Figure 4.24 Reconstructed temporal profiles for the spectrograms in figure 4.22. The inset shows the spectrum for each case. 131
Figure 4.25 The electric fields of the spectrograms extracted through Fourier filtering. 131
Figure 4.26 A streaked spectrogram from a xenon target with krypton as the detection gas. 133
Figure 5.1 (a) A streaked spectrogram from an 8 fs laser pulse. (b) The electric field of (a) extracted through Fourier filtering of the spectrogram. 136
Figure 5.2 (a) and (b) two non-stationary signals made up of 10, 25, 50 and 100 Hz signals. (c) and (d) are the frequency domain representations of the signals in (a) and (b), respectively. 137
Figure 5.3 The STFT of the signals in figure 5.2 (a) and (b) respectively. 138
Figure 5.4 The STFT of the electric field in figure 5.1 (b). 138

Figure 5.5 (a) A streaked spectrogram from a 25 fs laser pulse. (b) The electric field of (a) extracted through Fourier filtering of the spectrogram. 139
Figure 5.6 The STFT of the electric field in figure 5.5 (b). 139
Figure 5.7 (a) A streaked spectrogram from an 8 fs laser pulse chirped to ~80 fs. (b) The electric field of (a) extracted through Fourier filtering of the spectrogram. 141
Figure 5.8 The STFT of the electric field in figure 5.7 (b). 141
Figure 5.9 CCD images of a Bessel-Gaussian laser beam along the laser propagation direction and through the laser focus. 142
Figure 5.10 (a) Image of a Bessel-Gaussian intensity profile. (b) A lineout plot through the center of (a). 143
Figure 5.11 (a) Calculated profiles for different outer radii of the input beam (normalized). (b) The same plots in (a) but not normalized. 144
Figure 5.12 (a) Calculated on axis intensity for different outer radii of the input beam. (b) Experimental results for the same conditions as the calculation in (a). 145
Figure 5.13 (a) Spatial streaking with argon as the detection gas and (b) krypton as the detection gas. 146
Figure 5.14 (a) Spatial image with centroid indicated (white solid line). (b) Calculated electric field (solid line) and intensity (dashed line) of (a). (c) Temporal profile of pulse used generate (a). (d) Extracted temporal electric field (solid line) and intensity envelope (dashed line). 147
Figure 5.15 Energy level diagram for He. The purple arrows represent XUV photons. Case 1 is direct ionization while case 2 is double excitation followed by autoionization. 149
Figure 5.16 (a) Physical mechanism for probing the autoionization lifetime. (b) Energy level diagram for laser disturbed He. The purple arrows represent XUV photons and the red arrow is the IR pulse. Case 1 is direct ionization while case 2 is double excitation. 150
Figure 5.17 (a) Helium photoelectron spectrum. The blue arrow indicates the location of the 2s2p resonance. (b) The same spectrum after an intense IR field was added. 151
Figure 5.18 (a) Experimental and (b) retrieved streaked spectrograms from a 9 fs laser with neon as the generation gas. (c) The extracted temporal profile (black line) and phase (red dotted line). (d) The unstreaked (blue dotted line) and retrieved spectrum (black line) and phase (red line). 152

Figure 5.19 (a) Streaked spectrogram with helium as the detection gas. AI = 2s2p resonance, SB1, SB2 = sidebands, MP = mirror peak. (b) Population of the 2s2p autoionization resonance as a function of delay (data points). The red line is a Lorentzian fit added to estimate the lifetime. 153
Figure 5.20 (a) Streaked spectrogram with helium as the detection gas. AI = 2s2p resonance, SB1, SB2 = sidebands, MP = mirror peak. (b) Simulation using SFA. 154
Figure 5.21 Simulated 2s2p Fano resonance population vs. delay. 156
Figure 5.22 Experimental Fano population vs. delay showing control over the direct ionization channel. 156
Figure 5.23 (a) Fano resonance population as a function of laser inensity for the experimental (black squares) and calculated (red circles) cases. (b) The Population vs. delay near the center of the streaking laser for two different intensities. 157
Figure A.1 (a) The driving field, (b) gating field, and (c) vector sum of (a) and (b). The ionization probability is shown in (d). 176
Figure B.1 Polar plot of equation B.3. 178
Figure B.2 Field components including spectral phase after 1st quartz plate. 179
Figure B.3 Field components including spectral phase after both quartz plates and BBO. 180
Figure B.4 Vector sum of field component from figure B.3. 181
Figure B.5 Experimental setup for measuring quartz thickness. 182
Figure B.6 Spectral dips for (a) a short pulse spectrum passing through a 440 μm plate and (b) a long pulse spectrum passing through a 1.68 mm plate. 183
Figure C.1 Phase matching angle vs. wavelength for BBO. 185
Figure C.2 Polar plot of equation B.3 for BBO. 186
Figure C.3 Phase matching bandwidths for (a) 10 μm and (b) 141 μm thick crystals. 187
Figure C.4 Experimental spectra for (a) the BBO and (b) the fundamental laser pulse. 187
Figure C.5 Maker fringes for a 141 μm thick BBO crystal. 188
Figure C.6 Calculated SHG for a 141 μm thick crystal with 28 fs pulses from SNLO 189
Figure C.7 Calculated SHG for a 141 μm thick crystal with 8 fs pulses from SNLO 189
Figure C.8 (a) and (b) Delay between the gating and driving field versus BBO angle. 191
Figure D.1 Experimental setup of the interferometer locking. 193
Figure D.2 Stability measurement of the streak camera. 194

Figure E.1 Photodiode signals for XUV and IR (black line) and IR only (red line). 196
Figure E.2 Measured aluminum filter transmission..... 197
Figure F.1 KLS laser system. G = grating, AOM = accustom-optical modulator, PD = photo diode..... 198

List of Tables

Table 2.1 Gate Width Equation Parameters for Polarization Gating. 21
Table 2.2 Gate Width Equation Parameters for Double Optical Gating..... 27
Table 2.3 Gate Width Equation Parameters for Generalized Double Optical Gating. 55
Table B.1 Sellmeier equation parameters for quartz. 177
Table C.2 Sellmeier equation parameters for BBO. 184

Acknowledgements

I am indebted to many people for the completion of the work in this thesis. First and foremost I wish to thank my advisor Professor Zenghu Chang. As my mentor, he has been a great source of knowledge and advice for all aspects of my graduate career and his seemingly infinite patience with students has been an inspiration for how I hope to interact with colleagues in the future. I was very fortunate to have had the opportunity to work in his group. I also worked closely with several outstanding post-doctoral researchers in my time here. First was Dr. Hiroki Mashiko with whom I spent the vast majority of my time. Nearly all the experimental work done with DOG was accomplished in conjunction with him directly and my skills, techniques and overall research style were heavily influenced by my experiences with him. I also worked closely with Dr. Ximao Feng on the streak camera. The time he spent perfecting the TOF apparatus before I joined the project made for many smooth experiments. Finally, Dr. Chengquan Li spent many hours teaching me how to operate the CEP setup in the lab so that I could be more self sufficient for future experiments.

I was also lucky to have several excellent graduate student colleagues with whom to gain experience. He Wang was my first classmate and a good friend. I benefited from many discussions with him that (often) concerned research. More recently, I have been fortunate to work with Sabih Khan and Michael Chini on all the data analysis from the streak camera and Yi Wu and Dr. Kun "Harry" Zhao with the KLS laser operation. Other past and current KLS members who I have worked closely with are Dr. Mahendra Man Shakya, Dr. Eric Moon, Dr. Shouyuan Chen and Qi Zhang. The experiences with these coworkers have made a great impression on my research directions.

Additionally I would like to thank professors Uwe Thumm, Vinod Kumarappan, Zhijian Pei, and Virginia Naibo for agreeing to serve on my thesis committee.

Finally, I would also like to acknowledge my family and especially my wife, Eli. This work truly would not have been accomplished by me without her support over the past few years.

CHAPTER 1 - Introduction

Since the invention of the laser, the temporal duration of pulses has been significantly reduced [1, 2]. The advances in reducing the pulse duration while maintaining high laser pulse power has driven many areas of physics over the past several decades. The high intensity beams that lasers could provide were always beneficial to atomic, molecular, and optical physicists but once the pulse duration was reduced to picosecond (1 ps = 10^{-12} s) timescales and below, fast dynamic processes could be imaged. In order to image any dynamic process, a light pulse faster than the process itself is required to prevent blurring of the image. This is true for photography as well as electron dynamics in atoms. Once picosecond pulses were created, processes such as molecular rotation were available for full dynamic study. Femtosecond pulses (1 fs = 10^{-15} s) are still being used for the study of processes associated with femtosecond time scales, for example molecular vibration [3, 4].

The fastest events of interest in atomic physics are electron dynamics in atoms. These occur on the attosecond time scale (1 as = 10^{-18} s). For example, the atomic unit of time, or the time it takes for an electron in the first Bohr orbit to travel a Bohr radius, is ~27.2 as. This timescale is beyond the reach of even the shortest laser pulses ever produced directly by any laser amplifier in the world. In order to reach even sub-femtosecond pulses, transform limited spectra with full width at half maximum (FWHM) bandwidth of greater than 2 eV are required. As a comparison, some of the shortest femtosecond laser pulses ever produced (~2.8 fs) only required ~1.5 eV of spectral bandwidth [5]. This however is nearly a single cycle of the driving laser period. Obviously another method is required to reach sub-femtosecond pulse durations.

1.1 Attosecond Pulse Trains

About the time that sub 5 fs laser pulses were first being produced, the process of high-order harmonic generation was discovered [6]. When a ND:Yag laser at 1064 nm center wavelength was focused to an intensity of ~10^{13} - 10^{14} W/cm^2 in a rare gas, a series of odd-order harmonics of the fundamental laser was produced. It was expected that intensities of this magnitude would fully ionize a rare gas through multiphoton ionization [7] so the result was unexpected.

Some interesting characteristics of the spectrum were quickly noticed as well. For instance, only odd-orders were generated. This was explained by the isotropic nature of the target as well as its inversion symmetry [8]. If the symmetry of the target was broken in some way, even orders might also be present as with second harmonic generation in a non-centro-symmetric barium-borate (BBO) crystal. Another feature that was noticed was that the spectrum quickly decayed for the lowest orders but then remained relatively flat for the next several orders beyond this. The extent of the flat region, referred to as the plateau, was scalable with the intensity of the generating laser. This implied that extremely broad spectra could be generated with this method. Finally, the HHG radiation was found to have excellent temporal coherence [9] meaning it would be an attractive way to generate a broad spectrum, short wavelength source in a laboratory table top setup.

1.1.1 The Principle of High-order Harmonic Generation

In 1994, the so-called three step model was put forth to explain, in a semi-classical way, the process of high-order harmonic generation [10]. Figure 1.1 shows a schematic of the model.

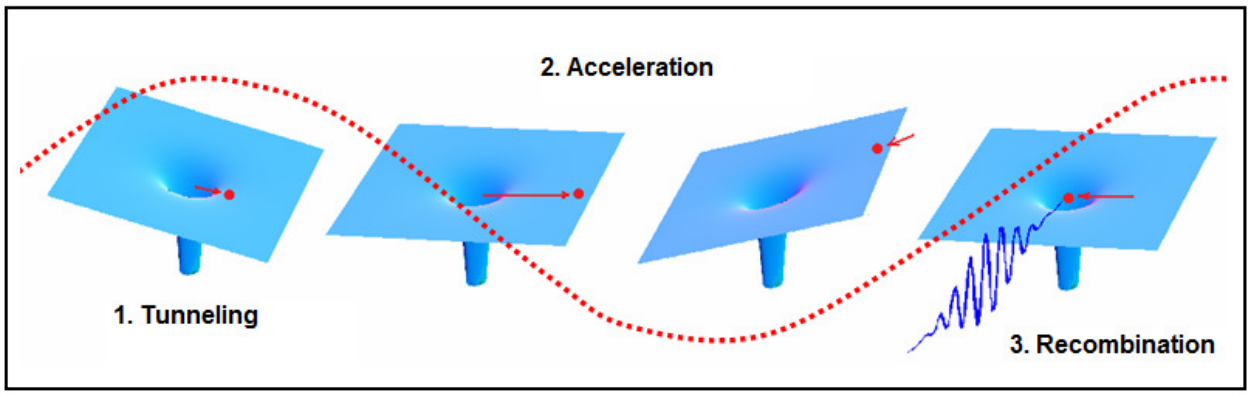

Figure 1.1 The 3 Step Model for HHG (adapted from [1]).

First, a ground-state bound electron in an atomic potential can tunnel through the atomic potential when a strong, oscillating electric field from a laser is applied. After the electron is liberated from the atom, it can be treated classically when two conditions, first introduced by Keldysh, are met [11]. First, the electron in the continuum states is no longer affected by the coulomb interaction of the atom. Second, only the ground state of the atom is considered in the

evolution of the system. All other states are ignored. This is true in the non-perturbative regime where the Keldysh parameter, γ, is less then 1. The equation for γ is:

$$\gamma = \sqrt{\frac{2I_p m\omega^2}{e^2 E_0{}^2}}, \tag{1.1}$$

where I_p is the ionization potential of the atom, m and e are the electron mass and charge, respectively, ω is the laser frequency, and E_0 is the laser field amplitude [12].

After tunneling, the electron's equations of motion can be solved analytically and the equation can be treated classically. An electron born at time t_0 will have acceleration in an oscillating laser field, $E=E_0 Cos(\omega t+\varphi_{CE})$ given by:

$$a(t) = \frac{eE_0}{m} Cos(\omega t + \varphi_{CE}) \tag{1.2}$$

where φ_{CE} is the carrier-envelope phase (CEP) of the laser. The electron will travel some distance from the parent ion and when the electric field of the laser switches sign, the electron will reverse direction and return. Integrating the acceleration from the born time to the final recombination time, t_f, and calculating the resulting kinetic energy of the electron yields:

$$KE = 2U_p(t)(Sin(\omega t_f + \varphi) - Sin(\omega t_0 + \varphi))^2 \tag{1.3}$$

where $U_p(t)$ is the cycle-averaged kinetic energy, or ponderomotive energy, of the electron "quivering" in the laser field. $U_p(t)$ is given by:

$$U_p(t) = \frac{e^2 E_0(t)^2}{4m\omega^2}. \tag{1.4}$$

After propagating in the laser dressed continuum, the electron has a probability of recombining with the parent ion. The electron releases all the kinetic energy it gained in the laser field in the form of an attosecond pulse once it returns to its ground state. The energy of the photons released depends on when the electron was born in the oscillating field. The ellipticity plays a strong role in this process and will be discussed in detail later.

Integrating the velocity of the electron from t_0 to t_f yields the time dependent position, x(t), of the electron. From x(t), it is a simple numeric exercise to plot the phase of the laser when the electron returns as a function the phase of the laser when the electron is born. Figure 1.2(a) shows this graph. Once this plot is obtained, the kinetic energy as a function of the born time

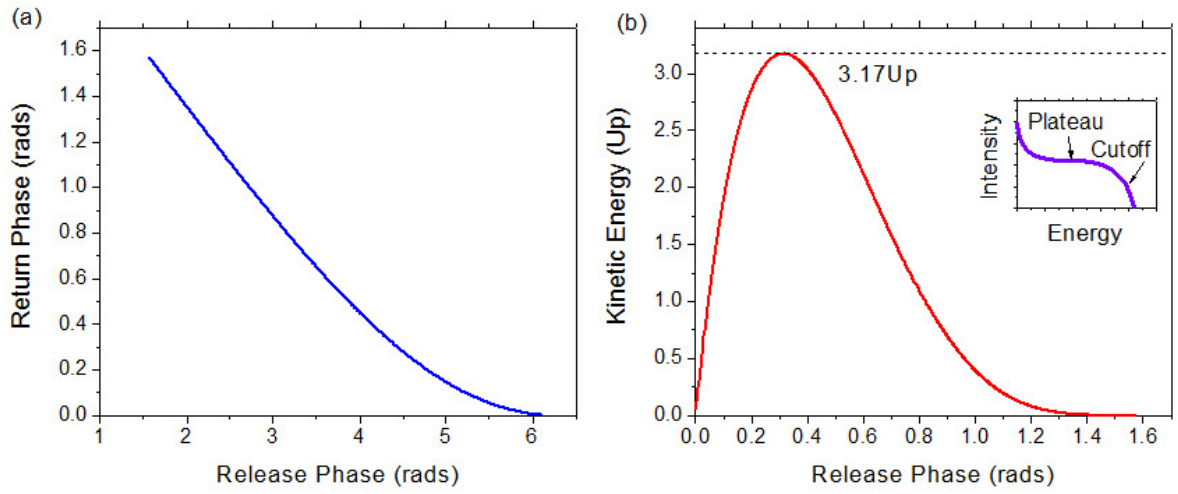

Figure 1.2 (a)Return phase versus release phase (b) Electron Returning Kinetic Energy

phase, t_0, of the laser can be calculated and is shown in figure 1.2(b). The inset of figure 1.2(b) shows a rough picture of what a continuous harmonic spectrum looks like. After a fast decrease in intensity of the low orders, the spectrum flattens out forming a broad plateau. Finally, the spectrum quickly decreases again at the cutoff orders. The cutoff orders are those calculated from the maximum value of figure 1.2(b). Since low order harmonic generation is a nonlinear process, this explains the sudden drop off in the spectrum up to ~ the 7th order. For example, second harmonic generation is a $\chi^{(2)}$ process. Similarly, third harmonic generation is a $\chi^{(3)}$ process and so on with each order becoming more nonlinear and hence requiring more intensity for the same output power. The same dependence might be expected for the high orders as well. Instead, after the first few low orders, the next harmonics, while still highly and increasingly nonlinear, do not have the same dependence giving rise to the relatively flat plateau of the spectrum. This is due to HHG occurring at intensities in the strong field, or non-perturbative, regime where normal nonlinear optics is no longer valid.

In 1.2(b), the kinetic energy of the electron reaches a maximum at a release phase of ~0.3 rads. The value at this point gives the following result for the maximum kinetic energy:

$$E_{co} = I_p + 3.17U_p \qquad (1.5)$$

where E_{co} is the highest energy photon possibly released and Ip is the ionization potential of the parent ion. Equation 1.4 implies that if the intensity of the driving laser is increased, the cutoff

order harmonic is increased as well. This means that the spectral bandwidth is limited only by properties of the target and the intensity of the laser being used. Phase matching plays a role here as well and will be discussed in chapter 2. Also, in figure 1.2(b), there are two regimes for electron recombination. All trajectories from release phase 0 to ~0.3 rads are known as the long trajectories while those from ~0.3 rads to $\pi/2$ rads are known as the short trajectories. Figure 1.3(a) indicates this more clearly. Both the long (green dashed) and short (blue dashed) trajectories reach a maximum energy at ~0.3 rads. The long trajectories are those whose time in the laser dressed continuum is longer than Eco (shown as a black solid line) and the short trajectories are those whose time is less than Eco.

From the results in figure 1.3(a), it can be seen that different energy photons return at different times in the oscillating laser pulse. This results in an intrinsic chirp of the attosecond pulse. Plotting the returning kinetic energy of the electron (and hence the photon energy) as a function of the return time yields the result in figure 1.3(b). Here it can be seen that energy of the harmonics far away from the cutoff (plateau harmonics) has an approximately linear dependence on the return time of the electron which generated them. This is the chirp associated with HHG and has been well known [13-15]. The short trajectories have a positive

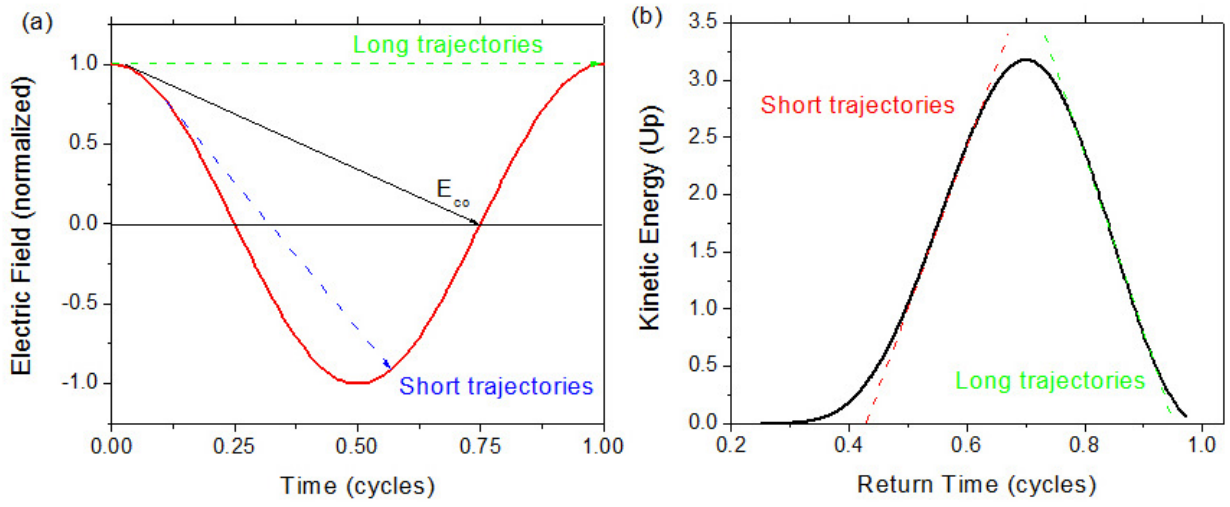

Figure 1.3 (a) Possible trajectories from an electron in a laser field. (b) The return kinetic energy versus return time. The long (green) and short (red) trajectories are indicated.

chirp (red dashed) and the long trajectories have a negative chirp (green dashed). The intrinsic chirp of the attosecond pulse will also be discussed in more detail in section 3.3.1. As will be seen in chapter 2, the long trajectory contribution can be significantly reduced through phase matching considerations meaning only the short trajectories are important for most applications. This is important for generating "clean" spectra since the long and short trajectories not only have different phases, but also different divergences [9, 16]. This process can also be treated quantum mechanically [17] and can accurately simulate the resulting single atom response to an intense laser field. However, the semi-classical 3 step model makes accurate predictions and is easy to use in an experimental setting.

HHG is intrinsically an attosecond process since the recombination of the returning electrons emit attosecond pulses. This tunneling, propagation, and recombination occurs once per half laser cycle meaning, for a multi-cycle pulse, a train of attosecond pulses is generated with a periodicity of half an optical cycle. While attosecond pulse trains have several applications [18-20], using an isolated pulse for pump-probe experiments is desirable since contributions from pre and post pulses can modify time-resolved experimental results.

1.2.1 Experimental setup

Generating a train of attosecond pulses from HHG is simple to do experimentally. Figure 1.4(a) shows an extreme-ultraviolet (XUV) spectrometer capable of measuring the spectrum of emitted harmonics [21]. A long, multi-cycle laser pulse is focused with an f=400 mm focal length parabolic silver coated mirror (Juno Optics) into a 1.4 mm long gas target. The gas target is a glass cell with two laser drilled holes in it. The cell is filled with (usually) either argon, neon or helium at pressures on the order of 10 Torr. The excess gas is evacuated from the chamber with three 7 l/s roughing pumps. This maintained a background pressure in the chamber of ~ 300 mTorr.

As long as the laser intensity is on the order of 10^{14} W/cm^2, a train of attosecond pulses is generated (see figure 1.4(b)). From here, the pulse train propagates along with the infrared (IR) driving laser to a thin (~300 nm) aluminum filter. This filter removes the residual IR laser leaving only the XUV photons. As will be seen in the temporal characterization section, the filter can be used to partially compensate the intrinsic chirp of the HHG process. However, since this is solely a spectral domain measurement, the filter is used for removing IR photons only.

The filter also acts as differential pumping, separating the high pressure HHG side from the low pressure detector side. This means the filter cannot be removed from the beamline. Since filters have a limited transmission bandwidth, care must be taken in selecting a filter which blocks the IR, remains strong enough to act as differential pumping, and transmits as many XUV photons as possible. For this, aluminum was found to work very well for a broad range of harmonics. The transmission range covers ~15 eV to 72 eV corresponding to the 9th harmonic to the 45th harmonic of an 800 nm laser [22]. After the filter, a XUV photodiode (AXUV 100, IRD Inc.) could also be inserted to measure the actual photon flux of the XUV beam online.

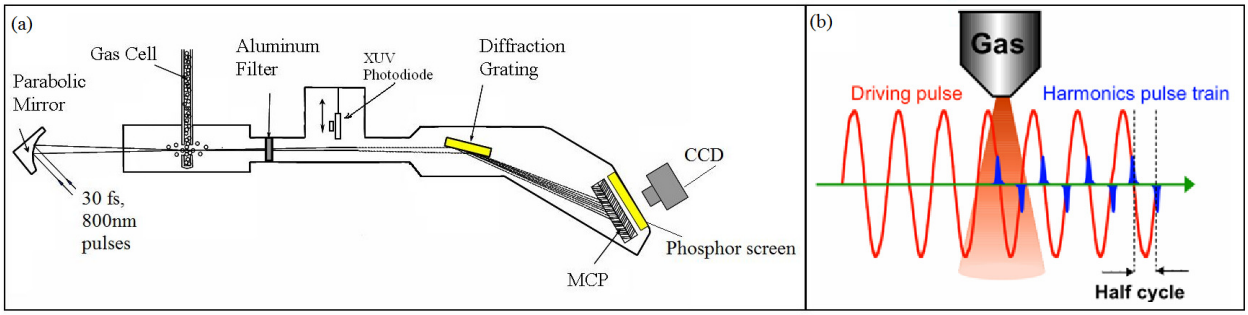

Figure 1.4 (a) XUV Spectrometer (b) Attosecond pulse train from a gas target

After the filter and photodiode, the harmonics were incident on a torroidal grating (Horiba Jobin Yvon). The grating had 384 lines per mm and gave a measured energy resolution of ~280 meV at 45 eV. Since the harmonics are odd orders, they are separated by two photons or ~3 eV. 280 meV is sufficient for resolving such harmonics. After the grating, the harmonics were incident on a microchannel plate detector with ~1200 V applied and phosphor screen with ~2000 V applied. The high gas density side of the chamber needs to be isolated from the microchannel plate detector to prevent arcing across the high-voltage plates which is why the filter needs to remain in place. A single turbo pump with pumping rate of 250 l/s with a roughing pump of 7 l/s was used to ensure the pressure on the detector side was never higher than ~5 x 10^{-6} torr at the location of the detector. An image of the spectrum was recorded with a water cooled CCD camera. Figure 1.5(a) shows spectra generated from an argon target (blue line) and from a neon target (red line) under the same experimental conditions. The two spectra are normalized with respect to each other but in reality, the argon spectrum is more than 10 times

stronger than the neon spectrum due to its low ionization potential. The spectra are both limited by the edges of the spectrometer but actually extend beyond the range indicated. The background in both cases is identical and is light leaking onto the spectrometer.

It is important to note that the argon spectra have a reduced cutoff as compared to the neon spectrum even though both spectra were taken with roughly the same intensity. This is because argon has a lower ionization potential (15.6 eV) than neon (21.6 eV) meaning that once the intensity gets too large, the target is fully ionized. This result can be seen is figure 1.5(b). This plot shows the ionization probability as a function of delay for a laser pulse in argon (blue line) and neon (red line) as calculated by the ADK method [23]. The calculation is outlined in Appendix A. The calculation was conducted using a 30 fs pulse duration and peak intensity of 5.6×10^{14} W/cm^2 which were the actual experimental conditions. Before the center of the laser pulse where the intensity is the highest, the argon target is full ionized while the neon target is only ~25% ionized. Since the highest order harmonic depends on intensity, the argon cutoff should be much lower than the neon cutoff which is what was found experimentally. The upper figure in 1.5(b) shows the shape of the 30 fs pulse used in the calculation. The ionization "steps" in the ionization probability calculation occur at each half cycle.

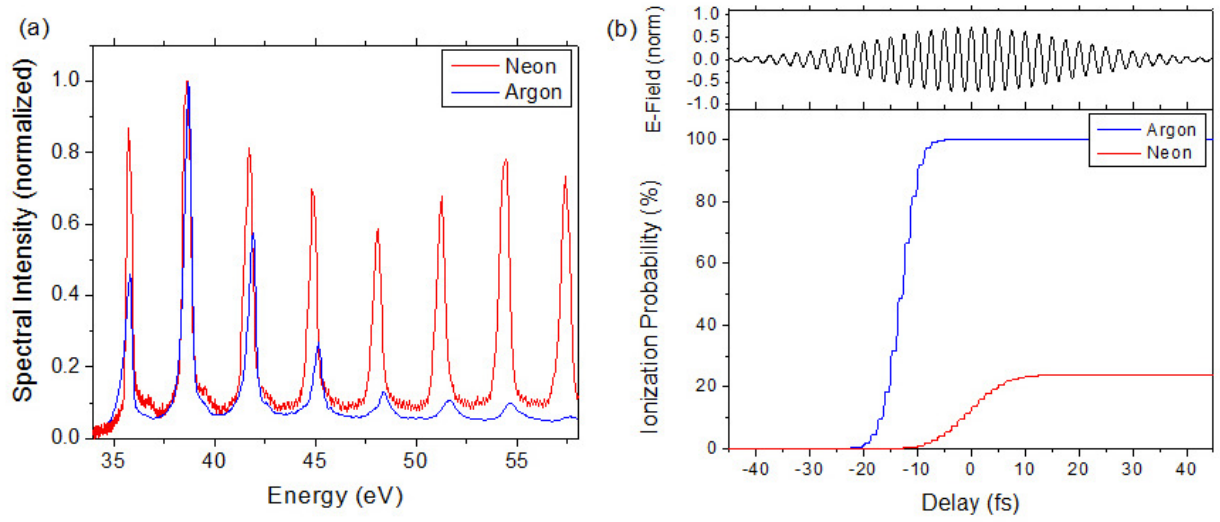

Figure 1.5 Long Pulse Spectra (a) and ADK Calculations (b)

1.3.1 Hints of Isolated Sub-femtosecond Pulses

The discrete harmonic spectrum in figure 1.5(a) is indicative of HHG from long (~30 fs) linearly polarized laser pulses. Since the harmonic spectrum is the energy domain representation of a temporal domain train of attosecond pulses, it is expected that increasing the number the pulses in the train should further narrow the individual harmonic bandwidths. This can be accomplished by positively chirping the driving laser pulses [24, 25]. Conversely, reducing the number of pulses in the train will increase the width of each peak. Of course if there was only one pulse in the train, the spectrum would be continuous and maximally broadened. Figure 1.6(a) shows a spectrum of harmonics from a 9 fs driving laser (black line). Clearly the peaks are broader than the 30 fs spectrum (red line). The peaks are also shifted with respect to the two pulse durations. This is because each spectrum consists of harmonics of the driving laser. For a 30 fs pulse from the Kansas Light Source (KLS) amplifier, the center wavelength is ~800 nm and the harmonics are integer multiples of 1.55 eV. For the 9 fs case, a pulse shortening technique was used - a hollow core fiber, which resulted in a very broad spectrum for the driving laser, but with a different center wavelength. In this case the center was at ~750 nm or 1.65 eV. Figure 1.6(b) gives an idea of what the temporal domain representation of such a spectrum might look like as compared with that from a 30 fs pulse. The upper electric field is from a 9 fs pulse while the lower field is from a 30 fs pulse. The blue peaks represent the attosecond pulses in the train and are generated at every half optical cycle. These results imply that by simply reducing

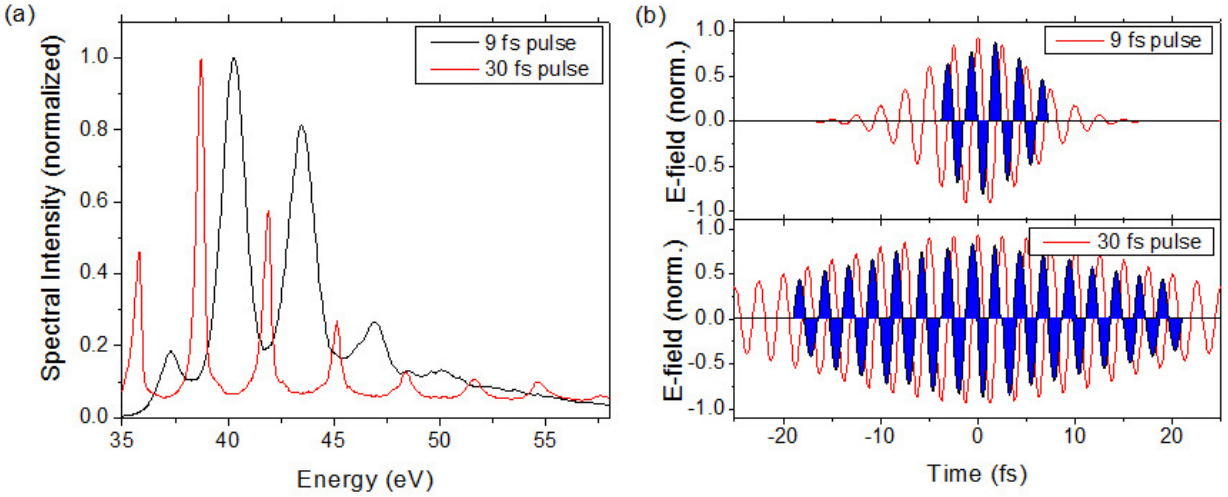

Figure 1.6 Long Pulse versus Short Pulse Spectrum (a) and representation of the attosecond pulse trains in each case (b).

the driving laser pulse duration as much as possible, a single attosecond pulse can be generated. This is the principle behind amplitude gating [refs]. Here, the driving pulse is made to have duration as close to half of an optical cycle as possible. Since the harmonic generation process is intensity dependent, the highest orders (near the cutoff of the spectrum) are generated only by the center cycle of the driving laser. The pre and post pulses are generated from lower intensity. As such, the cutoff is a continuum while the plateau orders are discrete. Simply using a mirror that reflects only the wavelength portion of the cutoff truncates the spectrum giving a single attosecond pulse. While this method is capable of generating short attosecond pulses [refs], it is very difficult to implement (only one group has thus far been able to demonstrate its effectiveness) and it purposely throws away a large portion of the harmonic flux, namely all of the plateau harmonics.

1.4.1 Overview of this Thesis

The overall goal of this work is to show that isolated attosecond pulses can be generated from multi-cycle lasers with relative ease. The pulses also must have usable amounts of flux to make them useful for pump-probe experiments. To this end, several demonstrations were conducted to show the effectiveness of the generation method we developed in the KLS.

First will be a demonstration of the spectral characterization of the attosecond pulses generated. This shows that the method used for generating the attosecond pulses agrees with all predictions in the spectral domain. This is nicely demonstrated with a carrier-envelope phase scan of the generating laser while recording the output spectrum.

To prove that the attosecond pulses are truly isolated in the temporal domain, attosecond streaking is carried out on the pulses generated. We also use this method to show the effectiveness of the method in generating high flux pulses and with very broad spectra.

Finally, the gating method is applied to generate the broadest isolated attosecond pulses ever and also to generate pulses under any laser pulse duration and carrier-envelope phase. The attosecond pulses themselves are also used in a pump-probe experiment to control electron dynamics in helium for the first time. All of these results represent a full analysis of the gating method while also demonstrating its effectiveness under a variety of conditions.

CHAPTER 2 - Attosecond Pulse Generation

This chapter will give an overview of the methods of DOG and GDOG for generating isolated attosecond pulses. The advantages of this method will be discussed in detail and compared with other gating techniques. The pulses will be fully characterized in the spectral domain and the method of how the flux of the pulses was optimized will be discussed. While this is not unequivocal proof that we have generated attosecond pulses, it does provide unique features only present in our methods while also providing evidence that our pulses are truly isolated.

2.1 Principle of Double Optical Gating

Double optical gating or DOG, as its name suggests, is a combination of two gating methods which have both been used previously in the production of broad spectra and single attosecond pulses. In this section, I will describe the two gating methods, known as two color gating and polarization gating, and discuss the benefits and disadvantages to using each one independently.

2.1.1 Two Color Gating

As was shown in section 1.2.1, a laser focused into a gas target will produce a spectrum of odd-order harmonics of the fundamental laser. Mathematically this is explained by the fact that the Fourier transform of a train of pulses separated by half an optical cycle of the driving laser will result in odd multiples of the fundamental frequency. This is physically explained by the symmetry of the target, which, for an isotropic rare gas with inversion symmetry, is centrosymmetric [8]. If the symmetry is somehow broken, like in a BBO crystal, even orders can also be produced since the Fourier transform of a pulse train with full cycle periodicity yields even and odd order harmonics of the fundamental. Breaking the symmetry of an isotropic gas target is, of course, difficult so an alternative way to accomplish this is by breaking the symmetry of the driving laser [26-28].

Since the harmonic generation process requires high intensity and is highly nonlinear in intensity, even a slight change to the laser field can drastically change the spectrum [29]. By adding a weak, linearly polarized second harmonic field to the fundamental driving laser, every

other half cycle is reduced while the other cycles are slightly enhanced for certain values of phase between the two pulses. The time varying electric field is described by the equation:

$$E(t) = E_0 \cos(\omega t + \varphi_{CE}) + aE_0 \cos(2\omega t + 2\varphi_{CE} + \phi_{rel}), \quad (2.1)$$

where a is ratio of the amplitude of the second harmonic with respect to the fundamental frequency, $2\varphi_{CE}$ is the carrier envelope phase of the second harmonic, and ϕ_{rel} is the relative phase between the second harmonic and fundamental. The role of the relative phase is important for deciding the nature of the total field. Figure 2.1 shows the fundamental and second harmonic

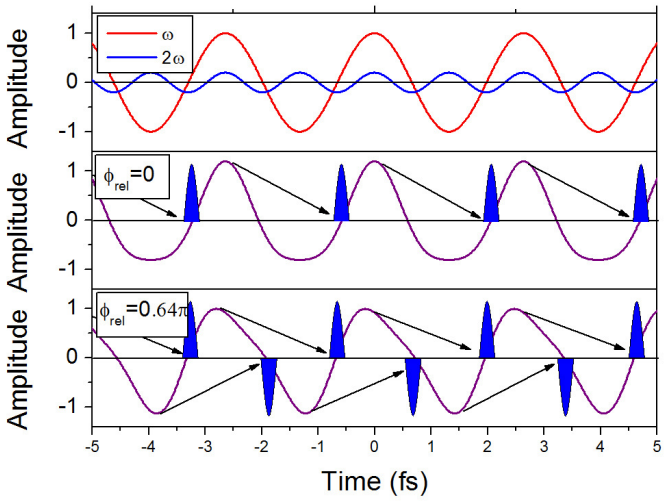

Figure 2.1 Two-Color Electric Field Distributions (a). Individual fields (b). Combined fields with ϕ_{rel}=0 (c) Combined fields with ϕ_{rel}=0.64π.

fields (with a = 0.2) individually (upper figure) followed by two total electric field distributions for $\phi_{rel} = 0$ (middle figure) and $\phi_{rel} = 0.64\pi$ (lower figure). When $\phi_{rel} = 0$, the resultant field has a broken symmetry. If the second harmonic amplitude is strong enough, every other cycle would not have sufficient intensity to generate an attosecond pulse resulting in a full cycle periodic train. In the case of the lower figure ($\phi_{rel} = 0.64\pi$), the attosecond pulse train would still have the same periodicity as a one color field.

Adding the second harmonic to the fundamental will obviously change the electron trajectory during its excursion away from the parent ion during the HHG process. It was found that a slight cutoff extension can be obtained if the relative phase of the second harmonic is chosen appropriately and that an attosecond pulse train with enhanced contrast between the

center pulse and any pre/post pulses can be produced in this way [30]. Figures 2.2(a) and (c) show the calculated return phase as a function of the release phase for

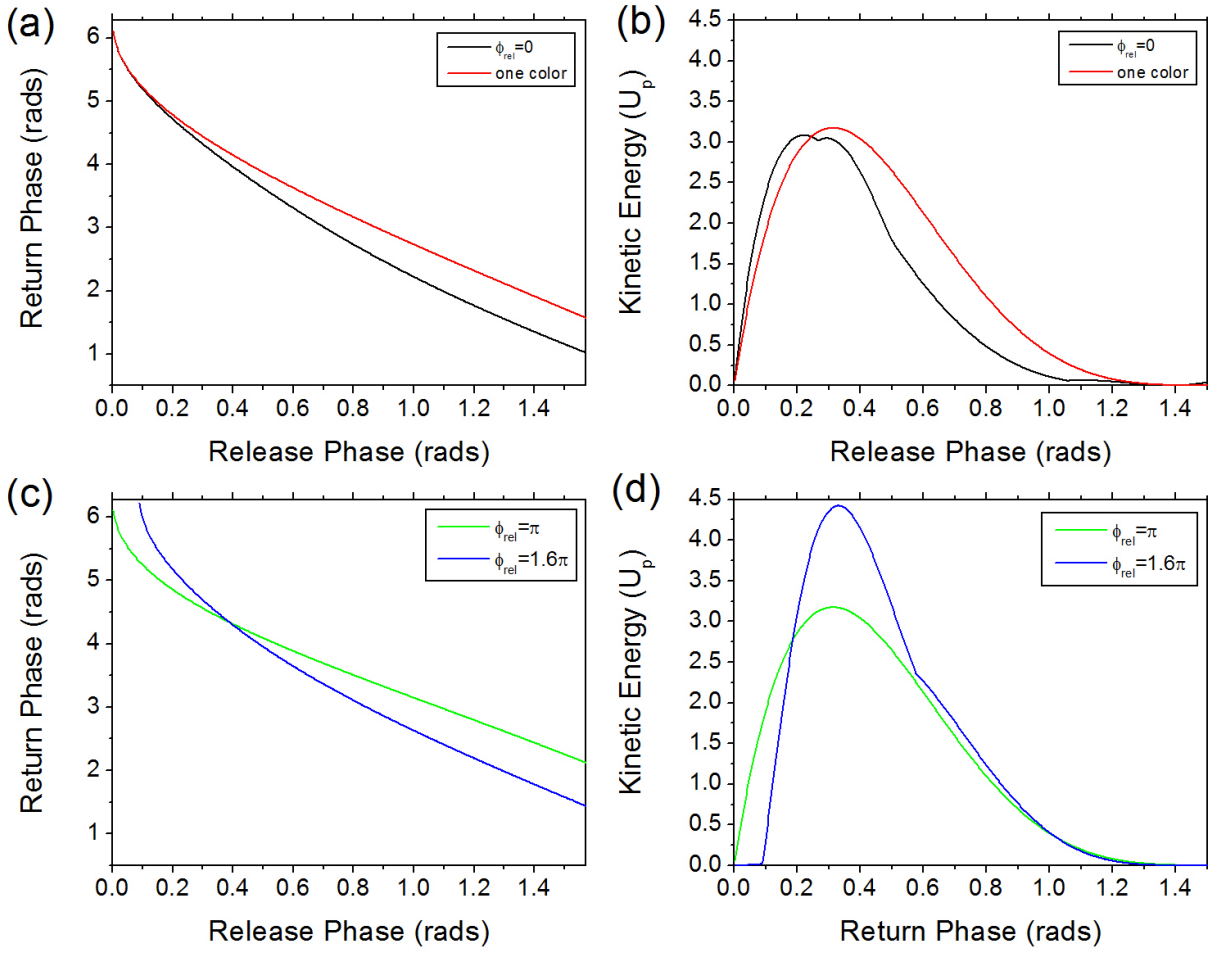

Figure 2.2 (a) Return phase versus release phase for ϕ=0 (black) and for a one color field (red). (b) Electron Returning Kinetic Energy in a Two-Color Field with ϕ=0 (black) and a one color field (red). (c) Return phase versus release phase for ϕ=π (green) and for ϕ=1.6π (blue). (d) Electron Returning Kinetic Energy in a Two-Color Field with ϕ=π (green) and for ϕ=1.6π (blue).

several values of relative phase between the second harmonic and the fundamental. The one color case is also shown for reference. From this result, the electron kinetic energy when the electron returns was calculated and is displayed in figures 2.2(b) and (d). In all cases, *a* was

chosen to be 0.2. This result indicates that the attosecond pulse train can have a cutoff extension when the relative phase is chosen properly and reaches a maximum around 0.64π. However, under this condition, the attosecond pulse is not truly isolated.

In order to generate a two color spectrum experimentally, an interferometer was used. Figure 2.3 shows the experimental setup. The input laser with pulse was separated with a

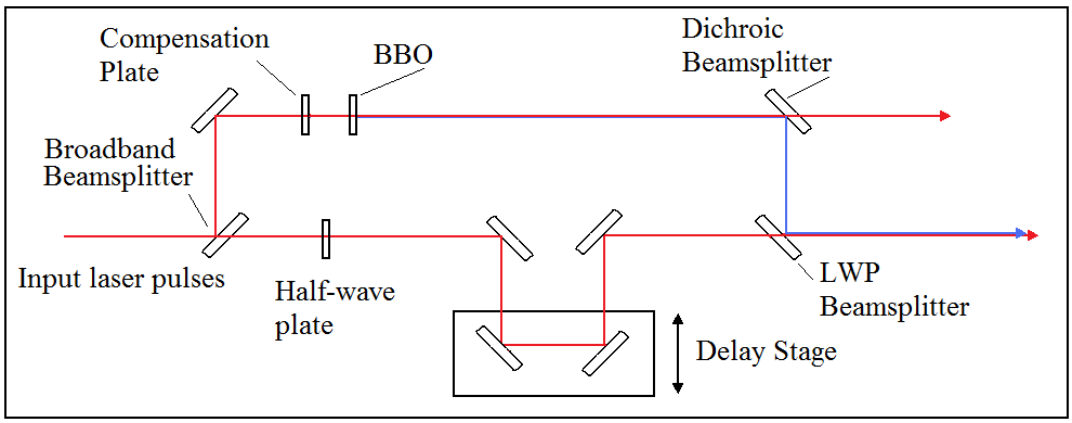

Figure 2.3 Interferometer for Generating a Two-Color Field

broadband 50/50 beamsplitter (LayerTec). Half of the beam was sent through a compensation plate to ensure equal dispersion to the other half of the beam and then through a BBO crystal (Altos Photonics) for second harmonic generation. The second harmonic and fundamental IR beams then reflected off a Dichroic beamsplitter (CVI) that reflected the second harmonic with ~90% reflectivity and transmitted the IR with ~95% transmittance. The remaining second harmonic then reflected from a long wave pass (LWP) beamsplitter. Meanwhile, the other half of the original IR laser passed through an equal optical path length as the second harmonic and recombined with the second harmonic at the LWP. This beam had an achromatic halfwave plate installed so that its polarization could be matched to the second harmonic. This is critical since the second harmonic is generated with an orthogonal polarization to the fundamental laser in type-1 BBO crystals. This beam also had a delay stage so that the relative phase between the second harmonic and IR beams could be controlled. After this, both beams entered the same XUV spectrometer as shown in figure 1.4.

To fully test the two-color gating method, HHG from several pulse durations was conducted. The Ti:Sapphire amplifier naturally produced ~30-35 fs pulses at 1 kHz to 2 kHz depending on the operating conditions. To reduce this to few-cycle pulses, the 2 mJ energy laser pulse was focused into a hollow-core fiber with an inner diameter of 400 μm. The fiber was filled with ~20-30 psi neon gas to generate self-phase modulation to spectrally broaden the pulse. After the fiber, several bounces on multi-layer chirped mirrors allowed the low order phase distortions from the fiber to be compensated. Adding extra mirrors also allowed the pulses to be pre compensated for any extra dispersive materials (waveplates, beamsplitters, etc.) that might be in the beam path later.

This system routinely produced spectra capable of supporting pulse durations of ~7-10 fs. It also generated spectra that could support ~5 fs pulses with high output power [31] if a lot of care was taken with the alignment and input laser conditions. To temporally characterize our pulses, we used the frequency resolved optical gating (FROG) technique. Figure 2.4 shows a FROG trace for a ~9 fs pulse; typical of our normal, everyday operations.
The spectrum output from the fiber is shown in figure 2.4(a). 2.4(b) shows the experimental and retrieved FROG traces. The reconstructed temporal profile is shown in 2.4(c).

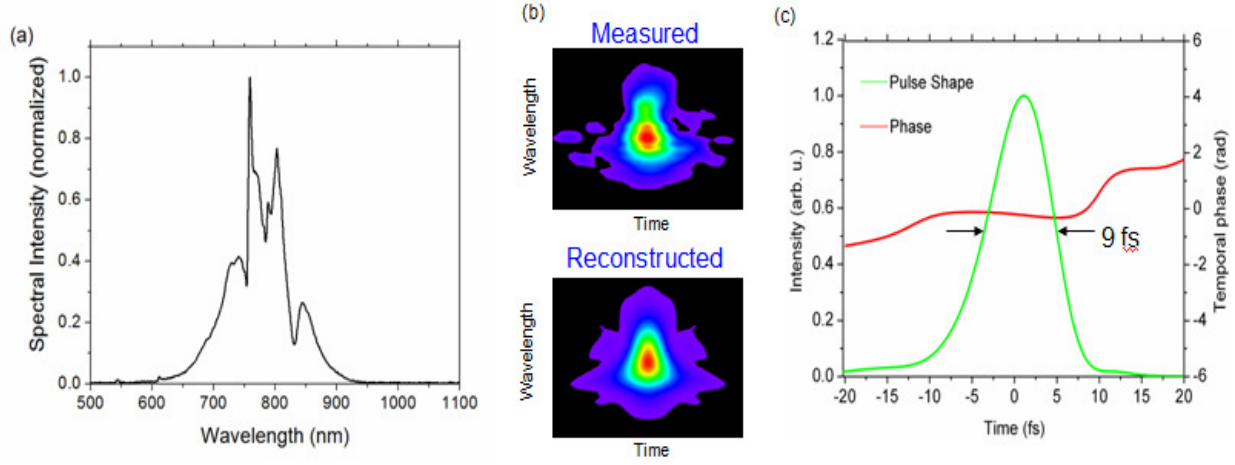

Figure 2.4 (a) Spectrum of a 9 fs pulse (b) FROG trace for a 9 fs laser pulse (c) reconstructed temporal profile and phase.

Figure 2.5 shows harmonic spectra from a two color field. The generating pulse durations were 30 fs (black line) and 9 fs (red line). The even and odd orders are clearly present and again, the

spectrum is broader for the shorter input pulse duration. These results are very similar to previous results with two-color gating [32].

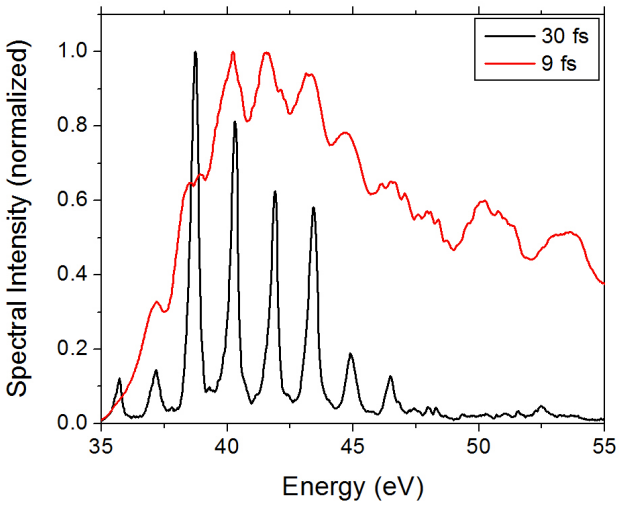

Figure 2.5 Two-Color Linear Spectra.

While this method is successful in generating broader spectra than a one-color field alone, the spectra is still modulated indicating multiple pulses in the train. However, since the individual harmonic orders broaden as the generating pulse reduces and due to limitations in the resolution of the spectrometer, the results of figure 2.5 do not guarantee a single attosecond pulse is generated, rather a train of pulses is instead likely. Simulations have been done suggesting that the attosecond pulse train can be reduced to a single attosecond pulse with a small train of pre and post pulses [30] but in order to use attosecond pulses for nonlinear experiments, the satellite pulses must be many orders of magnitude below the main pulse. This limitation means two-color gating alone will not work for true isolated attosecond pulse generation.

2.1.2 Polarization Gating

The second gating method included in DOG is polarization gating. This method has already been demonstrated to generate single isolated attosecond pulses independently [33, 34]. The method capitalizes on the strong ellipticity dependence of the HHG process to effectively gate a single pulse from an attosecond pulse train. It was shown previously [35-37] that as the ellipticity of the generating laser increases, the harmonic efficiency drops off quickly. This can

be explained with the 3-step model. After the electron is born into the laser dressed continuum, it is steered by the laser field itself. A linearly polarized field will cause the electron to return to the parent ion. If the generating field has some degree of ellipticity however, the electron can be steered away from the parent ion resulting in no recombination, and hence no attosecond emission. This effect is maximized for circularly polarized fields. Here, the electron will never return to the parent ion. Since this a cumulative effect incurred on the electron, the more time it spends in the continuum, the more likely it is to be steered away. Since, for the short trajectories, the highest energy electrons spend the most time away from the parent ion (see figure 1.3), they are more sensitive to the ellipticity of the generating field.

Experimentally, gating a single pulse from a train is accomplished by changing a linearly polarized, few-cycle laser pulse into a pulse with a time-varying polarization state. By superimposing a right and left circularly polarized laser pulse with some amount of delay, T_d, between them, a pulse that has circularly polarized leading and trailing edges and with a small linear portion in the center is created [38-42]. Figure 2.6(a) shows the pulse. By controlling the delay between the two counter-rotating pulses, the thickness of the linear portion can be controlled. The way this gates a single pulse from an attosecond pulse train is by only allowing attosecond pulses to be formed when the laser field is linearly polarized. If the linear portion is ~the periodicity of the attosecond pulse train, only one pulse can be formed. If the ellipticity varying pulse is broken up into its orthogonal components, they look like those shown in figure 2.6(b). The vector sum of the fields, given by $\vec{E}(t) = E_{drive}(t)\hat{i} + E_{gate}(t)\hat{j}$, results in the ellipticity varying pulse in 2.6(a). The upper figure in 2.6(b), called the driving field, is expressed as:

$$E_{drive}(t) = E_0[(e^{-2\ln 2\frac{(t+T_d/2)^2}{\tau_p^2}} + e^{-2\ln 2\frac{(t-T_d/2)^2}{\tau_p^2}})\cos(\omega_0 t + \varphi_{CE})] \quad (2.2)$$

and the lower figure is the gating field, described by:

$$E_{gate}(t) = E_0(e^{-2\ln 2\frac{(t+T_d/2)^2}{\tau_p^2}} - e^{-2\ln 2\frac{(t-T_d/2)^2}{\tau_p^2}})\sin(\omega_0 t + \varphi_{CE}) \quad (2.3)$$

where E_0 is the amplitude of the circularly polarized fundamental laser field with carrier frequency ω_0 (period T_0), pulse duration τ_p, and CE phase φ_{CE}. T_d is the time delay between the two circular pulses. In the figure τ_p is 7 fs, T_d is 11.76 fs, ω_0 corresponds to an 800 nm laser pulse, and φ_{CE} is 0.

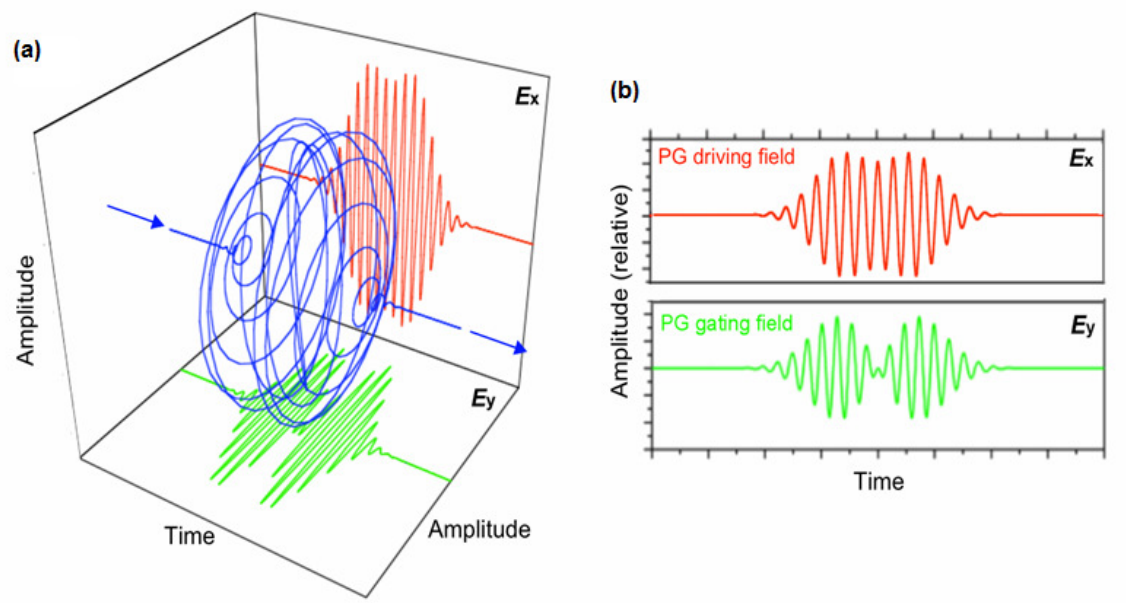

Figure 2.6 (a) Total Electric Field Components for Polarization Gating (b) Driving field (red line) and Gating field (green line).

The important feature of these two components it that the gating field goes to zero at the center of the pulse while the driving field is some non-zero value. Together, these two pulses give a linear portion at the center, and some degree of ellipticity everywhere else. Taking the ratio of the magnitude of the envelopes of the gating field to the driving field yields the time varying ellipticity:

$$\xi(t) = \frac{\left|E_{gate}\right|}{E_{drive}} = \frac{\left|1 - e^{\frac{-4\ln(2)T_d t}{\tau_p^2}}\right|}{\left(1 + e^{\frac{-4\ln(2)T_d t}{\tau_p^2}}\right)}. \tag{2.4}$$

Plotting this versus t yields the result in figure 2.7. At the center of the plot, the ellipticity is zero indicating linear polarization. As $t \to \infty$, the ellipticity goes to 1 implying circular polarization. Since the harmonic generation process depends on the recombination probability of the electron with the parent ion which in turn depends on the ellipticity of the laser, an understanding of where attosecond flux will be generated can be deduced from this plot. However, since the recombination probability depends on several factors, there is no hard edge where HHG no

longer works. In order to gain further understanding about the field, a Taylor expansion of equation (2.4) about the center of the pulse can be calculated. The first non-trivial term yields:

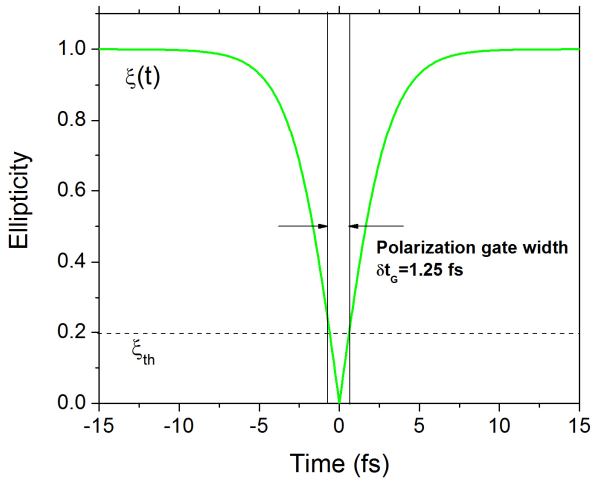

Figure 2.7 Time Dependent Ellipticity for Polarization Gating.

$$\xi(t) = \left| 2\ln(2)\frac{T_d}{\tau_p^2} t \right|, \tag{2.5}$$

which is the portion of the pulse where the ellipticity is ~linear. Solving equation (2.5) for t and multiplying by two gives the temporal window over which the HHG flux is maximized. This is called the "gate width" and is expressed as:

$$\delta t_G = \frac{\xi_{th}}{\ln(2)} \frac{\tau_p^2}{T_d}, \tag{2.6}$$

where ξ_{th} is the threshold ellipticity for harmonic generation. This is ~0.2 for the plateau harmonics from argon [35]. As an example, for a 5 fs laser pulse with 6 fs delay between the right and left circularly polarized pulse, δt_G = 1.25 fs which is half of an optical cycle of a laser pulse with center wavelength of 750 nm. This is the required gate width to effectively gate a single attosecond pulse from a half cycle periodic attosecond pulse train.

Experimentally generating such an ellipticity dependent pulse can be accomplished in a very simple way [33, 38, 42]. The setup is shown in figure 2.8. First, a linearly polarized laser pulse is incident on a multi-order, full order, birefringent quartz plate that has it optical axis

oriented at 45 degrees with respect to the input polarization. This automatically generates two orthogonally polarized pulses, one along the ordinary (o) axis and one along the extraordinary (e) axis of the quartz plate after the input pulse projects onto the two axes of the plate. Delay is also introduced between the two pulses since the e-axis has a higher index of refraction than the o-axis (quartz is positive uniaxial). A calculation showing the delay introduced between the two axes of birefringent quartz optics is discussed in Appendix B. After the first quartz plate, the two pulses then propagate to a zero order quarter waveplate. This plate is set so that its optical axis is between the two pulses polarization, or parallel to the input laser polarization. The two pulses again project onto the two axes of the quarter waveplate where on of the components is shifted with respect to the other component by exactly a quarter cycle. This results in the linear pulses being turned into circular pulses. Since the two original pulses project onto the optical axis of the quarter waveplate in different directions, the output pulses have opposite polarization with one being right circularly polarized and the other being left circularly polarized. The superposition of these two pulses gives the ellipticity varying pulse shown in figure 2.6(a). This method has been used for generating ~130 as pulses [34] and for generating extremely broad spectra, capable of supporting 45 as pulse durations.

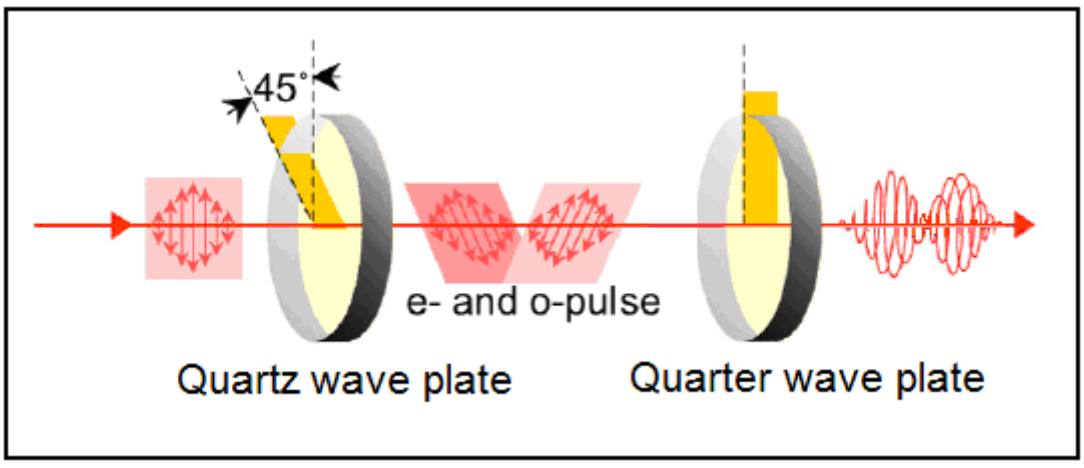

Figure 2.8 Optical Components for Polarization Gating

The experimental "knobs" for polarization gating are the laser pulse duration and the delay between the two counter-rotating pulses. The delay can be changed by simply changing the thickness of the plates either by using different plate thicknesses or, for fine control, by tuning the angle the surface makes with the input laser pointing. Since the first quartz plate must be a full order plate, only certain thicknesses are allowed. Appendix B discusses the calculations for these plates in detail. The other control, the pulse duration, is more difficult for polarization gating and relates to the disadvantage of using this method alone for generating attosecond pulses. Both controls cannot be modified independently however. The gate width must always be equal to the periodicity of the pulse train. Table 2.1 shows the values of T_d and τ_p so that δt_G always equals 1.25 fs.

In order to have the control over the gate width with polarization gating, a large portion of the input laser pulse is made to be unusable significantly reducing the conversion efficiency of

τ_p (fs)	3	4	5	6	7	8
T_d (fs)	2.16	3.84	6	8.64	11.76	15.36

Table 2.1 Gate Width Equation Parameters for Polarization Gating.

this method. The leading and trailing edges of the pulse do not contribute to the HHG process and in fact just deplete the ground state of the gas target. Since the returning electrons must recombine with the ground state according to the 3-step model, the HHG flux is destroyed when the ground state is destroyed. Looking at the quantum theory of HHG [43], generating harmonics of frequency Ω can be calculated from the Fourier transform of the dipole transition matrix element:

$$D(\Omega) = \int_{-\infty}^{\infty} dt \exp(i\Omega t) d(t) \tag{2.7}$$

where the dipole transition matrix element is given by:

$$d(t) = \int d^3\vec{r} \Psi_f(\vec{r},t) * \hat{d}_\varepsilon \Psi_i(\vec{r},t) \tag{2.8}$$

with $\hat{d}_\varepsilon = \vec{\varepsilon} \cdot \vec{r}$ being the dipole moment operator. For HHG, Ψ_i is the ground state meaning if depletion is too great, d(t)=0 and there is no flux.

To quantify when the ground state is depleted, an ADK calculation was conducted for polarization gating over all input pulse durations. Figure 2.9 shows a plot of the ionization probability as a function of input laser pulse duration. The conditions of the calculation are that the gas is argon, the gate width is 1.25 fs and the intensity of the laser in the gate width (the portion generating the HHG flux) is 2.8 x 10^{14} W/cm^2. This is the required intensity to generate harmonics extending to the edge of the aluminum filter. What this plot shows is that once the pulse duration of the input laser is greater than ~6 fs, the target is fully ionized by the leading edge of the pulse meaning there is total depletion of the ground state and no HHG flux. The result of figure 2.9 means the polarization gating technique is limited to pulse durations of ~5 fs maximum. This creates another problem for the gating technique as well. Since a <5 fs pulse

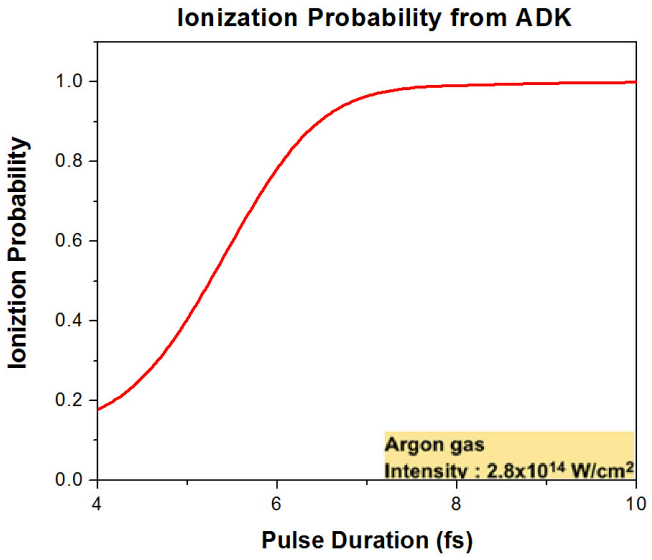

Figure 2.9 Ionization Probability versus Pulse Duration for Polarization Gating.

requires a very wide spectral bandwidth, all the optics in the setup must be capable of supporting such broad spectra. As mentioned before, the quarter waveplate must be a zero order plate. Even achromatic waveplates only have a quarter cycle retardation over a limited bandwidth (<200 nm) [44] which is still less than the bandwidth covered by a 5 fs pulse [31]. Since this technique should be used for pulses even below 5 fs, the optical properties become increasingly more critical.

2.1.3 Double Optical Gating

From the previous sections, it should be obvious that both two-color gating and polarization gating have serious disadvantages associated with them. Two color-gating can't truly isolate a single attosecond pulse and polarization gating requires very short pulses and has low conversion efficiency. Combining these two methods, however overcomes the limitations of each making a highly robust method for generating isolated attosecond that can be repeated on a daily basis.

Figure 2.10(a) shows a half-cycle attosecond pulse train under the influence of the polarization gating field when the gate width is 1 optical cycle. The color gradient indicates the ellipticity of the field with white being linear and blue being circular. The vertical lines indicate the gate width in this case. Clearly there will always be at least two pulses generated within this portion and in this case there are three pulses. The pulses on the edges of the gate width would be expected to have lower intensity than the center pulse since they are created in elliptical portions of the pulse, but they will still contribute a significant amount of signal to the total flux meaning the pulse train consists of three pulses. In figure 2.10(b), the attosecond pulse train is shown with a full-cycle periodicity by adding a weak second harmonic to the polarization gating

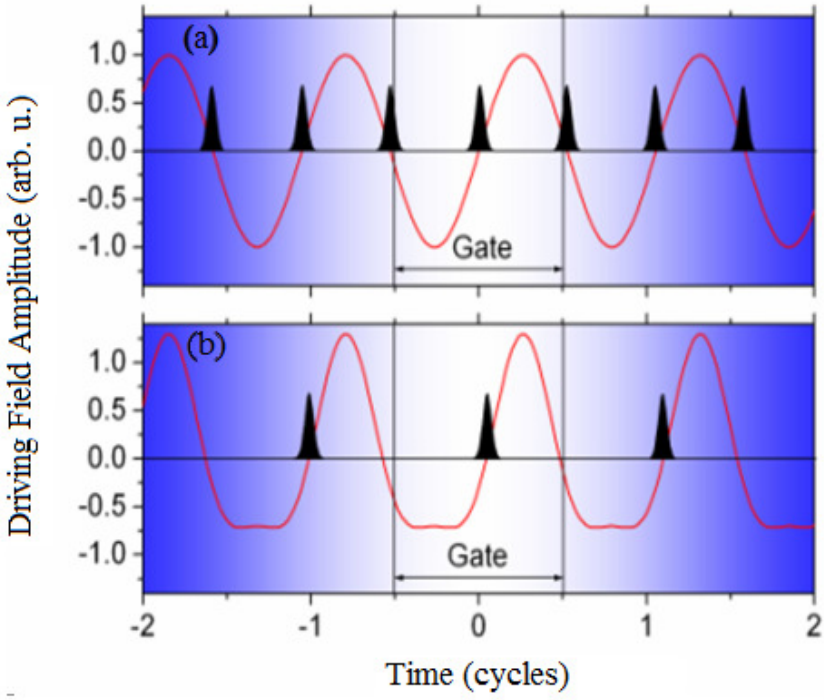

Figure 2.10 Attosecond Pulses trains in PG (a) and DOG (b).

technique. The second harmonic has ϕ_{rel}=0 and is polarized parallel to the driving field. Under this condition, a full cycle gate width can truly isolate a single attosecond pulse from the train. All the pulses outside the gate width in both (a) and (b) would be switched off by the elliptically polarized field.

The total field of DOG is shown in figure 2.11(a). The result is similar to PG except now a weak second harmonic field is added to the driving field distorting the 3-D image slightly. The second harmonic pulse has duration of ~30 fs according to nonlinear calculations from the SNLO software [45] and is discussed in Appendix C. The orthogonal components for DOG are shown in figure 2.11(b). The upper figure is the weak second harmonic component (purple line). This

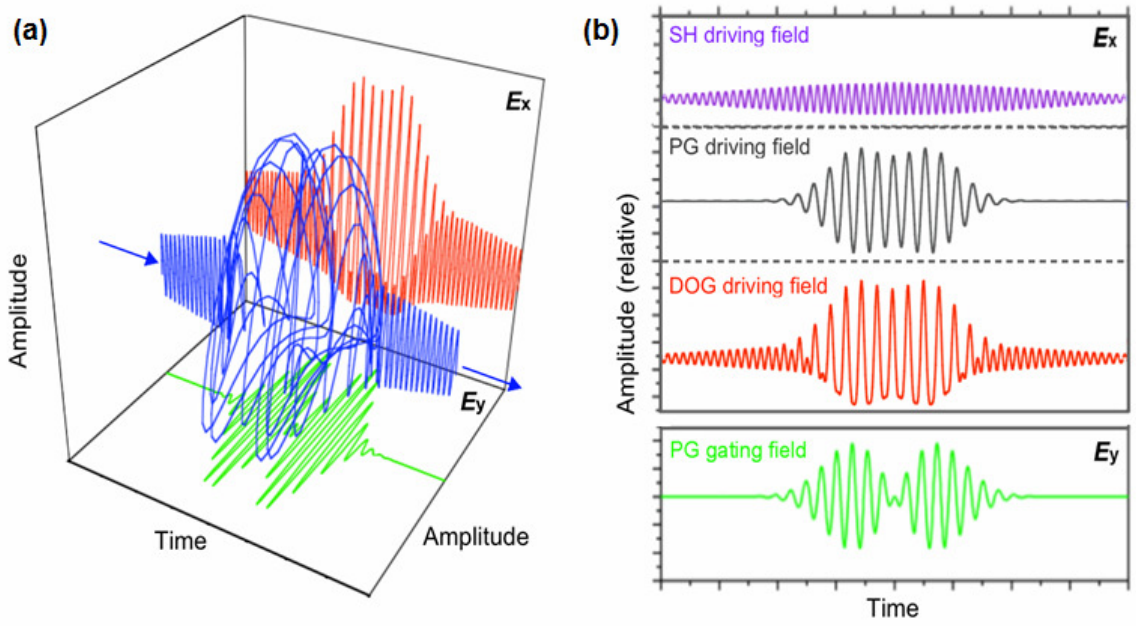

Figure 2.11 (a) Total field components for DOG. (b) SHG field (purple line), Driving field alone (black line), Driving field with SHG (red line), and Gating field (green line).

is followed by the PG field in the absence on the second harmonic (black line). When the second harmonic is present, the field component looks the like the red line. All of these components are polarized in one direction while the gating field (bottom green line) is polarized orthogonally to them. The values in the equations for the PG field are the same as in figure 2.6.

The equations of the field components are nearly identical to PG with the addition of the second harmonic. The driving field is now given by:

$$E_{drive}(t) = E_0[(e^{-2\ln 2\frac{(t+T_d/2)^2}{\tau_p^2}} + e^{-2\ln 2\frac{(t-T_d/2)^2}{\tau_p^2}})\cos(\omega_0 t + \varphi_{CE}) + ae^{-2\ln 2\frac{t^2}{\tau_{2\omega}^2}}\cos(2\omega_0 t + 2\varphi_{CE} + \phi_{rel})] \quad (2.9)$$

where $2\varphi_{CE}$ is the CE phase of the second harmonic, a is the ratio of the second harmonic with respect to the fundamental field amplitude, and $\tau_{2\omega}$ is the pulse duration of the second harmonic field. Note that the second harmonic pulse has a purely Gaussian temporal profile. The gating field is identical to the case of polarization gating and is written in equation (2.3).

The full cycle gate width with DOG is the source of all of the advantages that the DOG method possesses. From the gate width equation (2.6), it can be seen that if the gate width is one optical cycle (2.5 fs for a 750 nm laser pulse), the pulse duration can be increased or the delay decreased as compared to half-cycle gate widths. Figure 2.12(a) shows this dependence for DOG and polarization gating. All of the points on the blue line satisfy the gate width equation

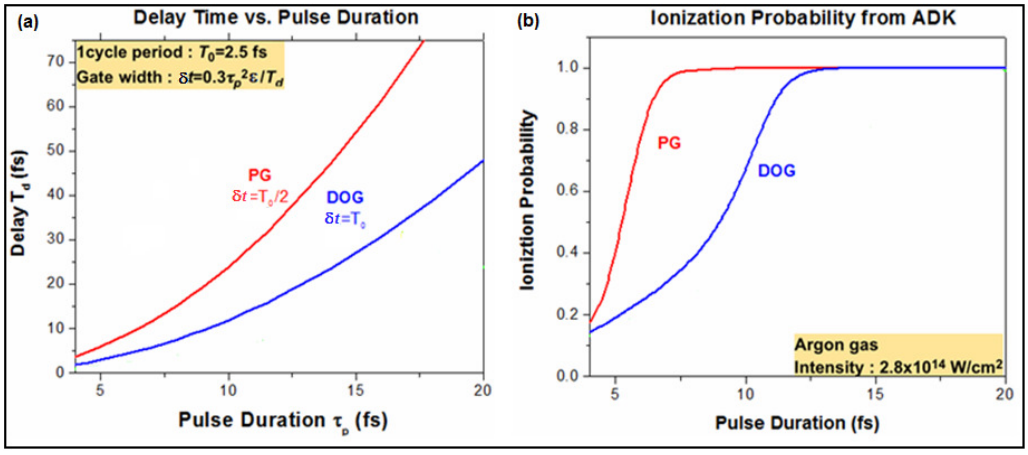

Figure 2.12 The Gate Width Equation (a) and Ionization Probability for DOG (b) PG results are also displayed for reference.

such that $\delta t_G = T_0$ like in the case of DOG. All of the points on the red line satisfy the gate width equation $\delta t_G = T_0/2$ as in the case of polarization gating (PG). The value of T_0 is the full cycle period of the fundamental IR laser (2.5 fs). This plot shows that for any pulse duration, DOG requires much less delay, T_d, than PG. It can also be looked at another way. For any value of delay, DOG allows longer pulse durations to be used. Both are major advantages for DOG since longer pulse durations are much easier to generate in the lab and can be repeated on a daily basis. An 8-9 fs laser pulse is practically trivial to generate as compared to a <5 fs pulse. Also, longer

pulse durations mean less spectral bandwidth. This eases the requirements on the types of optics that can be used, for Example, an achromatic quarter waveplate does have sufficient bandwidth to retard all frequency components of an 8 fs laser pulse uniformly.

Since less delay is also required for DOG as compared to PG, this results in a two-fold benefit. First, since the leading edge only contributes to the depletion of the target, reducing the delay should reduce the depletion. This effect is shown as an ADK calculation in figure 2.12(b). The ionization probability for DOG is less than PG for all values of pulse duration meaning the target will be less depleted resulting in a higher HHG flux. The values for the calculation are the same as in figure 2.9. This plot indicates that DOG can work with pulses as long as 12 fs. Second, the right and left circularly polarized pulse can combine together at a point where their combined electric field is stronger than PG would allow. This means there will be higher intensity within the gate width and since the harmonic cutoff is proportional to the laser intensity, DOG can generate broader spectra capable of supporting shorter pulses than PG alone. Figure 2.13 shows a plot of the gate width peak intensities for PG and DOG assuming initial pulse

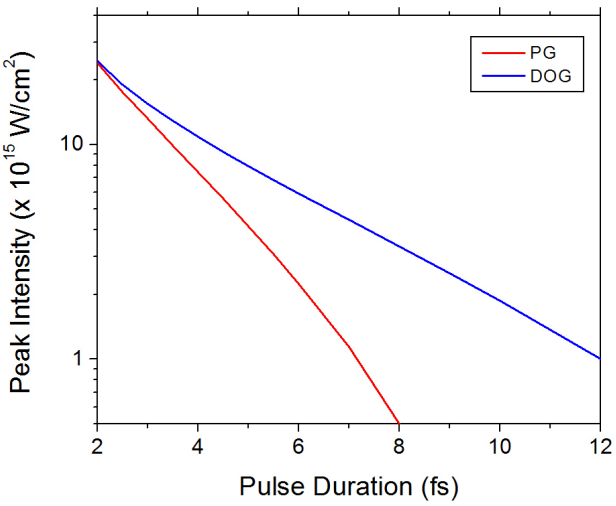

Figure 2.13 The Peak Intensity within the Gate Width for DOG and PG.

energy of 850 μJ and a focus spot size of 40 μm. The results of figure 2.12 and 2.13 clearly show that DOG works very well for longer, multi-cycle laser pulses but it should be noted that it will work better than PG alone for short pulses too. For the results in figures 2.12 and 2.13, Table 2.2 shows the values of τ_p and T_d that satisfy the gate width equation for a full optical

cycle width and center wavelength 780 nm. The delay in each case must be an integer number of laser cycles.

τ_p (fs)	4.8	6.7	8.2	9.5	10.6	11.7	12.6	13.4
T_d (fs)	2.6	5.2	7.8	10.4	13	15.6	18.2	20.8
T_d (cycles)	1	2	3	4	5	6	7	8

Table 2.2 Gate Width Equation Parameters for Double Optical Gating.

2.1.3a Interferometric DOG

Since DOG is the combination of two distinct gating methods, the most obvious way to implement the technique is interferometrically [46]. This allows each gating method to be added to opposite legs of the interferometer and gives total control to each method individually. Figure 2.14 shows the interferometric DOG setup. An initially linearly polarized ~8 fs transform

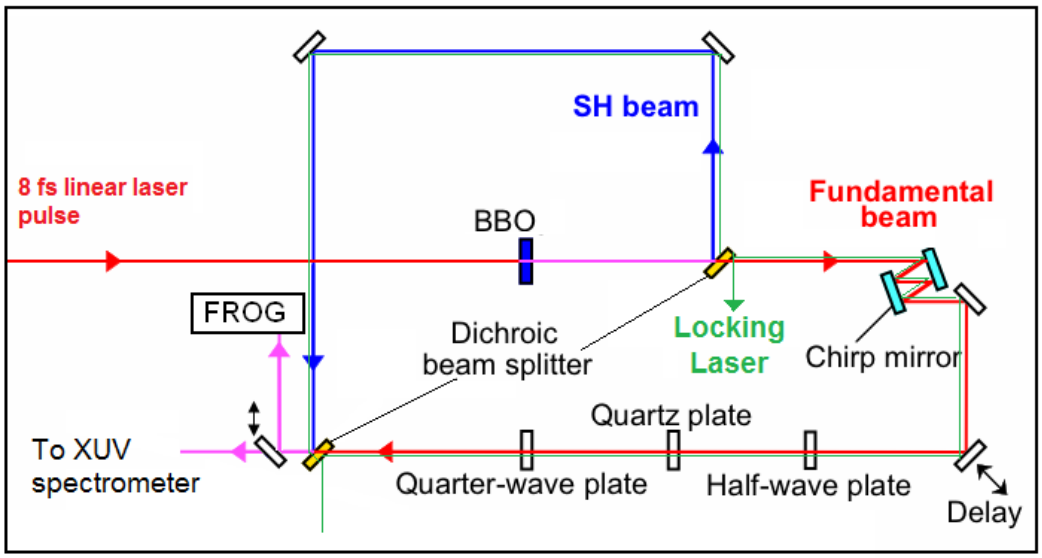

Figure 2.14 Interferometric DOG setup.

limited laser pulse with ~550 μJ pulse energy is first passed through a BBO crystal to generate a strong second harmonic contribution. The thickness of the BBO crystal is not too important at

this point, it just needs to have a wide phase matching bandwidth and high second harmonic generation (SHG) efficiency. For this original experiment, a 250 μm BBO was used because its SHG efficiency was measured to be ~10%. Since the BBO is type-1, it is ooe meaning the SHG is orthogonally polarized as compared with the input polarization.

After the BBO, the residual IR pulse and the SHG pulse are split by a dichroic long wave pass (LWP) beamsplitter (CVI). For the beamsplitter, >99% of the SHG is reflected while 85% of the IR is transmitted. The second harmonic beam then bounces off a couple of aluminum mirrors. These have broad reflectivity curves allowing ~85% reflection of the 400 nm light. Meanwhile, the transmitted IR first bounces several times off of multilayer chirp mirrors to compensate all the dispersive elements in the interferometer. The beam then passes through an achromatic half waveplate to flip its polarization parallel to the SHG polarization. It then passes through the PG optics – the first quartz plate and the quarter-waveplate. This generates the ellipticity varying pulse. The thicknesses of the first quartzplates used in the experiments will be discussed in detail in the next section but is chosen so that the gate width was less than one optical cycle. This plate was ~440 μm thick. The PG field recombines with the SHG at another dichroic LWP beamsplitter. At this point, the SHG is polarized parallel to the driving field component of the PG field. In order to control the temporal overlap of the SHG with PG field, a delay stage is built into the interferometer. After the interferometer, the DOG pulse entered the same XUV spectrometer shown in figure 1.4. To ensure the laser pulse is transform limited before entering the XUV spectrometer, the pulse was measured with FROG. The pulse energies after the full interferometric setup were measured to be ~150 μJ for the IR pulse and ~30 μJ for the SHG. The intensities corresponding to these pulse energies were 2.8 x 10^{14} W/cm^2 and 7 x 10^{13} W/cm^2 for the IR and SHG, respectively.

Since this is an interferometric design, it is inherently unstable. To partially correct this, a green (532 nm) CW laser was copropagated through the interferometer starting at the second beamsplitter and ending at the first beamsplitter. An interference pattern was then observed and by monitoring this pattern, the interferometer was actively locked through feedback control of the delay of one interferometer leg with respect to the other. Details of this technique are discussed in Appendix D.

The interferometric setup gives a lot of freedom since we can fully control the temporal delay of the second harmonic with respect to the PG field and as such, it was used mainly for

characterizing the spectra generated by DOG. Figure 2.15 shows actual experimental spectra generated under a variety of conditions with this setup. All are normalized to the same value.

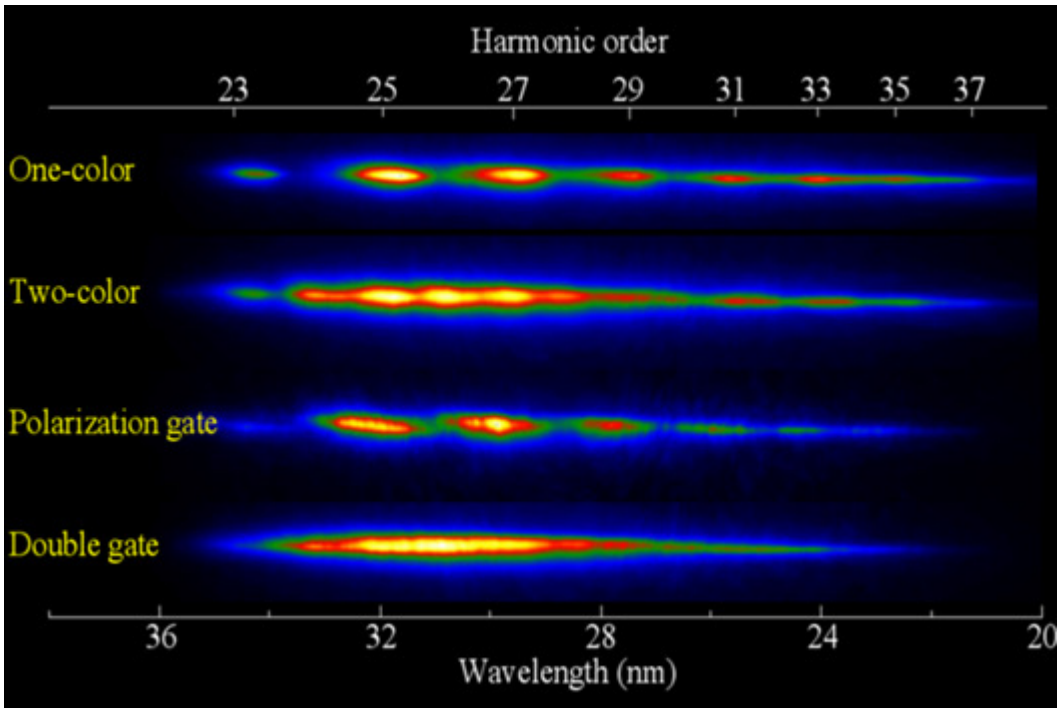

Figure 2.15 Spectra from Interferometric DOG.

The first spectrum is that of a one-color linearly polarized laser generating an attosecond pulse train in an argon target. The discrete odd orders are expected. Experimentally, this was generated by blocking the second harmonic component in the interferometer and not setting the first quartz plate to 45 degrees. This left the IR pulse linearly polarized.

The second spectrum is a two color attosecond pulse train in argon. Here, the second harmonic was not blocked and was polarized parallel to the IR pulse. The even and odd orders are indicative of a full optical cycle periodic pulse train. The individual harmonic orders are overlapped with each other creating a somewhat smooth spectrum. This is similar to results found in two-color gating [32].

The third spectrum is polarization gating alone. Since the gate width is one optical cycle, there should always be at least two attosecond pulses in the train. This manifests itself as a discrete odd order spectrum. The individual orders are slightly broader than the linear case, but overall the spectra are nearly identical. This spectrum was generated experimentally by again

blocking the second harmonic, but leaving the first quartz plate oriented at 45 degrees. Finally, the bottom spectrum is for DOG. Here, the second harmonic was added to the polarization gating field. Since the pulse periodicity was one optical cycle, only one pulse existed within the gate width and the spectrum showed a very broad, smooth, and continuous nature.

All of the spectra were taken under the same initial experimental conditions to get an accurate gauge of the efficiencies of each. The input laser pulse energy was ~150 μJ and the integration time for each spectrum was 10 seconds. To gain a more accurate comparison, figure 2.16 shows the lineout plots for the polarization gating spectrum (red line) and the DOG

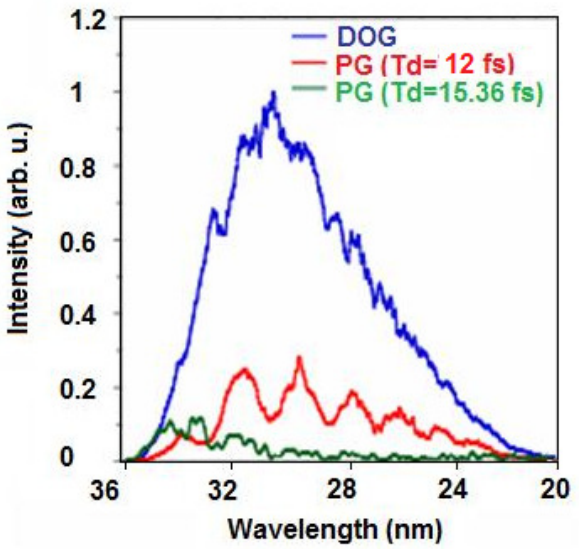

Figure 2.16 Lineout Plots from Interferometric DOG.

spectrum (blue line). The DOG spectrum is clearly much strong and in fact, the ratio of the total integrated signal between DOG and PG is 3:1. This is an important result since the PG spectrum isn't even a single attosecond pulse. To get an accurate comparison, the gate width should be made to be half an optical cycle (the necessary condition for PG to isolate a single attosecond pulse). This was accomplished by switching the first quartz plate from a ~270 μm plate to a ~530 μm thick plate. This changes T_d from 7.68 fs (DOG) to 15.36 fs (PG). The second harmonic pulse was also blocked. Under these conditions, the spectrum did smoothen out, indicating a single attosecond pulse, however the signal was further reduced. This condition is

displayed as the green line in figure 2.14. The ratio of DOG to PG was then 23:1. This dramatically shows the power of DOG to generate high flux attosecond pulses from multi-cycle lasers. The enhancement in the flux for DOG as compared with PG can be almost entirely attributed to the higher peak intensity in the gate width and the reduced depletion form the leading edge (see, for example, figures 2.12 and 2.13). To generate a single attosecond pulse in argon with an 8 fs pulse, PG requires much more delay and as a consequence, almost fully depletes the ground state of the target gas.

The main benefit to using the interferometric setup is the ability to control delays. In such an experiment, control over both fine delays and coarse delays is desirable. To this end, the delay stage in the interferometer consisted of a coarse motorized delay stage (Newport Unidrive) with a smaller delay stage mounted on this. The smaller delay stage was movable using a piezo-electric transducer stack (pzt) from Thorlabs. The larger Newport stage allowed scans ranging from 10s of femtoseconds to picoseconds. The smaller pzt stack allowed delay scans of a few femtoseconds only. The step size of the smaller stack was significantly smaller than the wavelength of the IR laser. This allowed us to scan the relative phase of the IR with respect to the SHG on sub-cycle scales.

The first scan that was conducted was a cross correlation between the IR and the SHG. This scan enabled an accurate measurement of the pulse duration of the SHG pulse. The IR laser was left linearly polarized and was scanned through the SHG. The total delay range was ~680 fs corresponding to a total delay of ~0.2 mm. The result, shown in figure 2.17, indicates that the temporal overlap occurred halfway through the scan. Since the IR laser alone would only generate odd order harmonics, the appearance of even orders indicated the presence of the SHG. Since the pulse duration of the IR laser was known from a FROG measurement to be ~8 fs in duration with a Gaussian temporal profile, the total signal, integrated along the wavelength axis, could be de-convolved to find an estimate of the pulse duration of the SHG. The right figure shows the integrated signal to have a FWHM of ~28 fs. Since this is much larger than the pulse duration of the IR, the SHG must have pulse duration of ~28 fs. A simulation of a cross correlation confirmed these estimated results.

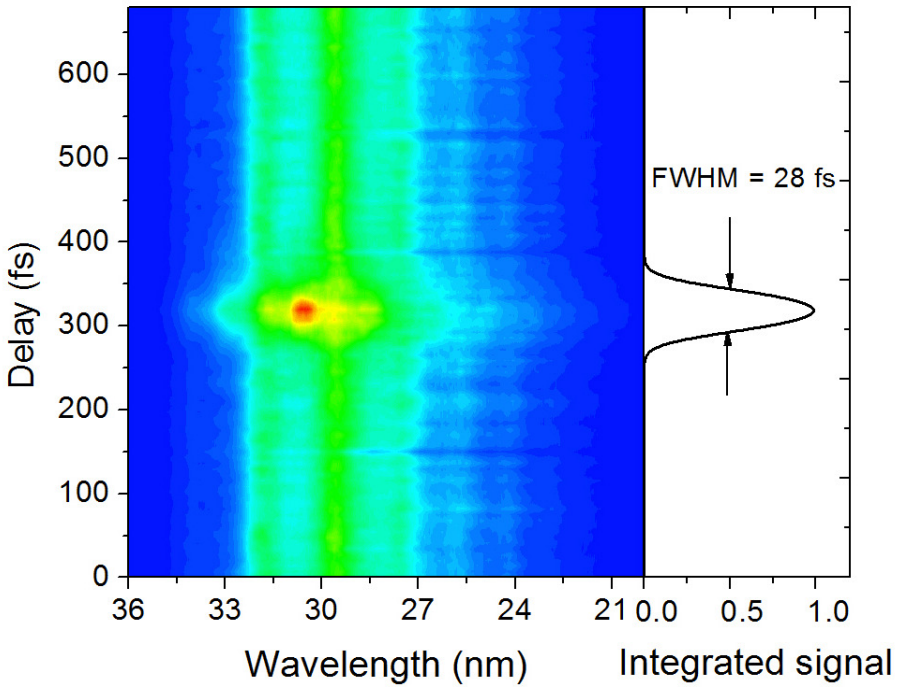

Figure 2.17 Cross Correlation Scan of IR and SHG.

Using a finer scan with the pzt, sub-cycle features in the spectrum could also be extracted. From figure 2.1, it is obvious that depending on the relative phase between the IR and SHG, the spectrum can change quite a bit. For a phase of 0, the pulse train has a full cycle periodicity and even and odd orders are expected. If the DOG method is employed, a continuum can be generated. If the relative phase is ~$\pi/2$, the attosecond pulse train has a half cycle periodicity and only odd orders are expected. Figure 2.18(a) shows the results of a fine scan between the IR and SHG [47]. The experimental conditions are a 9 fs IR laser pulse was gated with DOG. The scan range was ~5.5 fs which corresponded to a total distance of ~1.7 μm. Since the relative phase scan will repeat every half cycle of the fundamental laser (or full cycle of the SHG), there should be some periodicity in the spectrum. Figure 2.18(b) shows the signal integrated along the wavelength scale. The signal repeats every half cycle (~1.25 fs). Some interesting features are that the spectrum shows an enhancement in signal indicating increased conversion efficiency for some values of relative phase and also a cutoff extension for these same values. Both of these effects can be explained by the higher peak

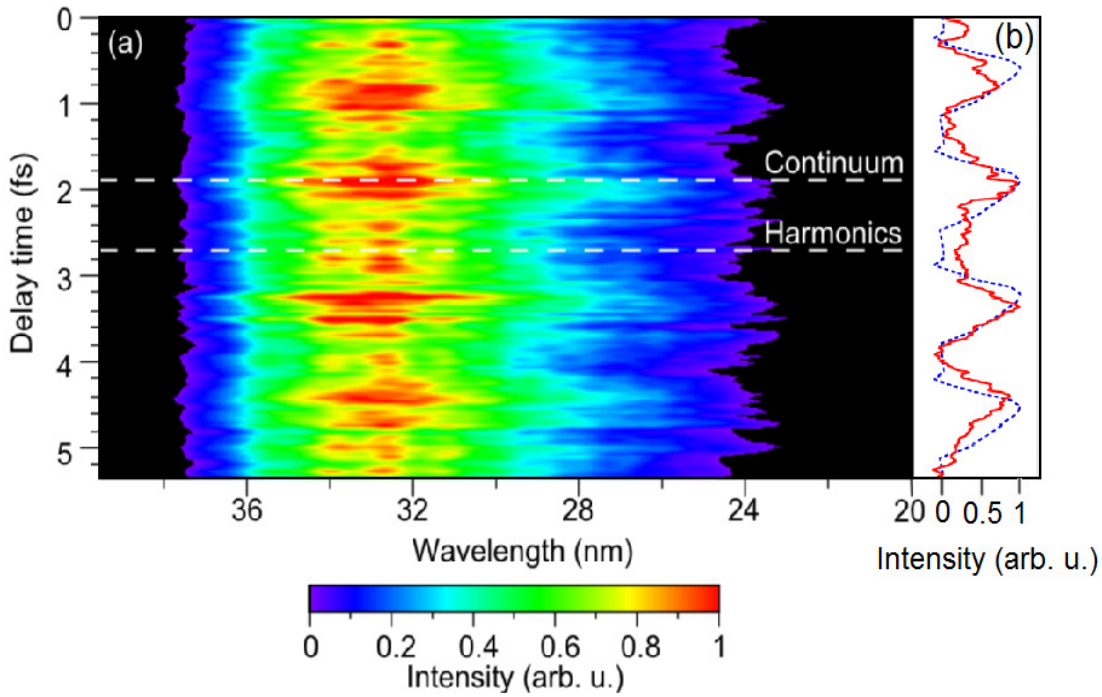

Figure 2.18 Fine Relative Phase Scan between SHG and IR.

intensity between the SHG and IR when the relative phase is 0. It should be noted that while the relative phase scans are conducted, the interferometer is not locked.

Since the main goal of the DOG technique is to generate the shortest single isolated attosecond pulses possible, the spectra collected were analyzed to find the lower limit on the attosecond pulse duration. This was done by taking the Fourier transform of the spectra assuming a flat spectral phase. The first test was to find the pulse duration from an attosecond pulse generated in argon. This spectrum has a lower cutoff due to the depletion of the gas for high intensities but it also has very high photon flux. Figure 2.19(a) shows the temporal profile of the attosecond pulse generated with the DOG spectrum shown in figure 2.16 (blue line). The spectrum can support pulse duration of ~190 as but the most important feature in the plot is the non-existent pre and post pulses. For a full cycle periodicity attosecond pulse train (as in the case of DOG), the pre and post pulses would exist at ~+/- 2.5 fs. If this case is compared to the PG alone spectrum (red line) in figure 2.16, strong pre and post pulses would be expected at temporal locations corresponding to a half-cycle periodic pulse train. These are clearly seen in figure 2.19(b) indicating the pulse is not at all a true isolated attosecond pulse.

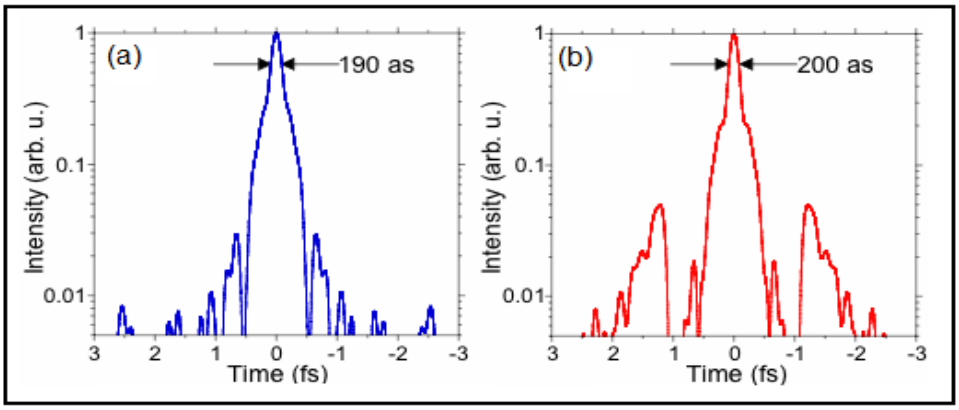

Figure 2.19 Temporal Profiles of DOG (a) and PG (b) Spectrum from an Argon Target.

To generate even shorter pulses, the same experiment was conducted with a neon gas target. Neon has a higher cutoff than argon and can then support shorter pulse durations. Figure 2.20 shows the results from neon. The upper image (a) is the actual broad continuous spectrum image. Figure 2.20(b) shows the spectrum and (c) shows the transform limited temporal profile

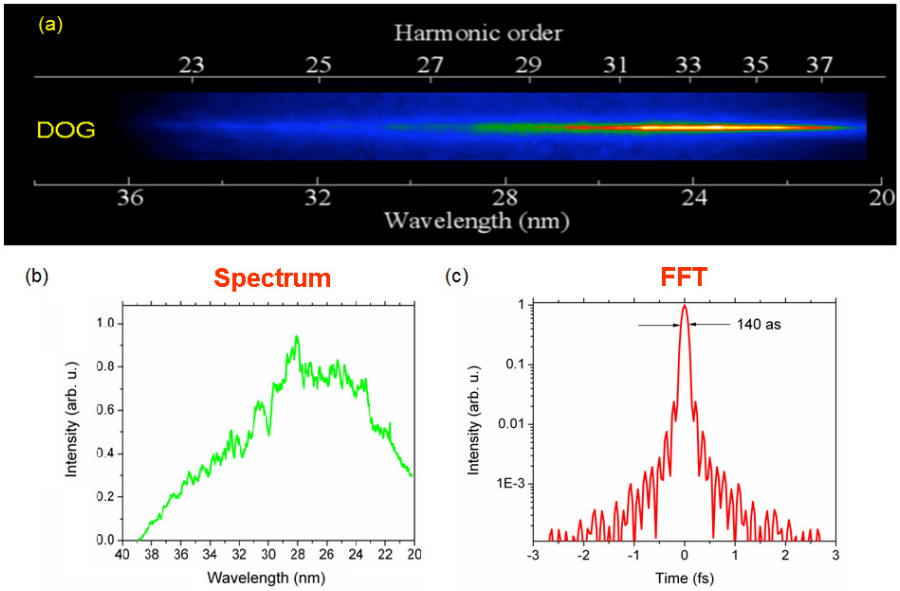

Figure 2.20 (a) Spectral image of a neon spectrum. (b) Lineout plot of (a). (c) Temporal Profile of DOG Spectrum.

from a Fourier transform of (b). The spectrum supports ~140 as duration with no pre and post pulse contribution. The vertical scale is a Log plot showing the satellite pulses are suppressed by more than 4 orders of magnitude. A plot showing the same effect with PG was not included because it is difficult to generate any spectrum in neon with such low power multi-cycle laser pulses.

As a final (and best) method for determining whether the pulses generated with DOG are true isolated attosecond pulses, a carrier envelope phase (CEP) scan was conducted. It is known from the previous discussion that the harmonic spectrum is highly sensitive to the intensity of the generating laser. As the CEP is scanned, the field strength at t=0 within the gate width can change by many orders of magnitude or even change signs while the envelope remains the same. Since the SHG is generated by the IR, the CEPs of both remain locked together which is why the CEP offset, φ_{CE}, for the SHG is twice the value of the IR (see equation 2.9).

The way the CEP is scanned with the KLS is by first locking the oscillator using the self referencing technique [48, 49]. Next, the slow drift introduced by the amplifier was compensated using feedback control of the separation of the gratings in the stretcher [50, 51]. To change the CEP, the separation of the gratings was changed with time. This method allowed CEP stability of ~190 mrads before the hollow core fiber, and ~370 mrads after [31].

The reason the CEP is a valuable test for determining the nature of the attosecond pulses generated is shown in figure 2.21. This figure shows the gate width region of the DOG field for four values of the CEP of the driving laser. The ellipticity of the laser field is given by the color gradient with blue being highly elliptical and white being linear. In figure (a), the CEP is 0

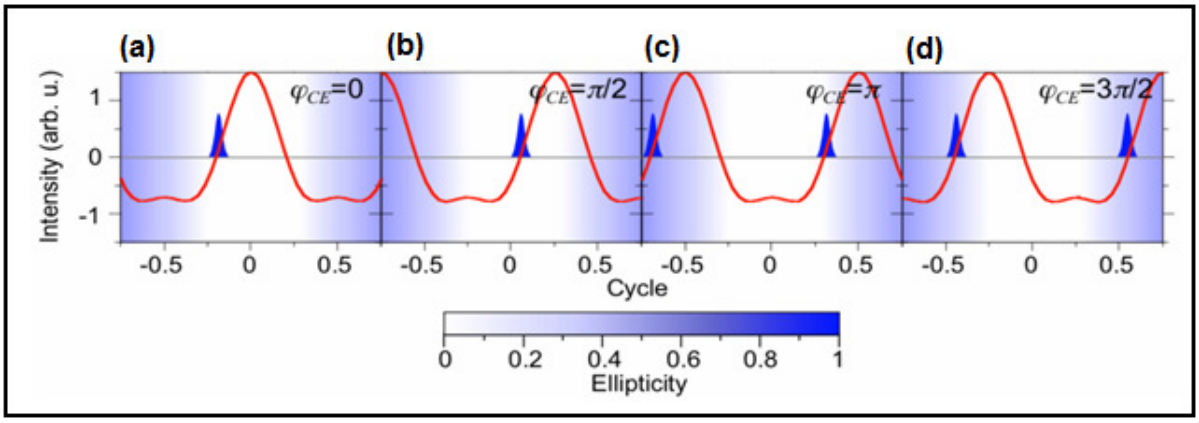

Figure 2.21 CEP Effect on DOG pulse.

which is referred to as a cosine pulse. The attosecond pulse generated here would be born in a field of high ellipticity but recombine when the field is linearly polarized which would result in a weak continuum. Figure (b) is similar to (a) but now the electron is born and recombines in a field that is mainly linear resulting in a much stronger continuum as compared with (a). Figure (c) is a π shift with respect to (a). Here, two pulses are generated with the first pulse being much weaker than the second. This results in a slightly discrete spectrum. Finally, figure (d) is similar to (c) except the ratio of intensity between the first and second pulses is different than in (c). An important feature to note is that the spectra generated at each value of CEP is unique. This means a 2π periodic structure is expected as the CEP is scanned. This feature serves as evidence that the DOG pulse is behaving properly since the 2π periodicity is only visible in two color gating methods. If the same CEP scan was conducted with PG, the periodicity would be π since the attosecond pulse train is generated every half cycle. The CEP of both 0 and π would have nearly identical attosecond pulses generated, one pointing up at 0 and another pointing down at π, but indistinguishable in the spectral domain.

Figure 2.22(a) displays the spectrum as a function of the CEP of the generating laser.

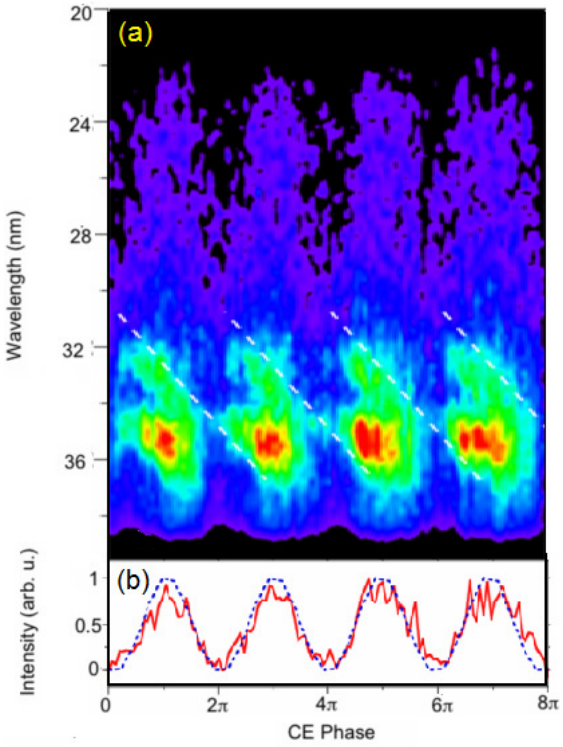

Figure 2.22 HHG Spectra as a Function of CEP from DOG.

The experiment was conducted by locking the interferometer to a relative phase value where the spectrum was a strong continuum. The CEP was then scanned. The 2π periodic structure is evident as is the unique spectrum generated at each value of CEP. Figure (b) shows a plot of the signal integrated along the wavelength axis. For an example of varying spectral shapes, at ~2π, the spectrum exhibits discrete order harmonics while at ~3π, the spectrum is a continuum. The fact that every spectrum is unique allows for an interesting application of this technique. Conducting a CEP scan with DOG can tell you the actual CEP of the driving laser. Previously this was accomplished using phase meters [52] but this only worked for ~5 fs pulses. Dog allows the CEP to be determined for pulses up to ~12 fs. In figure 2.22(a), the dashed white lines are there to guide the readers eyes. As the CEP is varied, the individual harmonic orders tend to shift to higher energy due to the plasma dependent blue shift.

A comparison of the spectra of DOG with PG is shown in figure 2.23. Here, the π periodicity is obvious with PG (right figure). This result was taken with the PG optics alone and under different experimental conditions, but the CEP effect is the same.

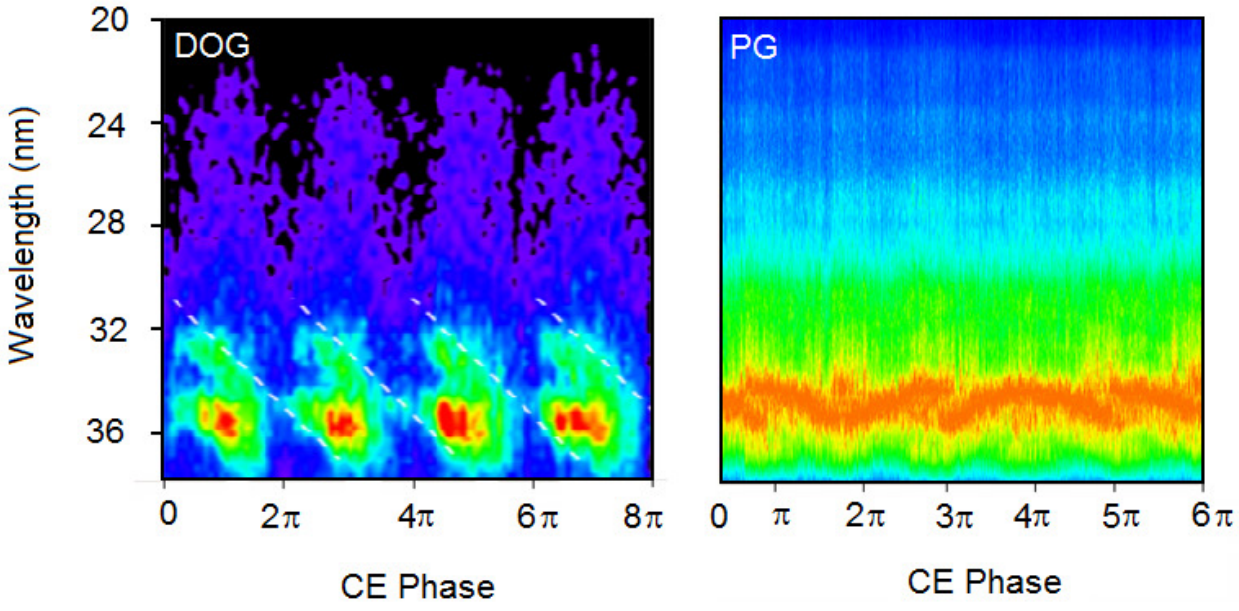

Figure 2.23 Comparison of CEP Effects in DOG (a) and PG (b).

While the interferometer method demonstrates the full strengths of DOG, it still has some major disadvantages. The image in figure 2.18 indicates the main problem associated with the interferometric setup. Obviously the spectrum is highly susceptible to the temporal jitter between the two legs of the interferometer which is why the active locking is required. However, even with the best case locking scenario, some jitter will still exist which is why the collinear configuration, discussed in the next section, was developed. A second disadvantage of the interferometric technique is the high loss associated with an interferometer. The reflecting optics in the setup are not perfect meaning up to 50% of the total power can be lost. The optics used in our experiments were specially chosen to reduce this loss but we still lost ~5% of the total input power in the SHG leg of the interferometer, ~15% of the IR was lost on each beamsplitter, and ~40-50% was lost on the chirp mirrors. This left ~150 μJ of pulse energy in the fundamental beam and ~30 μJ in the second harmonic beam for generating a spectrum. For experiments where count rates and intensity are important, this is unacceptable which is why the interferometric DOG method remains useful only for characterizing the DOG technique, not for generating usable amounts of photon flux.

2.1.3b Collinear DOG

As a way to overcome the disadvantages in the interferometric DOG setup, a collinear method was developed. This method was used exclusively for all of the results in the rest of this thesis. This section will discuss the method and will compare the collinear method to the interferometric method.

Figure 2.24 shows the experimental setup for the collinear method [47]. It is very similar to PG (see for example figure 2.8) and the principle is almost identical with the exception of the

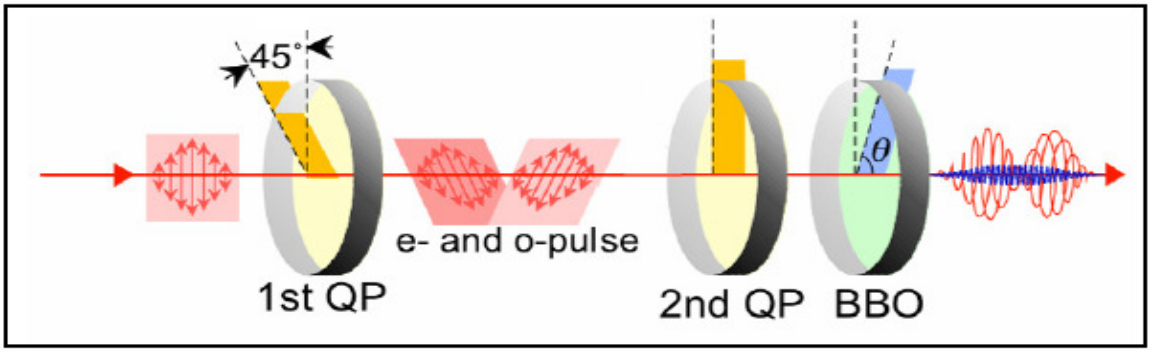

Figure 2.24 Experimental Setup for Collinear DOG.

addition of the weak second harmonic field. The first quartz plate (1st QP) is the same as before (CVI or CASIX). This separates a linearly polarized input beam into two orthogonally polarized pulses with delay between them. The thickness of the plate for collinear DOG is much more critical than for PG because it must be a full order multi-order waveplate. Appendix B discusses this in detail. For now, the reason it is critical is that this plate determines the polarization of the driving field with respect to the gating field. It will be obvious why this is so important later. After the first plate, the two orthogonal beams are incident onto an additional set of optics. The first optic is another full-order multi order quartz wave plate (2nd QP). The two pulses project back onto the optical axis of this plate generating two new orthogonal components. One component is polarized parallel to the input polarization and the other is orthogonal to this. Due to the birefringent nature of the quartz, more delay is introduced between these plates. After this plate, the two components are incident onto a thin BBO crystal. The optical axis lies 29 degrees from the normal. This is the proper phase matching angle for SHG of ~800 nm light. The BBO is negative uniaxial (no>ne) while quartz is positive uniaxial (ne>no). If this plate is oriented properly and the thickness is appropriately chosen, this plate can cancel the delay introduced by the 2nd QP to within a quarter cycle. The vector sum of the resulting two components is then the ellipticity dependent pulse synonymous with PG. Since the final plate is a BBO, a weak second harmonic field is generated. Again, care must be taken in the orientation of this plate. The BBO crystal is type-1 meaning the SHG is orthogonally polarized with respect to the fundamental beam. In order for the SHG to be overlapped with the driving field, it must be generated by the gating field component. This will then be projected onto the driving field. The field components of an initial 9fs laser pulse after each optic are shown in figure 2.25. In (b) and (c), the upper (red) figure is the driving field and the lower (green) figure is the gating field. The SHG is shown as the blue line in (c). Note that it has the same double-humped structure as the gating field since it was produced by it.

The collinear method is capable of generating the same shaped field as the interferometric method as evident from figure 2.25. This is accomplished without the disadvantages associated with an interferometer. For example, the only losses of laser energy would be reflections off the surfaces of each optic. This is at most ~4% for normal incidence but

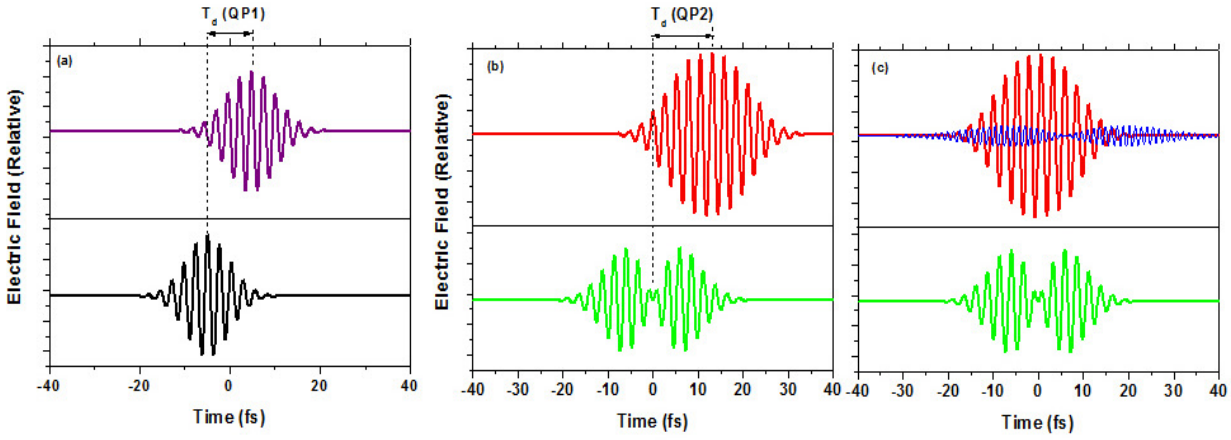

Figure 2.25 Field Components for Collinear DOG (a) After the 1st Quartz Plate, (b) After the 2nd Quartz Plate, and (c) after the BBO.

can be reduced if each optic is coated with an anti-reflection (AR) coating. For example, the BBO crystals we used are "P-coated" from the manufacturer (Altos Photonics) which is a broadband AR coating that covers both the fundamental and SHG wavelengths. Besides, these reflections would also be found in the interferometric version as well. The second, and most critical, advantage is that the collinear setup is very stable. There is no temporal jitter between the IR and SHG as is always found in the interferometer. A couple of less valuable benefits are that the collinear configuration is much easier to setup and implement on a daily basis in the lab and the total cost is less than the interferometer. For example, one leg of the interferometer requires chirp mirrors to compensate the dispersion caused by the BBO (see figure 2.14). This alone increases the cost of the interferometric method by several thousand dollars.

One disadvantage to the collinear setup however is the reduced control over the relative phase. However, if the BBO is phase matched for generating SHG at the proper wavelength, the IR and SHG are automatically in phase. This inherently generates the required spectrum for a single attosecond pulse. Appendix C shows the plot of the phase matching region for SHG of an 800 nm centered laser pulse.

The main parameter to change in the collinear setup is the BBO angle with respect to the laser propagation direction. This allows sub-cycle control over the delay between the gating and driving fields as they pass through the BBO. Since the BBO optical axis is for the SHG of 800 nm, the efficiency of SHG decreases as the angle is tuned. This is the trade-off for the delay

control. An important point to note here is how the BBO should be rotated. In order to fine tune the phase-matching angle of the BBO, it must be rotated about an axis perpendicular to the input polarization. So in figure 2.24, it should be rotated about an axis perpendicular to the page. This ensures the phase matching angle is being tuned in agreement with calculations.

For a birefringent optic, the two axes are characterized by two distinct refractive indices, no(λ) and ne(λ) (the Sellmeier equations used to calculate no and ne are given for both quartz and BBO in Appendix B and C, respectively). Light polarized parallel to the plane containing the propagation vector and the optical axis is the extraordinary ray (e-ray) and corresponds to ne while light perpendicular to this plane is the ordinary ray (o-ray) corresponding to no. However, if there is an angle θ between the optical axis and the propagation vector (as in the case of BBO), the e-ray experiences a refractive index ne(θ, λ). This is expressed as [53]:

$$n_e(\theta,\lambda) = \frac{n_e(0,\lambda)n_o(\lambda)}{\sqrt{n_o(\lambda)^2\sin^2(\theta) + n_e(0,\lambda)^2\cos^2(\theta)}}. \tag{2.10}$$

If the quartz plates are tuned so as to not have normal incidence, this equation becomes necessary as well. Since, by tuning the angle, the effective thickness of the medium increases, fine control over the relative phase between the driving and gating fields can be accomplished in the BBO as well as the quartz plates. Figure 2.26(a) shows the delay between the driving and gating fields for a 141 μm BBO crystal as a function of angle. Figure (b) shows a similar plot for

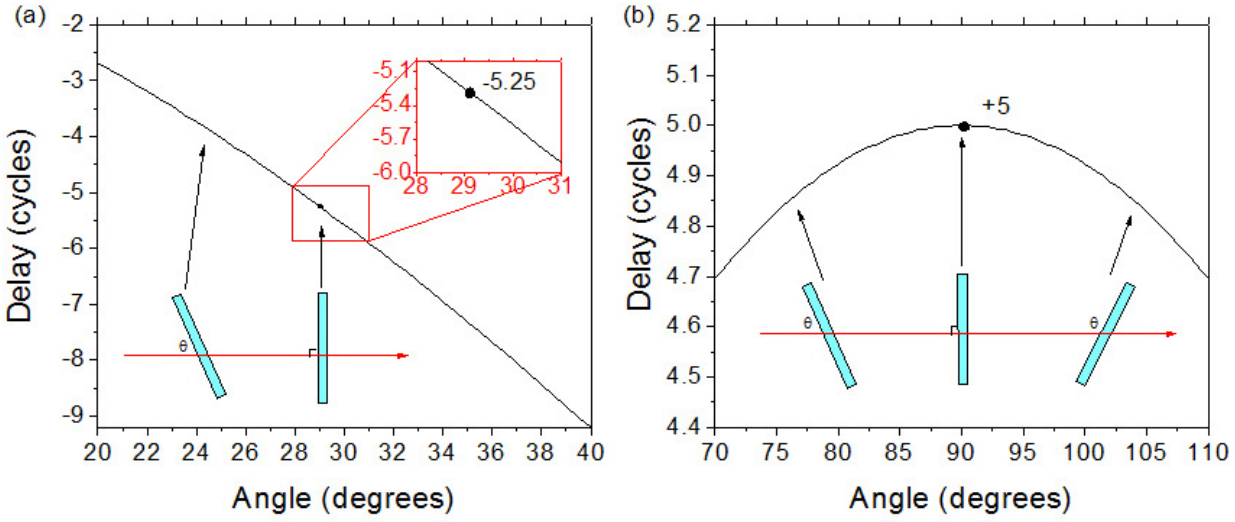

Figure 2.26 Phase Delay versus Angle for BBO (a) and Quartz (b).

a 440 μm thick quartz plate. These two thicknesses are the exact ones used in the experiments.

Some important features in these graphs can be noted here. First, the BBO at 29.2 degrees is perpendicular to the input laser propagation vector. This gives -5.25 cycles of delay between the driving and gating components as seen in the inset in (a). This compensates the delay introduced by the 2nd QP (b) to exactly a quarter cycle. Second, the quartz can be tuned in either direction since the optical axis is 90 degrees.

The previous figure demonstrates why the quartz plates must be full-order. If not, they would not compensate the delay the BBO introduces to a quarter cycle. Since the SHG also depends on the phase matching angle in the BBO, it is best for the BBO to remain in an orientation normal to the laser propagation thereby limiting the range over which it can be tuned. Figure 2.27 shows the values of the quartz plate thickness required for a certain value of input pulse duration so that the gate width is one optical cycle (blue solid line). The right axis indicates how many full cycles of delay each quartz plate introduces. The four points listed are those which were used in the experiments although any point on the line could be used, provided the correct pulse duration is maintained. In the upper left of the figure, the red solid line indicates the points that satisfy a half-cycle gate width – the necessary condition for PG. Clearly, this plot shows that DOG requires thinner plates and hence much less delay for the same pulse duration as compared with PG.

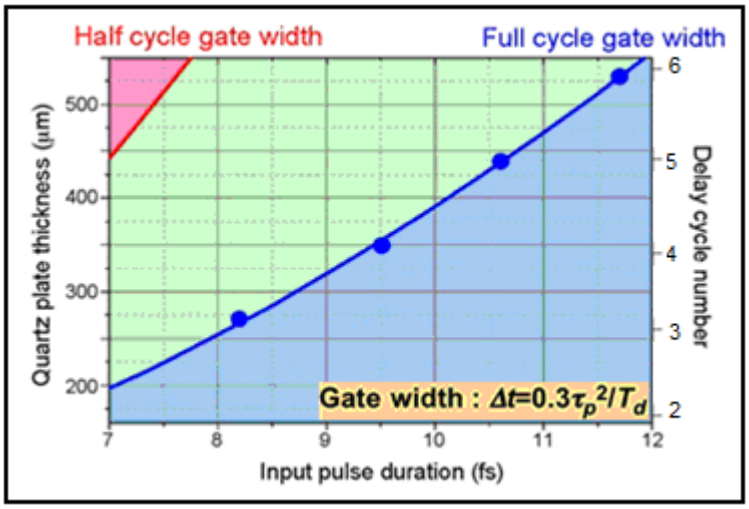

Figure 2.27 Quartz Plate Thickness versus Pulse Duration for Collinear DOG.

For different delays, the leading edge causes different amounts of depletion as discussed in figure 2.12. The contribution of the leading edge of the pulse can be seen in figure 2.28(a). This shows four different pulse durations with the correct amount of delay required to have a full

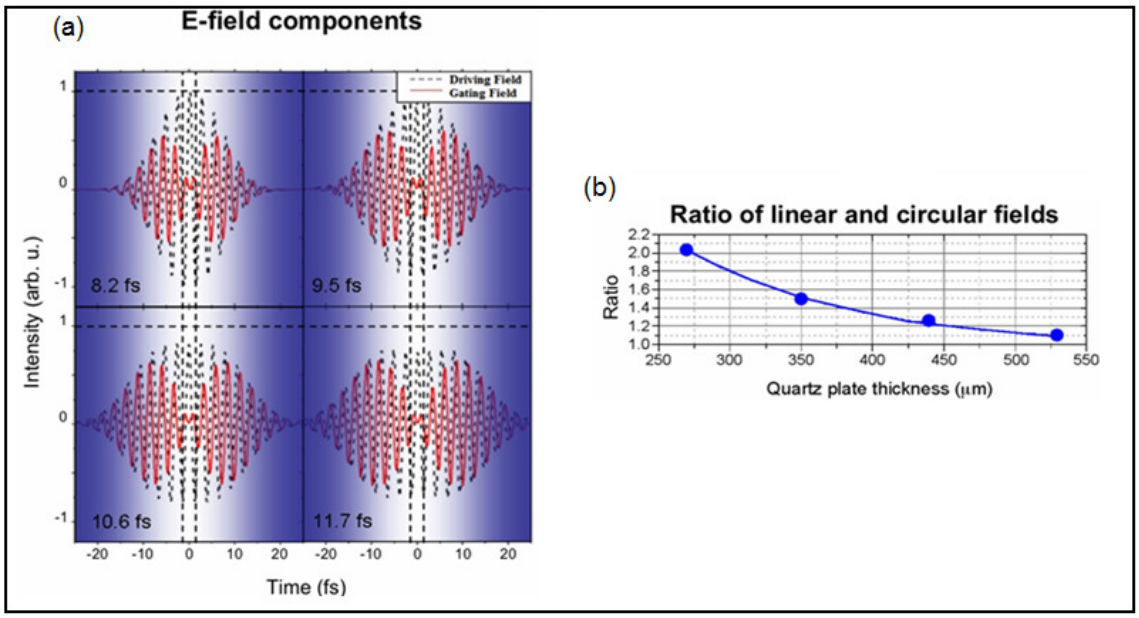

Figure 2.28 Field Components from Different Quartz Plates (a) and the Ratio of the Linear Contribution to the Circular Contribution of the DOG Field (b).

cycle gate width. The delays are 3 cycles, 4 cycles, 5 cycles, and 6 cycles corresponding to pulse durations of 8.2 fs, 9.5 fs, 10.6 fs and 11.7 fs, respectively. For the longer pulses, there is a larger circular contribution meaning more depletion of the target before the center of the pulse is reached. Also, the linear gate width is stronger for shorter pulses since less delay means more overlap in the gate width. Figure 2.14(b) shows the ratio of the strength of the linear component to the maximum circular component for each quartz plate thickness. Clearly shorter pulses with less delay have a higher ratio which is ideal for minimizing depletion and maximizing gate width intensity. This figure also demonstrates why shorter pulse durations are better than longer pulse durations, even for DOG.

To ensure the collinear method is just as capable of generating isolated attosecond pulses as the interferometric version, a CEP scan was again conducted. Figure 2.29 shows the results of a CEP scan from collinear DOG (a). The previous scan from the interferometer DOG is also shown for a comparison. It is clear the two results are very similar with discrete orders for some

CEP values (~0, 2π, etc.) and continua for others (π, 3π, etc.). This serves as the best evidence that the collinear method was functioning properly.

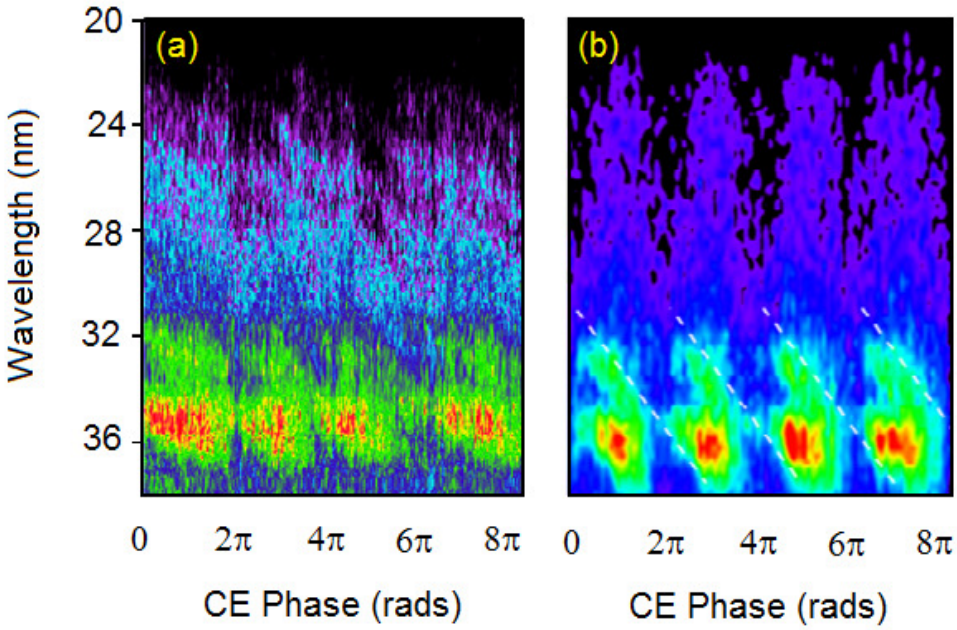

Figure 2.29 CEP Effect on (a) Collinear DOG and (b) Interferometric DOG.

Based on calculations, the collinear version of DOG seems to work, but how does it compare with the interferometric version of DOG? Without the high losses associated with an interferometer, the pulse energy focused to the gas target can be a few times higher than the interferometric DOG. This allows gases like neon, which was just barely accessible to the interferometer, and also helium, which was previously impossible, to be used for generating attosecond pulses. This is an important step since the bandwidth that these gases can generate can support very short pulse durations.

For all of the experimental results that will be shown, the experimental setup shown in figure 2.30 was used. It is identical to that shown in figure 1.4 except that the quartz plates used with DOG are before the spherical mirror and the BBO was located inside the vacuum. The reason for this was that the fused silica window at the entrance of the setup introduced too much delay between the second harmonic and the fundamental laser. This would cause the relative phase to change so much that the two beams would not be sufficiently overlapped as to create the

DOG pulse. Figure 2.31 shows a plot of the group delay and phase delay introduced between 400 nm and 800 nm laser pulses when passing through varying thickness of fused silica.

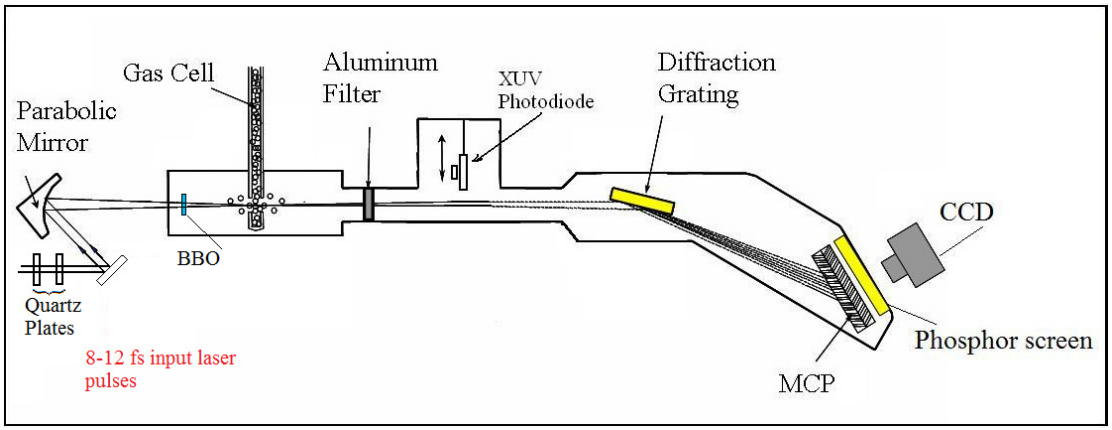

Figure 2.30 XUV Spectrometer with Collinear DOG Optics.

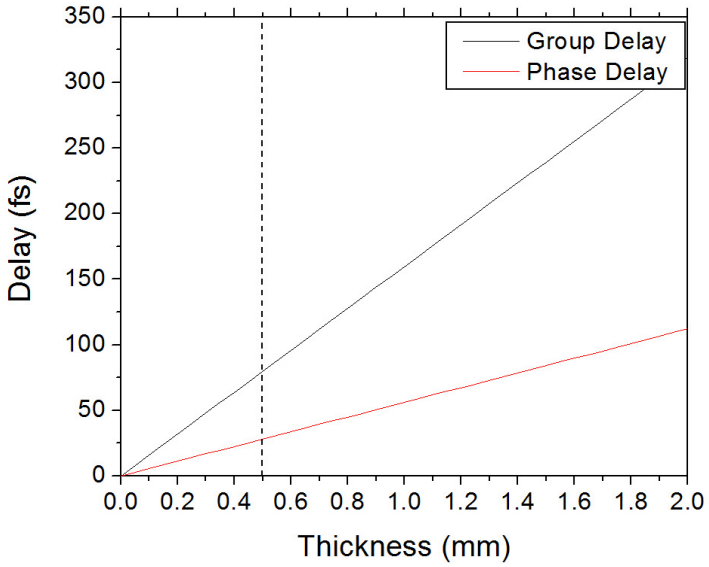

Figure 2.31 Group and Phase Delay between 800 nm and 400 nm in Fused Silica.

The dashed vertical line is the thickness (0.5 mm) of our entrance window. The calculations were done with the Sellmeier equations for fused silica found in ref [54]. It might be thought that this could be a way to control the relative phase between the IR and SHG but the thicknesses required for sub-cycle delay control would be too thin to be practical. Another benefit to having

the BBO in the vacuum is that the laser can be focused through it. Since the SHG efficiency is related to the intensity of the generating laser, its position along the laser focusing geometry can be chosen to optimize the SHG. Care must be taken not to place it too close to the laser focus to avoid damage to the optic itself however. Generally, the BBO is positioned roughly half the distance between the focusing mirror and the gas target. After the BBO, the laser is focused into the gas target as in the previous experiments. For these critical spectral measurements, the phase-matching properties of the HHG process were taken into consideration and optimized for highest HHG flux. These conditions will be described in section 2.3.

The first gas target chosen was argon. Its low ionization potential provides for a quick way to generate high flux spectra. Figure 2.32(a) shows the experimental spectral images for four input pulse durations. These were 8.2 fs, 9.5 fs, 10.6 fs, and 11.7 fs. The plate thicknesses chosen were 270 μm, 350 μm, 440 μm, and 530 μm, respectively to ensure a full cycle gate width in each case. The input laser pulse energy was 750 μJ for each duration yielding peak gate width intensities of 1.7, 1.4, 1.1, and 0.9 x 10^{15} W/cm^2, respectively. These four pulse durations were chosen to showcase the full range oven which the DOG method was successful.

The lineout plots of the spectra from (a) are shown in figure (b). The important feature to note is that the shorter pulse durations yield higher HHG flux than the longer pulse durations. This is to be expected since the peak intensity is higher for short pulses and the leading edge depletion is reduced. Since argon has a low saturation intensity, all the input pulse durations generated the same cutoff order. To characterize the attosecond pulse energy, the photodiode was installed (see figure 1.4) to measure the signal on an oscilloscope. This will be described in further detail in the phase matching section of this thesis. The measured pulse energies were 6.5 nJ, 3.7 nJ, 2.1 nJ, and 0.42 nJ from the shortest input pulse duration to the longest, respectively.

To fully characterize the attosecond pulses generated, each input pulse duration had a CEP scan conducted. The results are shown in figure (c). The 2π periodicity is obvious in each case meaning the DOG method was gating the attosecond pulse train properly. Also, the variation from discrete orders to continuum is seen in a couple of the images in agreement with the CEP effect on the DOG pulse. Each image looks different which we attribute wholly to the phase matching properties of the system. Shorter pulses have higher intensity than long pulses which is the driving factor in this. This too will be discussed in greater detail in the phase-matching section.

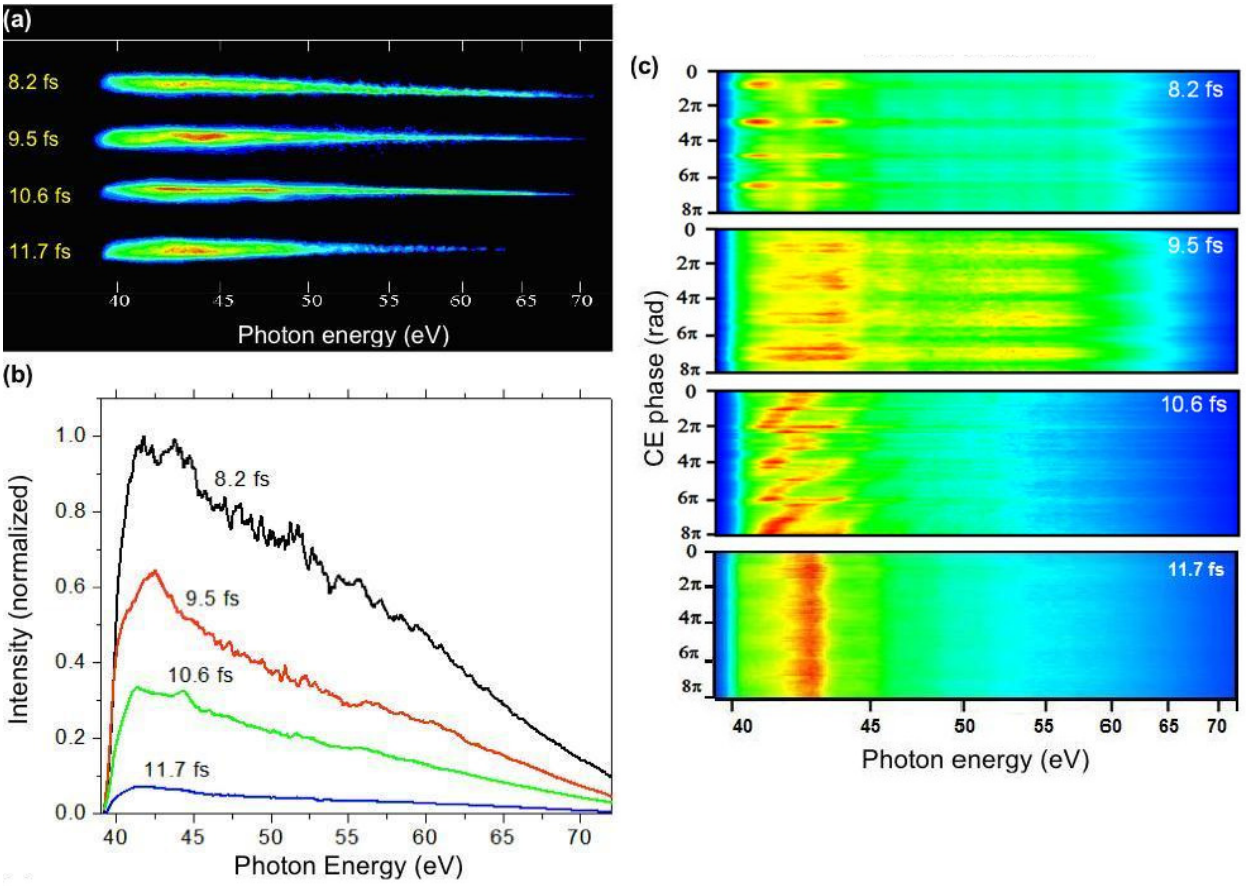

Figure 2.32 (a) Spectra in argon from Collinear DOG. (b) Lineout plots of (a). (c) CEP scans for each input laser pulse duration used.

The same experiment was next conducted with a neon target. The phase-matching conditions were re-optimized but the input laser condition was the same as in the argon case. The measured pulse energies were 170 pJ, 100 pJ, 60 pJ, and 40 pJ, from the shortest input pulse duration to the longest, respectively. The energy in each case is lower since the HHG flux from neon is lower due to its higher ionization potential (21.6 eV). Figures 2.33(a) and (b) show the spectral images and lineout plots, respectively. The CEP scans are shown in figure (c). In this case, all of the plots seem to show a continuum with and a strong modulation in intensity as the CEP is scanned. As discussed in chapter 1, the HHG process is highly ellipticity dependent. This is even truer for higher order harmonics since they come from the highest energy electrons which spent the most time in the laser dressed continuum. This means they were more likely to be steered away from

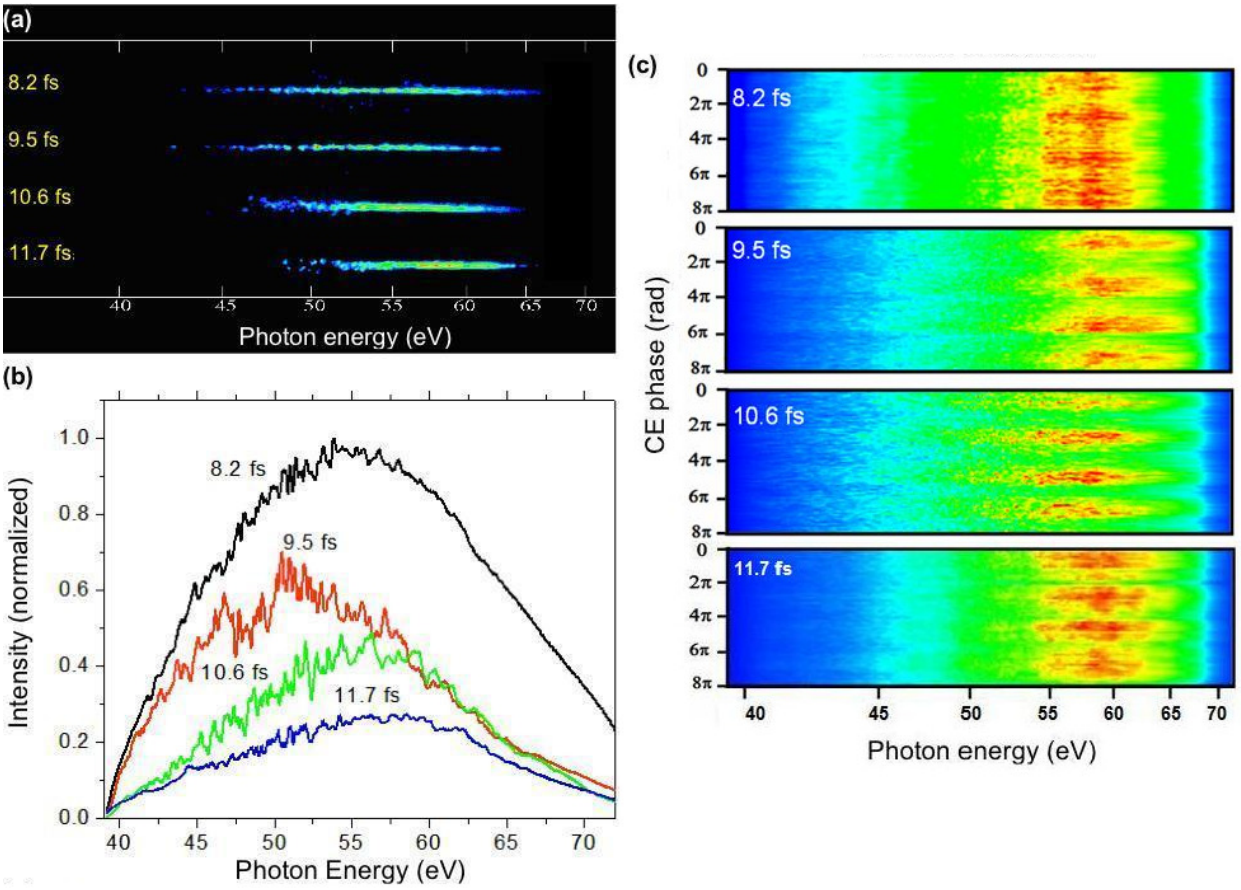

Figure 2.33 (a) Spectra in neon from Collinear DOG. (b) Lineout plots of (a). (c) CEP scans for each input laser pulse duration used.

the parent ion which effectively narrows the gate width. For a narrower gate width, only one pulse is ever found within the gate width but as it nears the edge of the gate, its intensity reduces due to the decreased recombination probability.

Finally, the same experiment was conducted with a helium target. The helium spectrum has a very high cutoff since the incoming laser energy is not nearly sufficient to saturate it. The spectrum does not even reach its maximum before the end of the transmission upper limit of the aluminum filter in the XUV spectrometer (~70 eV). Figure 2.34 shows the experimental results. The measured pulse energy for each input pulse duration was 45 pJ, 33 pJ, 25 pJ, and 16 pJ, for 8.2 fs, 9.5 fs, 10.6 fs, and 11.7 fs, respectively. Since these were measured after the aluminum

filter, they are not the true attosecond pulse energy because the high orders were not transmitted through the filter. Rather, they are the lower limit on what the attosecond pulse energy was.

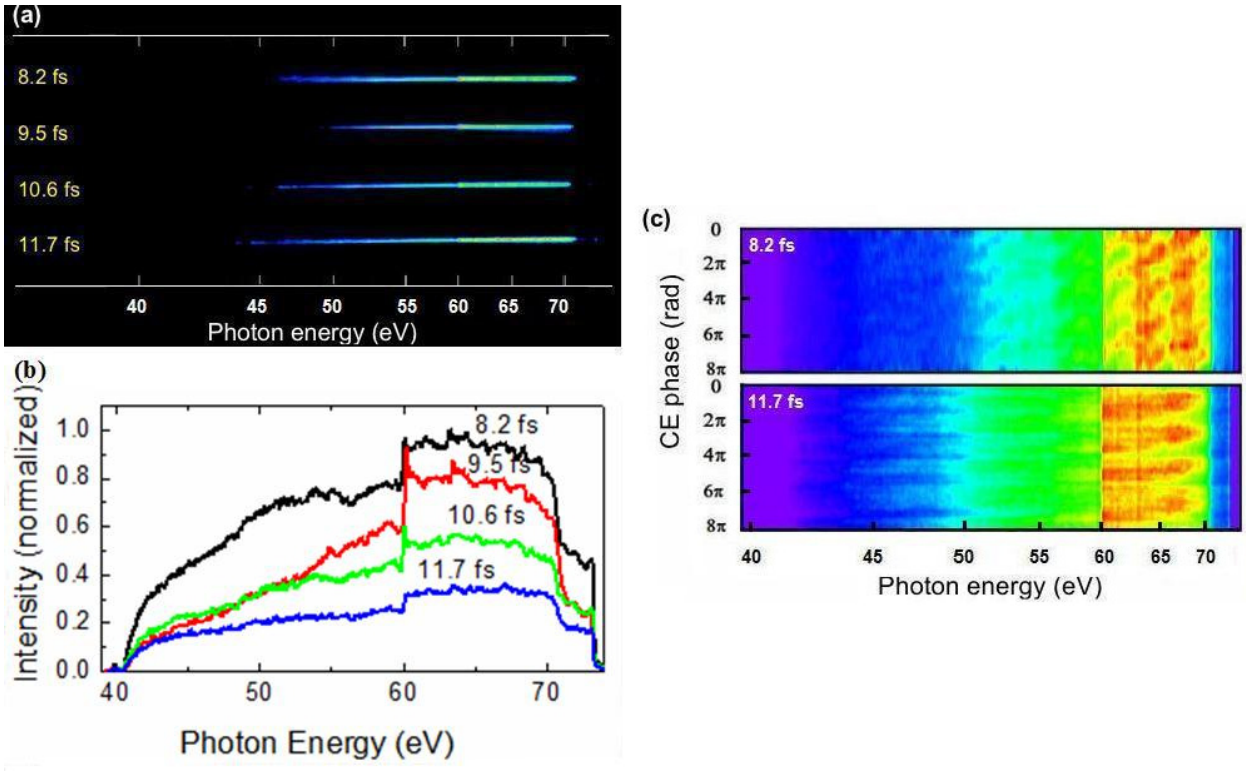

Figure 2.34 (a) Spectra in helium from Collinear DOG. (b) Lineout plots of (a). (c) CEP scans for each input laser pulse duration used.

In figure 2.34, CEP scans were only conducted for the shortest and longest pulse duration. Again, a 2π periodicity is observed. It was expected that the other pulse durations would exhibit similar effects for the CEP scan.

An important feature to note in the helium spectrum is the appearance of a sharp edge at ~60.1 eV. This is the 2s2p autoionization line in helium as first observed with synchrotrons in the 1960's [55]. This interesting feature will be discussed in much more detail in chapter 5, but for now the important aspect of this edge is that it is the first time it was observed with an attosecond pulse. If the spectrum was not a smooth continuum, it would not have been visible since it lies between two harmonic orders. This is a valuable observation since it was conducted with a table-top setup on a much smaller scale than a synchrotron facility at a national lab.

These previous 3 figures show the full value of the collinear method of DOG. First, the attosecond pulses were generated in gases capable of supporting very short attosecond pulse durations due to the high throughput of input laser energy. Secondly, the experiments were repeatable since the setup is so easy to implement. Finally, the method worked well for pulse durations as long as ~12 fs. This is a regime that is out of reach of the other gating methods since they require ~5 fs laser pulses.

2.1.3c Generalized Double Optical Gating (GDOG)

So far, the interferometric method and collinear methods of DOG have demonstrated their ability to effectively gate an attosecond pulse train even for multi-cycle input laser pulse durations. This method still has a disadvantage though in that it requires a secondary stage for pulse shortening after the amplifier. The output pulse duration of the KLS is ~25-35 fs which is too long for DOG to work. After the amplifier, the pulses are sent to a hollow core fiber and chirped mirror set for spectral broadening and temporal compression. While generating 8-12 fs pulses from such a setup is much easier than <5 fs pulses, it is still more difficult, of course, than no fiber at all. Also, even under the best conditions, the fiber and chirped mirror set only give ~50% coupling efficiency. This means that of the input laser energy of 2 mJ, only 1 mJ at most remains with which to be used for attosecond pulse generation. While the intensity of short pulse duration lasers is higher than long pulse durations, it was shown previously that target such as argon or xenon with low ionization potentials (I_p) will saturate before the highest intensity portion of the pulse. This means the increased intensity is not valuable for gases with low I_p. However, it was also shown that low I_p also results in much higher attosecond pulse energies due to the increased conversion efficiency of the HHG process. This implies that the full 2 mJ pulses from the amplifier could be used to scale the attosecond pulse flux to extremely high levels, like that sufficient for conducting nonlinear experiments. So our motivation is to develop a method for generating attosecond pulses with useable levels of flux directly from an amplifier without a secondary stage for pulse shortening.

The main limitation for using longer laser pulses for isolated attosecond pulse generation is the depletion of the target by the leading edge. DOG overcame this effect by reducing the delay required between the two circularly polarized pulses in PG. Another method to reduce the depletion is to change the ellipticity of the leading edge. This reduces the requirement on the delay between the two pulses even lower than DOG. This is the principle of generalized double

optical gating (GDOG) where the ellipticity is more general than requiring only circular polarization. The equations of the field components are similar to the case of DOG. The driving field, shown in figure 2.35(a) for a 20 fs pulse is expressed as [56]:

$$E_{drive}(t) = E_0\varepsilon[e^{-2\ln(2)\left(\frac{t-T_d/2}{\tau_p}\right)^2} + e^{-2\ln(2)\left(\frac{t+T_d/2}{\tau_p}\right)^2}]\cos(\omega_0 t + \varphi_{CE}), \tag{2.11}$$

where ε is the ellipticity of the right and left circularly polarized laser pulses that generate the PG field. For DOG, this equals 1 which demonstrates that DOG is just GDOG with $\varepsilon = 1$. Equation 2.11 does not have the SHG contribution included since it is generally much weaker than the fundamental field. The gating field (2.35(b)) for GDOG:

$$E_{gate}(t) = E_0[e^{-2\ln(2)\left[\frac{t-T_d/2}{\tau_p}\right]^2} - e^{-2\ln(2)\left[\frac{t+T_d/2}{\tau_p}\right]^2}]\sin(\omega_0 t + \varphi_{CE}), \tag{2.12}$$

is identical to DOG. These components can be used to find the time dependent ellipticity of the pulse by taking the ratio of the envelopes of the gating field to the driving field yielding,

$$\xi(t) = \min\left[\frac{\left|1 - e^{-4\ln(2)\frac{T_d}{\tau_p^2}t}\right|}{\varepsilon\left[1 + e^{-4\ln(2)\frac{T_d}{\tau_p^2}t}\right]}, \frac{\varepsilon\left[1 + e^{-4\ln(2)\frac{T_d}{\tau_p^2}t}\right]}{\left|1 - e^{-4\ln(2)\frac{T_d}{\tau_p^2}t}\right|}\right]. \tag{2.13}$$

The time dependent ellipticity is shown in figure 2.35(c). Since we are interested in the time range where the field is approximately linear, a Taylor expansion of equation (3) about the center of the pulse, or *t*=0, keeping the first non-trivial term yields:

$$\xi(t) = \left|2\ln(2)\frac{T_d}{\varepsilon\tau_p^2}t\right|. \tag{2.14}$$

Solving equation (4) for *t* and multiplying by 2 gives the gate width equation:

$$\delta t_G \approx \varepsilon\frac{\xi_{th}}{\ln(2)}\frac{\tau_p^2}{T_d}, \tag{2.15}$$

where $\xi_{th} \approx 0.2$ is the threshold ellipticity for harmonic generation. This equation is nearly identical as the gate width equation for DOG. For a 20 fs laser pulse with center wavelength of 780 nm and with $\varepsilon = 0.5$, T_d should be ~24 fs to ensure the gate width is one optical cycle which is the spacing between the adjacent attosecond pulses in the train.

A feature to note in figure 2.35 is that the driving field is reduced by a factor ε. This is accomplished by reflecting a portion of the driving field away. The gating field remains unchanged so that the GDOG pulse has an elliptically polarized leading and trailing edge.

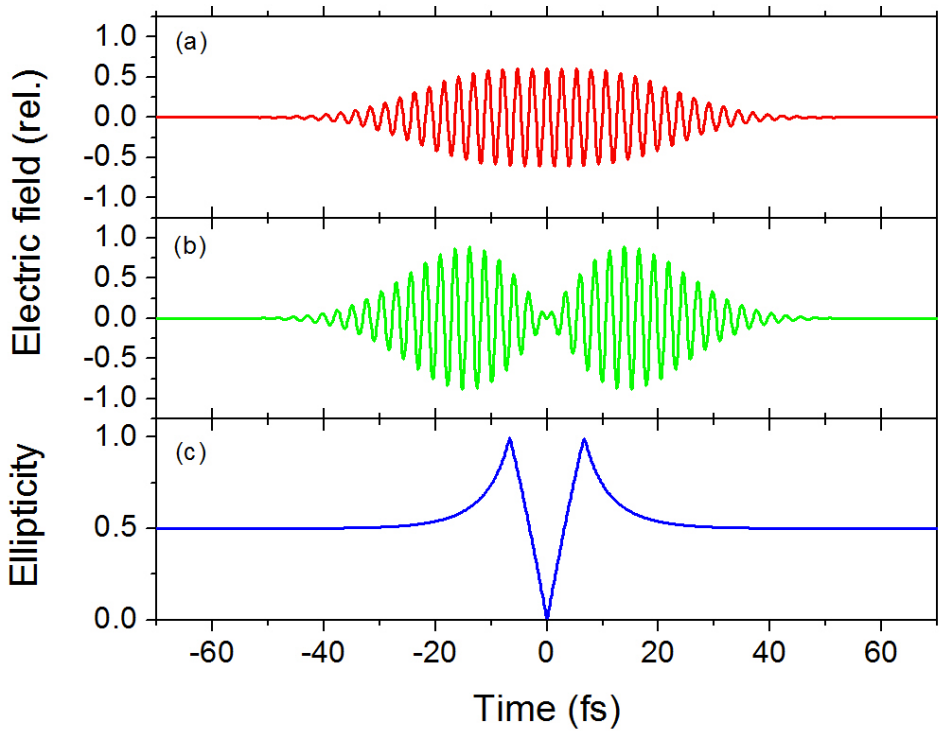

Figure 2.35 GDOG field components (a) Driving field (b) Gating field. (c) The time dependent ellipticity for GDOG.

Experimentally, this is done with the setup shown in figure 2.36(a). It is identical to the collinear method of DOG except that one or multiple Brewster windows are placed after the first quartz plate. If they are properly oriented, a component of the driving field can be reflected leaving the gating field unchanged.

Figure 2.36(b) and (c) show what the Brewster windows do in the setup. In the absence of the window, for a 20 fs laser pulse with 24 fs delay, the gate width (effective linear portion) is ~2 optical cycles. However, if the driving field is reduced (figure (c)) and the gating field remains the same, the ellipticity changes so that the gate width is now one optical cycle which is the necessary requirement for generating isolated attosecond pulses.

The properties of the Brewster windows are shown in figure 2.37. They are a half millimeter of fused silica to reduce material dispersion and have diameters of 2 inches. This allows for the angle to be tuned without clipping the input laser beam. The reflectivity of the

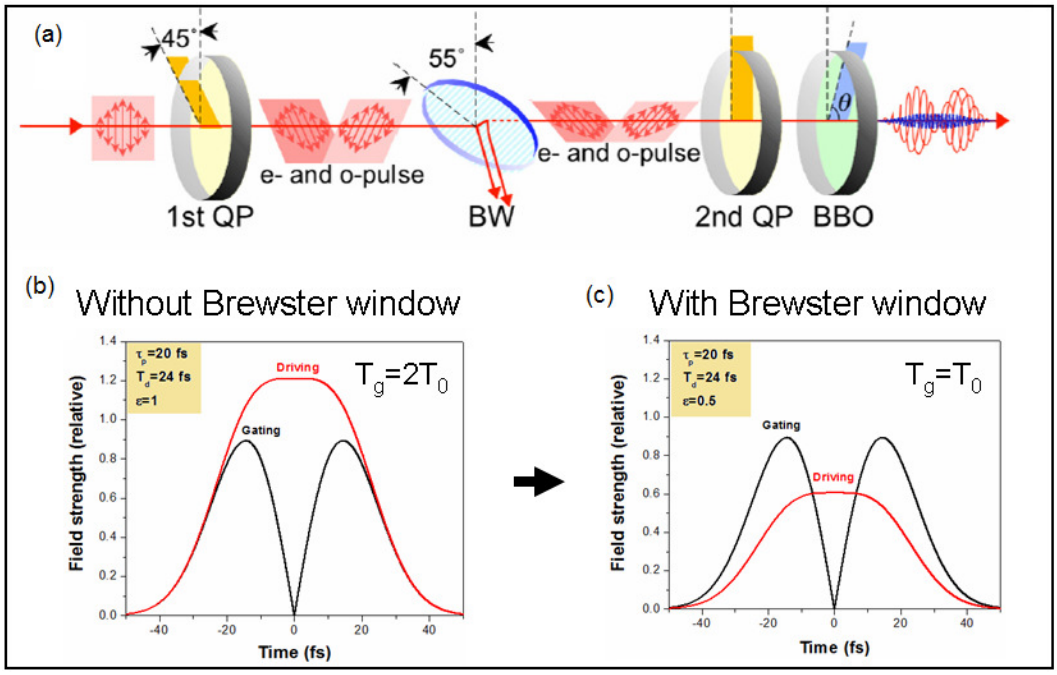

Figure 2.36 (a) GDOG optics. QP=quartz plate, BW = Brewster window. (b) the gating and driving field without the BW in place. (c) the same fields but after passing through the BW.

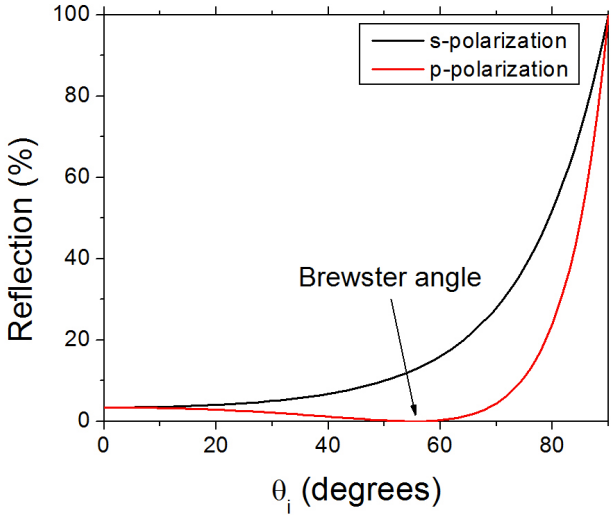

Figure 2.37 Reflectivity versus incident angle for fused silica.

material as a function of the incident angle is shown in the figure. A note on how polarization types are defined is warranted at this point. If the laser polarization lies parallel to the plane made up by the normal vector of the optic and the laser propagation vector, it is called "p". If the polarization is perpendicular to this plane, it is called "s". The plot shows that for s polarization input on the window, the laser is partially reflected while, at a certain angle (the Brewster angle), p-polarization is totally transmitted. This means for GDOG, the driving component must be s-polarized at the Brewster window and the gating component must be p-polarized. The calculation was done using reference [54, 57]. The window does not need to be set at exactly the Brewster window however. Tuning it to any other angle can change the ratio of the driving to the gating field and so provides a method to control the effective gate width of the GDOG pulse.

The main benefit of GDOG is that it further allows the reduction of delay between the two counter-rotating pulses that make up the GDOG pulse thereby reducing the leading edge depletion. Figure 2.38 shows an ADK calculation for GDOG as a function of pulse duration. The curves for PG and DOG are also shown for a comparison. This method clearly works without full depletion of the target for pulses longer than 20 fs. The values in Table 2.3 are

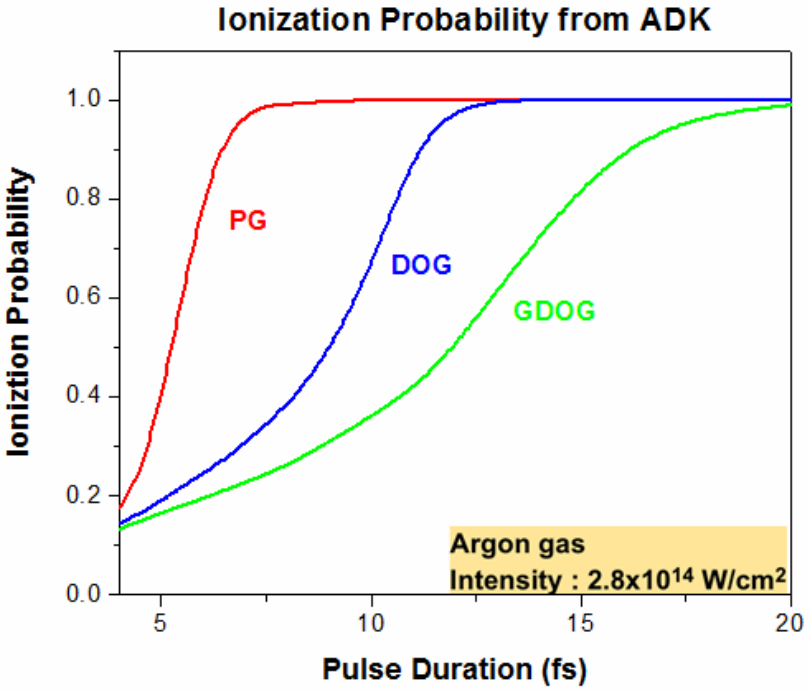

Figure 2.38 ADK calculation for GDOG (green line) as a function of input pulse duration.

the required delays for several values of the input pulse duration as calculated by the gate width equation. The gate width is one optical cycle in all cases and ε=0.5.

τ_p (fs)	9.5	11.6	13.5	15	17.8	20.2	22.3	24.2	26	27.7
T_d (fs)	5.2	7.8	10.4	13	18.2	23.4	28.6	33.8	39	44.2
T_d (cycles)	2	3	4	5	7	9	11	13	15	17

Table 2.3 Gate Width Equation Parameters for Generalized Double Optical Gating.

Since the driving field is reduced in GDOG but is responsible for the generation of the HHG, an analysis of how the peak field compares to both DOG and PG is required. Figure 2.39(a) shows the ratio of the linear portion to the maximum elliptical portion for each method. It seems that for GDOG, the reduced delay creating more overlap in the center of the gate compensates for the portion of the driving field lost when passing through the Brewster window. Figure 2.39(b) shows the calculated peak intensity in the gate width for the different methods

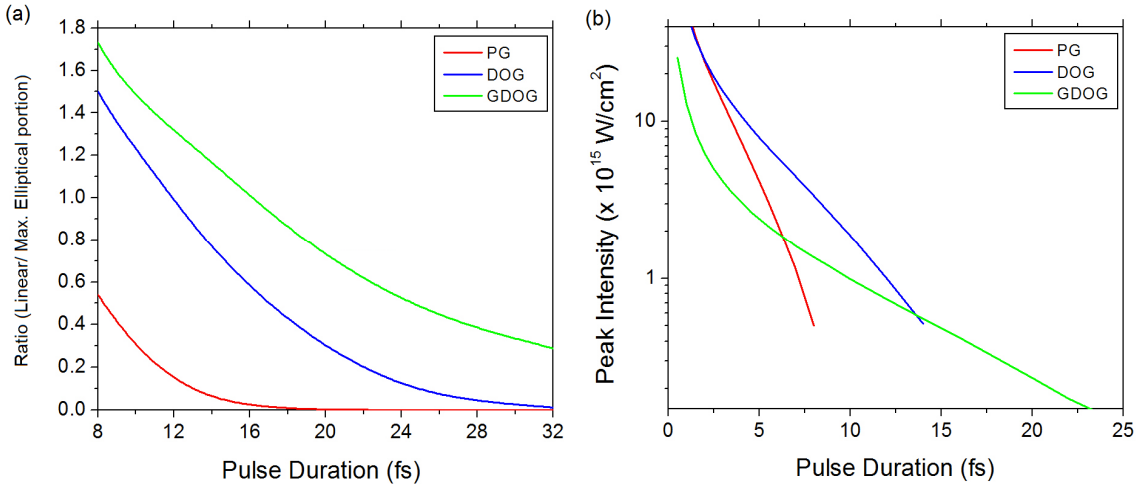

Figure 2.39 (a) Ratio of linear to maximum elliptically polarized portion for PG (red line), DOG (blue line), and GDOG (green line). (b) The calculated peak intensity in the center of the pulse for each method assuming identical input power.

assuming identical input laser energy. GDOG is the lowest until pulse durations of ~12 fs are reached meaning the cutoff is not as great as compared to PG and DOG for short pulses. Of course, the depletion is smaller than PG and DOG even for short pulses as seen in fig. 2.38.

As further evidence of the benefit of reducing the delay between the two counter rotating pulses, figure 2.40 shows the field components for DOG and GDOG assuming the same peak intensity in the gate width. As an example, for 20 fs lasers, the required gate width can be obtained by two extreme combinations, i.e., ε=1 and T_d=48 fs (a) or ε=0.5 and T_d=24 fs (b).

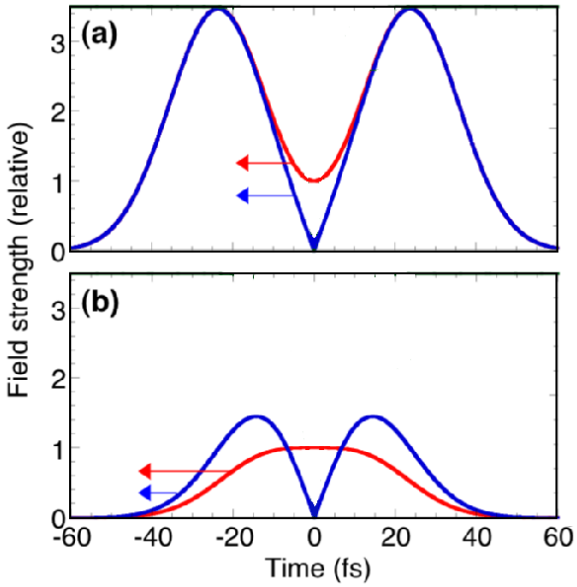

Figure 2.40 (a) DOG driving field (red line) and gating field (blue line) for 48 fs delay. (b) GDOG driving field (red line) and gating field (blue line) for 24 fs delay.

For the same driving field strength in the middle of the gate, the same gate width and the same laser pulse duration, calculations showed that the depletion of the ground state population by the laser field before the polarization gate decreases with the ellipticity ε. This is because both driving and gating field strength before the gate are lower for smaller ellipticity ε, which can be seen in Fig. 2.40. We define the saturation intensity I_s at the center of the polarization gate as that when the ionization reaches 98%. The calculated saturation intensity as a function of laser pulse duration for argon and neon gases is shown in Fig. 2.41. In the calculation using the ADK ionization rate, we chose $\varepsilon = 0.5$ and fixed the polarization gate width to $\delta t_G = 2.6$ fs. It can be seen that for 20 fs laser pulses, the saturation intensities for argon and neon gases are 3×10^{14}

W/cm^2 and 7×10^{14} W/cm^2, respectively which are strong enough for studying gating up to the 47th harmonic for argon and 99th order for neon.

Experimentally, the gating of high harmonic generation was performed for two laser pulse durations, 10 fs and 20 fs. Figure 2.42 shows typical frequency resolved optical gating

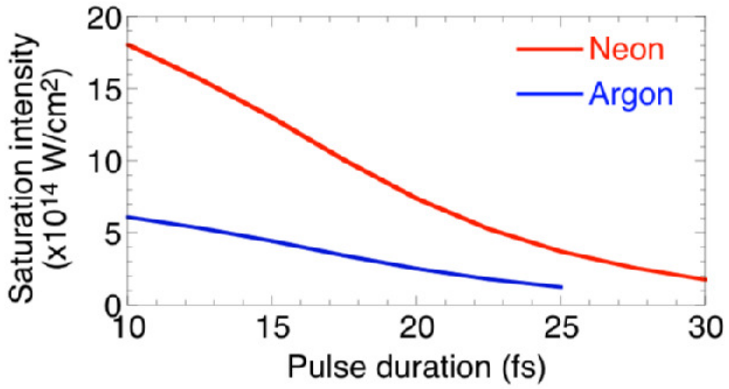

Figure 2.41 The saturation intensity as a function of pulse duration for neon (red line) and argon (blue line).

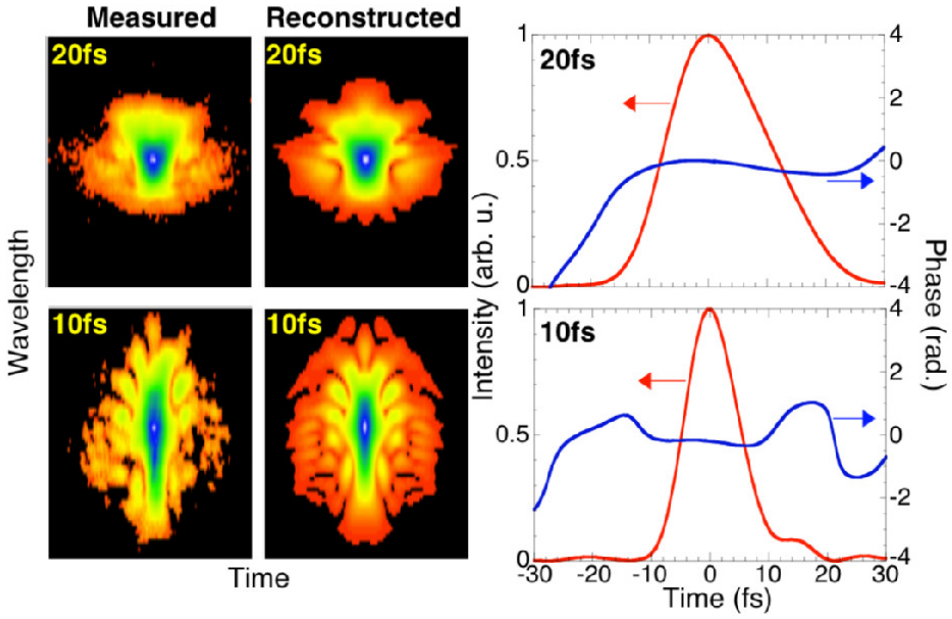

Figure 2.42 Typical FROG traces for 10 fs and 20 fs laser pulses. The left figures are the FROG images and the right figures are the reconstructed temporal profiles (red lines) and temporal phases (blue lines).

(FROG) traces for the 10 fs and 20 fs linearly polarized input pulses. The left figures are the measured and reconstructed traces whereas the right figures are the temporal domain representations. The temporal phase indicates the pulses are nearly transform limited.

Figure 2.43 (a) shows typical harmonic spectra from the argon gas target using the 20 fs laser pulses. The upper spectrum was obtained by removing the BW ($\varepsilon = 1$). In this case, we would expect the gate width to be two laser cycles, thereby allowing at least two attosecond pulses within the gate resulting in interference that leads to a spectrum with discrete harmonic peaks. The measured discrete spectrum contains both even and odd orders due to the full cycle spacing between the attosecond pulses. The lower figure shows a continuous spectrum from GDOG with the BW placed after the first quartz plate. The FWHM of the XUV continuum

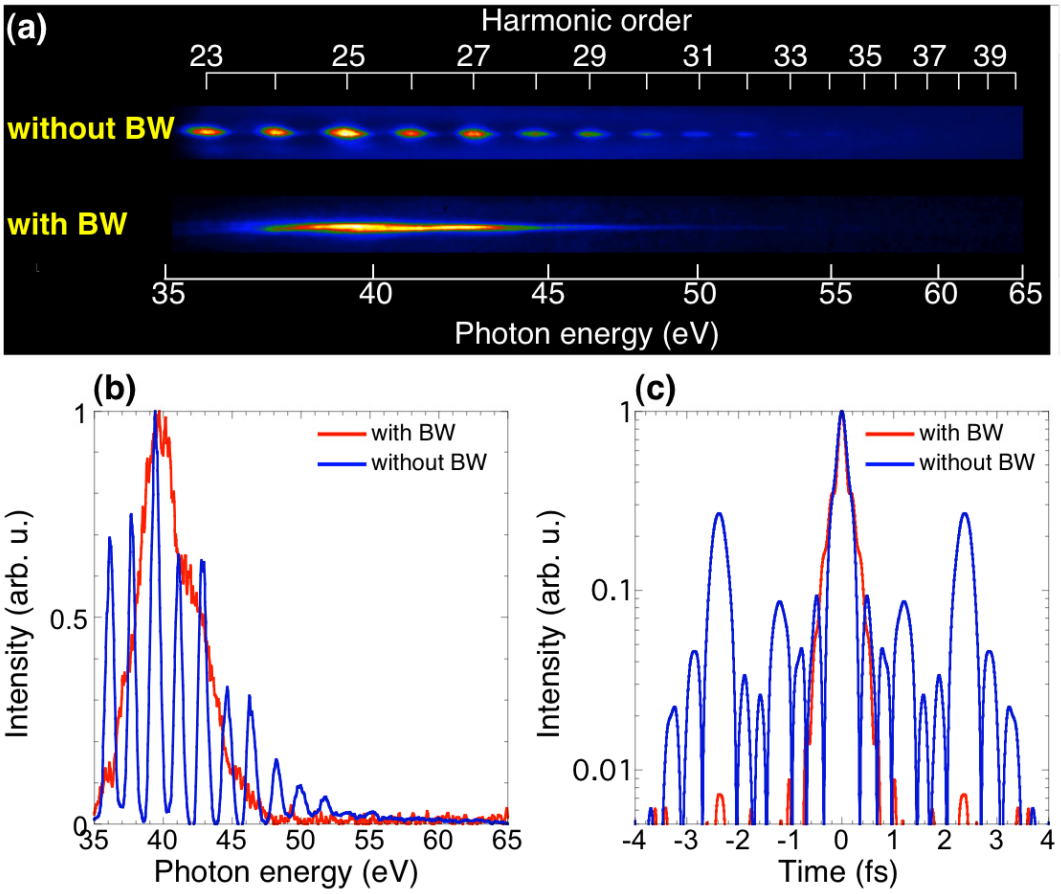

Figure 2.43 (a) Typical spectra from GDOG without and with the Brewster window installed. (b) Lineout plots of the spectra in (a). (c) Fourier transforms of the plots in (b).

was 5 eV, which supports a single isolated 200 as pulse. The normalized lineout plots of the spectra are shown in fig. 2.43 (b). Previous studies showed that the corresponding attosecond pulses are chirped [58], which can be compensated. Figure 2.43 (c) shows the Fourier transforms of the spectra in (b) assuming a flat phase. In the case of GDOG, the satellite pulses are nearly a factor of 100 lower than the main attosecond pulse. The dramatic change of the spectrum from discrete harmonic peaks to a continuum by inserting the BW is the first indication that the gating time was reduced by the GDOG down to the level of attosecond pulse spacing.

We compared the high harmonic spectra generated with three different gating methods in argon and neon gases. Figure 2.44 shows the lineout spectra for 10 fs and 20 fs pulses under the conditions for single cycle gating in (a) argon and (b) neon with the GDOG. Also shown are the results for single cycle gate widths in the DOG case and half cycle widths for polarization gating.

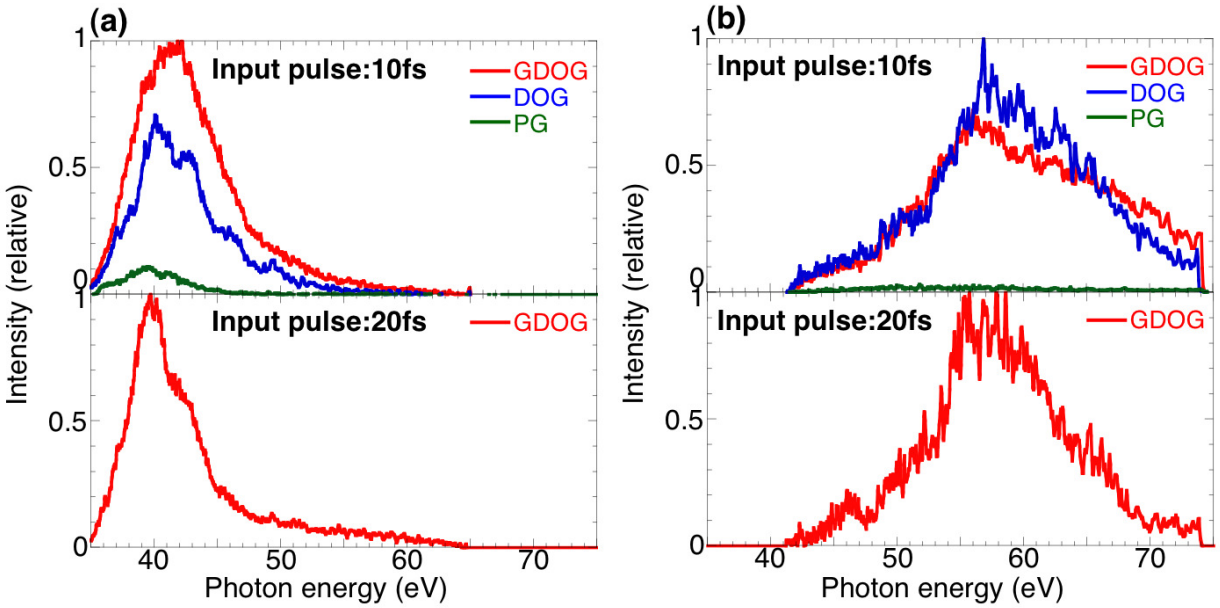

Figure 2.44 (a) Spectra from GDOG (red), DOG (blue) and PG (green) in an argon target for a 10 fs (upper figure) and 20 fs (lower figure) pulse. (b) Spectra from GDOG (red), DOG (blue) and PG (green) in an neon target for a 10 fs (upper figure) and 20 fs (lower figure) pulse.

All spectral distributions are nearly super-continua, as expected. For 10 fs lasers, the DOG works almost as well as the GDOG. Both of them are much more efficient than the polarization gating. However, only GDOG produces detectable spectra for 20 fs pump pulses because the ground state population is less depleted from the leading edge of the pulse while the peak intensity inside the gate width is also higher. For the 20 fs pump laser cases, Fourier transforms of the neon spectrum showed that it supports 120 as. We measured the pulse energies of the XUV continuum with an XUV photodiode, which were 230 pJ for argon and 25 pJ for neon.

A broad continuous XUV spectrum is a necessary but not a sufficient condition to demonstrate the extraction of a single attosecond pulse by the gate. We studied the CE phase dependences of the harmonic spectra to find out whether the continuum spectra originated from gating. For the generalized double optical gating, the CE phase of the laser determines where the attosecond pulses are generated in the polarization gate. Our simulations predicted that for a certain CE phase, a single strong attosecond pulse can be generated at the middle of the gate corresponding to a super-continuum in the spectrum domain. For another CE phase value, two attosecond pulses separated by one laser cycle can be generated. They are emitted close to the two edges of the polarization gate and therefore their intensities are lower due to the suppression power of the gating. The interference between the two pulses leads to intensity modulations in the spectrum domain. For other CE phases, the attosecond pulses evolve between one and two pulses. In the spectrum domain, the profile and intensity changes with a 2π periodicity. The dependence is very similar to that of DOG [58].

Figure 2.45 shows the measured dependence of the gated high harmonic spectra on the CE phase for (a) argon and (b) neon for 10 fs and 20 fs laser pulses. The CE phase variation of the laser was measured simultaneously with an *f-to-2f* interferometer. The expected 2π periodicity clearly showed up. The results from neon cover higher harmonic orders for which the polarization gate width is narrower than that for the lower orders from argon gases, which explains the stronger intensity modulation in the case of neon. For the same reason, the harmonic peaks from neon do not become as discrete as in the argon case. As far as we know, this is the first time that effects of CE phase on the high harmonic spectra emitted from the short quantum trajectories are measured with 20 fs lasers. In our experiments, the gas target was located after the laser focus where the phase-matching favors the short trajectories. The CE phase effects that originated from the GDOG were different from the observations of harmonic

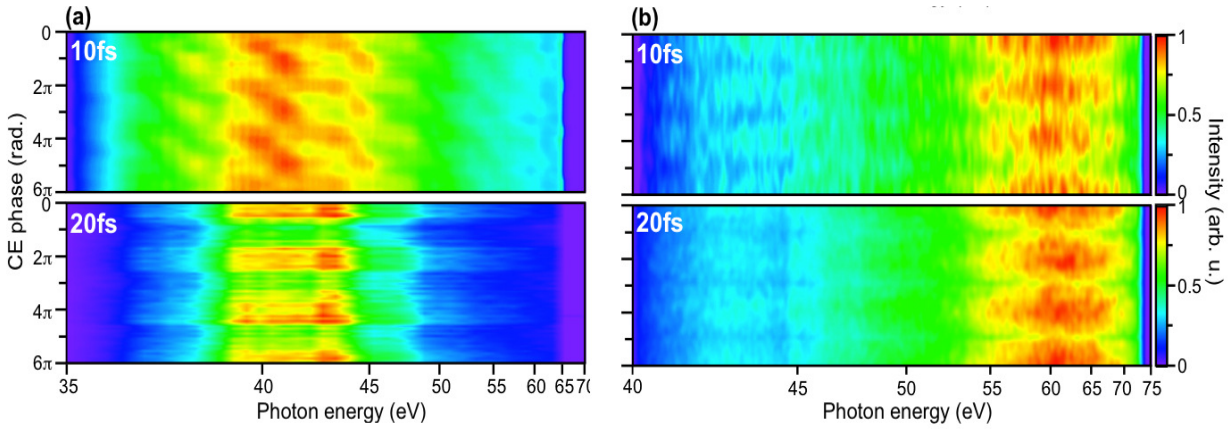

Figure 2.45 (a) CE phase scans for GDOG in an argon target for 10 fs (upper figure) and 20 fs (lower figure) pulses. (b) The same as (a) but from a neon target.

signals from long trajectories using similar laser pulse durations [14]. The dramatic variation of the high harmonic spectra as a function of CE phase could lead to a new method to determine the absolute CE phase with a window of 2π and can be applied to lasers as long as 20 fs. The method can complement the established phase-meter based on measuring asymmetry of above-threshold ionization electrons that works well for few cycle lasers [52].

In conclusion, the double optical gating method has been extended so that two counter-rotating *elliptically* polarized fields are used for generating single isolated attosecond pulses. As compared to the case that two counter-rotating *circularly* polarized fields were used, the GDOG has been demonstrated to work with much longer pump lasers. The gated harmonic spectrum from neon supports 120 as even when 20 fs laser pulses were used. Also, the 2π periodicity of the gated harmonic spectrum as a function of the CE phase with 20 fs lasers was demonstrated for the first time. Such long laser pulses can be generated from Ti:Sapphire CPA lasers directly with no further pulse compression from hollow-core fibers required. Therefore, the technique should allow more laser laboratories to generate single isolated attosecond pulses. So far, the highest laser energy produced from hollow-core fibers is on the order of a few mJ. The pulse energy from the CPA system can be much higher, which may allow scaling of the single isolated attosecond pulses to the level needed for studying nonlinear phenomena.

2.2 Phase Matching Considerations with DOG

Generating isolated attosecond pulses is an important step in laser development but, from a physicist's perspective, the photon flux needs to be as high as possible to make them a useful laboratory tool. Luckily, phase matching techniques allow the flux to be optimized to relatively high levels. The highest conversion efficiency for a single harmonic order from a neon target was 5 x 10^{-7} [59]. The highest conversion efficiency measured for a single isolated attosecond pulse was 6 x 10^{-6} [60]. Obviously these are still quite low even though they were obtained under the optimal phase matching conditions meaning special emphasis must be placed on the phase matching techniques. The point of this section is to lay out the methods used to generate the strongest pulse energies possible.

2.2.1 Theoretical Considerations

The definition of phase matching is that all of the harmonic photons are generated in phase with the generating laser so that the signal adds constructively and is maximized by the time it reaches the detector. However, normal dispersion is frequency dependent and tends to cause the harmonics to travel at a different phase velocity as compared to the generating laser through the target gas medium. This alone causes the phase to be mismatched and the output flux would be expected to reduce with increasing medium thickness. Luckily, other terms contribute which can offset the normal dispersion. The main goal is that the wavevector mismatch, Δk, which is equal to the difference between the wavevector of the fundamental laser and the harmonic should be equal to zero. The main terms associated with the phase matching are the material dispersion, focusing geometry, atomic dipole phase, plasma density, and any nonlinear effects. Each of these terms has a different sign meaning one effect can be cancelled by changing the effect of another. The total wavevector mismatch is then given as:

$$\Delta k = \Delta k_{neu} + \Delta k_{plasma} + \Delta k_{geom} + \Delta k_{atom} \tag{2.16}$$

The most obvious term is probably the dispersion due to the neutral atomic target. This is expressed as:

$$\Delta k_{neu} = k_{qneu} - q k_{1neu}, \tag{2.17}$$

where k_{qneu} is the wavevector of the harmonic, k_{1neu} is the wavevector of the fundamental laser, and q is the harmonic order. This type of mismatch obviously depends on the target properties,

for instance the type of gas and the pressure. Taking this into consideration, the formula can be re-written as [61]:

$$\Delta k_{neu} = -q\frac{2\pi}{\lambda_1} P\delta_1(1-\eta) \tag{2.18}$$

where N is the number of atoms per unit volume at 1 atmosphere, λ_1 is the fundamental wavelength, P is the pressure of the target in atmospheres, δ_1 is the difference of the refractive index of the fundamental and harmonic wavelength in the target, and η is the ionization level calculated from the ADK method. The important feature of this formula is that it is pressure dependent.

The second term in the total mismatch is the plasma contribution. Since the plasma has different refractive index properties depending on the wavelength of the harmonic, the fundamental and harmonic will react differently to the plasma. This term is written as:

$$\Delta k_{plasma} = qPN\eta r_e \lambda_1, \tag{2.19}$$

where r_e is the classical electron radius (2.8 x 10^{-13} cm). Again, this term depends on the pressure of the target.

The third term concerns the focusing geometry of the generating laser. Let z be the distance to the laser focus and $z_r=\pi w_0^2/\lambda$, where w_0 is the $1/e^2$ focus spot size, be the Rayleigh range [62]. When a Gaussian laser pulse passes through a focus, a phase shift $\psi(z)$ = Arctan(z/z_r) (referred to as the Gouy phase shift) occurs. This effect can be written as;

$$\Delta k_{geom} = qk_1 - q\left(k_1 - \frac{\partial\psi(z)}{\partial z}\right). \tag{2.20}$$

Differentiating the Gouy phase shift with respect z and simplifying the above expression yields:

$$\Delta k_{geom} = \frac{q}{z_r\left(1+\left(\frac{z}{z_r}\right)^2\right)}. \tag{2.21}$$

While this term is always positive, since a tighter focus results in a smaller focus spot size the contribution from this term can be reduced if a longer focal length is used.

The final term concerns the atomic dipole phase. As discussed previously, the Fourier transform of the dipole matrix element governs the generation of a harmonic [16, 63]. It was

shown previously [64] that the dipole moment can be written in terms of the quasi-classical action, *S*, as:

$$\vec{x}(t) \propto \int_0^\infty d\tau e^{-iS(\vec{p},t,\tau)} \tag{2.22}$$

where *p* is the momentum, t and τ are the times when the wavefunction propagated during and the time at which the electron makes a transition to the continuum, respectively. The expression for *S* is given as:

$$S(p,t,\tau) = \int_\tau^t dt' \left(\frac{mv(t')^2}{2} + Ip \right). \tag{2.23}$$

After taking the Fourier transform of equation (2.22), the signal of the q^{th} harmonic is given as:

$$x_q = A_q e^{i\Phi_q} \tag{2.24}$$

where A_q is an amplitude and the phase $\Phi_q=(-S_q+\omega_q t)$ is the atomic dipole phase. Since there are two sets of quantum paths (the long and short trajectories), the phase can have two values. Also, the classical action integral (2.23) can be written in terms of the ponderomotive energy as $S(\vec{p},t,\tau) \approx U_p \tau + ...$ which is linear in intensity [65]. This simplifies the atomic phase to:

$$\Phi_i(r,z,t) = -\alpha_i I(r,z,t) \tag{2.25}$$

where the subscript i refers to either the long or short trajectory and α is the slope of the phase as a function of the intensity for each quantum path. These values were calculated previously to be $\alpha_s = 10^{-14}$ cm^2/W for the short trajectory and $\alpha_l = 27 \times 10^{-14}$ cm^2/W for the long trajectory for the 15^{th} harmonic in argon. Once the atomic dipole phase term is known, the wavevector mismatch for the atomic dipole phase, Δk_{atom}, can be calculated by differentiating equation (2.25) with respect to the longitudinal position z. After simplification, this yields:

$$\Delta k_{atom} = q\alpha I \left(\frac{2zz_r^2}{(z_r^2 + z^2)^2} \right). \tag{2.26}$$

As was mentioned previously, the terms in equation (2.16) can be used to counteract each other resulting in the total mismatch being reduced. This is well demonstrated by comparing the last two terms, the geometrical considerations and the atomic dipole phase. Figure 2.46 shows a plot of the phases from the Gouy phase and atomic dipole phase contributions as a function of z. At z=0, the laser focus exists. The parameters are an 800 nm laser focused to a spot size 30 μm

and with intensity of 2.8 x 10^{14} W/cm^2. The red line and blue line represent the atomic dipole phase contributions from the short and long trajectories, respectively. Clearly the short trajectories have a much flatter phase. The green line is the contribution from the Gouy phase

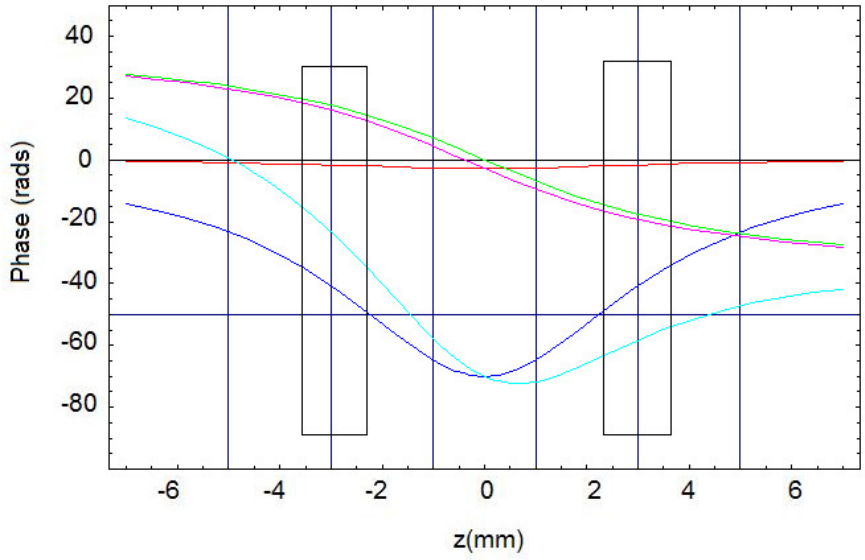

Figure 2.46 Gouy phase (green line) and atomic dipole phase for the short (red line) and long (blue line) trajectories. The sum of Gouy and atomic dipole phases are given for the short (magenta line) and long (cyan line) trajectories. The rectangular areas represent ~1mm long interaction regions that may be used in an experiment.

shift. When this is added to the atomic dipole phases, the blue line becomes the cyan line and the red line becomes the magenta line. The rectangles drawn on the plot represent a typical ~1mm interaction regions over which we wish to generate harmonic flux. One is drawn before the laser focus. Here, the long trajectories and short trajectories have somewhat flat phases inside the interaction medium. If the attosecond pulse was generated here, it would be made up of both long and short trajectories which, since the attosecond pulses have opposite phases, would make it difficult to characterize temporally such a pulse. However, if the interaction medium is placed after the focus, the sum of the short trajectory and long trajectory phase would be flatter than before the laser focus meaning the phase matching would be improved since the total phase is more constant. Attosecond pulses with much stronger signal can be generated by simply choosing the appropriate medium position within the focusing geometry.

Once the total wavevector mismatch is known, the number of photons generated for a particular harmonic order can be estimated. This number is expressed as [66]:

$$N_q = N_0 \left| d(q\omega_0) \right|^2 \frac{4(L_{abs}L_{coh})^2}{L_{coh}^2 + (2\pi L_{abs})^2} \left[1 + \exp\left(\frac{-L}{L_{abs}} \right) - 2\cos\left(\frac{\pi L}{L_{coh}} \right) \exp\left(\frac{-L}{2L_{abs}} \right) \right]. \qquad (2.27)$$

This equation depends on the coherence length $L_{coh} = \pi/\Delta k$, or the length over which the harmonics remain in phase, and the absorption length $L_{abs} = 1/2\alpha$, which is the length over which the harmonics become appreciably absorbed. α in this equation is the absorption coefficient and should not be confused with the slope of the atomic dipole phase from equation (2.25). In an experiment, the medium length, L, should be set $>3L_{abs}$. N_0 is the neutral gas density, and $d(q\omega_0)$ is the atomic dipole moment induced by the laser field. Since the number of atoms in the medium is most important, the length pressure product can be introduced in place of L_{coh} and L_{abs}. This modifies equation (2.27) to:

$$N_q = .N_0 \left| d(q\omega_0) \right|^2 \frac{1}{1 + 4\pi^2 \left(\frac{PL_{abs}}{PL_{coh}} \right)} \left[1 + \exp\left(\frac{-PL}{PL_{abs}} \right) - 2\cos\left(\frac{\pi PL}{PL_{coh}} \right) \exp\left(\frac{-PL}{2PL_{abs}} \right) \right] \times \exp\left(\frac{-PL'}{PL_{abs}} \right) \qquad (2.28)$$

where P is the pressure in the medium. The final exponential term in 2.28 represents absorption of the emitted harmonics by the residual gas in the experimental apparatus. The effective PL' is the pressure length product over which the photons travel from the generation region to the detector. No new photons are generated in the process meaning it is just an exponential decay. Equation 2.28 can be plotted ignoring the N_0 and $d(q\omega_0)$ terms to get an estimate of the behavior of the number for different values of the medium length. Figure 2.47 shows a plot of N_q in arbitrary units versus PL for different values of the pressure-coherence length product. This plot was adapted from reference [67]. When $PL_{coh}=PL_{abs}$ the output flux is small but as PL_{coh} increases, N_q quickly increases to an asymptotic value. Once the medium length becomes very long, the absorption of the harmonics by the gas target itself takes over. In the absence of absorption, the flux increases quadratically as shown by the black line. The conclusion from figure 2.47 is that, for optimal phase matching we require $L_{coh}>5L_{abs}$.

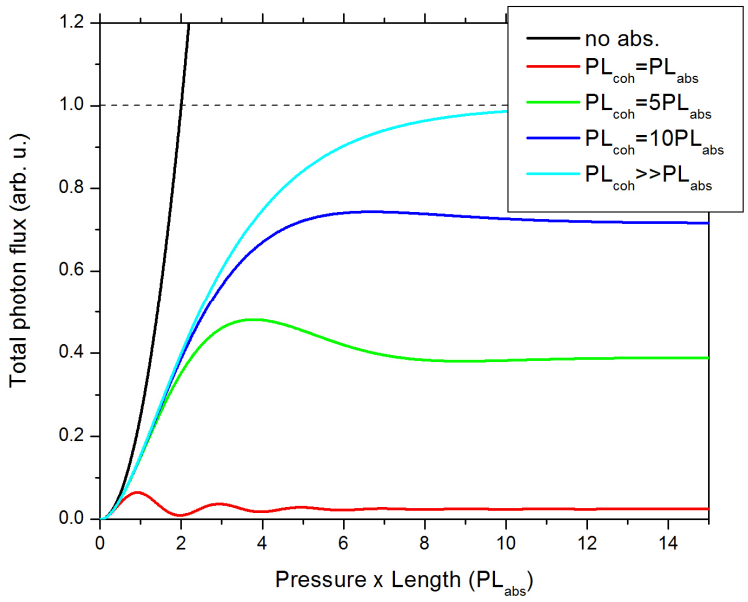

Figure 2.47 Output photon flux versus medium Pressure/length product for different values of pressure/coherence length products.

2.2.2 Experimental results

Experimentally, the knobs available to easily tune the phase matching are the location of the gas cell within the focusing geometry and also the pressure-length product of the medium. Since changing the gas cell is not a quick process, simply varying the pressure accomplishes the same thing. From equation 2.16, it is obvious that these two "knobs" are sufficient to modify all 4 terms in the total wavevector mismatch equation. Unfortunately the adjustment of each knob can modify multiple terms simultaneously.

The first parameter that was modified was the gas cell position along the laser focus while holding all other parameters constant. The experimental parameters were 8 fs laser pulses with 850 μJ pulse energy and peak intensity within the gate width of 1.9 x 10^{15} W/cm^2 at the laser focus [60]. The corresponding Rayleigh range was 6.3 mm. The gas cell was 1.4 mm in diameter with a laser drilled hole on both sides and the rest of the experimental setup was identical to figure 1.4. To ensure a single cycle gate width, the first quartz plate was 270 μm corresponding to 3 cycles of delay. Figure 2.48 shows the result for argon and neon gas targets.

Figure (a) shows the spectrum plotted versus gas cell position with the negative values representing positions before the laser focus and the positive values representing positions after the focus. The signal obviously reaches a maximum after the laser focus at about +3 mm. Figure (b) shows the pulse energy as a function of position. The energy was measured with an XUV photodiode and the process by which the pulse energy is recorded is explained in detail in appendix E. These values represent the pulse energy before passing through the aluminum filter which had a transmittance of ~10-25% due to thin AlO_2 layers on each side. The peak value was ~6.5 nJ. The error bars indicate the range of values measured in multiple trials. Figure 2.48(c)

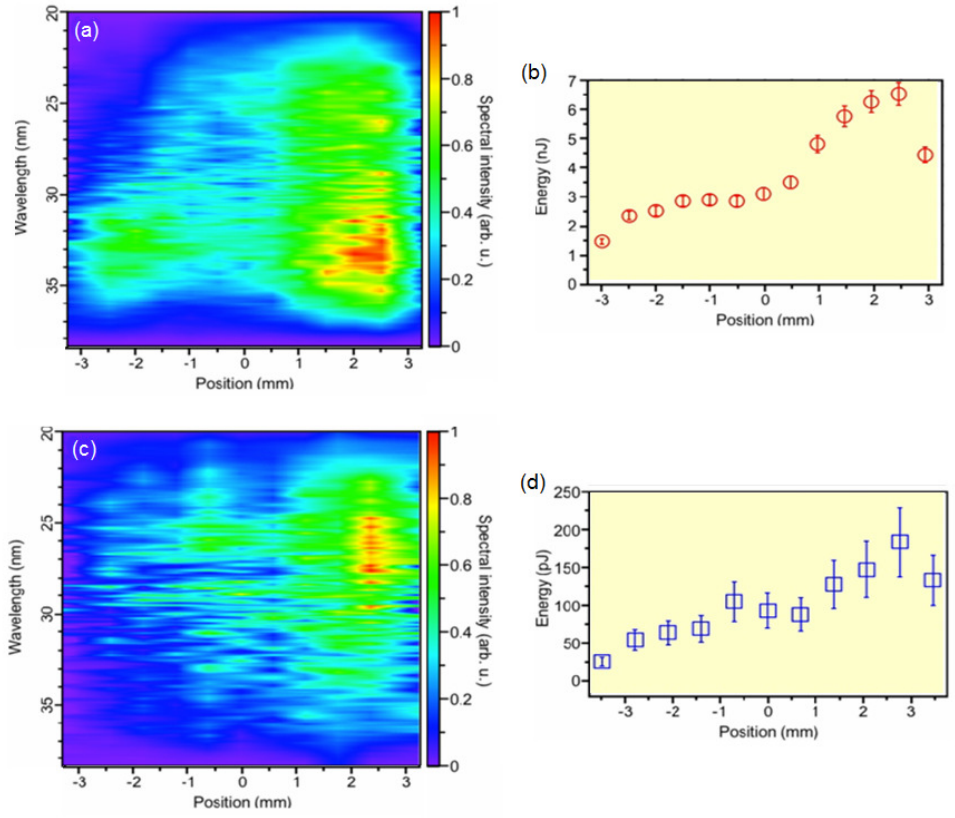

Figure 2.48 (a) Spectra dependence on gas cell position for HHG from argon. (b) The measured pulse energy for each position. (c) Spectra dependence on gas cell position for HHG from neon. (d) The measured pulse energy for each position.

shows a similar plot as in (a) but from a neon target. Since neon has a higher ionization potential as compared with argon, the plasma effect should be greatly reduced. Again, the best position was found to be ~3 mm after the laser focus in agreement with the theoretical considerations.

Figure (d) shows the measured pulse energy at the gas target with a peak value at ~170 pJ. These results represent the strongest single attosecond pulses ever generated. The corresponding conversion efficiencies were 6 x 10^{-6} from ~9 x 10^{8} photons per pulse in argon and 2 x 10^{-7} from ~2 x 10^{7} photons per pulse in neon. An interesting point to note is that since the harmonic flux actually is generated by only a single cycle of the DOG pulse, the conversion efficiency using only this fraction of the pulse energy was 4 x 10^{-5} in argon and 1 x 10^{-6} in neon.

Once the optimal gas cell position was located, the second experimental knob that was tuned was the gas pressure. Changing the gas pressure varied both the neutral atom dispersion and, depending on the laser intensity, the amount of free electrons generated. Once the pressure

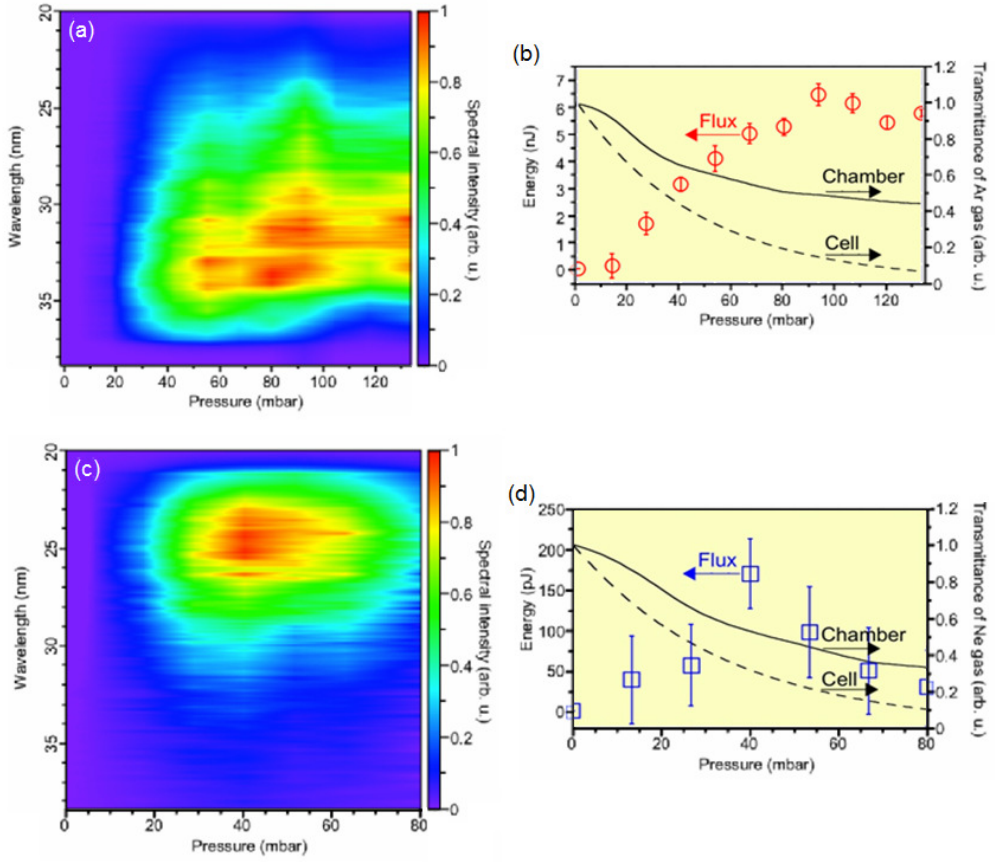

Figure 2.49 (a) Spectra dependence on gas cell pressure for HHG from argon. (b) The measured pulse energy for each position. (c) Spectra dependence on gas cell pressure for HHG from neon. (d) The measured pulse energy for each position.

gets too high, absorption by the gas itself can begin to reduce the total flux of photons. Figure 2.49(a) shows the spectrum as a function of the backing pressure in the gas cell for an argon target. What is most interesting about this figure is that there seems to be an ideal pressure where the spectrum is broadest occurring ~80 mbar. For short pulse generation, this would probably be the best pressure. Figure (b) shows the measured pulse energy at each pressure (red circles) with error bars indicating the range of measured values from multiple trials. Also plotted on the same figure is the transmission of argon gas as a function of pressure from residual gas inside the chamber (solid line) and the gas cell itself (dashed line) for 32 nm photons. The absorption from the chamber can be reduced by increasing the pumping rate of our vacuum system meaning a higher flux is expected. Figure (c) shows the same plot as in (a) but from a neon target. The neon HHG spectrum is centered at shorter wavelengths which can be seen in the figure. Also, the neon gas reaches a definite maximum but quickly drops off due to absorption of the photons by the residual gas pressure. Figure (d) shows the measured pulse energies at each pressure (blue squares) with the corresponding error bars. The error is larger in the case of neon since the photon flux is much lower as compared to argon giving a worse signal to noise ratio. Also shown on the plot in (d) are the neon gas XUV photon transmission curves for residual gas in the chamber (solid line) and gas cell (dashed line) for 25 nm photons. In both argon and neon, the spectrum remains smooth and continuous at the pressure that yields the maximum photon flux.

In order to verify that the spectra generated at each pressure still represent single attosecond pulses, a CE phase scan was conducted for several values of gas pressure. Figure 2.50 shows the CE phase effect on an argon gas target (a) and a neon gas target (b). In the case of argon, all the spectra exhibit a 2π periodicity just as would be expected from a two color gating method. The spectra in each case do show differences that can be associated with the different gas pressures. In the case of neon, the spectra also show a 2π periodicity with a strong modulation of the overall signal due to the ellipticity dependence of the higher order harmonics. This result can be compared with those shown in figure 2.32 and 2.33. In the case of neon, the effect remains relatively the same regardless of the gas pressure even though the overall counts reduce for very high and very low pressures. In the case of argon however, the effect changes quite a bit. This can probably be partially explained by the increased plasma density at the interaction region for argon as compared with neon. Since argon has a much lower ionization

potential than neon and the laser intensity in all cases was the same, the number of free electrons would be much higher for argon. This is really the only difference between the argon and neon cases.

Once the experimental data was obtained, the degree to which our phase-matching was successful could be ascertained. From the pressure scan results in figure 2.49, the relative strength of the signal generated at the pressure giving the highest flux was extracted. For

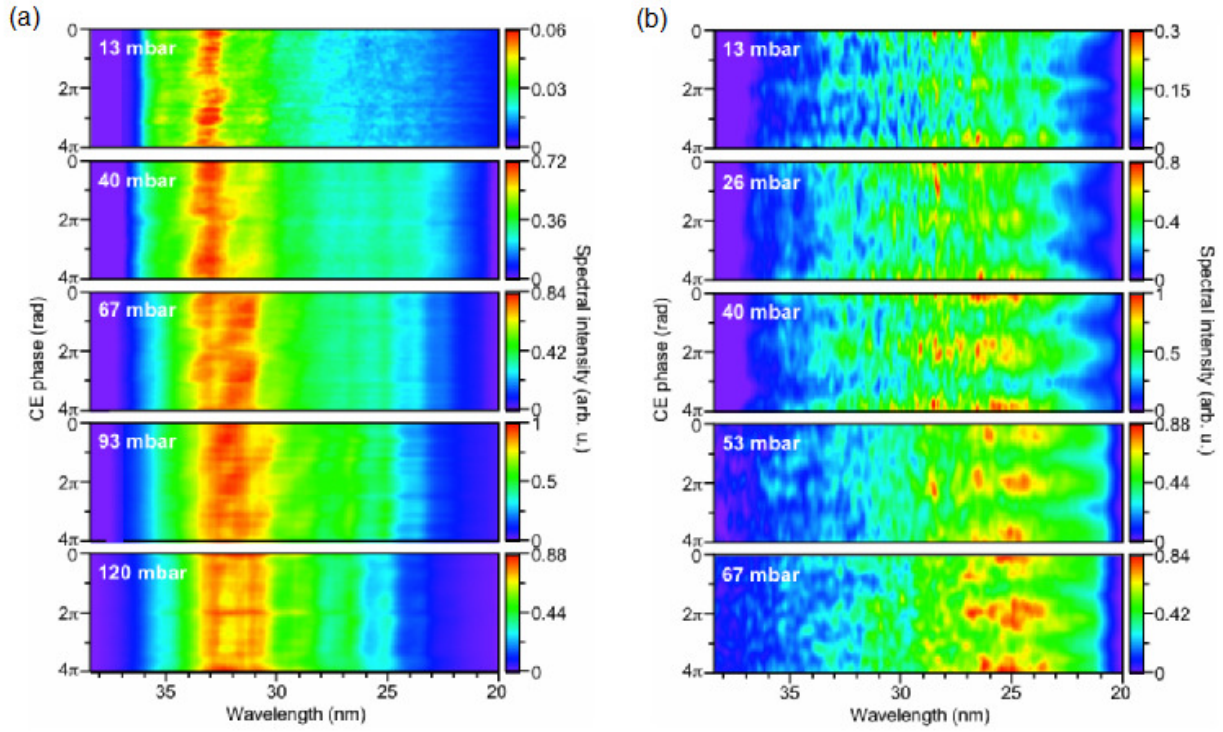

Figure 2.50 CE phase scans in (a) argon and (b) neon for several values of gas pressure.

argon, this was ~32 nm corresponding to the 25th harmonic and in neon it was ~25 nm corresponding to the 33rd harmonic. Taking into consideration the absorption of the photon flux by the residual gas in the rest of the 214 mm chamber, equation 2.28 was fit to the experimental data. The value of $PL_{abs}=1/N_0\sigma_q$ was calculated from reference [22] where N_0 is the number density and σ_q is the photoabsorption cross section. The calculation was done assuming the density of atoms at room temperature is 3.3 x 10^{16} atoms/(cm^3 torr) and is plotted as a function of photon energy in figure 2.51 for argon (red line) and neon (black line). The two gray circles

represent the values used in the calculations (49 mm torr for argon and 41 mm torr for neon). Once these values were obtained, the only free parameter in equation 2.28 was L_{coh}. This was used as a fitting parameter. By selecting $L_{coh}=x*L_{abs}$ where x is some constant, a line could be fit

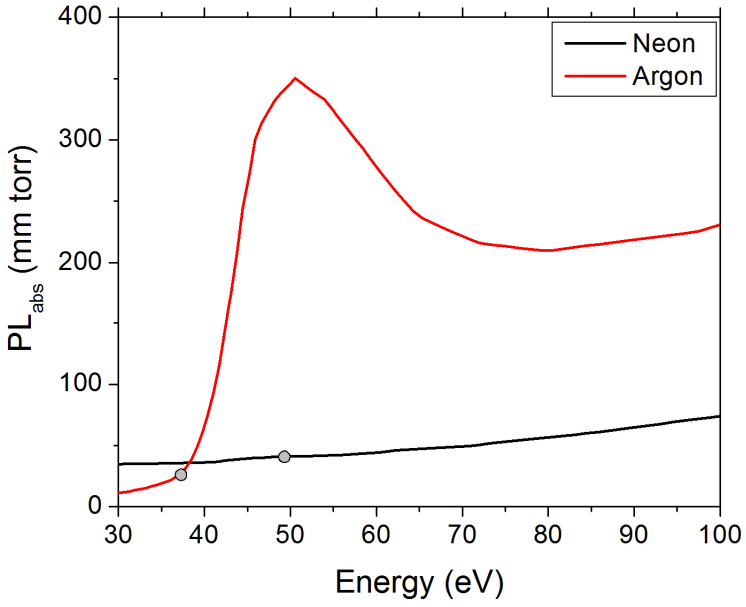

Figure 2.51 Pressure-length product versus Energy for neon (black) and argon (red).

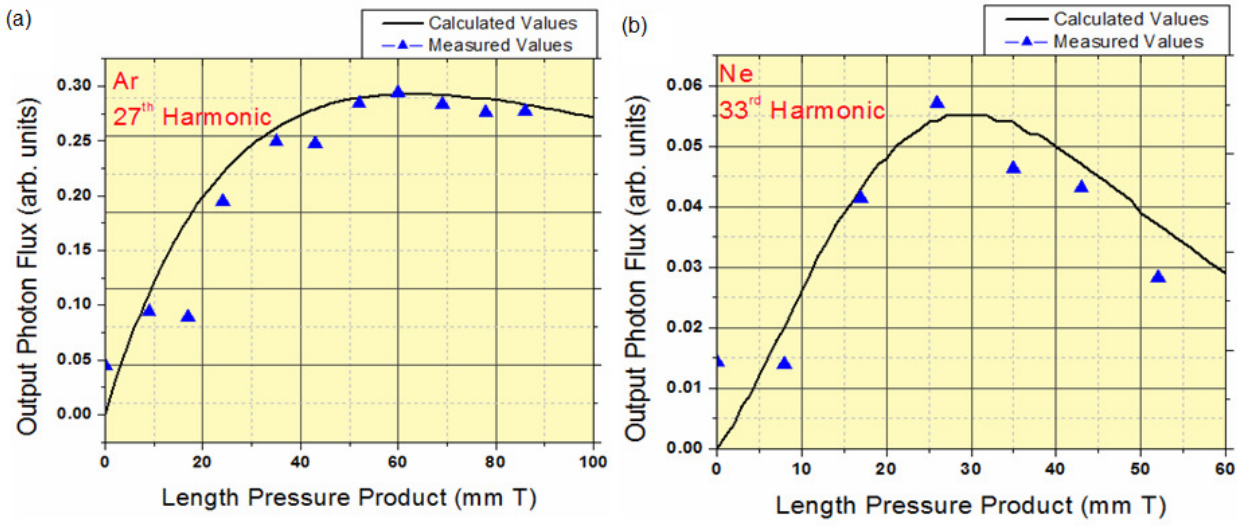

Figure 2.52 Experimental (triangles) and calculated (solid line) values for output photon flux in (a) argon and (b) neon.

to the experimental data. The value of "x" was the factor that determined how successful our phase-matching was (the criteria for optimal phase matching is $L_{coh}>5L_{abs}$). Figure 2.52 shows the experimental data (blue triangles) and the fitted line of equation (2.28) (black line) for both argon (a) and neon (b). For the case of argon, $L_{coh}=10L_{abs}$ implying excellent phase matching. Neon on the other hand was only $L_{coh}=2L_{abs}$. While this is reasonable for generating usable amounts of flux, there is still room for improvement. Improving the vacuum system on the setup should significantly reduce the absorption of photons thereby improving the signal.

In conclusion, the DOG technique generates very high levels of flux from both argon and neon due to its low depletion and high peak intensity. Phase matching of DOG is easily accomplished with significant enhancements to the output flux without degradation of the spectral width. This is important for generating short attosecond pulses with high pulse energy. The results of the phase matching analysis can be conducted for other pulse durations and peak intensities as well but similar outcomes are expected. Characterizing the phase matching with the GDOG technique should also yield similar results but differences could arise from the reduced intensity of the leading edge. This will reduce the amount of plasma generated, especially in argon and may further improve the output photon flux.

CHAPTER 3 - Temporal Characterization of Attosecond Pulses

The point of this chapter is to discuss how the attosecond pulses generated with both DOG and GDOG were temporally characterized. First, the method of attosecond streaking is explained followed by a description of the experimental setup. Next, all of the experimental results using the DOG technique are shown and evidence of the intrinsic chirp of the HHG process is provided. Finally, attosecond pulses from the GDOG technique are shown.

3.1 Principle of Attosecond Streaking

The temporal characterization of extremely fast processes (~fs) can be accomplished with a streak camera [68, 69]. A beam of light impinges onto a metal photocathode and generates a bunch of photoelectrons. These are then mapped spatially onto a phosphor screen by adding a fast varying high voltage transverse to the direction of propagation of the electrons (the electrons are said to be "streaked"). The fastest pulses that can be measured with this method are determined by how fast the voltage signal can be varied and the lower limit is on the order of ~100 fs [70].

To measure pulses with sub-femtosecond duration requires the use of a much faster varying field. This can be accomplished by using a single cycle (~2.5 fs) of an oscillating femtosecond laser pulse as the streaking field. This is because the field can change from 0 to a maximum value in a quarter of one cycle or ~0.63 fs which is a significant enhancement in the resolution. The basic idea of the attosecond streak camera is the same as the femtosecond case. A burst of light (the attosecond XUV pulse) impinges on a gaseous target to generate a burst of photoelectrons. The photoelectrons are then streaked with a few cycle intense IR laser field giving a momentum shift to the electrons. In the Coulomb gauge, an electron of charge *e* in a linearly polarized electric field gets a momentum shift [71]:

$$\Delta p(\vec{r},t) = \int_{t}^{\infty} eE(\vec{r},t)dt = eA(\vec{r},t) \tag{3.1}$$

where *A(r,t)* is the vector potential of the laser field. This momentum shift can then be recorded as a function of delay between the IR and attosecond pulse with a position sensitive time of flight detector. Once the momentum of each photoelectron is known, the corresponding energy can be

calculated. The maximum kinetic energy shift the electron with initial energy K_0 can gain from the laser field is given as [72]:

$$\Delta K \approx \sqrt{8K_0U_p} \tag{3.2}$$

Since the initial kinetic energy of the electrons depends on which gas the electron is born from, the proper choice of detection gas is important. The photoionization cross sections for the various gases used in the streak camera are shown in figure 3.1 [73]. The results show some

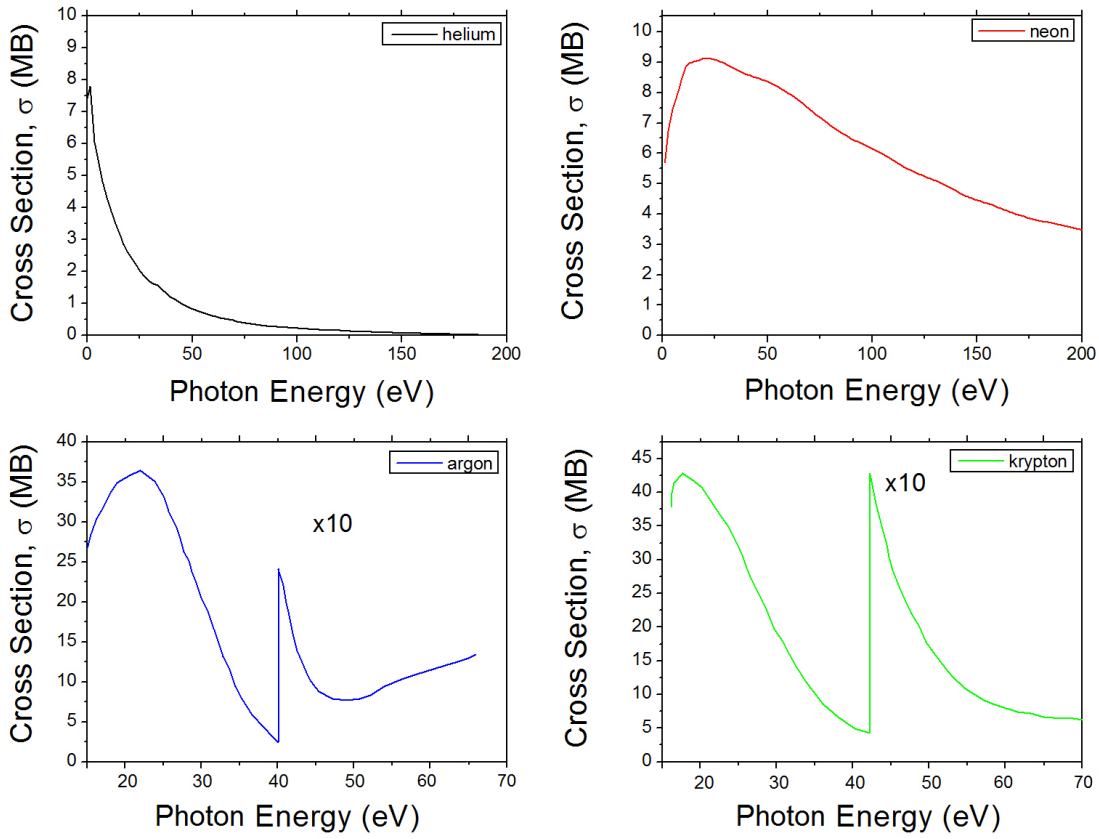

Figure 3.1 Photoionization cross sections for (a) helium (b) neon (c) argon and (d) krypton.

interesting features. Both argon and krypton ((c) and (d), respectively) have very high cross sections for low orders. They would be useful in generating a large signal if the cutoff of the XUV spectrum is also low. Neon on the other hand (b) is relatively flat and covers a very large energy range. This is the gas of choice if short pulses with broad spectra are trying to be measured. For gases with high ionization potentials, the electrons are born with lower kinetic

energy meaning the energy shift they experience would be less than electrons born from gases with low ionization potentials. Figure 3.2(a) gives an explanation of this process. In figure (b), a

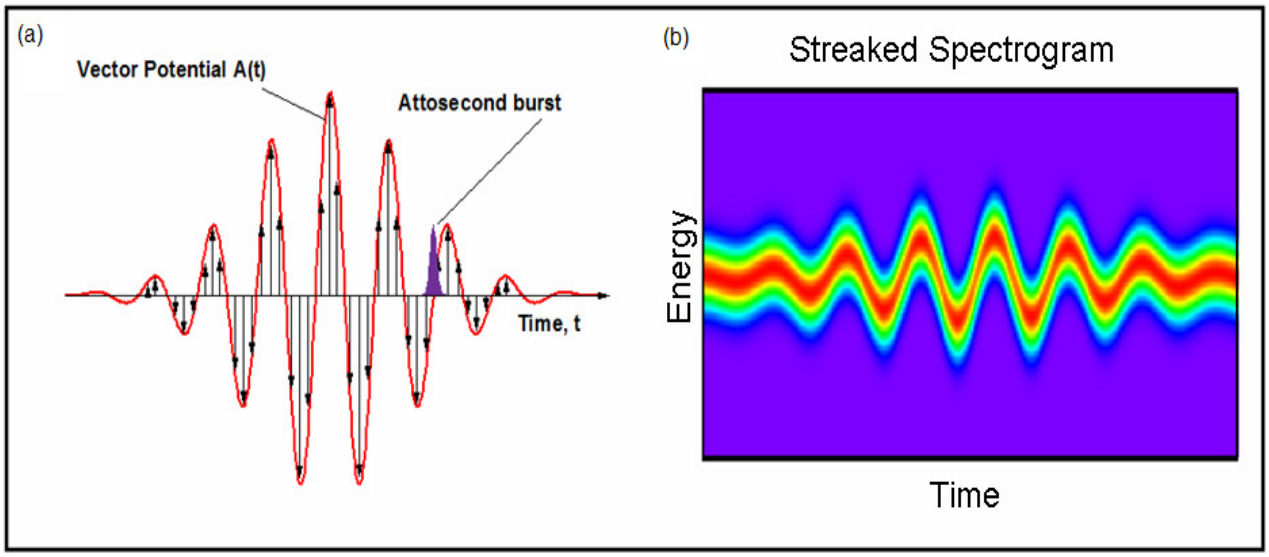

Figure 3.2 (a) Photoelectron burst in an oscillating laser field. The red line represents the vector potential of the laser field and the vertical arrows indicate the momentum shift the photoelectrons receive at each point. (b) A simulated streaked spectrogram for a ~200 as TL pulse in a 9 fs laser field.

streaked spectrogram is shown. This is a simulated spectrogram of energy as a function of delay. The oscillation in the spectrogram is a mapping of the femtosecond IR laser vector potential.

Normally, the frequency resolved optical gating for complete reconstruction of attosecond bursts (FROG-CRAB) technique is used to extract the temporal profile and phase of the attosecond pulse from the streaked spectrogram [74]. While this method gives the full phase, much information can be deduced from the spectrogram image alone. Figure 3.3 shows a simulated 160 as pulse streaked by an 800 nm, 6 fs laser pulse with 5 x 10^{12} W/cm^2 intensity. Figure (a) shows a transform limited pulse while (b) and (c) show the same conditions as (a) but with -50 as^2 and 50 as^2 second order chirp (GDD), respectively. Once the chirp is present, an asymmetric feature in the energy domain becomes obvious. In (a), the spectrum at any particular delay slice is pretty much the same as that half of a cycle away. This is not true in (b) and (c).

Also, the sign of the chirp can be deduced from the image as can be seen when comparing (b) and (c). Figure 3.4 explains this behavior more clearly. A positively

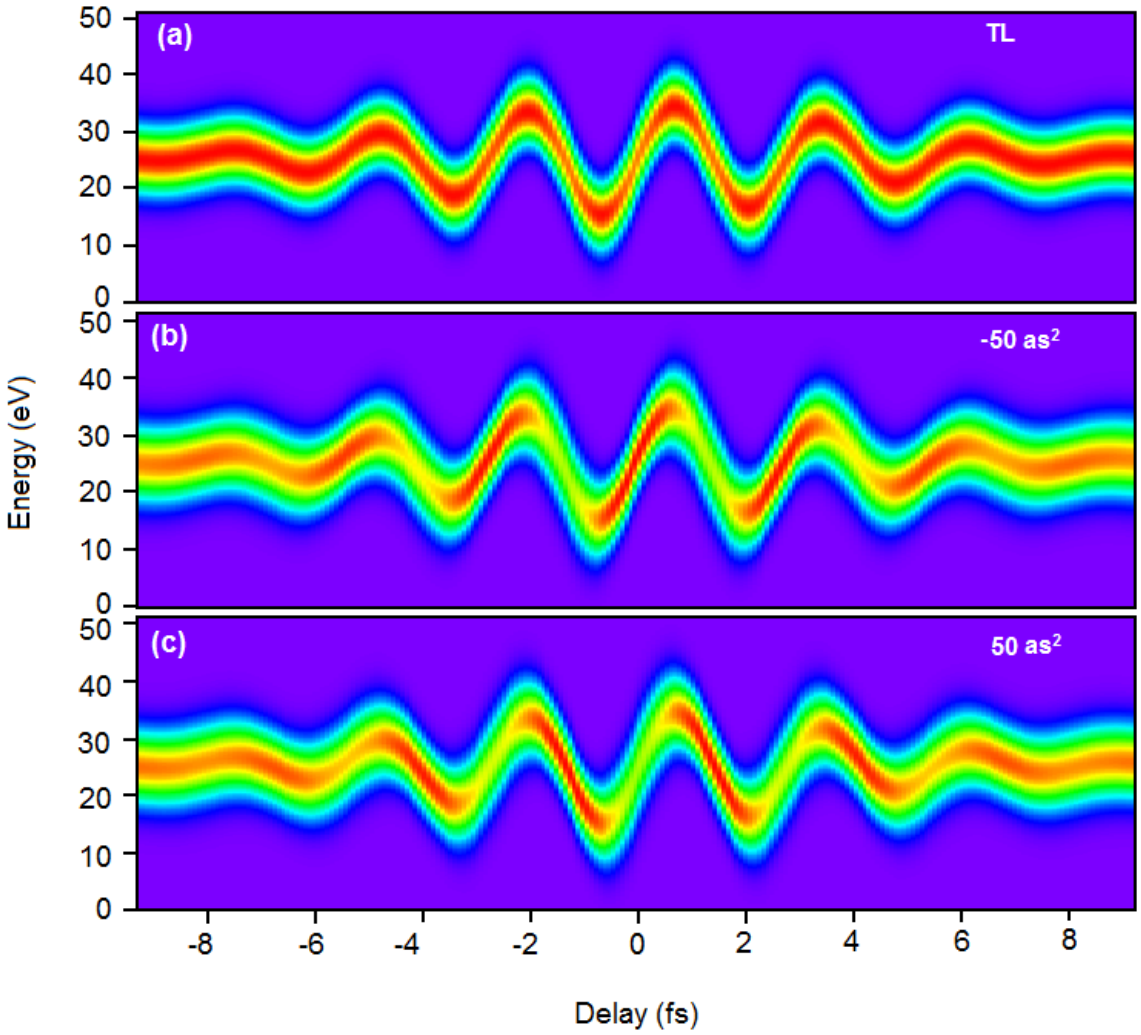

Figure 3.3 Simulated streaked spectrograms of a 6 fs pulse with 5 x 10^{12} W/cm^2 intensity streaking a 200 as pulse with (a) no chirp added, (b) -50 as^2 chirp, and (c) 50 as^2 chirp.

chirped (low energy photons on the leading edge) pulse's spectrum will compress as compared to the spectrum from a transform limited pulse for certain values of delay (a) and become broader for delays a half cycle later (b). The transform limited pulse case is shown in figures (c) and (d). For both delays, the momentum domain spectrum is the same width.

Qualitatively, some information about the temporal structure of the attosecond pulse can be extracted in this way. However, a quantitative method is required to retrieve the full phase. The rest of this section will lay out how this is done. First, a brief description of the retrieval algorithm will be presented followed by the experimental method used to produce streaked spectrograms.

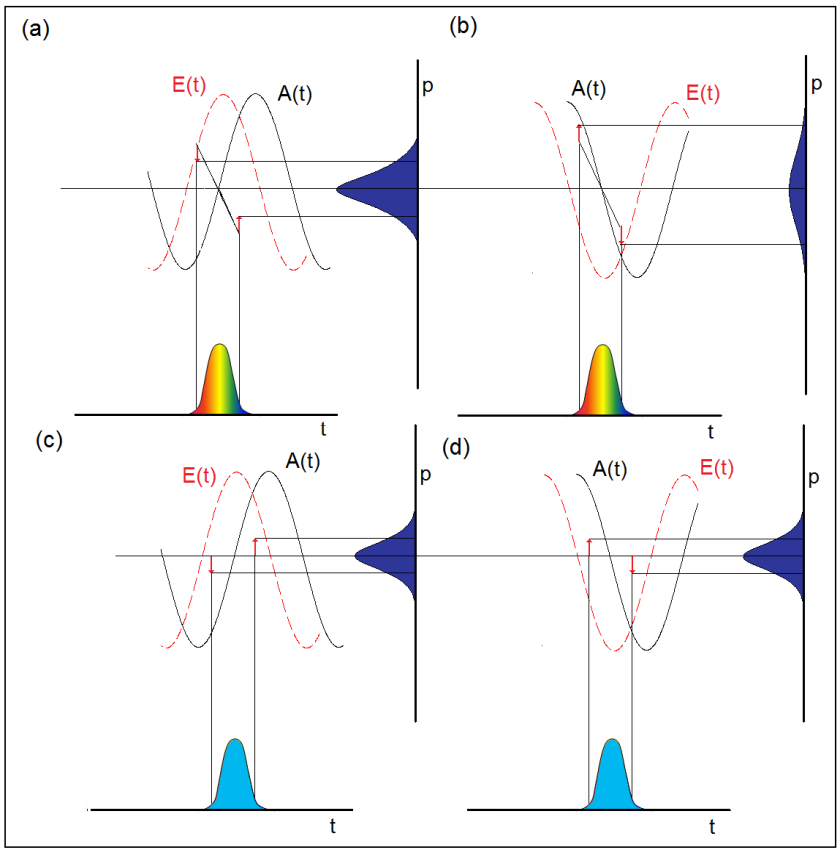

Figure 3.4 (a) and (b) Energy domain representation of temporal pulse with positive chirp at two different delays. (c) and (d) The same delays in (a) and (b) but with a TL pulse.

3.1.1 Reconstructing Attosecond Pulses

Reconstructing the temporal profile and phase of an attosecond pulse is a complicated task. Since the profile and phase is completely unknown, an iterative algorithm is implemented to basically guess parameters to generate a simulated trace which is then compared to the experimental result and the error is extracted. Using the principle components generalized

projections algorithm (PCGPA), [75] changes are made to the simulated spectrogram to more closely match the experimental result and the process is repeated until convergence to a final answer is achieved. In each case, physical constraints to the new simulation are included so that the answer continues to make sense physically.

A streaked spectrogram [74] is given by:

$$S(\omega,\tau)=\left|\int_{-\infty}^{\infty}E_x(t)d_{\vec{p}(t)}e^{i\phi(t-\tau)}e^{-i(p^2/2-\Omega_x+Ip)t}dt\right|^2 \tag{3.3}$$

where τ is the delay between the IR field, $E_x(t)$ and the attosecond XUV pulse with center energy Ω_x, and momentum p. The term $d_{p(t)}$ is the dipole transition matrix element from the ground state to a continuum state. The term $\phi(t)$ induces a time domain phase modulation on the electron wave packet that was created by the attosecond pulse. Equation (3.3) can be simplified if the dipole transition matrix element and the time varying phase are combined as one "gate" term, G(t), analogous to conventional FROG [76] as:

$$S(\omega,\tau)=\left|\int_{-\infty}^{\infty}E_x(t)G(t-\tau)e^{-i(p^2/2-\Omega_x+Ip)t}dt\right|^2. \tag{3.4}$$

In this equation, both E(t) and $G(t-\tau)$ are unknown meaning the algorithm is double blind. These are the fitting parameters that can be varied as the algorithm cycles. Equation 3.4 is all that is required to generate the streaked spectrogram simulations shown in figure 3.2.

The FROG-CRAB method listed above works well with reconstructing simulated spectrograms [77] under a variety on conditions as long as one condition is met. The method relies on the approximation that the bandwidth of the generated photoelectron spectrum is much less than the center energy of the spectrum; a requirement known as the center momentum approximation. This is a strong requirement for any spectrogram but especially for attosecond pulses generated with DOG. Since the spectrum covers both the plateau and cutoff region and extends all the way to zero energy, obviously the width can be comparable or greater than the central energy. Also, from equation 3.2 it is seen that as the initial energy of the electron is reduced, the energy shift the electron can experience reduces as the square root of the streaking laser intensity. This means more intensity is required to streak electrons born with less kinetic energy, but, as the laser intensity is increased, ionization of the target gas used to produce the photoelectrons can occur from the streaking laser itself. This manifests itself as a strong above

threshold ionization (ATI) spectrum at the low energy portion of the spectrum. This can overlap with the actual photoelectron spectrum from the attosecond pulse and make the reconstruction impossible. This is a serious disadvantage to the method and as the width of the spectrum increases, the retrieved result becomes less and less accurate. While this is not ideal, it is the best algorithm available for attosecond pulse reconstruction.

3.1.2 The Attosecond Streak Camera

Figure 3.5 shows the experimental setup of the streak camera [78]. The setup is interferometric and is inherently unstable. Appendix D discusses the method for which the setup was temporally locked as well as all of the modifications made to improve the stability. A linearly polarized laser pulse with p polarization was first separated by a broadband 80/20 beamsplitter (BS) (LayerTec), with the majority of the beam being transmitted. This beam passed through the two DOG quartz plates (QP1 and QP2), and possibly the Brewster window (BW) if GDOG was being implemented, and was then focused with an f=375 mm focal length

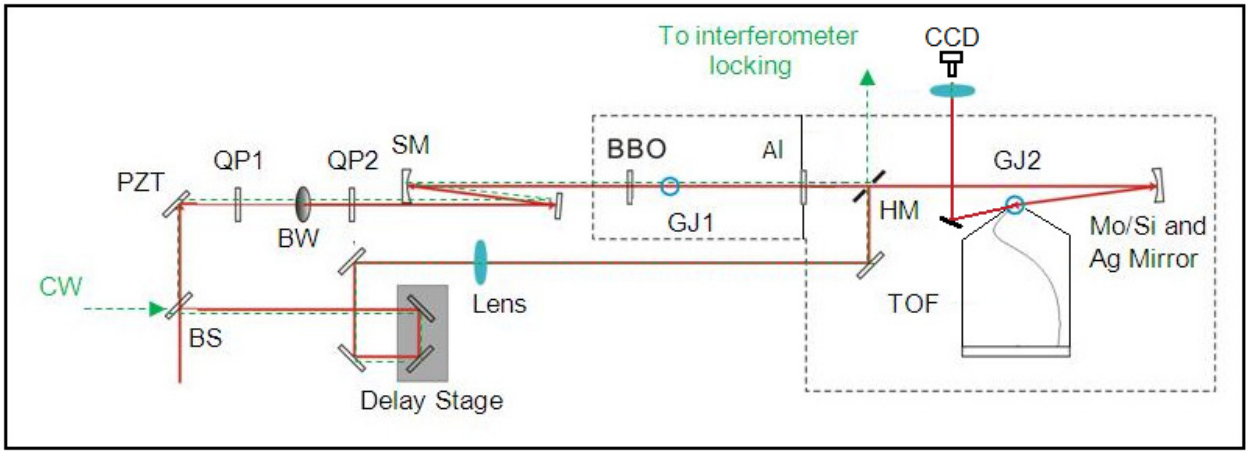

Figure 3.5 Experimental setup of the streak camera.

spherical silver mirror (SM) into the vacuum chamber. The angle of incidence on the mirror was ~5 degrees which resulted in a slightly astigmatic focus. The distance between the foci was calculated to be ~2 mm assuming an 8 mm diameter initial spot size. The reason the spherical mirror was chosen for the experiments was that it could be coated with a high damage threshold coating (protected silver) which would ensure it lasted longer than the unprotected parabolic

mirror. The source of the damage on this mirror was the back reflection from the entrance window which, although the window was anti-reflection coated, was still large enough to generate a damage spot after an extended period of time. Once inside the chamber, the beam focused through the BBO crystal to generate the SHG necessary for the full DOG pulse and to compensate the delay introduced by the second quartz plate. The BBO was located ~half the distance between the focusing mirror and the gas target. This gave sufficiently high SHG for DOG while still keeping the crystal safe from damage. The focused beam then generated an attosecond pulse from a 1.4 mm long gas target (GJ1) typically filled with either argon, neon, or xenon. The chamber had a turbo pump (250 l/s) installed over the gas cell that could be used if absorption of the HHG flux by the residual gas was to be minimized. The pulse then propagated through a custom made fused silica window with a 1.5 mm hole drilled in the center and covered with an aluminum filter to remove the residual IR photons. The filter was also used to isolate the high pressure GJ1 from the rest of the chamber. This custom filter was also necessary for the locking of the interferometer. Details of this are explained in appendix D. Since the streak camera is a temporal measurement device, the material dispersion properties of the filter could be used to also partially compensate the intrinsic chirp of the HHG process. Details of this are given in section 3.3.1. After the filter, the attosecond pulse passed through the center of a hole drilled silver mirror (HM). The mirror was 1.6 mm thick and the 3.5 mm diameter hole was drilled at 45 degrees.

At the same time, the reflected portion of the beam (called the streaking beam) from the first beamsplitter remained linearly polarized and passed through an equal optical path length and recombined with the attosecond pulse at the hole-drilled mirror. This leg of the interferometer also had a coarse delay stage implemented in order to roughly temporally overlap the two beams and an f=400 mm lens so that the divergence of this beam could be controlled independently of the other beam. At the hole-drilled mirror, only the outside of the beam was reflected so that the two beams were collinear with the attosecond pulse inside the IR pulse. These two beams then propagated to the two-component annular mirror assembly. The outer mirror was a 50 mm diameter silver coated spherical mirror with focal length of 250 mm. A hole 18 mm in diameter was drilled into the center for the XUV reflecting mirror. The XUV mirror was a Mo/Si multilayer mirror with diameter 12.7 mm and focal length 250 mm (NTT optics).

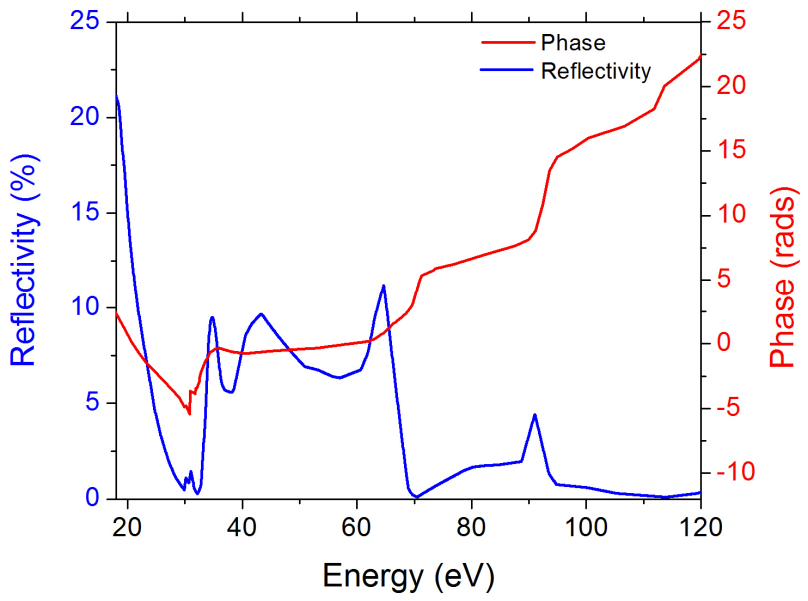

Figure 3.6 Reflectivity (blue) and phase (red) of the Mo/Si XUV mirror.

The reflectivity as a function of photon energy of the mirror is shown in figure 3.6 (blue line). The region from ~30 eV to 70 eV is typically used for the experiments and it is in this region that the mirror phase is the most well behaved (red line). Also, the aluminum filter does not transmit photons with energy above ~72 eV. The portion of the spectrum from 30 eV to 70 eV could support a minimum pulse duration of ~94 as, not including any phase distortions present in the attosecond pulse itself.

After the annular mirror, the two beams were focused to the second gas jet (GJ2). This jet was a 50 μm inner diameter stainless steel tube ~1-2 mm long. The backing pressure for this gas "needle" was sometimes as high as 1000 torr. The goal was to generate the highest local density possible at the output of the needle while maintaining the lowest background pressure possible. The reason this was important was that volume effects from the laser and gas interaction tend to wash out the streaking effects. Since the intensity across the profile and in the longitudinal direction of the laser changes quickly, photoelectrons streaked from different portions of the beam would streak different amounts even if the photoelectrons were created with the same energy photon. The vacuum system in this part of the streak camera consisted of 2 250 l/s turbo pumps and a 500 l/s turbo pump. These were used to allow the local density of the gas jet to be as high as possible while maintaining safe pressure for the detector. At the second gas

needle, the attosecond XUV photons generated photoelectrons and the IR laser pulse provided the momentum shift to streak the freed electrons which were then detected in a position sensitive time of flight detector (TOF). In order to scan the temporal delay between the two beams, the XUV mirror was mounted on a 3-axis pzt stage. The stage could travel a total distance of 30 μm with a step size of 1 mm (PI S-325) which corresponded to a total delay scan range of 200 fs with a step size of 6.7 as (including a factor of 2 for the round trip distance). This is substantially smaller than the steps normally taken in the experiment. For the results shown in the following sections, the delay step size was 0.05 μm corresponding to a round-trip time of 333 as (~12% of the femtosecond laser cycle).

To determine the spatial overlap in the longitudinal and transverse directions, the two beams were reflected outside the chamber and focused with an f-250 mm focal length lens to a CCD camera in a 1-1 configuration. This allowed the spot sizes of each focused beam to be measured. Figure 3.7 shows the profiles of the two beams. The outer (streaking) beam (a) reflects from a larger mirror and so has a smaller spot size as compared to the inner beam (b). The images are intentionally saturated to show the full structure of the focused beams. It is expected that the XUV beam is much smaller than the IR beam shown. Also, the outer beam shows a distinct Bessel-Gaussian intensity distribution. This is because the beam is reflected from a mirror that truncates the central portion. In the far field, this gives the interference pattern shown. The two beams in the figure are shown separated spatially so they can be seen individually. This is controlled with a picomotor mirror mount for the inner mirror. Under normal experimental conditions, the two beams would be overlapped. Also, temporal overlap

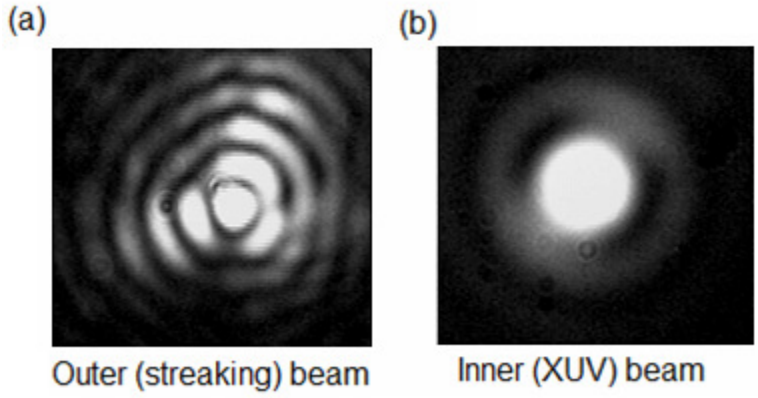

Figure 3.7 Focused spot profiles for the (a) outer mirror and (b) inner mirror.

between the two beams is monitored by looking for an interference pattern between the inner and outer mirrors. More details on the Bessel-Gaussian nature of the outer beam will be discussed in chapter 5.

To control the longitudinal positions of the two beams with respect to each other, the lens in the streaking arm is used. By moving it parallel to the direction of the laser propagation, the focus position at the second gas jet can be controlled. The geometry of this arrangement is an object position located ~1100 mm from the outer annular mirror with focal length 250 mm. This gives a longitudinal demagnification of ~11:1 meaning the lens must be moved 1.1 cm to move the focus at the second gas jet 1 mm.

At the location of the second gas jet, the photoelectrons are born and enter a hole in the tip of a cone 1 mm in diameter. The purpose of the cone hole is to isolate the higher gas density second gas jet from the detector. The detector side of the cone also had a dedicated 250 l/s turbo pump to further reduce the pressure. From here the electrons propagate to the detector. From when the electrons are born to when they are detected, they propagate in a region of uniform magnetic field generated by a Helmholtz coil arrangement. The purpose of the magnetic field is to increase the acceptance angle of the detector. The large area detector that is used (discussed later) coupled with the field gives an acceptance angle of +/- 13 degrees for 45 eV photoelectrons [79]. The field points toward the detector and has a magnitude typically 1-1.7 Gauss. To cancel the earth's magnetic field, parallel loops of ribbon cables surround the entire arrangement in the remaining directions. By applying current to these cables independently, components of the earth's field not parallel to the field from the Helmholtz coils can be cancelled. Since each electron has a unique velocity vector (and hence momentum and energy), the position sensitive detector, combined with the time of flight, allows the vector to be reconstructed for each electron [80].

3.1.2 Streak Camera Electronics and Resolution

A schematic of the detector setup can be seen in figure 3.8. The photoelectrons propagated along the full length of the drift tube (295 mm) towards the chevron stack micro channel plate (MCP) detector until they passed a grounded wire mesh. The mesh was located about 3 mm in front of the detector and was used to ensure the drift tube was electric field free and not influenced by the MCP potentials. After the mesh, the photoelectrons were accelerated

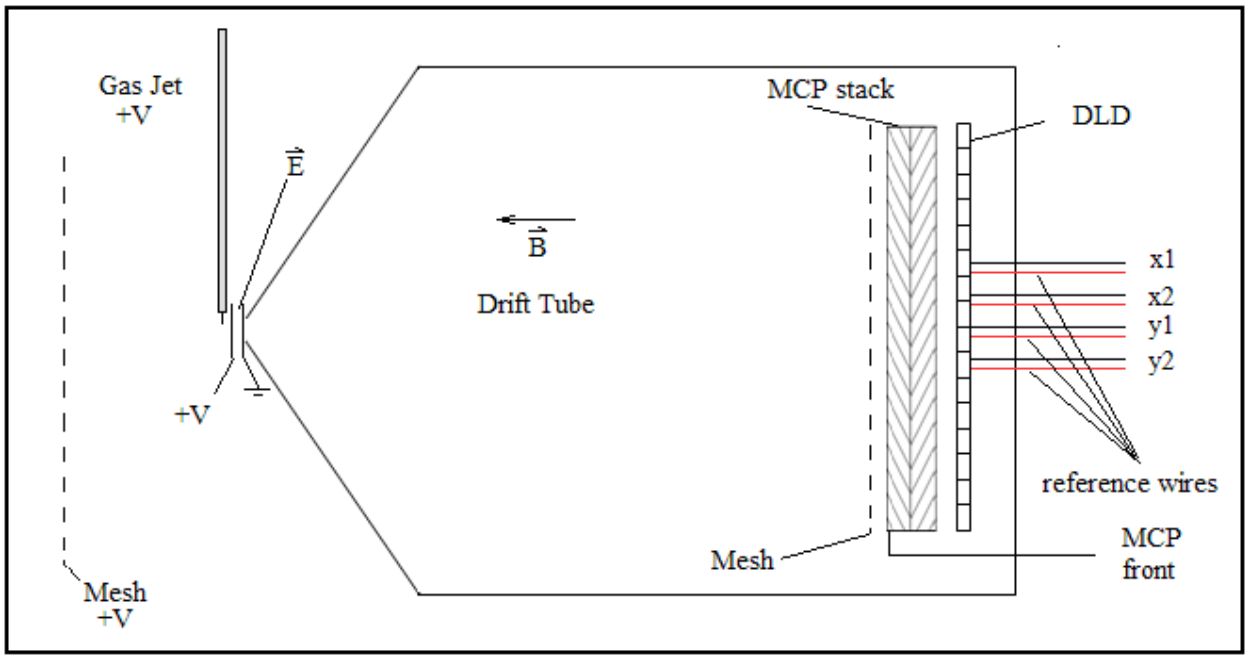

Figure 3.8 Schematic of streak camera position sensitive TOF detector.

towards the MCP by a potential of +300V applied to the front MCP. The voltage is controlled with a potentiometer between the voltage applied to the MCP back and the MCP front. This voltage was used to ensure the electrons had enough energy to begin a cascade of electrons in the MCP. The second MCP in the stack, also called the MCP back, was given a potential of 2600V. This further accelerated the electrons through the stack giving more secondary electrons. The total gain of the MCP stack was ~10^7.

After the MCP stack, the multiplied electron signal was incident on the position sensitive delay line detector (DLD). The detector consisted of orthogonally crossed sets of wires to give position information in both the x and y directions. The detector consisted of 10 turns of wire per cm in both directions and was 12 cm square. When the electron bunch from the MCP stack was incident on the detector, a signal was sent along the lengths of the wires and was detected at the ends. By measuring the difference in time between when the signals arrived at the two ends of the wire, the location along the wire could be found. The detector itself had a position resolution of ~25 μm and a time resolution of ~1 ns. The time resolution of the detector limited our total resolution the most.

In order to measure the time, a data acquisition system and timing electronics were used. A schematic is shown in figure 3.9. During the experiments, a photodiode collected a signal

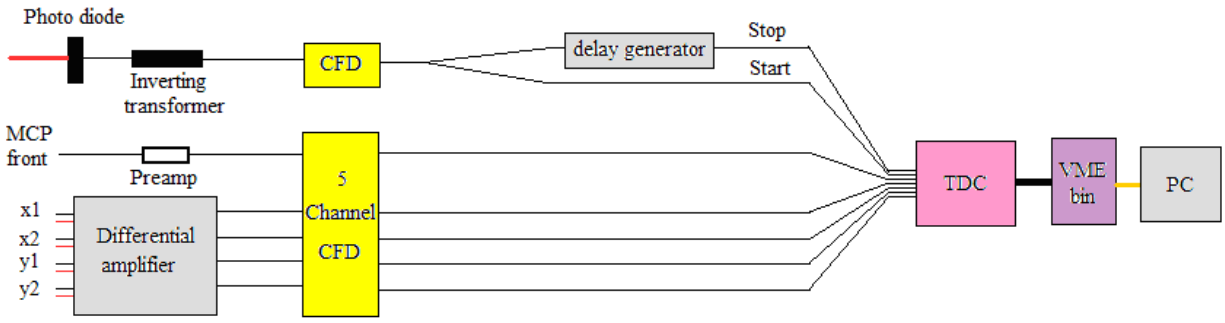

Figure 3.9 Electronics diagram for the streak camera.

from the laser pulse which was used as an overall start signal. This signal was sent to an Ortec IT100 inverting transformer to make it a falling edge signal. The transformer has the capability for 0.8ns rise times. After the signal was inverted, it was sent to a homemade constant fraction discriminator (CFD). The model of the CFD used with the streak camera is CF4000 quad. This CFD has a resolution of 15ns for a pulse pair and gives the user control over the fraction via the walk control. The total resolution of the CFD is ~200 ps meaning a delta function signal will become 200 ps in width after the CFD. In order to ensure timing of the correct portion of the signal, a threshold can be set to eliminate noise that rises above some level and could be mistaken for the actual signal.

The operation of the CFD was to first split the pulse into 2 replicas and attenuate one to 20% of its original value while inverting and delaying the other one. The amount the signal is attenuated to is known as the fraction and can be adjusted during the experiment. Next, the two signals are recombined and, if the delay is chosen properly, a zero crossing occurs at the location of the rising edge of the original pulse. A NIM signal similar to a negative square wave is then generated with the leading falling edge at the location of the zero crossing. This new signal allows the timing to be determined with high accuracy later through the time to digital converter (TDC).

After the CFD, the altered NIM photodiode signal is split with one signal continuing to be used as the start signal while the other NIM signal is sent through a delay generator (LeCroy

model 222 dual gate generator) where a delay of ~500 ns is added to the signal with respect to the start signal. The generator allows gate delays of less than 100ns to more than 11 seconds which is well beyond our requirements. This new signal is the overall stop signal and indicates at which time to ignore further data (which are typically slower electrons).

At the same time that the start signal is being recorded, a signal from the MCP front is being sent to the TDC as well. This signal gives the time from the start signal to when the electron actually strikes the MCP. The signal is first sent through a potentiometer to control ringing, or the unwanted oscillations of the voltage due to various capacitances and inductances in the total circuit. Next, the signal is sent to a fast preamp (Ortec model VT120B) to increase the signal. The preamp is a wide bandwidth (10-350MHz) inverting amplifier with an amplitude gain of 200. After this, the amplified signal is sent to another 5 channel CFD (Phillips Scientific model 715) which acts in a similar fashion to the CF4000. The pulse pair resolution is <10ns and the maximum frequency is 100MHz. Like the homemade CFD, the resolution of this one was also 200 ps.

The additional 4 channels of the 715 CFD are used for the four position signals from the DLD. The DLD wires are actually pairs set close to each other. One wire acts as the signal and receives a potential of 2800V while the other wire acts as a reference and receives a signal of 2750V. The difference in voltage means the actual electron signal will most likely be collected by the signal wire with the reference only seeing background noise. The difference in the signals between these wires gives a better actual signal. To find and amplify the difference, a homemade differential amplifier is used. The bandwidth of the amplifier is 1GHz meaning it is very fast for our application, and the gain is ~500. So, the input of the amplifier is 8 signals (four positions and four references) and the output is four amplified, high quality position signals. Each of these signals is sent to the model 715 CFD along with the MCP front signal. After finding the zero crossing and generating an appropriate NIM response, the signals are sent to the time to digital converter (TDC) (CAEN V1290N).

The TDC is a 16 channel VME compatible unit which simply outputs the time arrival for each pulse it receives. The resolution of the TDC was 25 ps with a pulse pair resolution of 5 ns. After the TDC, the signal is sent to a PC for analysis via a fiber optic cable.

To improve the energy resolution of the TOF, increasing the distance from the gas jet to the detector is ideal. However, this was not an option for the setup because the magnetic field

created “nodes”. When an electron flies to the detector with energy, E, the wiggle spectrum, that is, the radial position versus the arrival time, t, can be written as:

$$r = \frac{2\sqrt{2m_e E - (m_e S/t)^2}}{eB}\left|\sin\left(\frac{eBt}{2m_e}\right)\right| \tag{3.5}$$

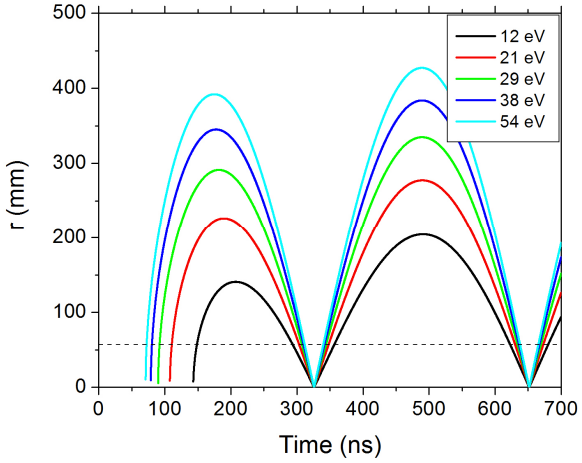

Figure 3.10 Wiggle pattern calculated from equation 3.5.

where m_e is the electron mass, e is the electron charge, S is the flight distance, and B is the magnetic field generated from the Helmholtz coils. Figure 3.10 shows a plot of equation 3.5 for electrons with different energies from an argon target (Ip = 15.8 eV). The horizontal dotted line shows the radial boundary of the detector, beyond which the electrons cannot be detected. From the figure, one can see that all the electrons hit the center of the detector with a cyclotron period $T = 2\pi/(eB/m_e)$ which, with B=1.1 Gauss, is ~325 ns. All electron trajectories, independent of their initial kinetic energies, cross at these magnetic nodes. In the energy domain, they form a series of “holes”, where there is no energy information. To retrieve the single attosecond pulse, these “holes” must be avoided by choosing S such that $T>t_{max}$ and $t_{min}>0$ where t_{max} and t_{min} are the maximum and minimum electron flight times [81]. This sets a limit on the flight time and the flight length of the electrons. The current magnetic field of ~1.1 gauss, which gives a node around 2.5 eV, is a compromise between the acceptance angle and the node position.

To get around the problems associated with extending the flight tube, a retarding potential was added to the detector assembly to change the flight time of the photoelectrons. A

large mesh, the gas jet itself, and a smaller mesh near the cone opening had a positive voltage applied to them. A small mesh was used at the cone opening only because the gas jet needs to be as close to the opening as possible but it shouldn't come in contact with the mesh itself. After the small mesh, another mesh, electrically isolated from the first, was added. This mesh was grounded and set as parallel as possible to the mesh with the voltage applied. The meshes can be

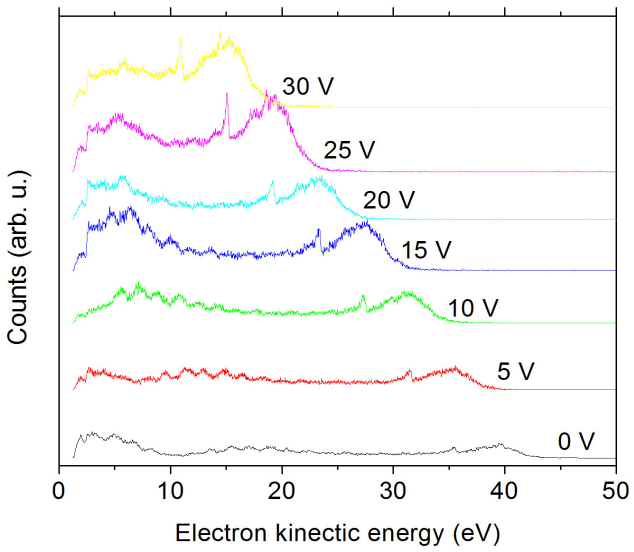

Figure 3.11 Helium spectra for different values of retarding potential.

seen in figure 3.8. This created a region of uniform electric field which could retard the electrons by a constant amount. This increases the time of flight thereby improving the resolution of the detector.

To test the resolution, the autoionization line in helium was used as a source. It has a width of ~38 meV and is located at 60.1 eV and will be discussed in more detail in chapter 5. This line was used to confirm the energy calibration of the detector. A continuous spectrum was generated with DOG so that the only feature visible was the 2s2p line. Then, the retarding potential was increased so that the peak shifted to lower energies. The photoelectron spectra from helium measured with different retarding potentials in the TOF are presented in Fig. 3.11. All the other curves are shifted vertically with respect to the 0 volt spectrum to see each spectrum individually. The *2s2p* autoionization peak shifts from 35.5 eV when the retarding

potential is 0 to ~11 eV when the retarding potential is 30 V. It should be noted that the energy shifts of the peak are not exactly equal to the applied retarding potentials. This is probably due to stray fields or that the meshes are not perfectly parallel. The electron energy scale is calibrated with the high order harmonic peak positions generated from neon using linearly polarized 30 fs laser pulses.

From the results, our spectrometer resolution is at least five times wider than the width of the autoionization peak. Therefore, the contribution of the intrinsic Fano peak width to the

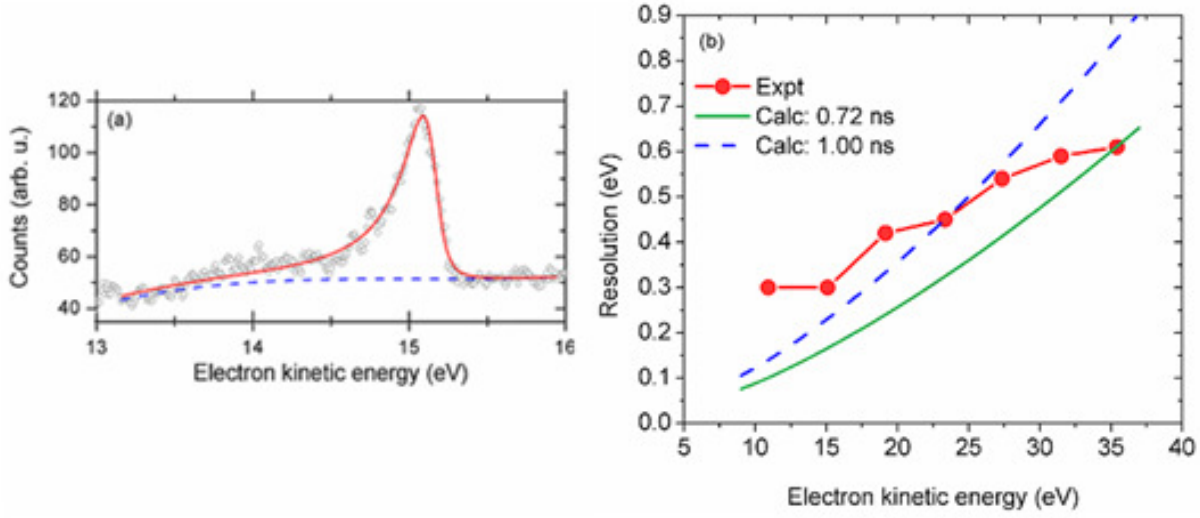

Figure 3.12 (a) Experimental data (circles), Pearson fitting (red line) and cubic background (dashed line). (b) Resolution vs. kinetic energy for experimental data (red circles), and calculated resolution for two different time resolutions (green and blue lines).

measured peak width is neglected. We fitted the *2s2p* peak with a Pearson type IV function [79] and a nonlinear background. The full width at half maximum (FWHM) of the measured peak gave us the energy resolution. As an example, Fig. 3.12(a) shows the fitting results for the spectrum when the retarding potential is 25 V. The FWHM of the Pearson function is 0.30 eV, and the peak position is at 15.1 eV.

The TOF spectrometer energy resolution for electrons with different kinetic energies obtained from the fittings is plotted in Fig. 3.12(b) as the red line and circles. The resolution changes from 0.3 to 0.6 eV when the electron energy increases from 10 eV to 35 eV. Since the

resolution is better than ~0.8 eV, it is sufficient to image individual harmonic peaks separated by 1.5 eV. This means our resolution is acceptable for the measurement of isolated attosecond pulses since a smooth spectrum can be fully trusted.

The improvement of energy resolution of the TOF by adding the retarding potential serves as evidence that the time resolution of the detection system is one of the dominating factors that limit the energy resolution. The contribution of the time resolution to the energy resolution was calculated using the well-known relation between the resolution of the spectrometer, ΔE, and the electron energy E:

$$\Delta E = \frac{2^{3/2}\Delta t}{m_e^{1/2} S} E^{3/2}. \tag{3.6}$$

where Δt is the total time resolution of the MCP detector and electronics including the amplifier, CFD's, and the TDC.

The calculated energy resolution as a function of the electron kinetic energy is plotted in Fig. 3.12(b) for two different time resolutions: 0.72 ns (green solid line) and 1 ns (blue dashed line). One can see that four of the experimental data points on the high energy side fall between these two curves. Since the resolution of the streak camera has been demonstrated to be sufficient for attosecond pulse generation, the rest of this chapter will be devoted to the results obtained using the DOG and GDOG gating methods.

Since attosecond pulse generation generally requires the CE phase of the laser system to be stabilized, a retest of the CE phase effect from DOG was conducted with the streak camera. The previous CE phase results were taken with a photon XUV spectrometer while the streak camera uses a photoelectron spectrum. With each laser pulse only 1-2 photoelectrons are typically generated due to the MCP quantum efficiency (~10%), cross section of the target (~0.1%), reflectance of the XUV mirror (~6%), transmission through the aluminum filter and residual argon gas (~50% each), and acceptance angle of the detector (~3%). This means a significantly longer integration time is required to obtain a photoelectron spectrum than for a photon spectrum. To ensure the CE phase effect is still visible, a photoelectron spectrum was taken from an argon target with neon as the detection gas while the CE phase of the generating laser was scanned. The results are shown in figure 3.13. The input laser pulse duration was ~9 fs and the gating method was DOG. Each delay slice was integrated for 30 s. Clearly a 2π

periodicity is visible and the overall result is very similar to that produced in the photon spectrometer (see figure 2.29). This result proves that the CE phase does influence the photoelectron spectrum in a predictable way and can be trusted to produce continuous spectra or discrete spectra when the CE phase is locked to some value.

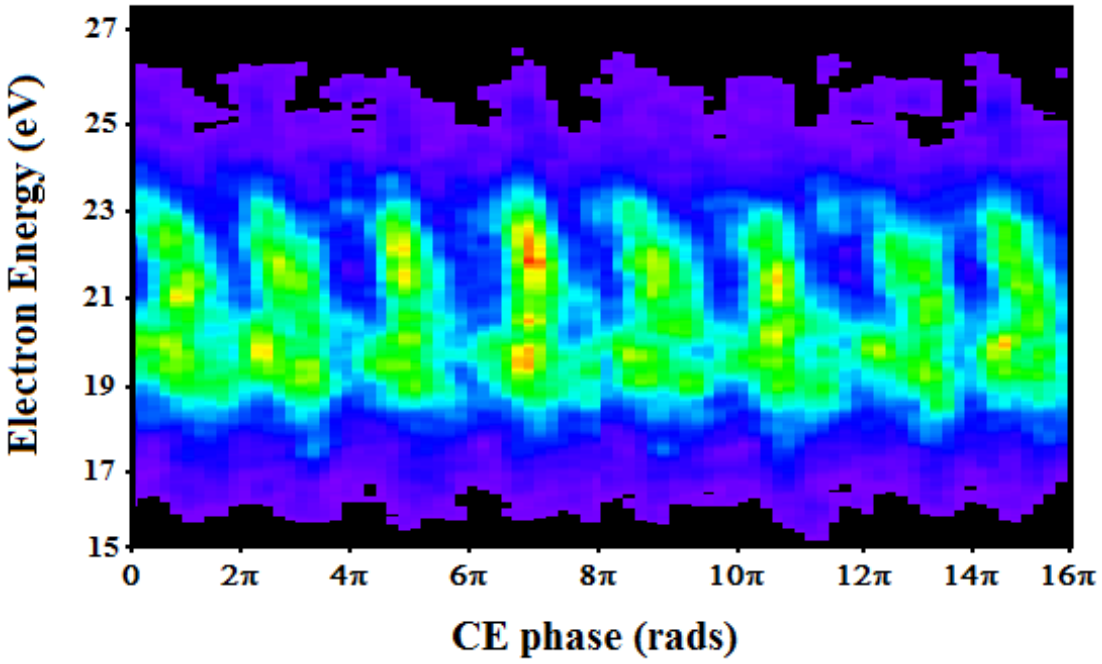

Figure 3.13 CE phase effect form a spectrum generated in argon and used to produce photoelectrons in neon.

3.1.2a Alignment procedure for the streak camera

To generate a continuous spectrum and measure the attosecond pulse duration is a straight forward process with the streak camera. The following list is the steps typically used during an experiment.

1. The input laser (p-polarized) is aligned through the XUV arm of the interferometer after reducing the power to ~100 mW. More power than this could damage the sensitive coating of the Mo/Si mirror. The beam pointing can be adjusted by tuning only the mirrors before the interferometer. The beam must pass through the center of the entrance window, the hole drilled gas cell, the center of the aluminum filter, the center of the hole drilled mirror and finally it

should appear only on the inner Mo/Si mirror. If this vector is aligned properly, the full alignment of the system is almost perfect.

2. The streaking beam is next aligned for spatial overlap with the XUV arm. The quality of the mode for this beam is critical and should look like figure 3.7(a). The beam can be adjusted using only the final two mirrors before the hole drilled mirror in the streak camera. This beam is blocked after alignment is complete to ensure the second gas jet does not get damaged. Since the gas jet is stainless steel, the damage threshold is very small and even a little IR intensity can severely damage it.

3. Rough temporal overlap should be achieved by tuning the delay stage in the streaking arm of the interferometer while monitoring the fringe pattern between the XUV and IR arms of the interferometer..

4. The aluminum filter is next inserted and the IR power increased to maximum.

5. The desired spectrum (normally a continuum) is generated in the first gas cell by gating the DOG optics (first quartz plate is oriented to +/- 45 degrees to input polarization). The spectrum can be optimized by playing with the gas pressure and other phase matching conditions. The BBO crystal can also be tuned at this point. The second gas jet typically is backfilled with a pressure that raises the rest of the chamber pressure to ~10^{-5}-10^{-4} Torr. The gas jet position can also be optimized for maximum counts and to ensure the XUV beam is not incident on it.

6. The DOG optics are next reset for linear polarization and the streaking IR laser is added at the second gas target for optimization of sidebands. Normally the sidebands are optimized first temporally (using the fine control knob on the streaking laser delay stage), followed by transverse spatial overlap (using the 5-axis kinematic stage under the lens in the streaking beam) and finally the longitudinal focus position (using the coarse delay stage under the lens). The optimization process is first the sidebands are adjusted to be ~100% the amplitude of the harmonic peaks. If the peaks are difficult to see, fused silica can be added before the interferometer to chirp the input pulse and narrow the harmonic peaks. Next, the IR intensity is reduced using the ND filter in the streaking arm and the sidebands are re-optimized for ~100% peak height. This is repeated until the IR intensity can not be further reduced. Under optimal conditions, the sidebands will be ~60% the harmonic peaks with only 1-2 μJ of pulse energy measured before the hole drilled mirror. Typically, only the temporal overlap needs to be

adjusted for this condition to be satisfied. However, a full temporal, transverse, and longitudinal scan was conducted to map the IR intensity. Figure 3.14 shows the results of this scan.

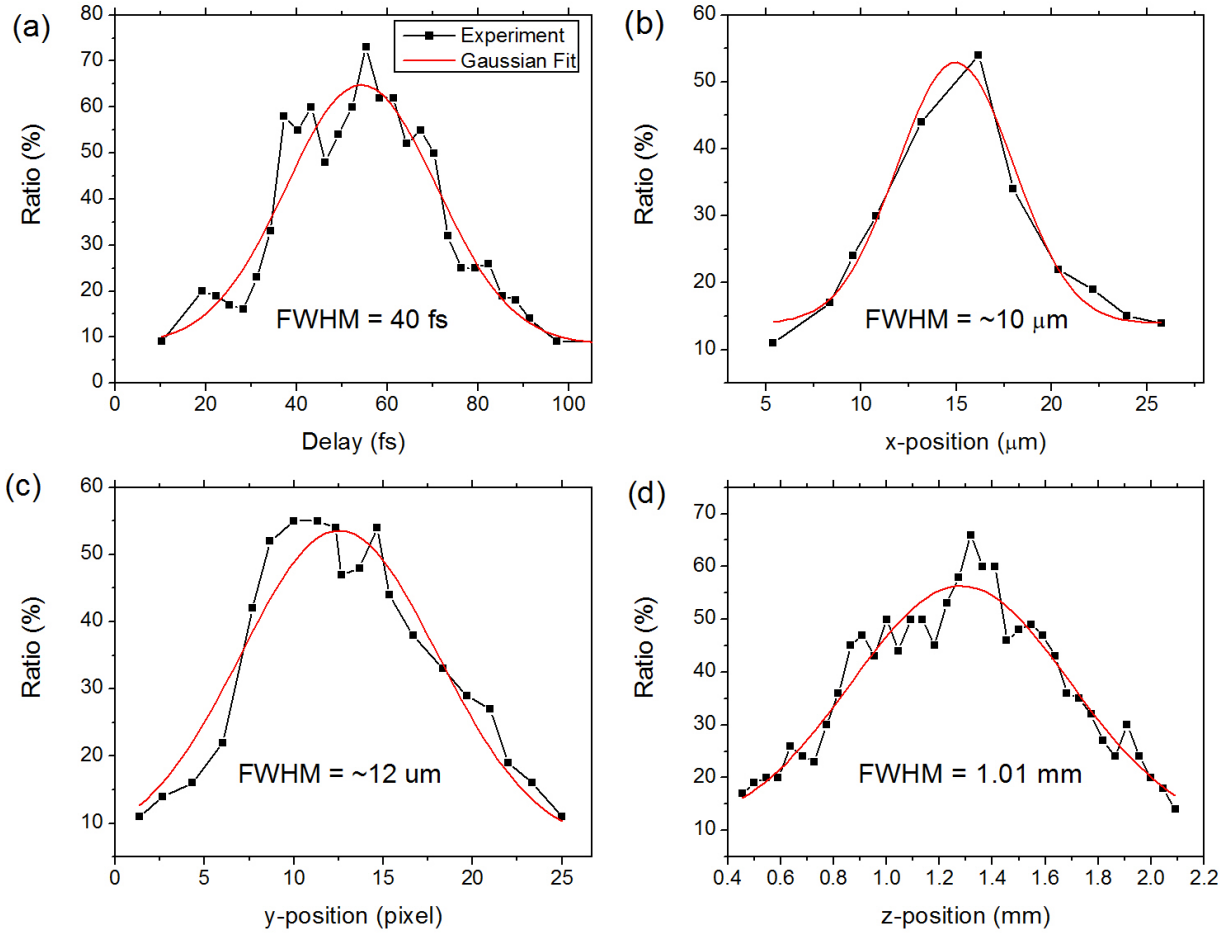

Figure 3.14 Sideband ratio vs. (a) delay, (b) x-position, (c) y-position, and (d) z-position. In all cases, the black squares represent experimental data points and the red lines are Gaussian fits to the data.

The laser pulse used for the scans in figure 3.14 was a long pulse (~35 fs). The temporal scan, as seen in figure (a), indicated 40 fs delay over which the sidebands could be seen. Translating the lens position in the transverse direction gave the results in (b) for motion in the x direction and (c) for motion in the y direction. The transverse profile of the beam gave a width of ~10-12 μm. This is larger than the CCD measured center spot size but can be partially explained by the fact

that the temporal stability of the interferometer was not fully locked meaning the result shows an average effect. Finally, figure (d) shows that the full range of the longitudinal position was just over 1 mm. This is longer than the calculated confocal parameter of the beam (~280 μm) assuming purely Gaussian wave propagation. In all figures, the red lines represent Gaussian fits of the experimental data (black squares). The fits are used simply to guide the eye.

7. Once the sidebands are optimized, the DOG optics should be re-gated (set to +/- 45 degrees again). The spectrum should still be a continuum. A quick test can be conducted at this point to see if the spectrum broadens when the IR laser is added. If the spectrum is not still a continuum, the BBO can again be tuned but the sidebands must then be re-optimized. Tuning the BBO usually changes the temporal overlap slightly.

8. The IR ND filter is set to allow ~10-50 mW through (whichever yields the best streaking vs. ATI) and the interferometer is locked. The CW 532 nm laser is let through the setup. At the output of the hole drilled mirror, the inner and outer beams should form a ring with a bright dot in the center. The ring comes from the XUV arm reflecting off the back of the hole mirror while the dot comes from the streaking arm passing through the hole in the mirror itself. These beams are then overlapped spatially using the second small interferometer until good contrast fringes are visible. The fringes are next incident on a photodiode so that the intensity can be measured on the locking electronics. For additional stability, a HeNe laser can be propagated through the small interferometer to lock it in the same manner that the green laser is used with the streak camera. For the full details of the locking scheme, including the electronics, see appendix D.

9. Once the interferometer has been successfully locked, the streak camera is ready to be used. To avoid jumps in the interferometer stability, no one should be working on the table while data is accumulating.

3.2 Two Color Streaking

The phenomenon of streaking is merely a high intensity version of the generation of sidebands. When an attosecond pulse train is generated with HHG, the discrete ordered spectrum in the frequency domain will generate a similar discrete energy spectrum of photoelectrons. When an IR laser is added to the photoelectrons, each individual electron can be given an upshift or downshift by a single photon energy (~1.55 eV) depending on the sign of the

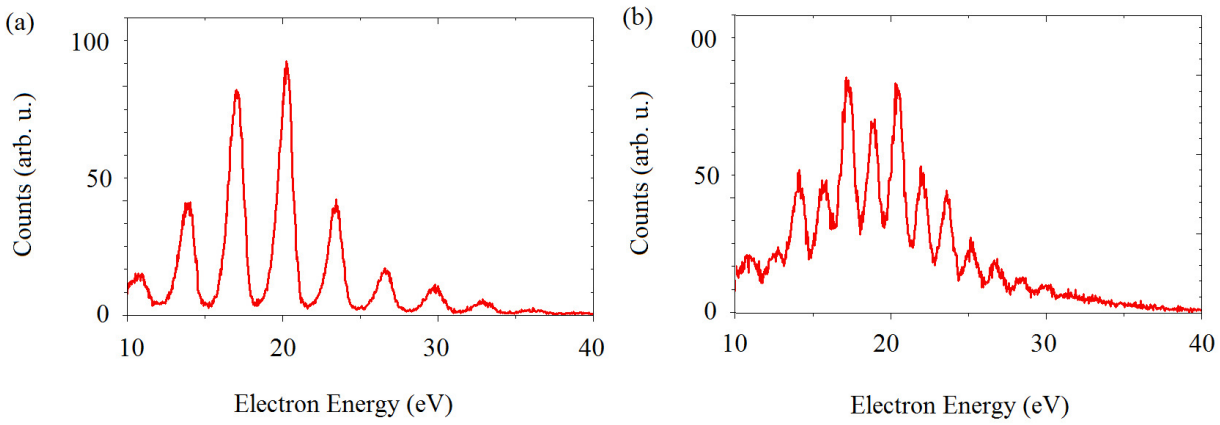

Figure 3.15 (a) Photoelectron spectrum from a linear one color laser field. (b) Photoelectron spectrum including sidebands after an IR laser field is added to the spectrum in (a).

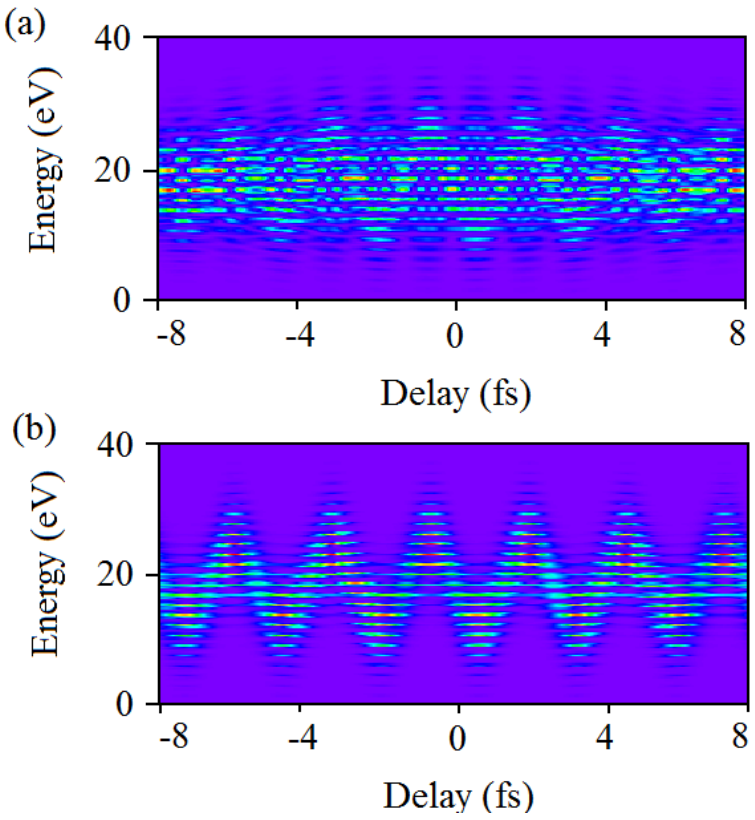

Figure 3.16 (a) Simulated streaked image for a half cycle attosecond pulse train and (b) full cycle pulse train.

laser vector potential. Figure 3.15 shows a photoelectron spectrum without (a) and with (b) sidebands added. Increasing the intensity of the IR laser increases the probability of multi photon sidebands forming. Once the intensity is high enough, the original spectrum can be significantly shifted to different energies. If the original spectrum is continuous, the full spectrum shifts up and down giving the spectrograms seen in figure 3.2(b). Figure 3.16 (a) and (b) show the simulated streaking pattern of a one color (half cycle periodic pulse train) and two color (full cycle pulse train) spectrum for the same IR laser intensity and 5 attosecond pulses in the train, respectively. The two color case shows a streaked image of discrete orders while the one color case shows a complicated pattern resulting from streaking of the adjacent attosecond pulses in opposite directions simultaneously.

The most obvious test for the streak camera is to generate experimental results similar to the simulation shown in figure 3.16(b). This can be accomplished by using a long (~30 fs) laser pulse directly from the KLS amplifier and sending it through the DOG optics with a few cycle delay quartz plate as the first optic. Obviously this will not gate a single pulse from the train and instead multiple pulses will remain. The resulting photoelectron spectrum would then exhibit discrete peaks.

Figure 3.17(a) shows an experimental streaked spectrum under the conditions of a 30 fs laser pulse with pulse energy of ~900 μJ pulse energy. The simulated spectrum shown in figure

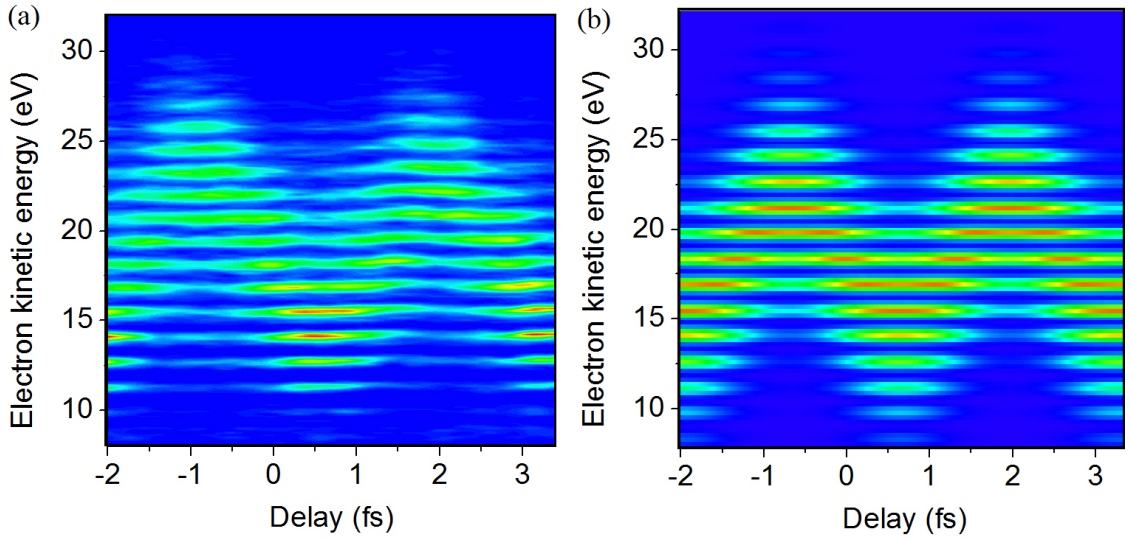

Figure 3.17 (a) Experimental and (b) simulated streaked spectrogram for two-color streaking.

(b) is conducted from a pulse train of 5 pulses and IR intensity of 1 x 10^{12} W/cm^2.

Figure 3.17 exhibits one of the properties of two color gating techniques. Since the pulse train is separated by one optical cycle, each pulse experiences the same sign of the vector potential from the IR streaking beam. This means that the train will automatically give a streaked pattern. If the pulse train had a half-cycle periodicity, consecutive pulses would streak in opposite directions giving a similar result as shown in figure 3.16(a). The results of figure 3.17 also serve as evidence that the streak camera functions properly but obviously the pulse is not isolated. The remainder of this chapter will be devoted to results from isolated attosecond pulse generation.

3.3 Attosecond Pulses with DOG

Setting the gate width to one optical cycle and using short ~8-9 fs laser pulses allows the DOG technique to efficiently generate isolated attosecond pulses. Figure 3.18 shows the very first isolated attosecond pulses generated using the DOG technique. Due to technical difficulties associated with the temporal stability of the setup when DOG was first implemented, the results only exhibit 4 cycles of delay between the IR and the XUV. While more cycles results in a more accurate reconstruction since the redundant information is repeatedly encoded in every cycle of the spectrogram, technically only two slices are really needed to characterize the attosecond pulse [82]. The experimental parameters were 550 μJ, 9 fs pulses for the generation arm and 50 μJ pulses for the streaking arm. This result was measured before the hole mirror. The aluminum filter was 300 nm thick and the generating gas was argon at ~50 torr backing pressure. The detection gas was neon since neon has a flat cross section and a flat transmission. This means no correction was needed to be made to the output spectrum to account for differences in photoelectron yield as a function of energy. The pressure of the neon gas in the chamber itself was ~6 x 10^{-5} Torr. Each delay slice in the spectrum in the image was integrated for ~1 minute and the delay step was 333 as. The first turbo was not operated meaning the low energy photons were reabsorbed by the generation gas which is why the spectrum is so narrow.

Figure 3.18(a) shows the experimental result and figure (b) shows the image created by the reconstruction algorithm. The similarity between these two images indicates that the algorithm worked very well. The extracted temporal profile (black line) and phase (red line) are

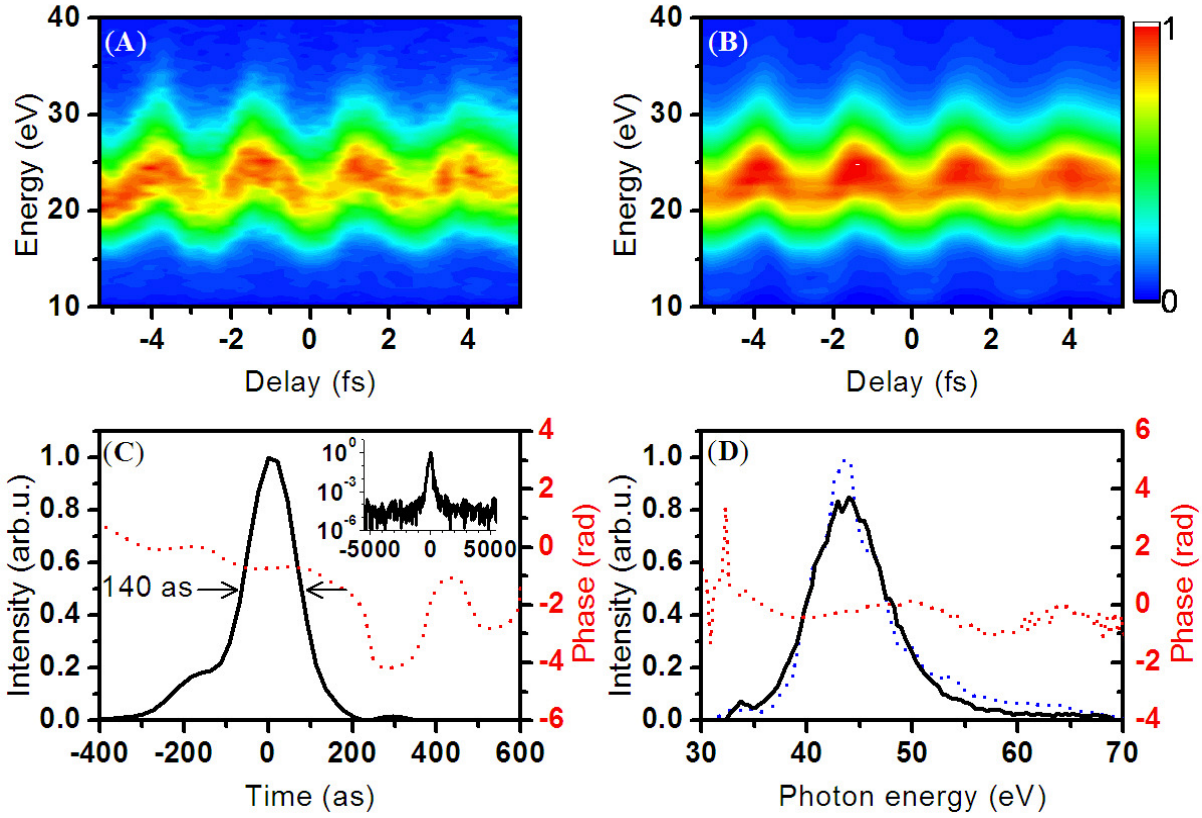

Figure 3.18 (a) Experimental and (b) retrieved streaked spectrograms from a 9 fs laser with DOG in argon and with neon as the detection gas. (c) The extracted temporal profile (black line) and phase (red dotted line). The inset shows the temporal profile over a longer delay. (d) The unstreaked spectrum (blue dotted line) and retrieved spectrum (black line) and phase (red dotted line).

shown in figure (c). The pulse duration was ~140 as and the phase was somewhat flat indicating a near transform limited pulse duration. The inset of (c) shows the same temporal profile but plotted on a log linear scale over a wide delay range. The purpose of this was to show that the pulse was truly isolated since no pre or post pulse existed at the single cycle delay points of +/- 2.6 fs. Finally, figure (d) shows a comparison between the unstreaked spectrum (blue line) and the Fourier transform of the profile and phase of figure (c) (black line). The similarity indicates an accurate reconstruction. The retrieved phase (red line) shows a somewhat flat shape with an extracted positive chirp of 3010 as^2. The spectrum is narrow with the lower orders missing.

This is due to absorption of the low orders by residual gas in the chamber reabsorbing the low energy XUV photons.

After the interferometric streak camera was improved upon, the stability was able to be locked to ~10 as temporal jitter for extended periods of time. Also, since DOG has a higher conversion efficiency as compared with PG, the amount of time required to integrate could be reduced significantly. Figure 3.19 shows a streaked spectrogram reconstruction for multiple cycles of delay. This shows the full temporal profile of the streaking beam and as such, could be used to fully characterize a femtosecond laser pulse through a cross correlation experiment. Figures (a) and (b) show the experimental and reconstructed images respectively. Figure (c) shows the extracted temporal profile (black line) and phase (red line). Again, the attosecond

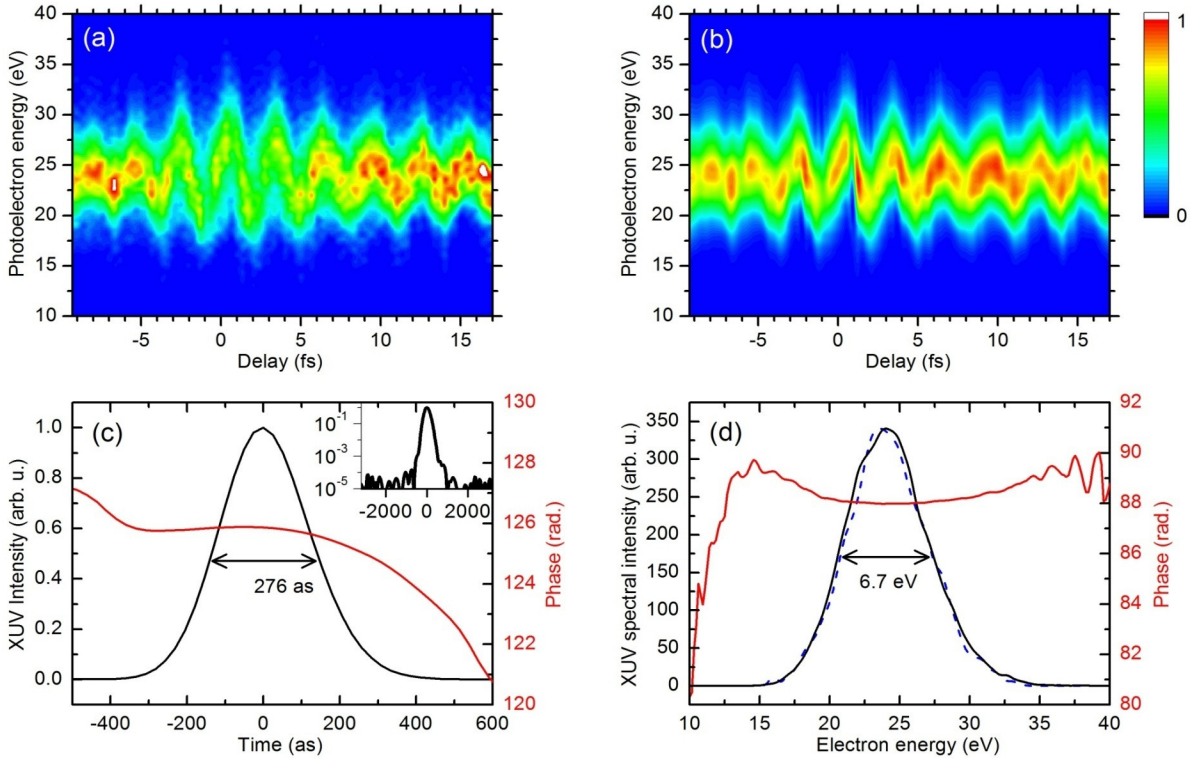

Figure 3.19 (a) Experimental and (b) retrieved streaked spectrograms from a 9 fs laser with DOG in argon and with krypton as the detection gas. (c) The extracted temporal profile (black line) and phase (red dotted line). The inset shows the temporal profile over a longer delay. (d) The unstreaked spectrum (blue dotted line) and retrieved spectrum (black line) and phase (red dotted line).

pulse can be regarded as a true isolated pulse since there are no pre or post pulses (see inset). Finally, (d) shows the comparison between the retrieved spectrum (blue line) and the experimental spectrum (black line). The phase (red line) is very flat indicating a near transform limited pulse was created. Overall, the results of figure 3.19 are similar to 3.18 except the bandwidth is narrower in 3.19. Also, the detection gas used was krypton (Ip ~ 14 eV) and was at a pressure in the chamber of 9 x 10^{-5} Torr. The reason for this was to shift the photoelectrons to a higher initial kinetic energy as compared to those generated with neon (Ip = 21.6 eV). This resulted in a larger energy shift. The most important difference however was that figure 3.18 only required 12 seconds of integration per delay slice meaning the full spectrogram could be completed in 15 minutes. The four cycles in 3.18 required 32 minutes as a comparison.
Since DOG has higher peak intensity in the gate width as compared to PG, harmonics generated from neon are also possible. Neon is an attractive target for attosecond pulse generation because it can generate a much broader spectrum than argon. Figure 3.20 shows the reconstruction of an attosecond pulse generated with neon in the first (25 Torr) and second gas targets (3 x 10^{-5} Torr). In this case, the first turbo was turned on to improve the count rate of HHG from neon with its broad spectrum. The pressure when the turbo was running was ~2 mTorr. Such a broad spectrum is not expected to be accurately retrieved since the center momentum approximation is not valid however FROG-CRAB is the only method available for the reconstruction of such pulses. 3.20(a) and (b) shows the experimental and reconstructed spectrograms. Figure (c) shows the temporal profile (black line) and phase (red
line) and again the inset shows the pulse is a true isolated pulse. Finally, (d) shows the comparison of the experimental spectrum (black line) and the retrieved spectrum (blue line) and phase (red line).

The phase in this case is more complicated than that of the previous two cases. The most striking feature of this result is the fact that in the experimental image, the spectrum seems to be transform limited from 0-35 eV while above this it exhibits the asymmetry associated with a chirped pulse. This gives rise to the complicated retrieved phase in (d) and will be discussed in detail in the next section.

The choice of neon as the detection gas was only a matter of convenience. As discussed earlier, gases with lower Ip will have larger energy shifts since their initial kinetic energy is greater. Figure 3.21 shows this effect for a few different cases. In figure (a), the generation gas

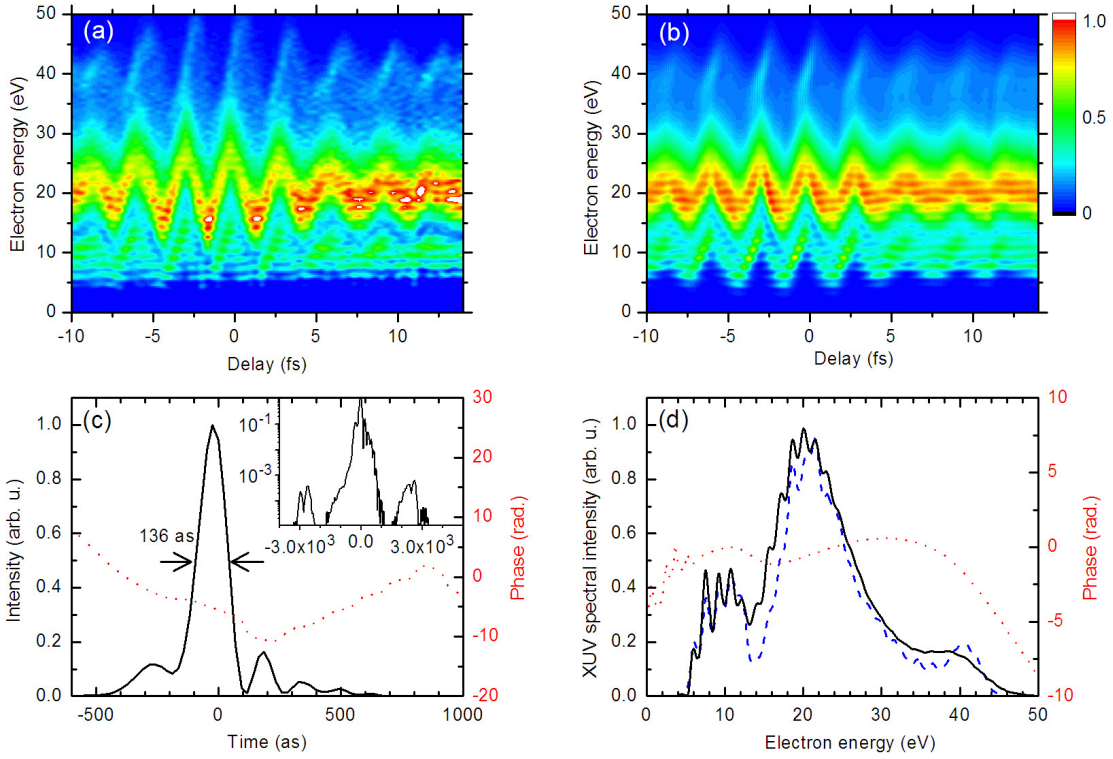

Figure 3.20 (a) Experimental and (b) retrieved streaked spectrograms from a 9 fs laser with DOG in neon and with neon as the detection gas. (c) The extracted temporal profile (black line) and phase (red dotted line). The inset shows the temporal profile over a longer delay. (d) The unstreaked spectrum (blue dotted line) and retrieved spectrum (black line) and phase (red dotted line).

was argon and the detection gas was krypton (Ip=14 eV) at a pressure of 6 x 10^{-5} Torr. The electron spectrum is centered at ~25 eV. In (b), the detection gas was argon (Ip=15.8 eV) with all other parameters the same. The spectrum then shifts 1.8 eV lower and is centered at ~23.2 eV. In (c), the detection gas changed to neon (Ip=21.6 eV) thereby shifting the spectrum to ~17.4 eV. In each case, the streaking amplitude is reduced as the spectrum shifts to lower energy. Figure (d) shows this effect from a streaked spectrogram generated from neon and with neon as the detection gas. The broad spectrum exhibits very large streaking above ~35 eV, moderate streaking around 20 eV, and almost no streaking around 10 eV. If the goal is a streaked spectrogram with large streaking amplitude, gases with low ionization potentials are good targets. The disadvantage to low Ip gases is that the IR laser can also begin to ionize the

detection gas meaning a large contribution from the ATI can build up. This is the trade off. For low Ip, lower IR intensities are also required.

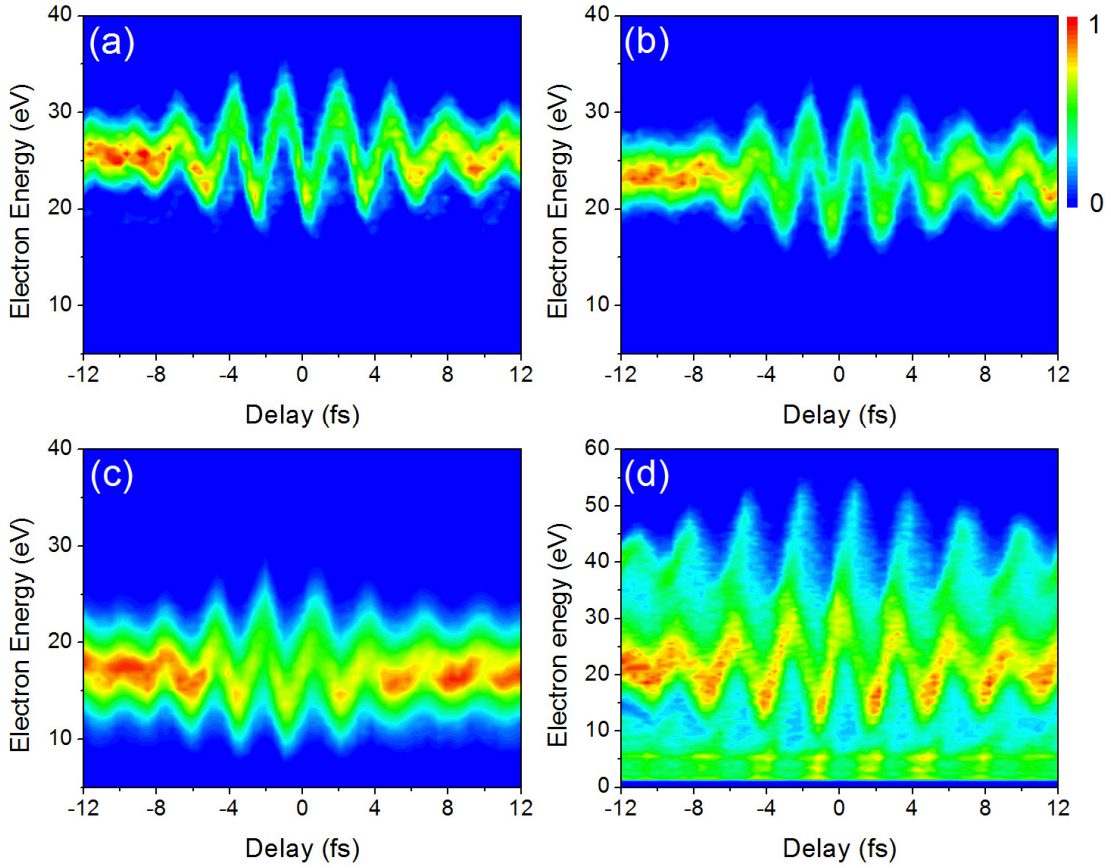

Figure 3.21 Streaked spectrograms generated from argon with the detection gas as (a) krypton, (b) argon, (c) and neon. (d) Neon as the generation gas and detection gas.

3.3.1 Intrinsic Chirp of Attosecond Pulses

As mentioned in chapter 1, the attosecond pulse generation process results in an intrinsic chirp for the phase of the pulse. While both the long and short trajectories are chirped, through phase matching techniques, only the short trajectories are used for the attosecond pulse production. Figure 3.22 shows a plot of the returning phase in radians of the fundamental laser period, T_0, versus the energy of the photon in terms of the ponderomotive energy, U_p. The short trajectory portion of the plot is shown with a line fitted to the curve. This line actually gives the

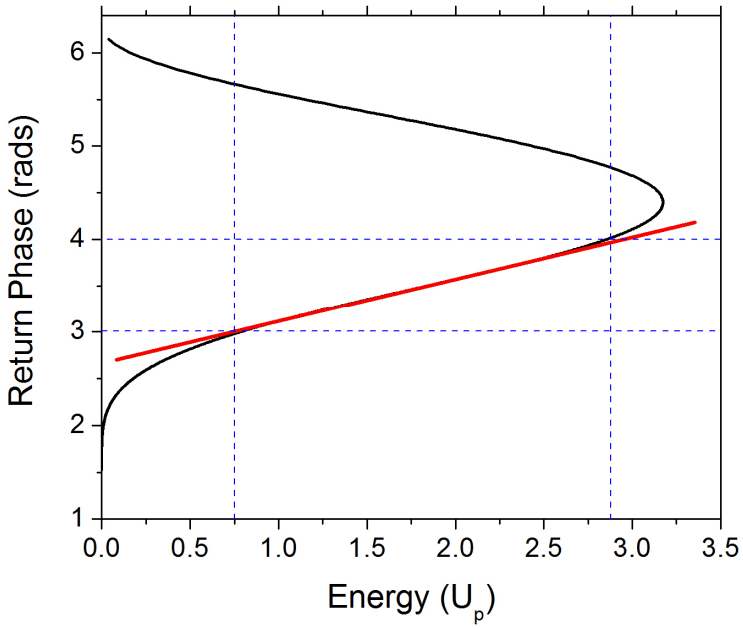

Figure 3.22 Returning phase as a function of energy. The red line is a linear fit of the short trajectory contribution.

phase of the attosecond pulse. Since the line has a positive slope, we expect the short trajectories to also have a positive chirp. The chirp is defined as:

$$GDD = \frac{dt}{dE} = \frac{dt}{d(\hbar\omega_x)} \tag{3.7}$$

where GDD is the group delay dispersion (or chirp) and ω_x is the frequency of the XUV photon. This is just the slope of the line in figure 3.20. The time, t, can be written in terms of T_0 and the phase, k, in rads as $t=kT_0/2\pi$. Since the energy of the photon can be written as $\hbar\omega_x = xU_p - I_p$ where x has a maximum value of 3.17. Since Ip is just an offset, it can be ignored when calculating the slope. Rewriting equation 3.7 with these terms yields:

$$GDD = \frac{k}{x}\frac{T_0}{2\pi U_p}. \tag{3.8}$$

The value of k/x is a constant slope with k in radians and x in units of Up. From figure 3.19, this slope is ~0.434 rads/Up. This gives a concise formula for the chirp as:

$$GDD = 0.07\frac{T_0}{U_p}. \tag{3.9}$$

Since U_p is proportional to I and λ^2, this formula says that using longer wavelength lasers (with longer periods) or higher intensities will result in reduced chirp.

Compensating the intrinsic chirp is a goal for temporal measurements. One possibility is to use dispersion through a gas target. If the gas gives a negative value of GDD over the energy range of the pulse, the chirp can be compensated [83]. However, for the streak camera setup, a filter is already in place to isolate the high gas density side from the detector side and to filter the residual IR. However, by choosing the thickness and material of the filter appropriately, the intrinsic chirp may also be partially compensated. Figure 3.23(a) shows the transmission of an aluminum filter that is 200 nm thick (red line) and 300 nm thick (black line). Figure (b) shows the total phase and (c) shows the group delay (GD) associated with each filter. The GD was calculated using reference [22]. The total real spectral phase from the filter of length L is given by:

$$\varphi = -Nr_e f_1 L\lambda \tag{3.10}$$

where N is the number density of the material, r_e is the classical electron radius, f_1 is the real part of the atomic scattering factor obtained from ref [22], and λ is the wavelength of the xuv photon. From the total spectral phase given by equation 3.10, the GD and GDD can be calculated. The GD exhibits a quadratic shape indicative of a strong linear chirp contribution. From 3.23(c), the GDD can also be calculated and is shown in figure 3.23 (d). The GDD was calculated by fitting a polynomial to the GD in order to avoid errors associated with numerical differentiation.

Figure 3.23(d) shows two important features. First, the thicker the material, the more negative the GDD is for values below ~50 eV. This can be used to compensate the intrinsic positive chirp of the HHG process. Second, for values above 50 eV, the chirp becomes more positive for thicker materials. This will overcompensate spectral components above 50 eV. This can be seen clearly in figure 3.21 (d). When a broad spectrum from a neon target is compensated by a 300 nm thick aluminum filter, spectral components below ~30 eV in photoelectron energy (50 eV in photon energy) are transform limited while those above 30 eV are strongly chirped. This implies the spectrum can be used to measure the phase introduced by some dispersive material. As further evidence of this feature, figure 3.24 shows two spectra generated from an argon target with a krypton detection target for two different values of aluminum filter thickness. Figure (a) shows a 200 nm filter while figure (b) shows a 300 nm filter. The results in

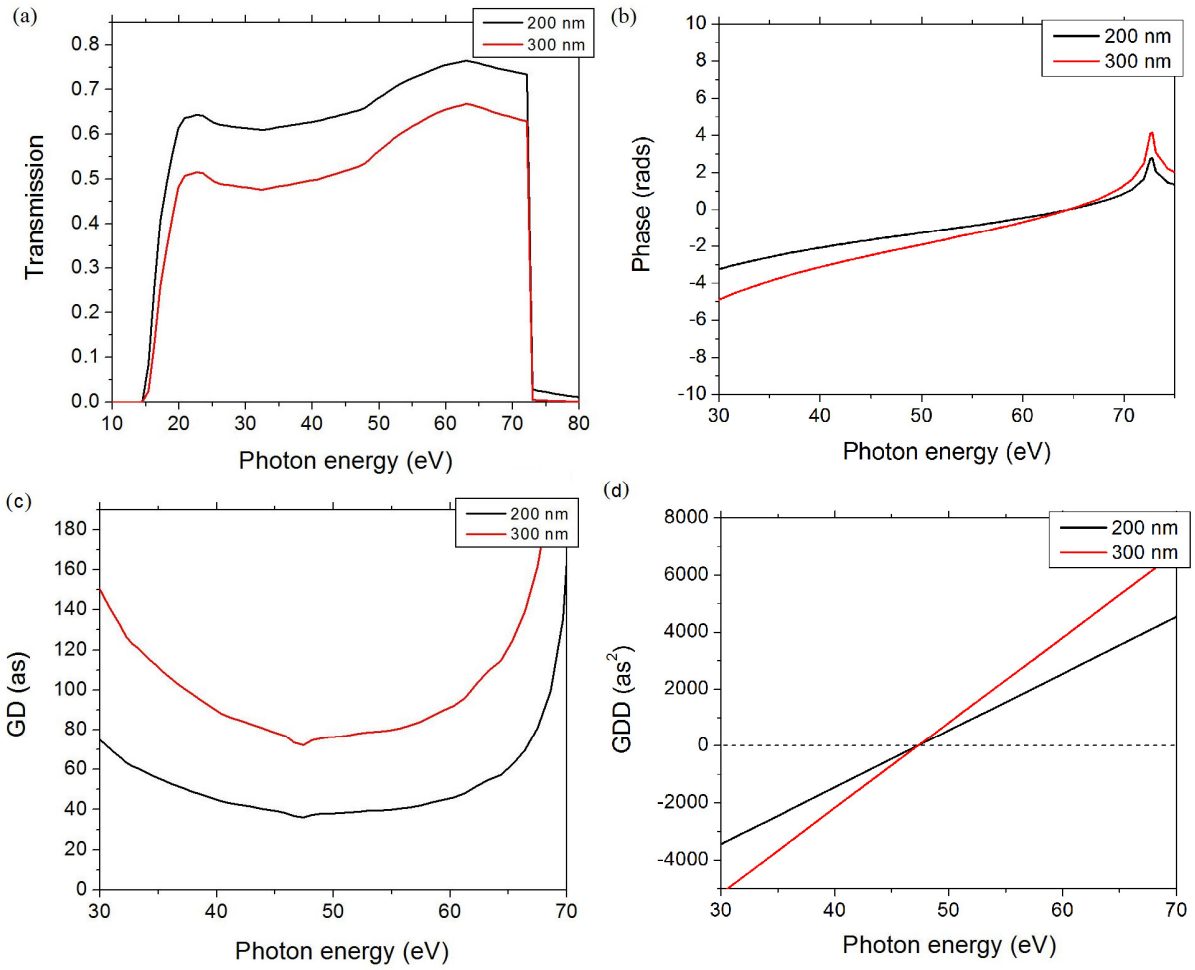

Figure 3.23 (a) Al filter transmission, (b) total phase, (c) group delay, and (d) group delay dispersion for 200 nm (black line) and 300 nm (red line) filter thickness.

(b) are more symmetric than the positive chirp in (a) implying a more compensated attosecond pulse in agreement with figure 3.24. The result in (a) appears to be the opposite as shown in figure 3.2 because the experimental scanning was done by shifting the XUV beam through the IR beam. This means the negative delays are the trailing edge of the IR pulse while in the simulations, the negative delays are the leading edge. This gives the opposite slant for the asymmetric chirp.

The choice of filter can also be used to compensate much broader spectra. Aluminum was chosen for these first experiments simply because it was strong enough to act as a gate for the high pressure side of the apparatus while also reflecting all of the residual IR and highly

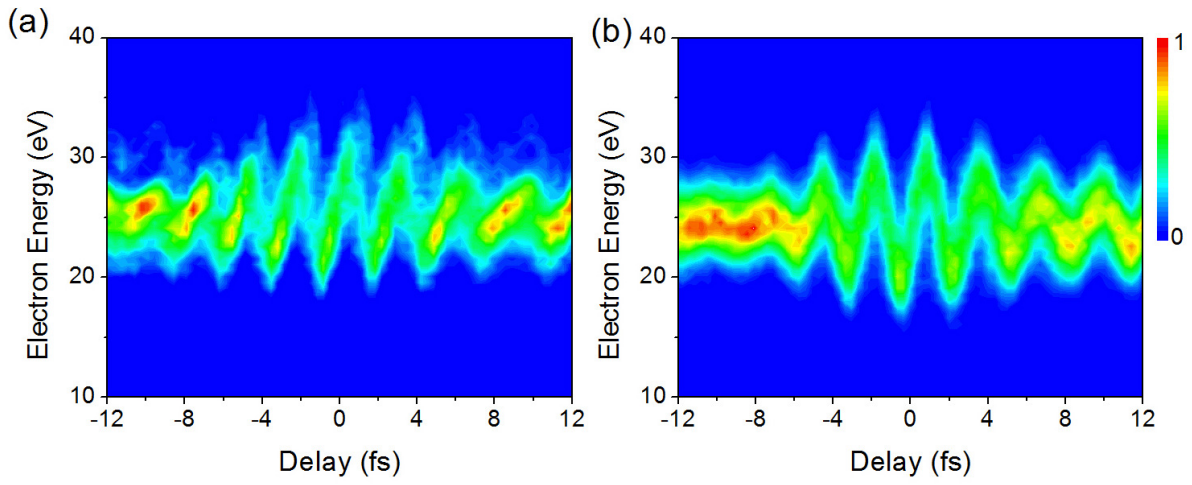

Figure 3.24 Spectrograms generated with argon and krypton as the detection gas with phase compensation from a (a) 200 nm and (b) 300 nm aluminum filter.

transmitting the XUV. Filters such as Zr for example would give negative GDD for a broad XUV range but the IR is also transmitted partially while Be compensates a broad range and reflects the IR well but is extremely weak.

3.4 Attosecond Pulses with GDOG

Double optical gating works very well for generating high flux attosecond pulses from multi cycle lasers. However, the GDOG method allows the pulse duration of the generating laser to be extended to even greater values. Figure 3.25 shows a streaked spectrogram and reconstruction for an attosecond pulse generated from a 20 fs laser. The turbo in the first target was not operational for this result yielding a narrower spectrum. Figures (a) and (b) show the experimental and reconstructed images, respectively. Again, four cycles were chosen for ease in the experiment and because all of the phase information is encoded in such a short scan. Since a portion of the driving field is rejected in the experiment, the peak intensity in the gate width is lower than the DOG case resulting in a slightly narrower spectrum and longer pulse duration. Figure (c) shows the temporal profile (black line) and phase (red line) supporting a 260 as pulse. The inset indicates that the pre and post pulse contributions are negligible indication the attosecond pulse is truly isolated. Figure (d) shows a comparison between the frequency domain representation of the retrieved temporal profile (solid line) and the measured XUV only spectrum

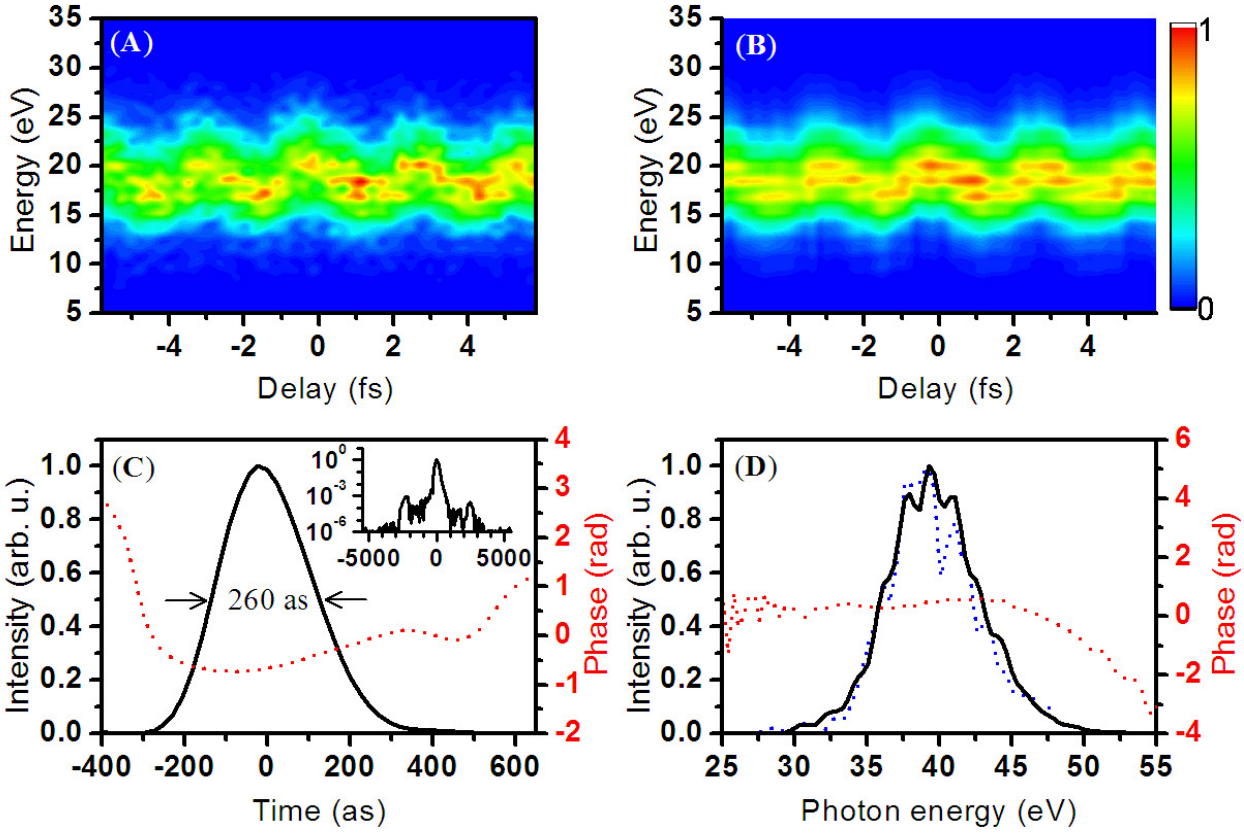

Figure 3.25 (a) Experimental and (b) retrieved streaked spectrograms from a 20 fs laser with GDOG in argon and with neon as the detection gas. (c) The extracted temporal profile (black line) and phase (red dotted line). The inset shows the temporal profile over a longer delay. (d) The unstreaked spectrum (blue dotted line) and retrieved spectrum (black line) and phase (red dotted line).

(blue dashed line). The results are similar indicating the robustness of the retrieval algorithm. Also shown is the spectral phase (red dashed line). The phase shows a positive chirp of ~3010 as^2. For a 20 fs laser pulse, 9 laser cycles of delay, and an ellipticity of ~0.9, the gate width was calculated to be ~4.5 fs. While this can still isolate a single attosecond pulse, the pre and post pulse contributions are slightly larger than the DOG case. This results in the modulated spectrum seen in (d).

The results of this chapter represent the temporally confirmed attosecond pulses generated using the DOG and GDOG techniques. Generating such pulses is relatively easy

meaning that the pulses can begin to be applied to different experiments. The rest of this thesis will discuss how the DOG and GDOG methods can be used to push the limits on the types of attosecond pulses that can be produced (chapter 4) and how the pulses themselves were used in experiments (chapter 5).

CHAPTER 4 - Applications of DOG and GDOG

The results in chapter 3 are the first attosecond pulses generated using our gating methods. These pulses do not represent the limitations of the DOG and GDOG methods however. This chapter will lay out uses for the robust gating methods to produce different attosecond pulses. Utilizing the high conversion efficiency and high peak intensity of DOG, ultra-broadband spectra are demonstrated. Also, since the techniques are robust, the methods are demonstrated to generate attosecond pulses from CEP unstabilized laser pulses and directly from a CPA for the first time. This represents a significant enhancement in attosecond technology.

4.1 Extreme Broadband Attosecond Pulses

The generation of ever shorter attosecond pulses is a main goal in this field. As the pulse duration reduces, the ability to study faster processes is created. The way this can be accomplished is first by reducing phase distortions in the attosecond pulse. As seen from the previous chapter however, the phase is already quite flat. This means the spectral bandwidth must be increased in order to further reduce the pulse duration. Luckily, the HHG cutoff is intensity dependent meaning higher peak intensities within the gate width can automatically produce much broader spectra [10]. Attosecond pulse trains with harmonics reaching the so called "water window", or the wavelength region where water becomes transparent to XUV photons, were demonstrated in 1997 [84, 85]. This is of particular importance in biology since biological systems can then be imaged with the internal structure visible with nanometer precision. Reaching this region is also necessary for attosecond pulse durations approaching the atomic unit of time (1 a.u. = 24.2 as). Since DOG has a higher peak intensity within the gate width as compared with polarization gating and is able to generate a spectrum covering both the plateau and cutoff orders as opposed to amplitude gating, it is the best choice for generating very short attosecond pulses.

The experimental setup used to generate the extreme broadband spectrum was an XUV spectrometer as shown in figure 4.1. An 8 fs laser pulse entered the vacuum chamber where it passed through the quartz plates for DOG and was focused through a BBO crystal. For this experiment, the first quartz plate was 270 μm thick and the second was 440 μm thick. The BBO

was 141 μm thick. The focal length of the spherical mirror was 125 mm which gave an estimated spot size of ~10 μm and peak intensity within the gate width of 1.4 x 10^{16} W/cm^2.

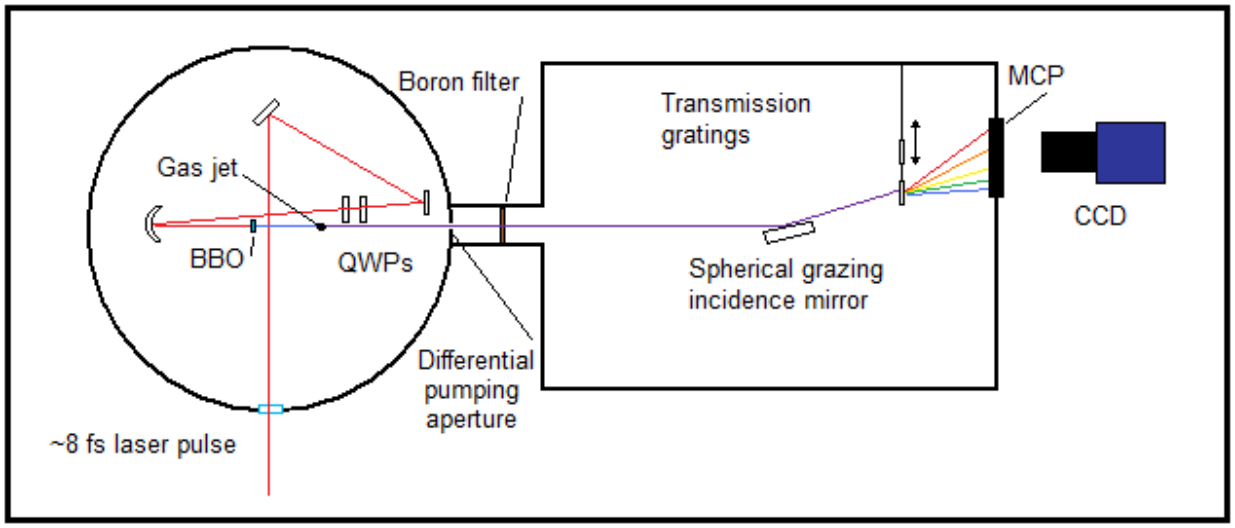

Figure 4.1 XUV spectrometer for measuring broad spectra.

This intensity theoretically could generate harmonics of ~1.5 nm. Such a tight focusing mirror was difficult to align while keeping the astigmatism minimized which is why all of the optics were located inside the vacuum. The laser was focused into a neon gas target that was a 1.4 mm long laser drilled glass tube. The beam then passed through a ~0.5 mm hole used to isolate the high pressure gas jet side from the detector side and also to clip most of the residual IR laser since it had a larger divergence than the XUV. The beam then passed through a boron filter which could be easily removed from the beam path. Next, the XUV reflected off of a grazing incidence spherical mirror to focus the XUV into a transmission grating [86]. There were two gratings available, one with 2000 lines per mm and the other with 5000 lines per mm. The 2000 lines grating could be used for wavelengths from 45 nm to 15 nm with a diffraction efficiency of ~4% while the 5000 lines grating could be used for wavelengths below 15 nm with an efficiency of 1.5%. The resolutions for the two gratings were 0.013 nm at 15 nm for the 2000 lines grating and 0.05 nm at 2 nm for the 5000 lines grating. The XUV photons were then imaged onto a microchannel plate and phosphor screen combo and the images were captured with a water cooled CCD camera.

Actual experimentally obtained spectra are shown in figure 4.2 [87]. The upper figure shows a broad continuous spectrum from DOG while the lower plot shows an XUV spectrum from a linearly polarized input laser pulse. Both spectra are the integration of 100,000 laser shots for signal to noise reasons. The yellow line indicates the interface between the two gratings. The longer wavelength portion is from the 2000 lines per mm grating while the short wavelength

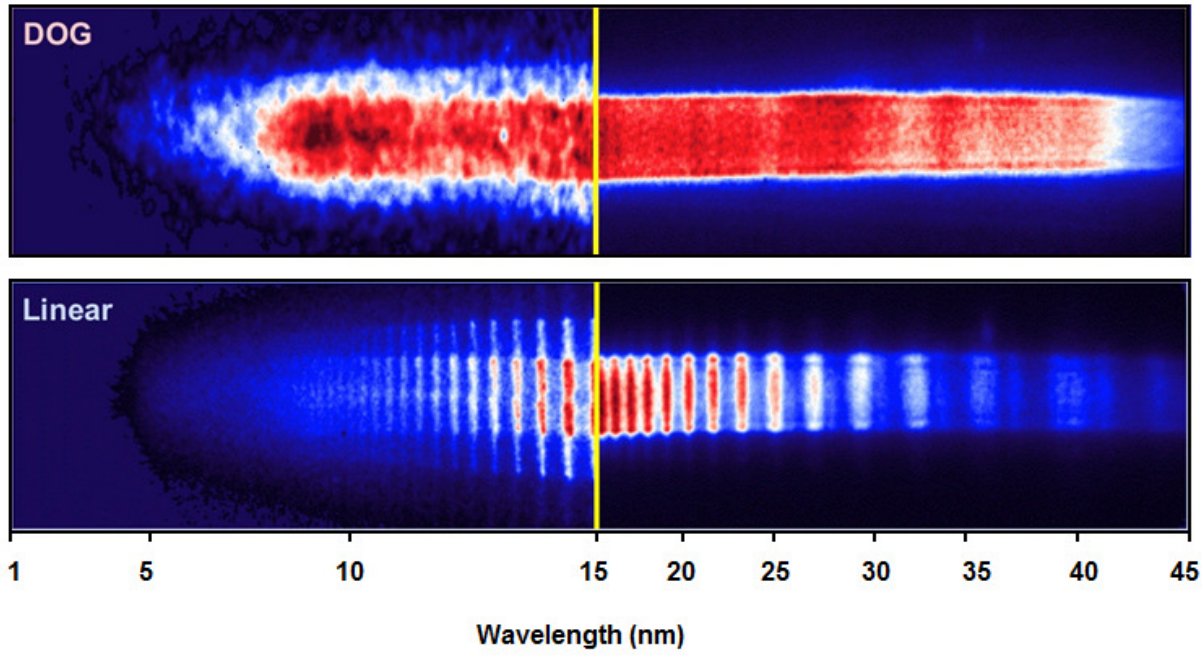

Figure 4.2 XUV spectra from DOG (upper figure) and a linear pulse (lower figure).

portion is from the 5000 lines per mm. Although the resolution of the spectrometer is not sufficient for the short wavelengths, since the spectrum is continuous in the long wavelength region it is expected that the cutoff is also continuous since the harmonic generation process depends more heavily on the ellipticity of the driving laser for higher orders.

Figure 4.3 shows the lineout plots (a) of the two spectra while (b) shows the time domain representation of the continuous spectrum assuming flat spectral phase. This spectrum is capable of supporting a 16 as pulse which is below the atomic unit of time. As a calibration of the spectrum to ensure the high harmonics are truly water window orders and not simply

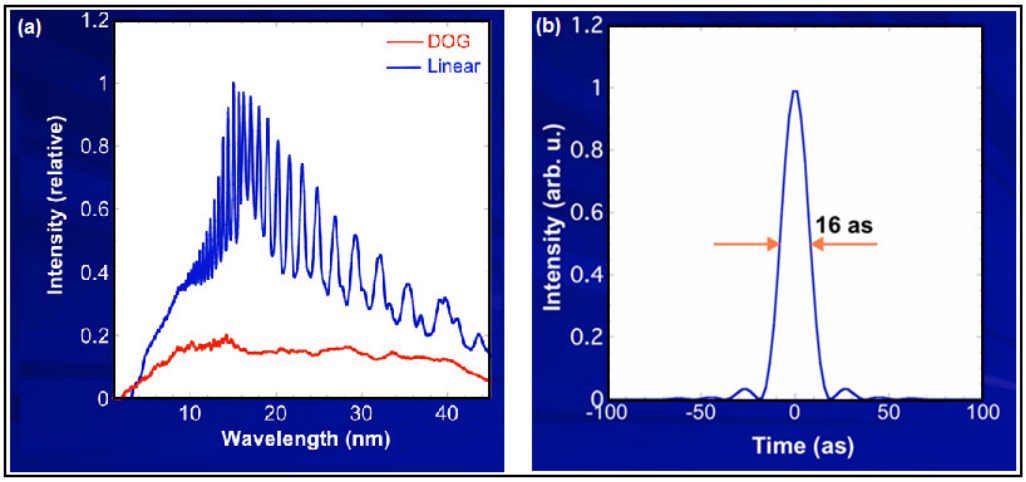

Figure 4.3 Lineout plot of the DOG spectrum (a) and the TL pulse duration (b).

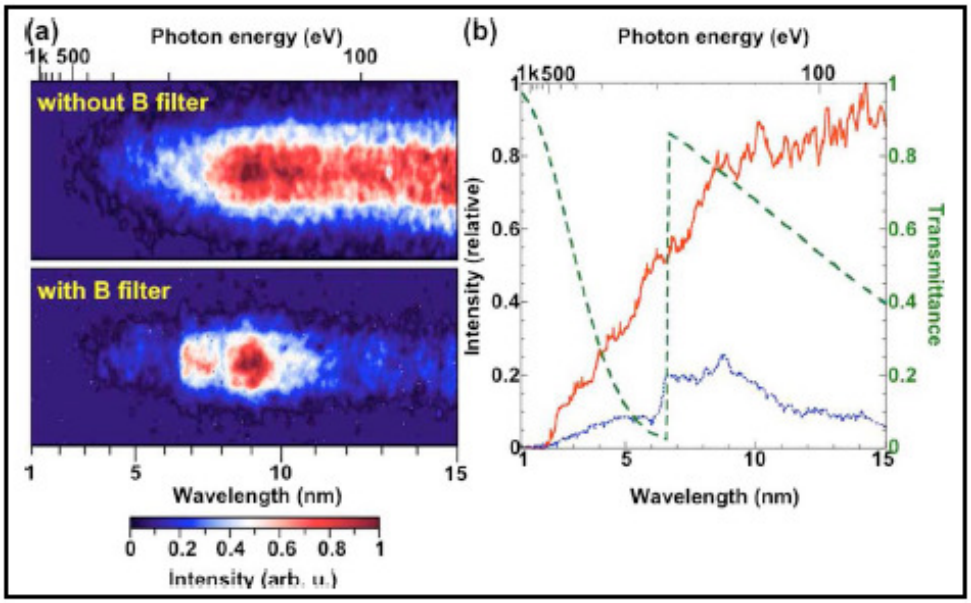

Figure 4.4 (a) Spectrum images without (upper) and with (lower) the filter in place. (b) The lineout plots of the spectra in (a) for the case without (red) and with (blue) the filter in place. The green dashed line is the filter transmission (figure taken from ref. [87]).

background noise, a boron filter was inserted and a reference spectrum was taken. Clearly there is a reduction of the signal below ~6 nm which corresponds to the transmission edge in boron.

Figure 4.4 shows the calibration. The green dashed line in (b) is the boron transmission while the red solid line is the spectrum without the filter added and the blue line is the spectrum with the filter in place.

While the results shown in figure 4.2 indicate an extremely short pulse duration, a temporal measurement of such a pulse is currently not possible. Besides the strong resolution requirements, there is no way to reflect such a broad spectrum with a normal incidence mirror in the streak camera and there is not good way to compensate the intrinsic chirp of the HHG process. However, in the absence of a temporal measurement, the attosecond pulse can be partially characterized with a CE phase scan. Figure 4.5 shows a CE phase scan in a similar style

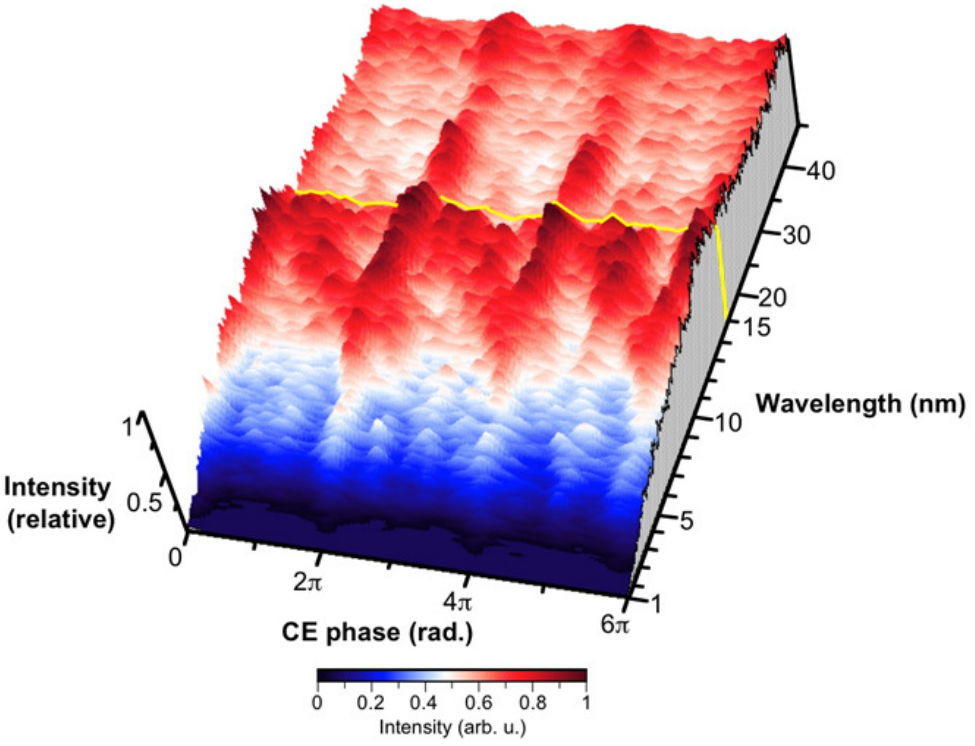

Figure 4.5 CE phase scan of DOG pulse for water window photons.

as the previous CE phase scans. A 2π periodic structure is still visible indicative of the two color gating method and the spectrum exhibits very broad spectra for certain values of the CE phase. These two effects provide evidence that the gating method is functioning properly and that the pulse is probably an isolated attosecond pulse.

The shortest attosecond pulse generated with our streak camera is currently ~107 as and the result is shown in figure 4.6. (a) and (b) show the experimental and reconstructed images and (c) shows the extracted temporal profile (black line) and phase (red dashed line). The inset indicates the pulse is an isolated attosecond pulse. In (d), the marginal comparison shows the retrieval is fairly accurate. While this result is the shortest currently generated, it is a very small portion of the total spectrum that can be possibly generated. Figure 4.7 illustrates this point clearly. The total spectrum generated is shown as the red line while the mirror reflectivity of the Mo/Si mirror used for the reconstruction in figure 4.6 is shown as the small green shaded region in the corner. Obviously there is much room for improvement and the attosecond pulses that have thus far been generated have a spectrum that represents only a tiny fraction of the total spectrum available.

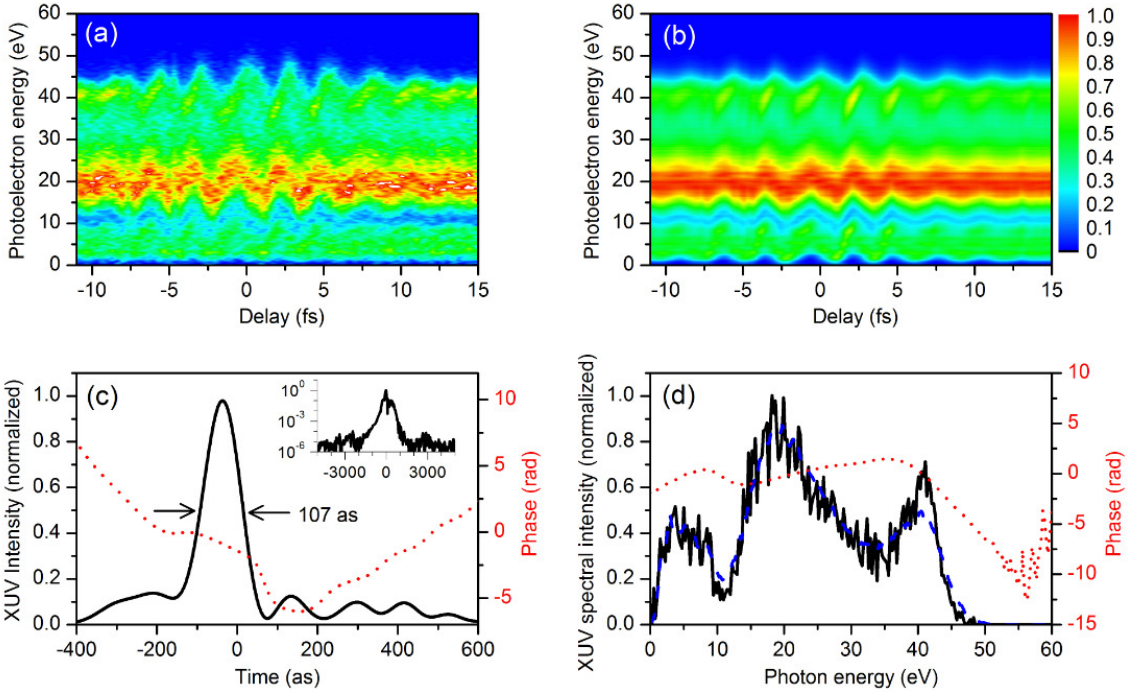

Figure 4.6 (a) Experimental and (b) retrieved streaked spectrograms from a 9 fs laser from neon. (c) The extracted temporal profile (black line) and phase (red dotted line). (d) The unstreaked (blue dotted line) and retrieved spectrum (black line) and phase (red line).

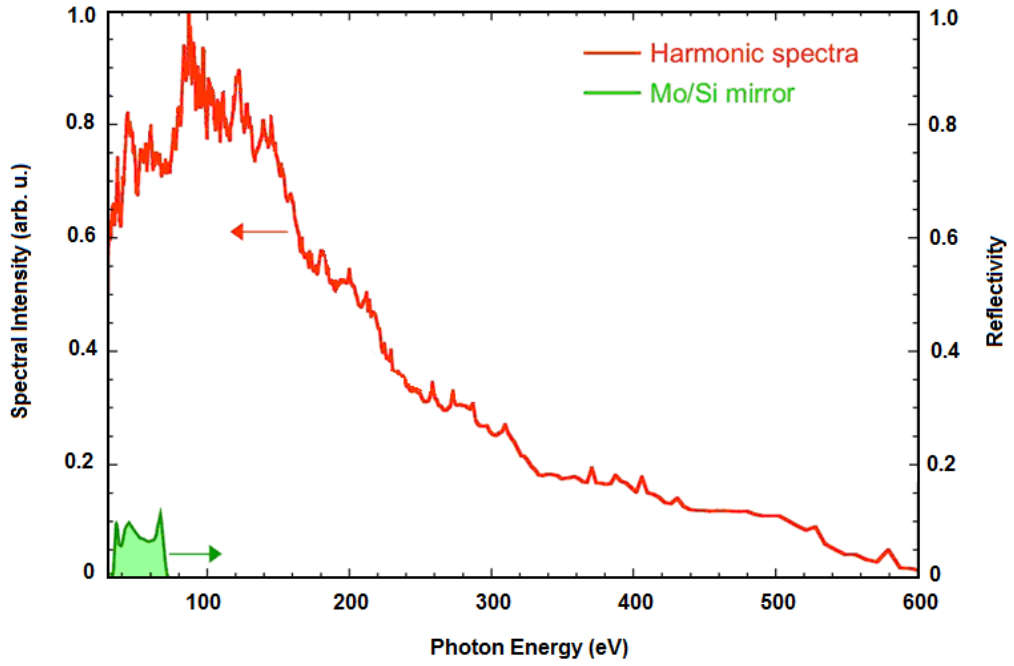

Figure 4.7 The experimental spectrum (red line) as compared with the reflectance of the Mo/Si mirror in the streak camera.

4.2 Attosecond Pulses from any Laser

At this point, the DOG and GDOG methods have been shown capable of generating attosecond pulses efficiently under many different laser conditions. The point of this section is to extend the methods further and show that attosecond pulses can be generated from any laser. First, attosecond pulses will be generated directly from a CPA for the first time. Then, attosecond pulses will be generated from a laser system without the need for CE phase stabilization. Finally the methods will be combined by using GDOG to generate attosecond pulses directly from the amplifier and without the need for CE phase stabilization.

4.2.1 Attosecond Pulses Directly from an Amplifier

Laser systems with pulse durations below 30 fs are currently commercially available (Amplitude Technologies, Femtolaser, Coherent). Since the GDOG method can be used for laser pulses nearly 30 fs in duration [78], this creates the opportunity for isolated attosecond pulses to be generated from any lab with such a laser system. In our experiments, the KLS laser routinely

produces pulses with duration in excess of ~30 fs meaning the laser must first be slightly modified to first produce pulses with duration of ~25 fs. This is accomplished with spectral shaping of the laser pulse halfway through the amplification process. Figure 4.8 shows a schematic of the full KLS laser system [88]. Further details are given in appendix F. The beginning of the KLS laser system consisted of a Kerr-lens mode-locked Ti:Sapphire oscillator.

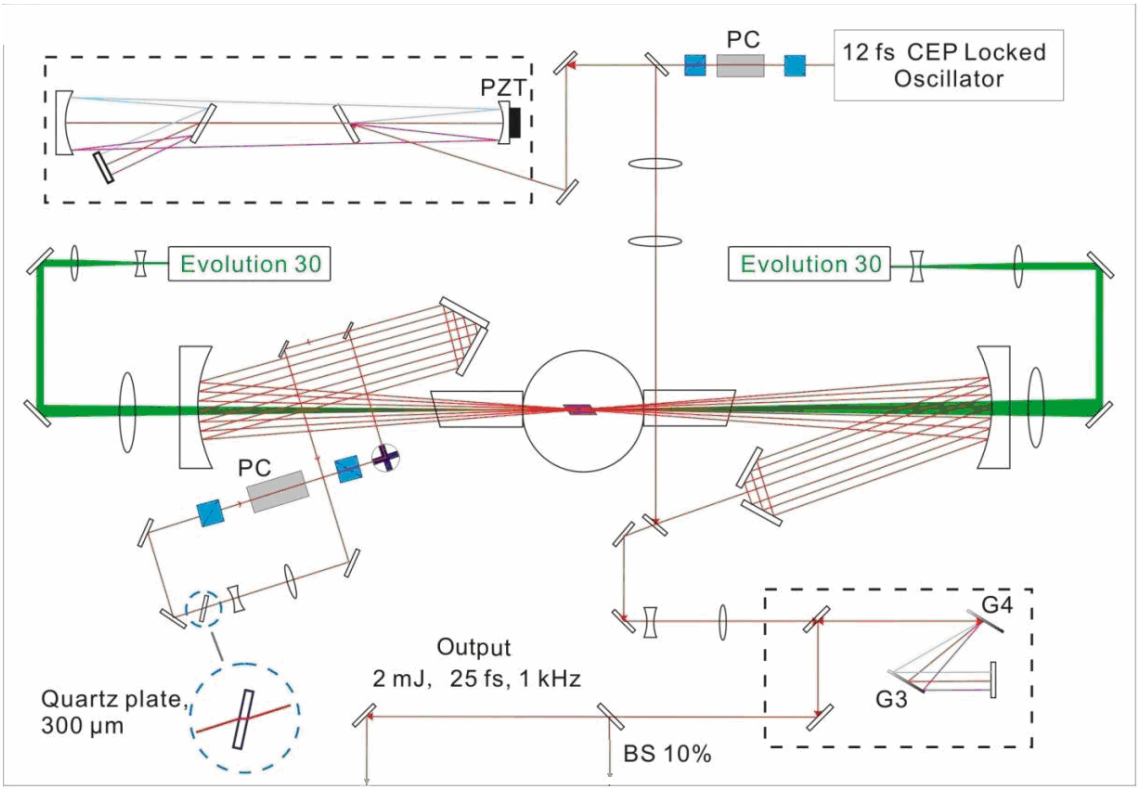

Figure 4.8 The KLS laser system. G = grating, PC = Pockels cell, BS = beamsplitter.

Next, 1.5 kHz pulses with ~100 nm bandwidth and 3 nJ energy are picked by a Pockels cell from the oscillator pulse train. These were then stretched to ~80 ps by a grating-based Martinez type stretcher. The CE phase of the oscillator and the amplifier were locked as discussed earlier [48-51]. Then, the stretched pulses were amplified to 5 mJ with a Ti:Sapphire 14-pass amplifier. After the amplification, the pulses were compressed by a pair of gratings to 2 mJ, 33 fs with 26 nm FWHM spectrum bandwidth.

In order to generate a spectrum capable of supporting 25 fs for the GDOG experiment, a 300 µm thick birefringent quartz plate (BP) was inserted as a spectrum shaping filter before the polarizer between the first and second 7 passes. It introduced higher loss at the central frequency than that of the wings of the gain, thus compensating the effects of the gain narrowing [89]. Fig.

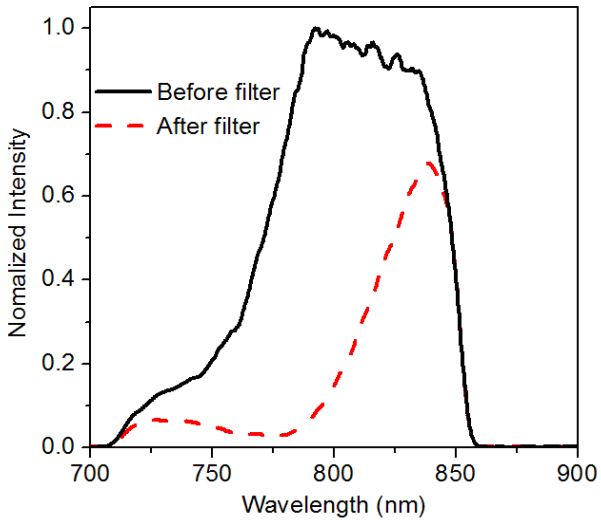

Figure 4.9 The KLS spectrum before (solid line) and after (dashed line) the spectral filter.

4.9 shows the measured 7 pass spectrum before (solid curve) and after the plate and a polarizer (dashed).

We characterized the final output pulses by using a single-shot, second-harmonic generation frequency-resolved optical gating (SHG-FROG). The 25 fs pulse FROG trace was measured after the quartz spectrum filter was installed. Fig. 4.10 (a) is the measured trace and

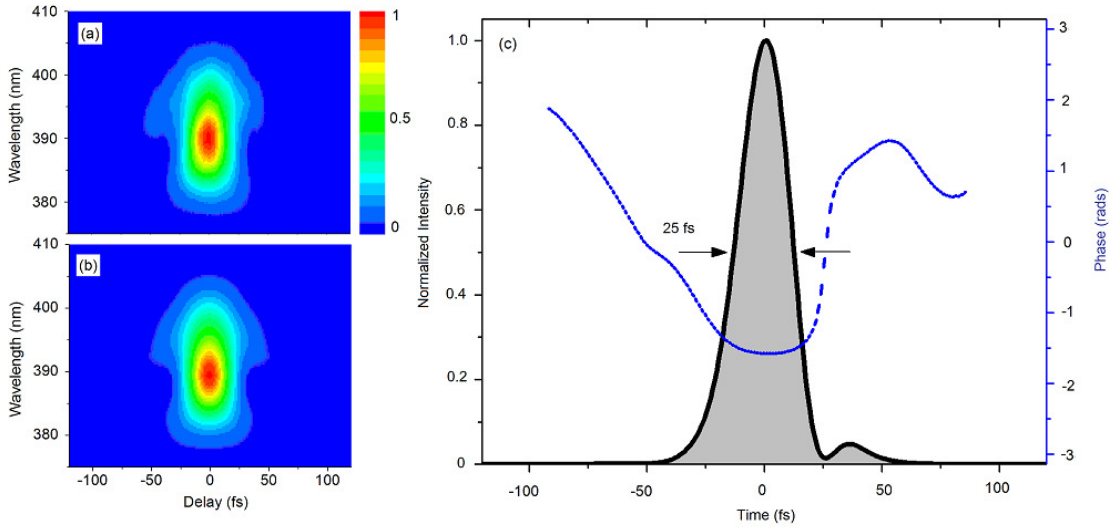

Figure 4.10 FROG trace of a 25 fs laser pulse. (a) Experimental trace, (b) retrieved trace, (c) temporal profile (black solid line) and phase (blue dashed line).

Fig. 4.10(b) the retrieved trace. Fig. 4.10 (c) shows the retrieved pulse shape (black solid line) in the time domain along with the temporal phase (blue dashed line). This result indicates that the pulse duration has been reduced to the point that depletion effects from GDOG are no longer an issue and instead an isolated attosecond pulse can possibly be generated.

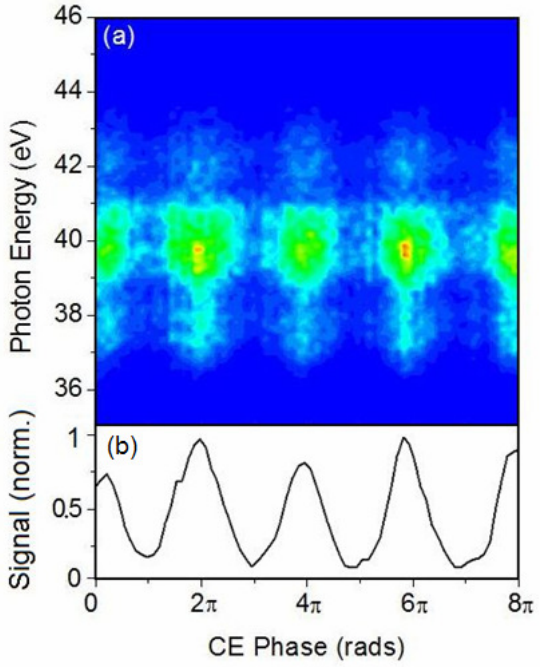

Figure 4.11 (a) CE phase scan from an argon target generated with a 25 fs pulse. (b) Integrated signal showing the modulation depth and periodicity.

The 25 fs laser pulses were next used with the GDOG setup. The first quartz plate was chosen to be ~2 mm resulting in 24 cycles of delay. For e = 0.9, the gate width was slightly less than one optical cycle. To see this effect more clearly, a CE phase scan was conducted for a photoelectron spectrum generated from the 25 fs laser pulse. Figure 4.11 (a) shows the CE phase scan results from an argon target. The 2p periodicity serves as evidence of the success of the gating method. The spectrum integrated along the energy axis is shown in (b). The 2π periodicity is visible and the modulation depth of the signal indicates a narrow gate width.

Since the goal of this part of the experiment was to show that attosecond pulses can be generated, special attention was paid to the quality of the streaked spectrogram. To this end, the

first turbo pump in the streak camera was turned off to purposely absorb the low order harmonics from the spectrum. This gave a narrower spectrum which supported a longer pulse duration, however the streaking is more evident which allowed a more accurate reconstruction of the temporal profile and phase. Figure 4.12 (a) shows actual unprocessed data taken with the

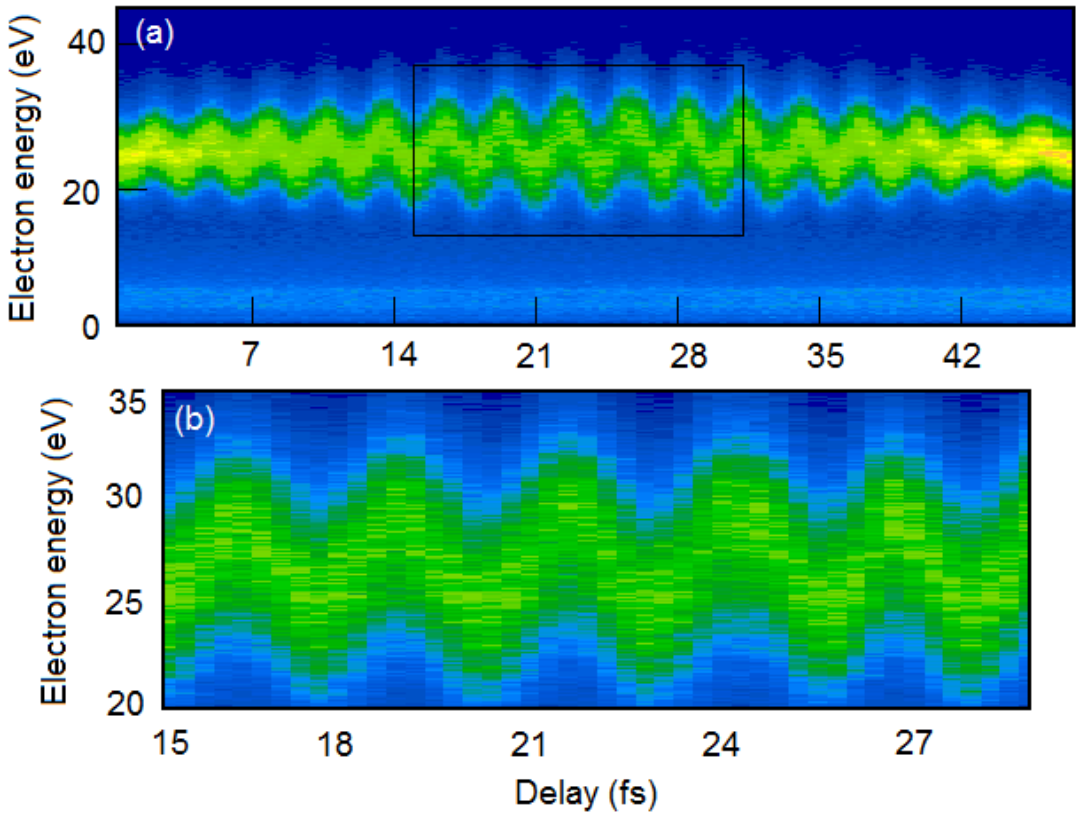

Figure 4.12 (a) Streaked spectrogram from 25 fs laser pulse (b) zoomed in portion as indicated in (a).

streak camera for attosecond pulse generation from a 25 fs laser pulse. The smaller portion in (b) is a zoomed in portion of (a) and shows that the streaking amplitude is nearly equal to the bandwidth of the spectrum. The integration time for the spectrogram was 1 min per delay slice to improve the statistics and the full spectrogram consisted of more than 120 temporal delay slices. The full temporal characterization of this pulse is shown in figure 4.13. Figures (a) and (b) show the experimental and reconstructed spectrograms, respectively. Figure (c) shows the retrieved temporal profile (solid black line) and phase (red dashed line). The pulse duration of 163 as is nearly transform limited since the phase is so flat. Also, the inset reveals that the pre

and post pulses are several orders of magnitude lower than the main peak indicating a single isolated attosecond pulse. Finally, the frequency domain representation of the reconstructed temporal profile (black line) has excellent agreement with the XUV only experimental spectrum (blue dashed line) indicating an accurate reconstruction. Again, the spectral phase is nearly perfectly flat indicating a transform limited pulse duration.

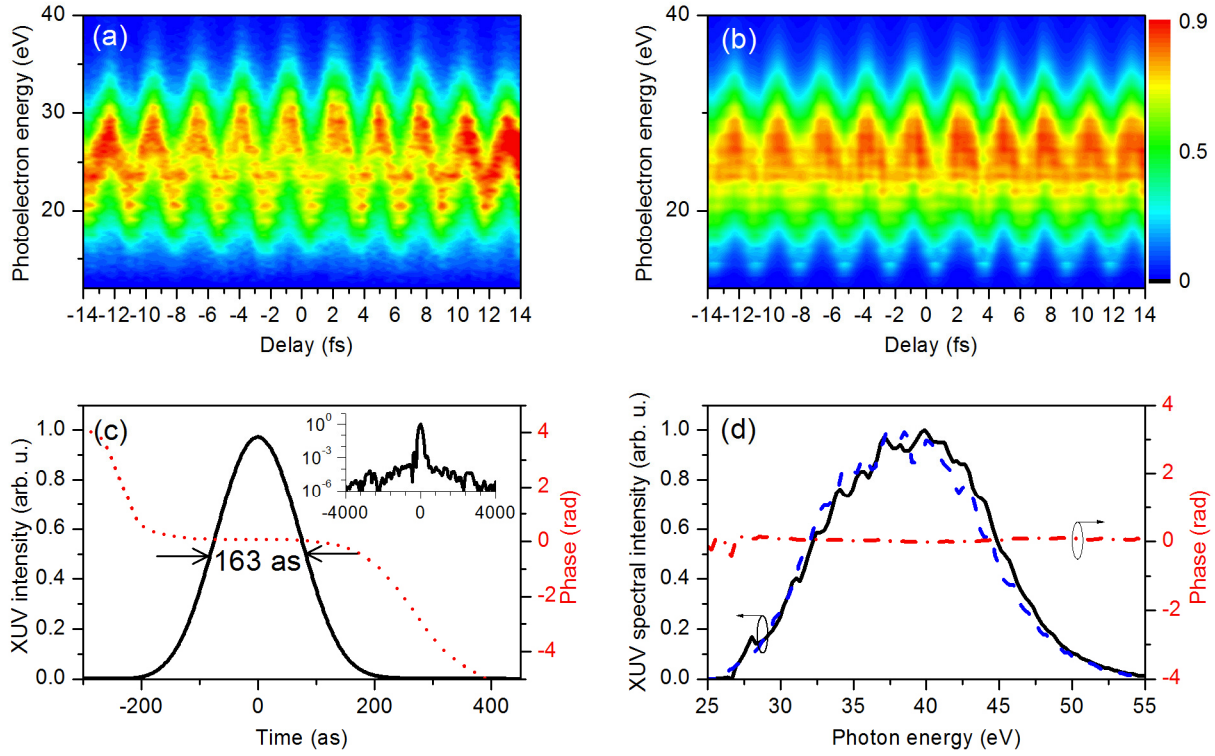

Figure 4.13 (a) Experimental and (b) retrieved streaked spectrograms from a 25 fs laser with argon as the generation gas. (c) The extracted temporal profile (black line) and phase (red dotted line). (d) The unstreaked (blue dotted line) and retrieved spectrum (black line) and phase (red line).

The result in figure 4.13 provides evidence that attosecond pulses can indeed be generated directly from an amplifier but for the sake of the experiment, the spectrogram was integrated for 1 minute per slice and consisted of over 120 slices. This means the dataset required more than 2 hours to accumulate. For daily generation of attosecond pulses this is not really acceptable. Ideally the attosecond pulse should be able to be characterized during an

experiment on a daily basis with the same effort as femtosecond FROG measurements. To accomplish this, a lower limit on how quickly the data can be accumulated and still give an accurate reconstruction was required.

It was previously found in the case of DOG [77] that the peak count of the XUV spectra is the deciding factor in whether the attosecond pulse can be reconstructed or not. To find the lower limit of the peak count number and hence the integration time necessary to accurately reconstruct an attosecond pulse, we compared reconstructions of traces with varying integration times. Since our data acquisition software saves the full photoelectron spectrum for each laser shot, we can simply extract the data accumulated in differing temporal windows. These new data sets were then individually reconstructed.

Figure 4.14(a) shows a comparison of the temporal profile for the same attosecond pulse shown in figure 4.13 but with accumulation times of 60 seconds (red solid line) and 1 second (blue solid line). Also shown are the corresponding temporal phases for the 60 s (red dashed line) and 1 s (blue dashed line) cases. The widths of both pulses are nearly identical and the temporal phases have similar shapes. An extended view of the temporal profile is shown in figure (b). Here the extended time range shows almost no contribution from pre and post pulses. The 1 s integration (blue line) has a higher noise level than the 60 s (red line) integration time due to the increased statistical noise in the 1 s integration time.

To more accurately compare the reconstructions, figure (c) shows the reconstructed XUV power spectra for the 60 s (red solid line) and 1 s (blue solid line) cases. The agreement is close. Also shown are the spectral phases for the 60 s and 1 s cases (red and blue dashed lines, respectively).

Finally, figure (d) shows the attosecond pulse duration plotted as a function of integration time. The horizontal dashed lines on the plot show ±5% of the 60 s pulse duration result (163 as). The points from 60 s to 1 s lie within this range and are considered to be accurate reconstructions. The blue square represents the 1 s integration time while the red square represents the 60 s integration time. The peak count of the 1 s integration time was ~50 which agrees with the results of other work [77]. This implies that the peak counts of the spectrum should be at least 50 to accurately reconstruct the pulse. Since the integration time can now be reduced to ~1 s per delay slice, the full spectrogram can be accumulated in just over 2 minutes.

This significantly increases the utility of the attosecond streaking method to accurately characterize the attosecond pulses.

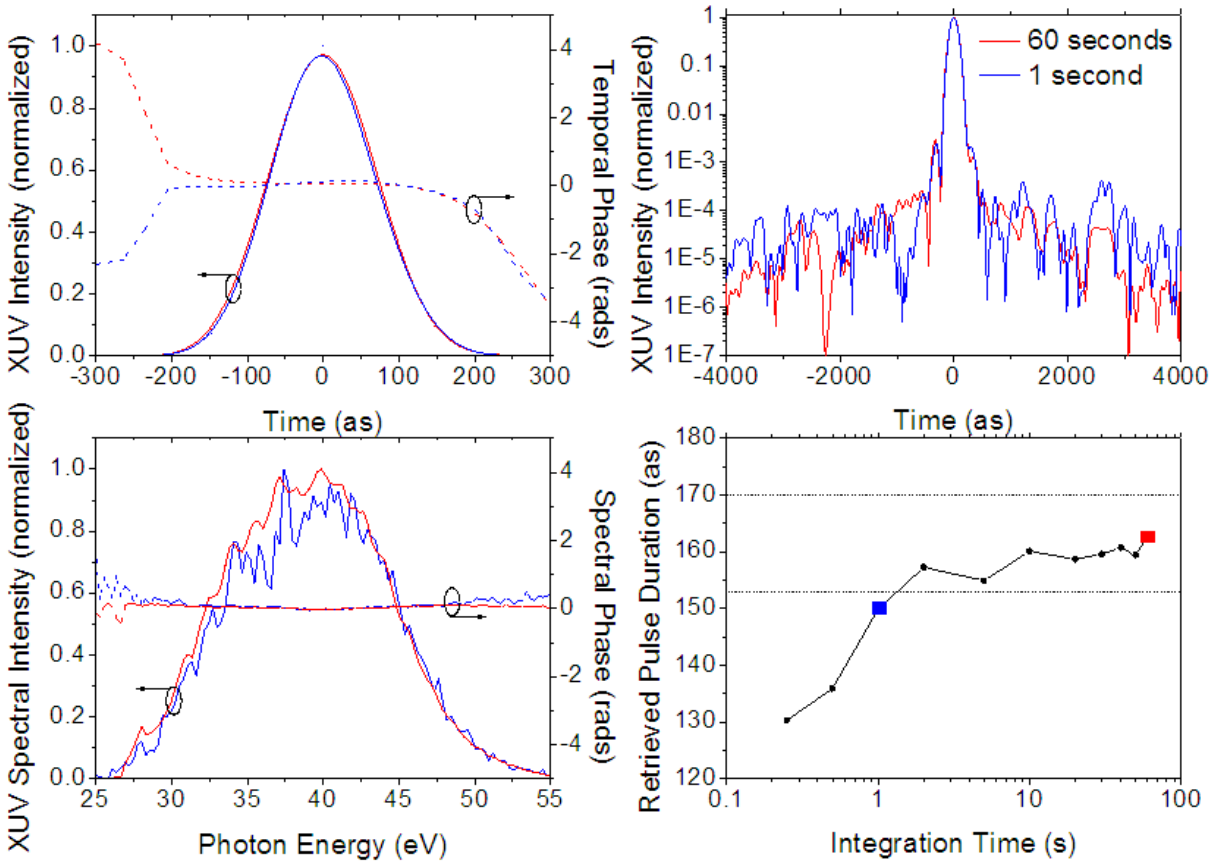

Figure 4.14 (a) Comparison of temporal profiles and phases for 60 s (red line) and 1 s (blue line) integration times. (b) Temporal profiles on an extended time scale. (c) Reconstructed spectra and phases for the pulses in (a). (d) Comparison of the retrieved pulse duration for different integration times.

The results of this section show that attosecond pulses can be generated efficiently from long (~25 fs) laser pulses. This allows any lab the option of generating attosecond pulses from a commercially available Ti:Sapphire amplifier.

4.2.2 Attosecond Pulses from Carrier Envelope Phase Unstabilized Lasers

Reducing the requirement on the generation laser pulse duration is a big step in making attosecond technology available to many more labs. However a second, and perhaps more difficult, requirement on the generating laser is CE phase stability. As shown by the CE phase scans throughout this thesis, the spectrum of an attosecond pulse can be significantly altered by simply changing the offset between the carrier and envelope of the generating laser. This is due to the nonlinear nature of the HHG process. To overcome this problem, choosing a gate width much less than one optical cycle can ensure only a single attosecond pulse is ever generated. This is shown in figure 4.15 [90]. For a gate width of ~1 fs, all pulses in the attosecond pulse train far

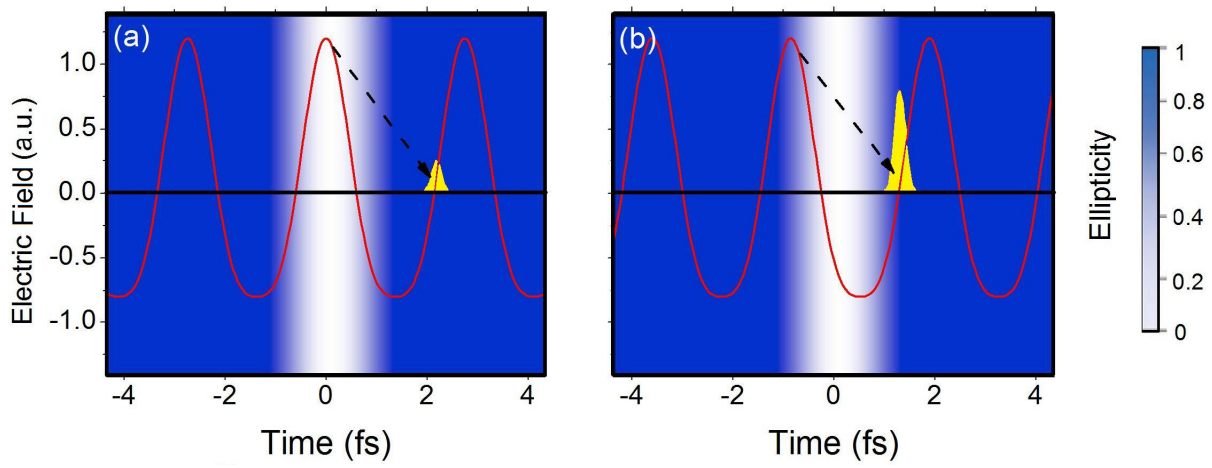

Figure 4.15 CE phase effect on an attosecond pulse when the gate width is less than one optical cycle. In (a), the CE phase is 0 and in (b) the phase is π/2.

from the gate have practically no probability of being generated. This leaves only the pulse closest to the gate for all values of CE phase. However, has is seen in the figure, for certain values of CE phase, the attosecond pulse might be born in a strongly linear portion of the pulse but recombine in an increasingly elliptical portion of the pulse (a). If however the CE phase is some other value, the pulse may spend its entire excursion distance away from the parent ion in a fairly linear portion of the pulse (b). These two cases would yield quite different HHG flux levels since the ionization, propagation, and recombination probabilities are so different. To

ensure the effect is real, a CE phase scan was experimentally conducted for attosecond pulses generated in an argon target and detected with krypton and with a gate width of ~1.5 fs. In this experiment, the laser pulse energy was 0.8 mJ after the chirp mirrors of the hollow core fiber and the pulse duration was 9 fs. The first quartz plate was 530 μm which yields 6 cycles of delay and the Brewster window was set so that ε=0.9. Figure 4.16 shows the experimental result. Clearly the modulation of the spectrum is strong with a 2π periodicity indicating the gate width is quite narrow. Also, for every value of the CE phase, the spectrum is always a continuum but with different amounts of total signal strength. This agrees with the interpretation laid out in figure 4.15. The lower plot shows the signal integrated along the energy axis. This highlights the full cycle periodicity but also demonstrates that since the modulation depth is so strong, the gate width must be less than one optical cycle.

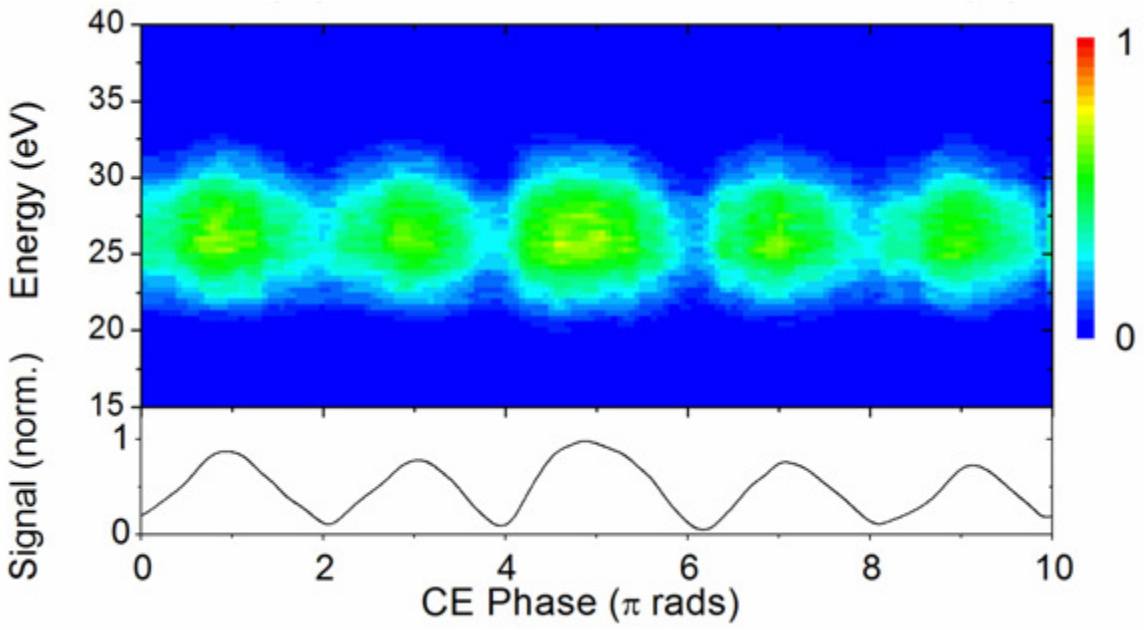

Figure 4.16 Experimental CE phase effect on an attosecond pulse when the gate width is less than one optical cycle. The upper plot shows the energy vs. CE phase and the lower plot shows the total signal integrated along the energy axis.

While the result of figure 4.16 implies that the generated pulse is always a single isolated attosecond pulse, a temporal measurement is required for unambiguous proof. In order to do this, a streaked spectrogram would be required for every value of the CE phase. This obviously

would be difficult for technical reasons, however a few values of the CE phase can be chosen and a streaked spectrogram can be generated when the CE phase is locked at each of these values. Figure 4.17 shows four streaked spectrograms generated from a 9 fs DOG pulse in argon and with krypton as the detection gas for four different values of the CE phase. All are normalized to the same value as figure (a) with the exception of (c) which is multiplied by 5.

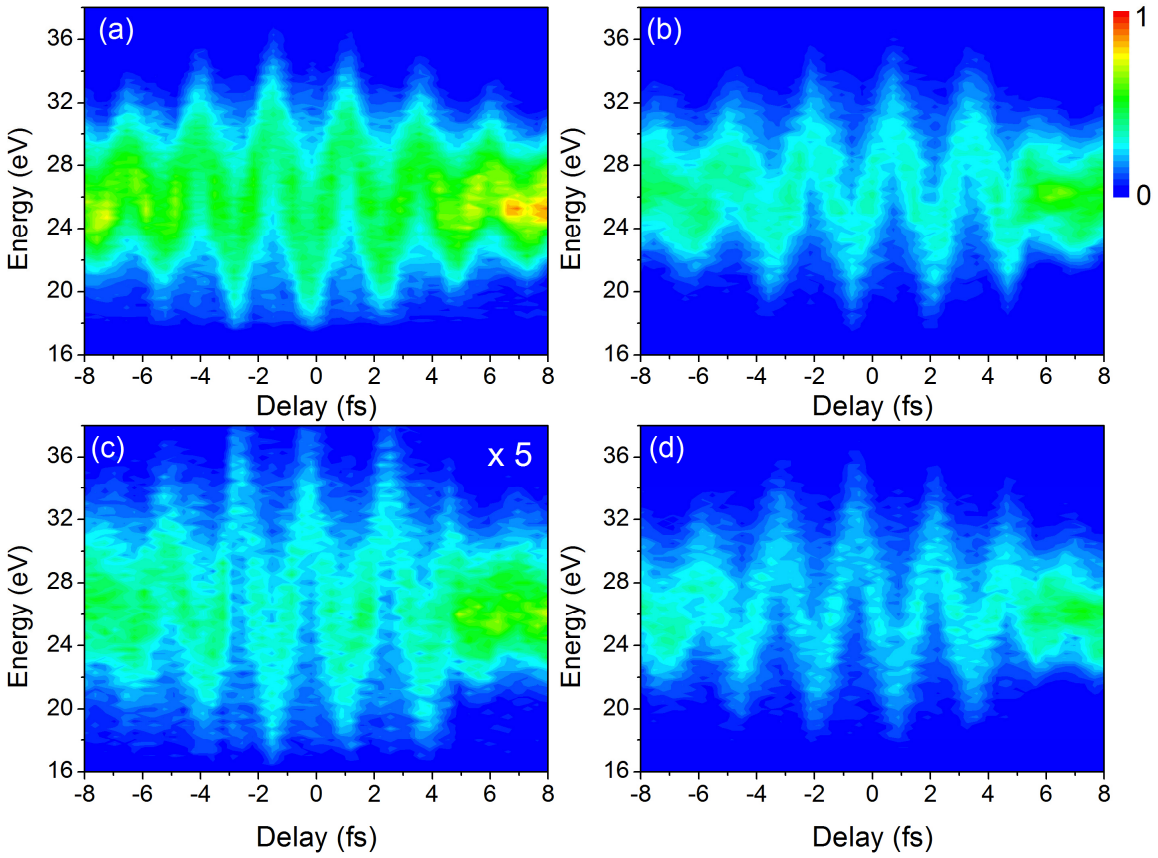

Figure 4.17 Streaked spectrograms for four different values of the input CE phase. Figure (a) is π, (b) is π/2, (c) is 0, and (d) is 3π/2.

However, the peak counts for even (c) is greater than 50 which is the requirement for reconstructing an accurate temporal profile [77]. The integration time per delay slice was the same for all spectrograms and was 18 seconds. The important features in the figure are first that each spectrogram has a significantly different peak count rate. For example, figure 4.17(c) is multiplied by 5 so that the signal is visible on the same scale as the others. This result agrees with the CE phase scan shown in figure 4.16. Secondly, the CE phase of the streaking laser can

be seen in all four plots. For example, in (a) the field points down at delay 0 while it points up at delay 0 in (c). Figures (b) and (d) show a similar effect as well. While this is the CE phase of the streaking laser and while the CE phase between the XUV and streaking arms of the streak camera interferometer are locked, this is not necessarily the CE phase of the laser pulse used to

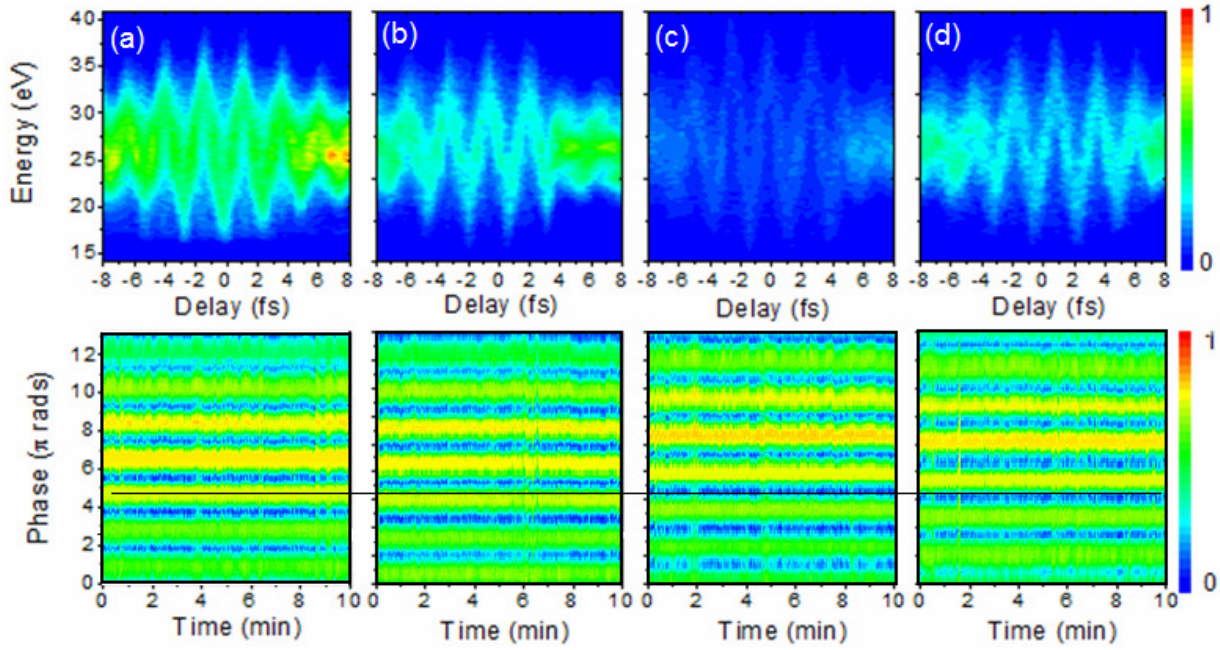

Figure 4.18 Streaked spectrograms (upper figures) and f-2f interference fringes (lower figures) for four different values of the input CE phase. Figure (a) is π, (b) is π/2, (c) is 0, and (d) is 3π/2.

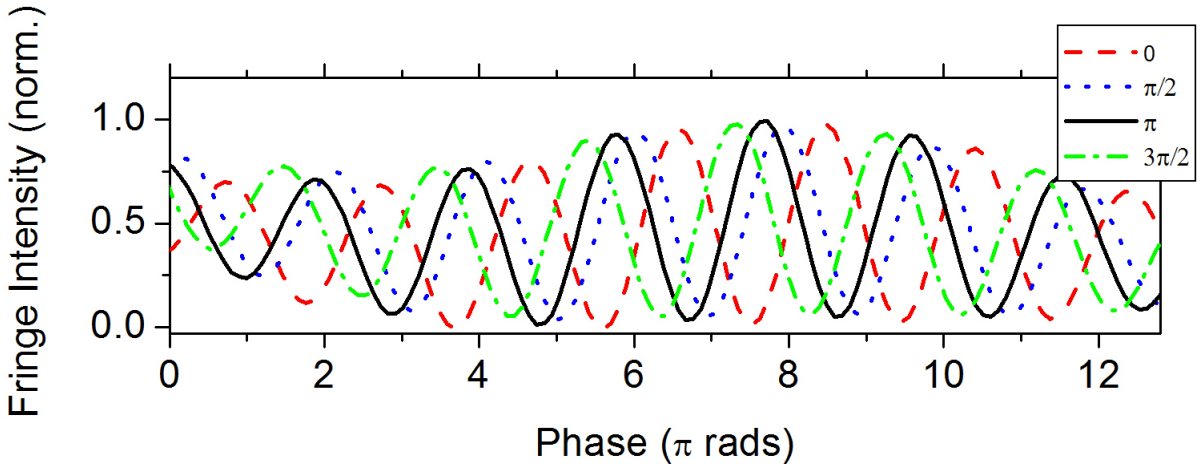

Figure 4.19 Lineout plots of the CE phase fringe patterns of the lower plots in figure 4.18.

generate the attosecond pulse. The CE phase was measured by locking the fringe pattern in the amplifier f-2f interferometer to different arbitrary values. Since the f-2f does not give the absolute phase and rather gives the relative phase instead, the values are just varied by some amount with respect to each other. Figure 4.18 shows the streaked spectrograms along with the corresponding CE phase fringe spectrograms extracted from the interferometer and plotted as a function of time. The important feature is that the patterns are shifted by an obvious amount with respect to each other. The horizontal line is to indicate that the patterns do indeed exhibit shifts. For example, (a) and (c) show a π shift in both the spectrograms and fringe patterns. This can be seen more clearly in figure 4.19 which is a lineout plot of each of the fringe patterns. Clearly the fringe pattern shifts for each CE phase value.

As further evidence for the CE phase effect, figure 4.20 (a) shows a streaked spectrogram for the case of the CE phase being unlocked. Clearly the image shows one additional cycle as

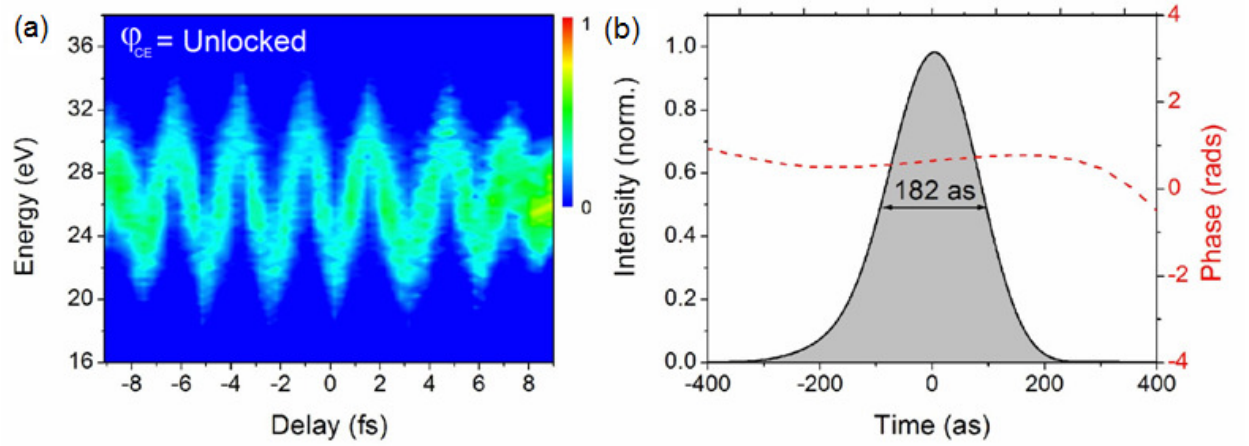

Figure 4.20 (a) streaked spectrogram from a CE phase unlocked pulse. (b) The reconstructed temporal profile (solid line) and phase (dashed line).

compared with the results of 4.18. This is because the envelope of the pulse is not locked and so it can take any value up to one more cycle. The carrier is still locked however which is why the cycle to cycle variation is still so evident. Figure 4.20(b) shows the FROG-CRAB retrieved pulse duration and phase. The result is ~180 as.

A more detailed analysis of the four spectrograms seen in figure 4.17 is presented in figure 4.21. Figure (a) shows the XUV only spectrum for each value of the CE phase. This plot

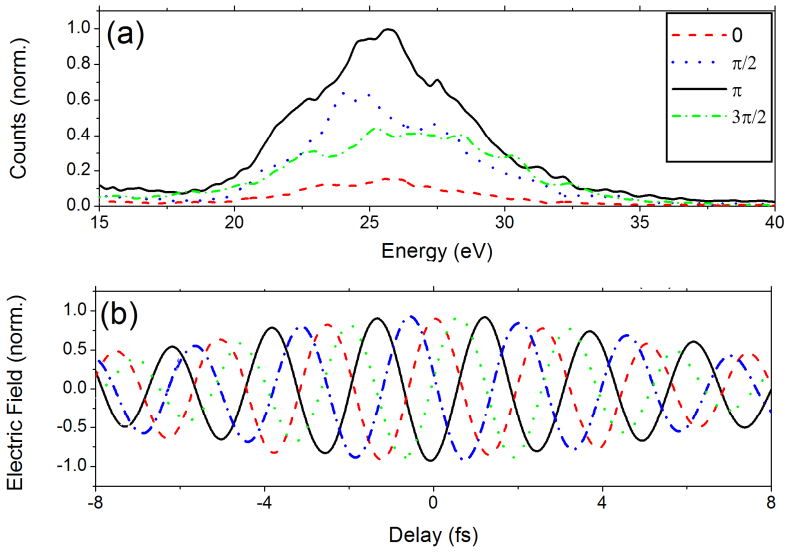

Figure 4.21 (a) The XUV only spectrum for the spectrograms in figure 4.17. (b) the electric fields of the spectrograms extracted through Fourier filtering.

shows how the count rate depends on the phase of the generating laser in agreement with the CE phase scan results. Also shown is a spectrum taken when the phase was unlocked. This is roughly the average of the other phases. Figure (b) shows the actual electric field temporal distributions for each spectrogram extracted using Fourier filtering. This shows clearly that the carrier phases within the envelope of each spectrogram are shifted with respect to each other.

Finally, the temporal profiles and phases of the attosecond pulses were extracted by reconstructing each spectrogram individually. As mentioned before, the peak counts of each were above 50 meaning the reconstruction could be expected to be accurate. Figure 4.22 shows the temporal profiles and phases for each reconstruction. Figure (a) shows the reconstructions for the phases of 0 and π and (b) shows the cases of $\pi/2$ and $3\pi/2$. All four cases exhibit pulse duration very nearly 180 as with the error within the experimental error. Also, the temporal phases show nearly identical shapes further proving the pulses are the same. This result shows that the attosecond pulse is always the same when the DOG gate width is much less than one optical cycle. The only downside to this is that the spectral intensity of each is different. This means the method can be used for linear experiments such as imaging or the phase can be tagged and sorted later. The main advantage of being able to generate attosecond pulses from

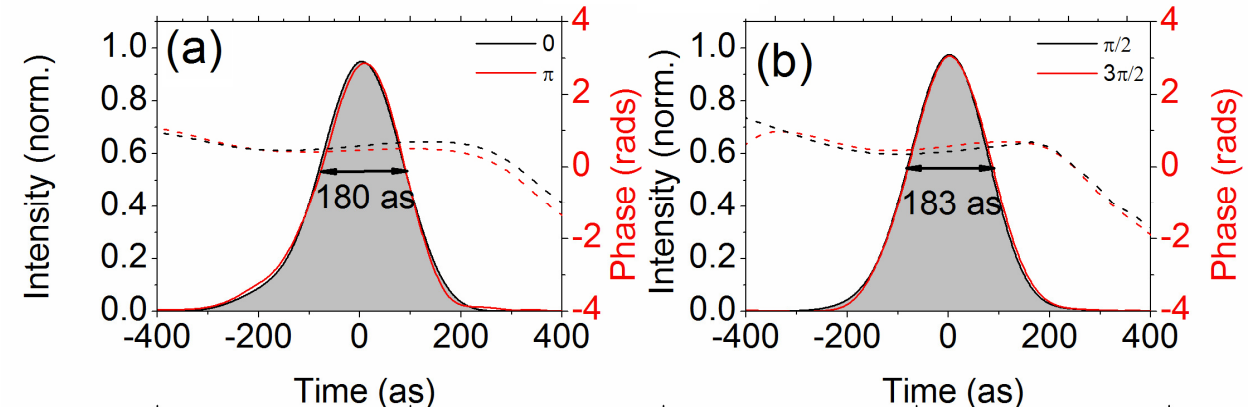

Figure 4.22 The temporal profiles for (a) 0 and π and (b) π/2 and 3π/2.

unstabilized lasers is that TW class laser systems currently have too high of power fluctuations to actually stabilize the laser system. However, since the power of the attosecond pulse can be scaled extremely high with the high input power, single shot nonlinear experiments could be conducted almost immediately with such a system.

The ultimate test of generating attosecond from CE phase unstabilized lasers is to combine the narrow gate widths with the GDOG method. For this portion of the experiment, 23 fs laser pulses were produced from the amplifier using the same spectral shaping procedure used for the previous GDOG temporal measurements. The gate width was calculated to be slightly less than one optical cycle in this case. Figure 4.23 shows the spectrograms for two different

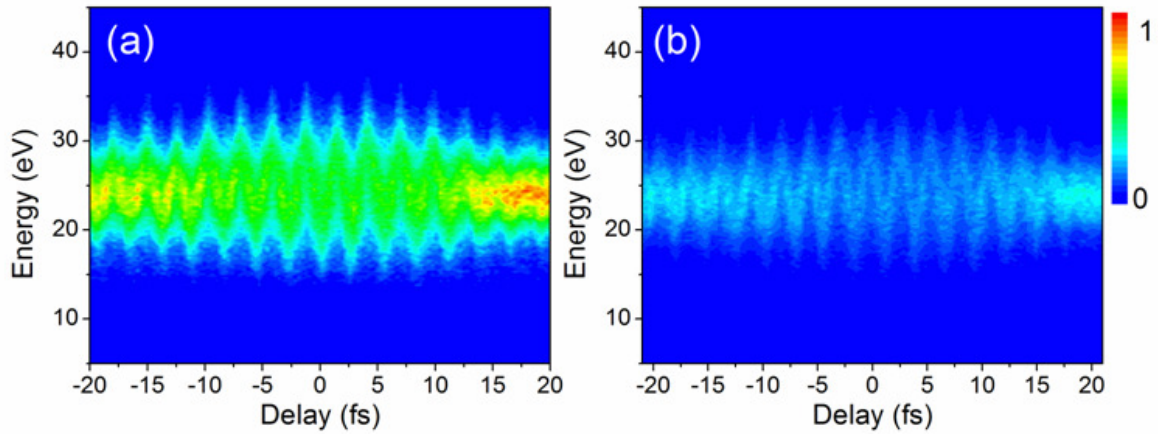

Figure 4.23 Streaked spectrograms from GDOG for CE phases of (a) π and (b) 0.

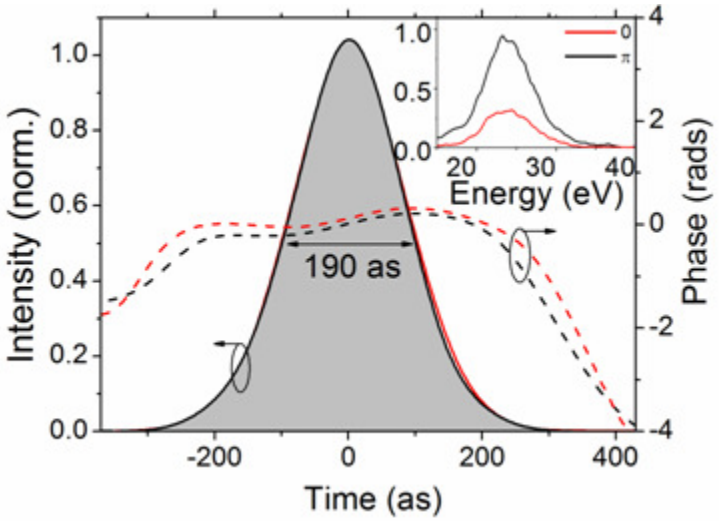

Figure 4.24 Reconstructed temporal profiles for the spectrograms in figure 4.22. The inset shows the spectrum for each case.

values of the CE phase. Figure (a) is π and figure (b) is 0. In this case, the f-2f fringes were shifted by π with respect to each other. Clearly there is a count rate reduction between the two cases. The reconstructed temporal profiles and phases are shown in figure 4.24. Both cases gave nearly identical shapes of phase and the pulse durations were ~190 as in each case. The inset of the figure shows the XUV only spectrum for each case as well. While the CE phase was shifted

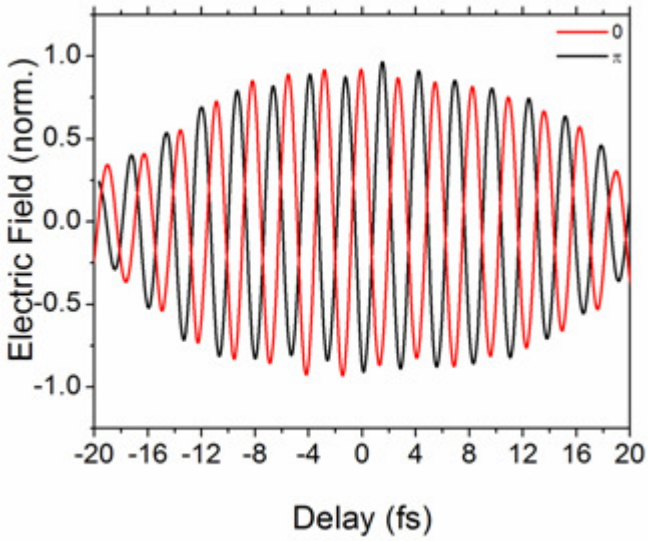

Figure 4.25 The electric fields of the spectrograms extracted through Fourier filtering.

by π, the two cases don't show the same reduction as the shorter pulse cases in figure 4.21(a). This can probably be attributed to the fact that the gate width was slightly longer in the GDOG case as in the short pulse DOG case. The extracted electric fields are shown in figure 4.25. These indicate a π shift between the two cases in agreement with the f-2f interferograms. However, since there is so much ambiguity in this result (the delay could easily be shifted by a half cycle and still look accurate), the true evidence that the effect was present is in the fact that the count rates were different when the CE phase was changed.

The results presented in this section represent a great advancement in attosecond technology. Combining narrow gate widths with the GDOG method allows attosecond pulses to be generated from nearly any Ti:Sapphire laser system that has pulse durations below ~30 fs. This opens the possibility of generating extremely high power attosecond pulses directly from a TW class laser system which can then be used for nonlinear atomic physics experiments with attosecond precision.

4.3 High Energy Attosecond Pulses

Previously it was shown that the DOG technique can generate attosecond pulses with ~6.5 nJ of pulse energy [60]. While this is high, it is just at the threshold for conducting nonlinear experiments. The GDOG method can be used with TW class laser systems to greatly increase the pulse energy however it would be nice to be able to do so as well with a table top Ti:Sapphire laser system. The only option left to generate a high flux pulse is to use a different gas target. Xe has been used previously to generate high flux pulse trains but never to generate a single isolated attosecond pulse. Here, evidence of a single attosecond pulse is presented. The pulse energy is still not totally measured but it is expected that the result will yield the highest single attosecond pulses energy yet measured.

To conduct the experiment, 9 fs laser pulses were used with DOG and focused to a xenon gas target. Xe was chosen as the generating medium and krypton as the detection gas. Due to the lower ionization potential of Xe (~13 eV) as compared with Ar, the depletion of the target is larger and the XUV spectrum is shifted to lower energy. Since the streaking shift is proportional to the square root of the central energy, choosing Kr as the detection gas will shift the spectrum to higher energy and yield a slightly more obvious streaked spectrogram. Since the count rate is so strong using xenon as a target, the integration time per delay slice was only ~10 seconds.

Figure 4.26 shows a streaked spectrogram from a Xe generation target. While the streaking effect is noticeable, the lowest orders exhibit almost no effect at all. The reconstructed pulse

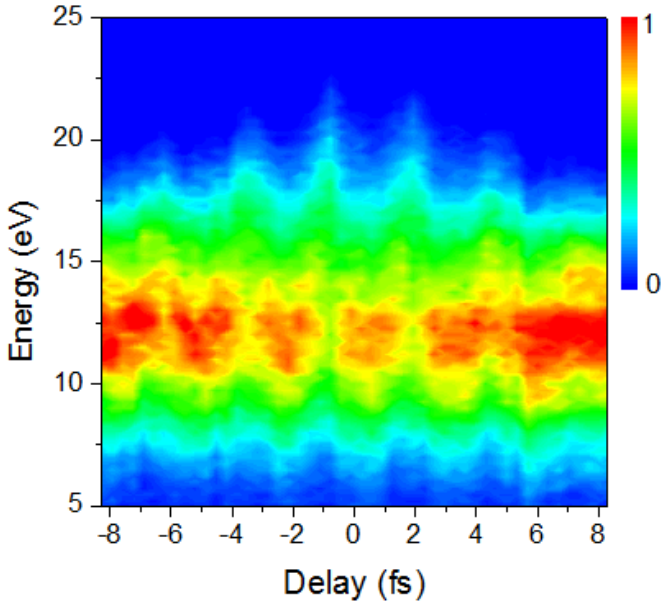

Figure 4.26 A streaked spectrogram from a xenon target with krypton as the detection gas.

duration, using the FROG-CRAB method, was ~250 as but with very large error. This is not expected to be accurate however since the center momentum approximation is definitely not valid for such a spectrum. A new method to reconstruct the pulse durations of any attosecond pulse has been developed and is required for such a pulse. The method, dubbed PROOF (Phase retrieval by omega oscillation filtering [91]) is capable of measuring such pulses and yielded a pulse duration of 196 as. This result shows the utility of DOG coupled with attosecond streaking to generate attosecond pulses with pulse energies expected to be much higher than previous values.

The results of this section demonstrate the effectiveness of both DOG and GDOG to generate extremely high flux and broad bandwidth attosecond pulses. These pulses represent the possibility for the shortest light pulses ever created and the highest power isolated attosecond pulses. Also, since the GDOG method loosens the requirement of the pulse duration of the driving laser to the point that a second method for pulse shortening is no longer necessary, many labs will be able to generate attosecond pulses on a daily basis. Finally, since DOG and GDOG

can be used with CE phase unstabilized laser systems, an attosecond pulse can be created by every pulse generated from a commercially available femtosecond laser.

CHAPTER 5 - Applications of Attosecond Pulses

High flux attosecond pulses can now be efficiently generated under a large variety of laser conditions. However, simply possessing the pulses is not enough. The isolated attosecond pulses were next applied to actual experiments. In this section, two uses for attosecond pulses are laid out. First, using an attosecond pulse to simply characterize longer events is described through an attosecond pump/ IR probe cross correlation. This allows the full temporal and spatial properties of the femtosecond electric field to be fully mapped. Second, using the attosecond pulses to observe and control the fastest events in atomic physics, namely electron dynamics in atoms, is described. Both of these experiments are the most obvious first experiments to be conducted with attosecond pulses [71, 92].

5.1 Attosecond / Femtosecond Cross Correlations

The idea behind femtosecond SHG-FROG is that a laser pulse is first split into a pulse replica and the two pulses combine in a nonlinear medium with one pulse used to "gate" the other. The reason pulse replicas are required is that to measure a very short duration laser pulse, something even shorter is required. However, there was nothing shorter than the few cycle pulses created meaning the pulse itself was the only thing that could be used. This is no longer true with the advent of attosecond laser pulses. Now, an attosecond pulse with duration less than 10% of a single cycle of a femtosecond laser pulse can be used to temporally map the electric field distribution directly. That is, of course, the idea behind the attosecond streak camera.

5.1.1 Temporally Varying Electric Fields

Figure 5.1(a) shows a streaked spectrogram generated from an attosecond pulse produced in an argon target with krypton as the detection gas. While the attosecond pulse reconstructed to ~160 as with a flat spectral phase, the important feature in the figure is the electric field oscillation of the femtosecond multi-cycle streaking laser pulse. The attosecond pulse is able to probe every variation in the temporal distribution of the streaking laser with attosecond precision. The electric field was extracted with Fourier filtering and is shown in figure 5.1(b).

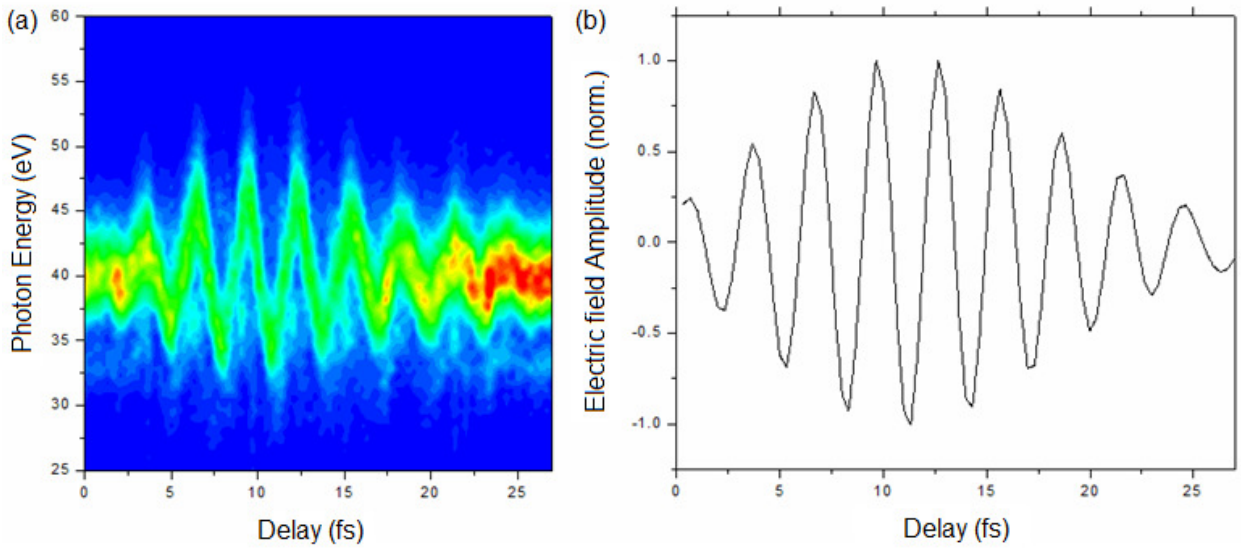

Figure 5.1 (a) A streaked spectrogram from an 8 fs laser pulse. (b) The electric field of (a) extracted through Fourier filtering of the spectrogram.

The distribution shows a Gaussian profile with the same pulse duration as what SHG FROG indicated.

An analysis of 5.1(b) is required to fully understand the temporal profile. For this, the short term Fourier transform (STFT) was used. The STFT method overcomes the ambiguities associated with simply taking Fourier transforms of non-stationary signals. Consider for example the two signals shown in figure 5.2(a) and (b). They are clearly very different in the time domain while their corresponding Fourier transforms, shown in (c) and (d) are very similar. It would be difficult to distinguish these signals with a Fourier transform alone.

The STFT gets around this problem by multiplying the time varying signal by an appropriate gate and taking the Fourier transform of the product. The result is then plotted as a function of delay between the gate and the original function. The STFT is given as [93]:

$$STFT(\tau, f) = \int [x(t)\Omega(t-\tau)]e^{i2\pi ft}\,dt \qquad (5.1)$$

where x(t) is the time varying signal, Ω is the gate function, and τ is the delay between the two functions. The gate function is chosen as a gaussian with an appropriate width. This is the limitation of the STFT. If the width is chosen wide, the energy resolution is good but the time

resolution is poor. Conversely, if the width is narrow, the time resolution is good but the energy resolution is poor. This is the trade off for this method.

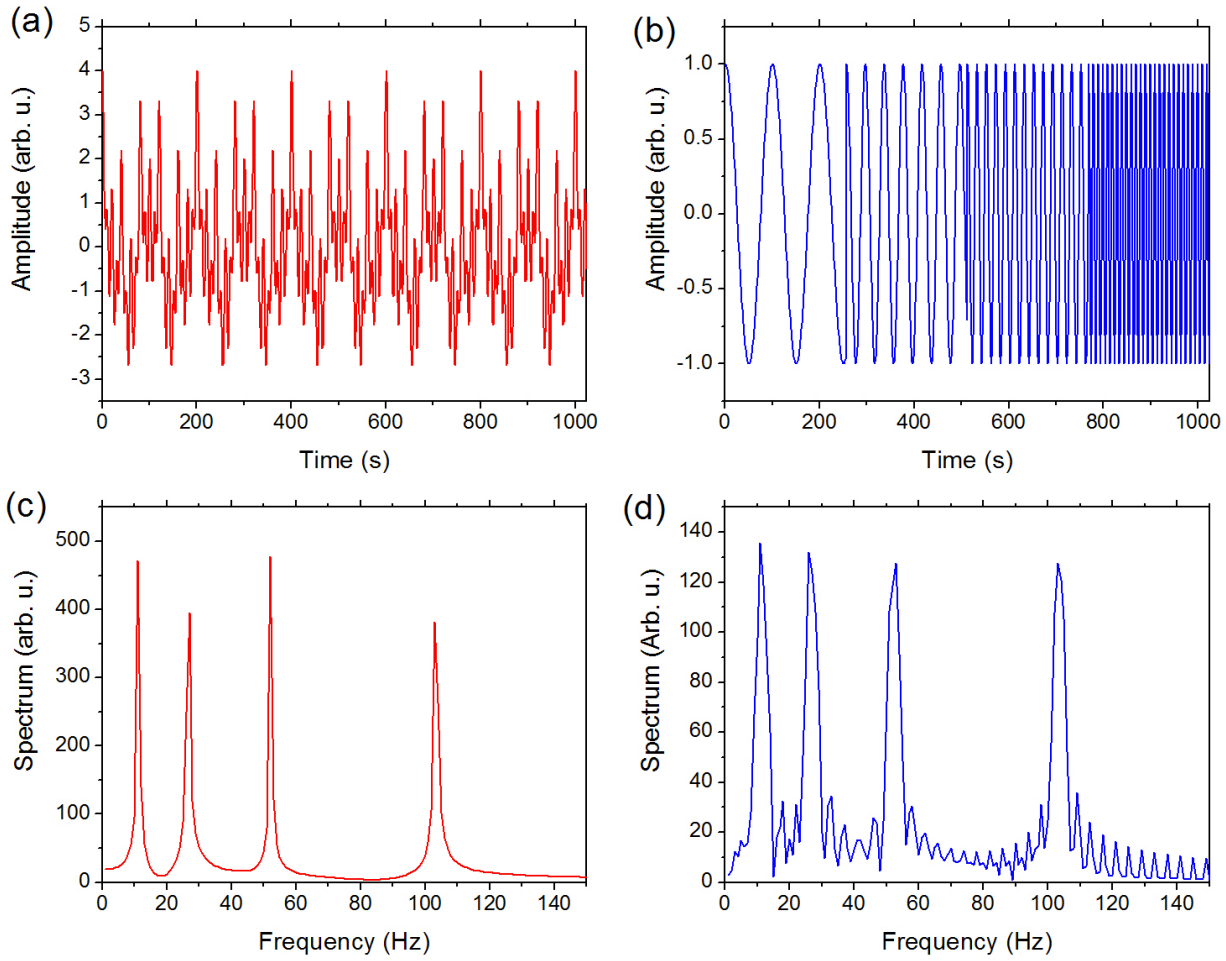

Figure 5.2 (a) and (b) two non-stationary signals made up of 10, 25, 50 and 100 Hz signals. (c) and (d) are the frequency domain representations of the signals in (a) and (b), respectively.

Using the STFT method for the results in graphs (a) and (b) is shown in figure 5.3. Here the difference between the two signals is more obvious. In 5.3(a), the four frequencies are present but are distributed uniformly in time. In (b), the four frequencies are still present but occur at different times.

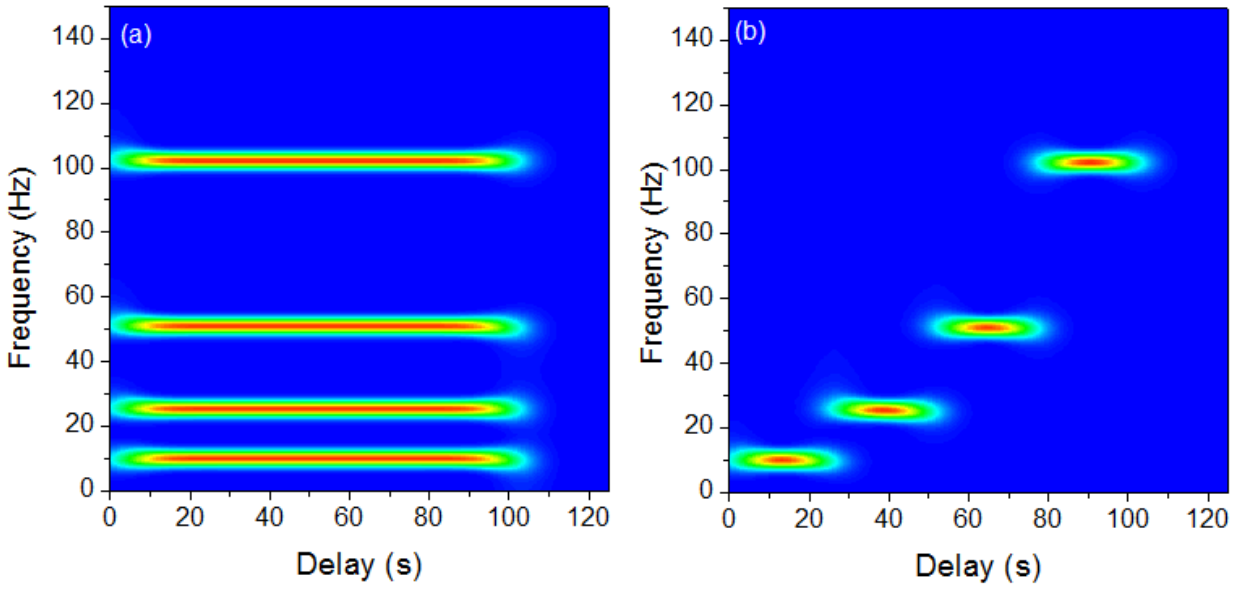

Figure 5.3 The STFT of the signals in figure 5.2 (a) and (b) respectively.

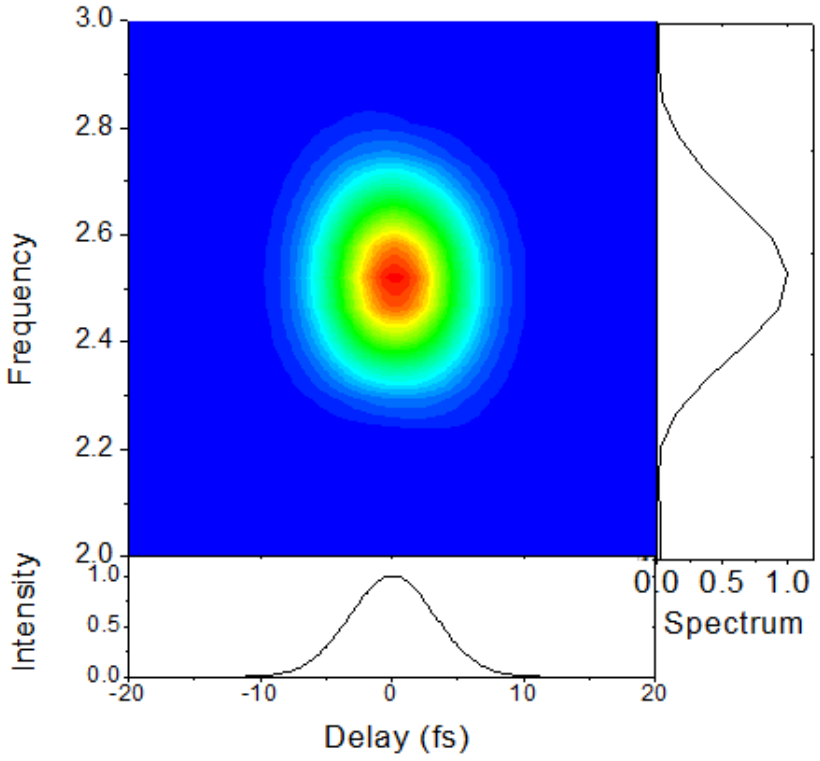

Figure 5.4 The STFT of the electric field in figure 5.1 (b).

Applying this method to the temporal electric field distribution given in figure 5.1(b) is shown in figure 5.4. The 2-D plot is the STFT and shows a symmetric Gaussian spot. The projection on the right of the figure is frequency marginal and the projection of the bottom is the time marginal. The spectrum supports an 8 fs pulse in agreement with the FROG measurement

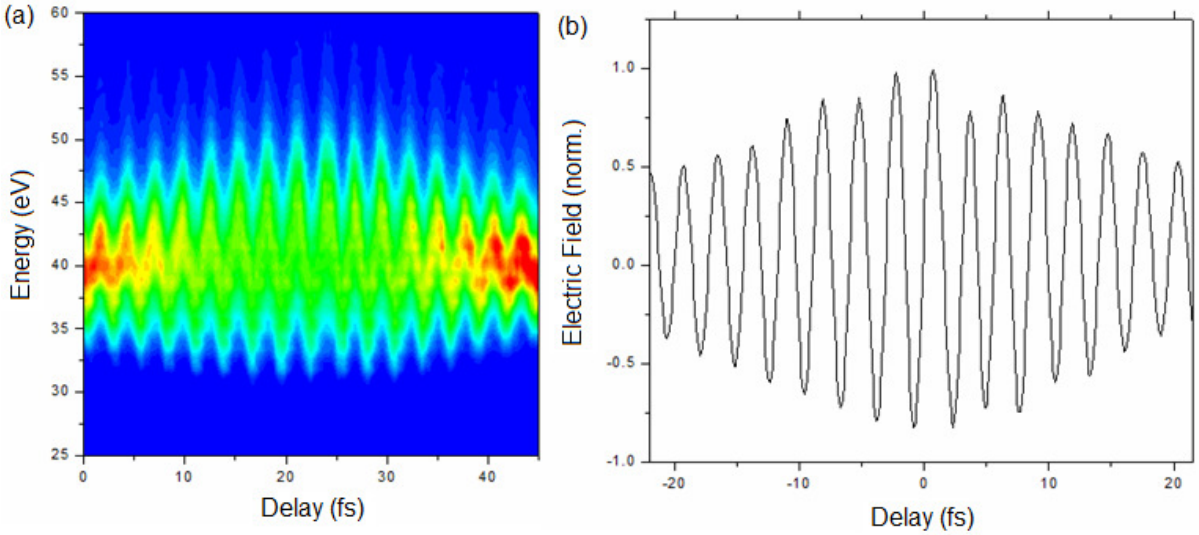

Figure 5.5 (a) A streaked spectrogram from a 25 fs laser pulse. (b) The electric field of (a) extracted through Fourier filtering of the spectrogram.

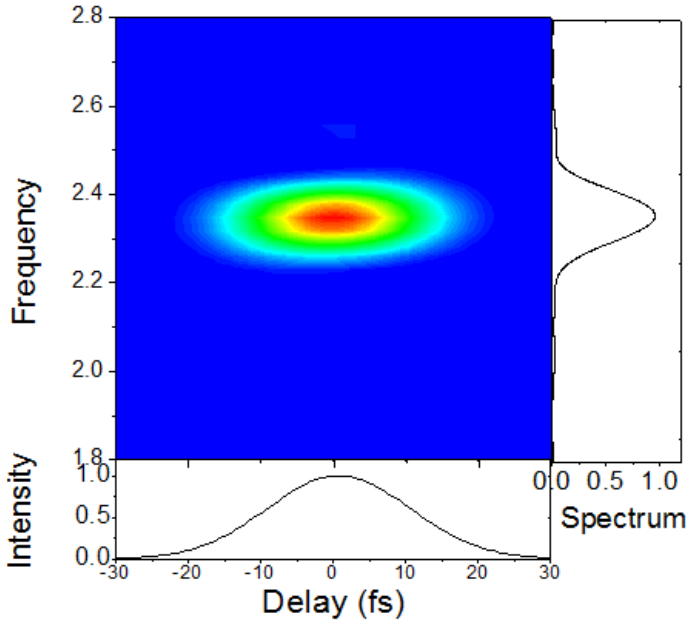

Figure 5.6 The STFT of the electric field in figure 5.5 (b).

while the time marginal also shows an 8 fs pulse duration. This result represents one option when using FROG, namely reconstructing a pulse with a short duration and a broad spectrum. An alternative is to reconstruct a pulse with a long duration but a narrow spectrum. For this, the electric field was extracted from a spectrogram generated using GDOG with 25 fs laser pulses. The result shown in figure 5.5(a) is a streaked spectrogram and the corresponding time varying electric field (b). The result clearly indicates a Gaussian temporal distribution again in agreement with SHG-FROG. The resulting STFT is shown in figure 5.6. Here the STFT image is oblong since the spectrum is narrower than the result in 5.4 while the duration is longer. The time marginal agrees with the result from FROG.

Both of the previous pulses can be accurately reconstructed using SHG-FROG. However, if the pulse has a very complicated phase, the result becomes more difficult with FROG. For example, if the pulse has a broad spectrum and a long duration, as in the case of a strongly chirped femtosecond pulse, FROG has trouble with the reconstruction. However, since the attosecond pulse is a direct probe of the time varying field, the total field can still be mapped. Figure 5.7(a) shows a spectrogram generated from a laser pulse chirped from an 8 fs duration to ~80 fs by adding 6 mm of fused silica to the streaking arm of the attosecond streak camera. Figure (b) shows the extracted electric field. Clearly the phase is complicated and is very long, indicative of a highly chirped pulse. The STFT result of figure 5.7 is shown in figure 5.8. The pattern is not at all symmetric like in the case of the transform limited pulses shown previously. The interesting features of this figure are first that the frequency marginal on the right of the figure has the same bandwidth as the pulse shown in figure 5.4. This makes sense since both pulses started as 8 fs pulses and should therefore contain the identical spectral components. Secondly, the time marginal indicates the pulse duration was stretched to ~80 fs in agreement with the amount of dispersive media added to the pulse. Finally, the slope of the Wigner image itself indicates some information on the phase of the pulse too. Fitting a line to the image and calculating the corresponding slope gives a result of 212 fs^2. Since fused silica has a GVD of 36 fs^2/mm, this corresponds to ~5.9 mm of fused silica. This is very close to the experimentally chosen value of 6 mm. These results show that all temporally varying electric field distributions from femtosecond laser pulses can be reconstructed.

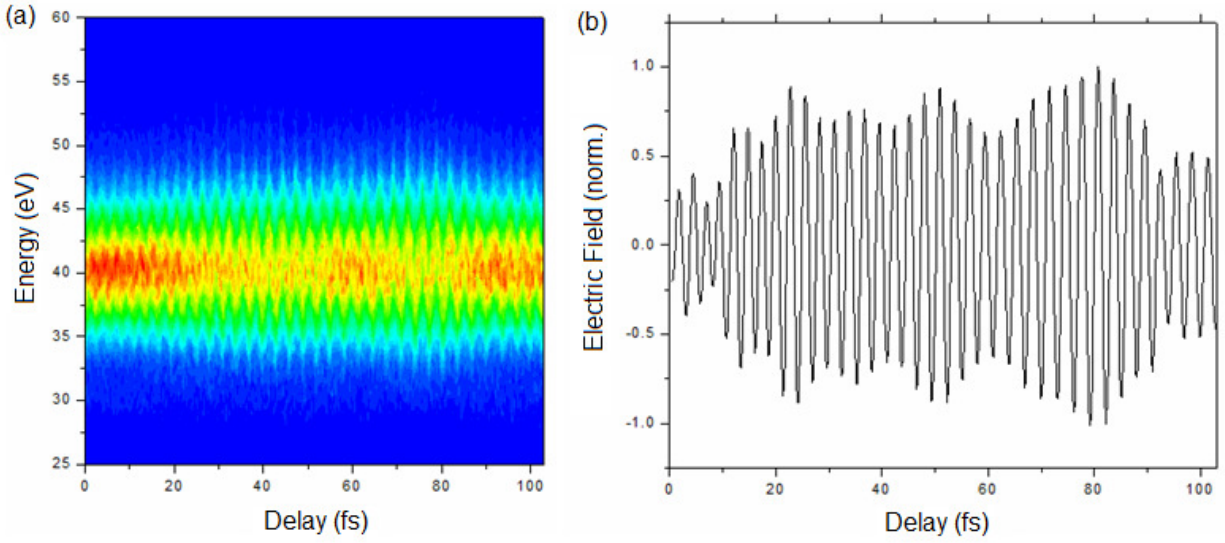

Figure 5.7 (a) A streaked spectrogram from an 8 fs laser pulse chirped to ~80 fs. (b) The electric field of (a) extracted through Fourier filtering of the spectrogram.

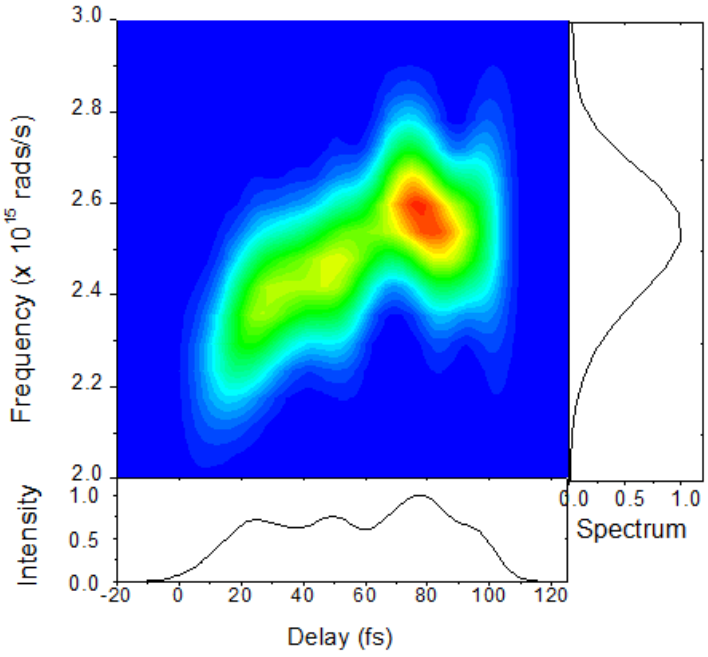

Figure 5.8 The STFT of the electric field in figure 5.7 (b).

5.1.2 Spatially Varying Electric Fields

The results of the previous section are an obvious use for attosecond pulses. A less obvious, but equally interesting use is to map spatially varying electric field distributions. As was mentioned previously in chapter 3, the streaking field in the attosecond streak camera has a Bessel-Gaussian spatial profile due to the fact that the center of the beam is truncated by the hole mirror and central XUV reflecting mirror.

The electric field of a Bessel-Gaussian beam is given by [94]:

$$E(r,z,t) = \int_a^b S(\omega) J_0(k_\rho r) \exp[i(k_z z - \omega t]d\omega \qquad (5.2)$$

where, S(ω) is the spectrum, J_0 is the zero order Bessel function of the first kind, k_ρ is the radial wave vector, k_z is the axial wave vector, *a* is the inner radius and *b* is the outer radius of the beam. A Bessel-Gaussian beam was shown in figure 3.7(a). A true Bessel beam is "nondiffracting" meaning the spatial intensity distribution does not change as the beam propagates. This is a useful property for applications such as optical tweezers [95], electron acceleration in plasma waveguides [96], and low and high order harmonic generation [97, 98]. Figure 5.9 demonstrates the non-diffracting nature of a Bessel beam. For all values of position

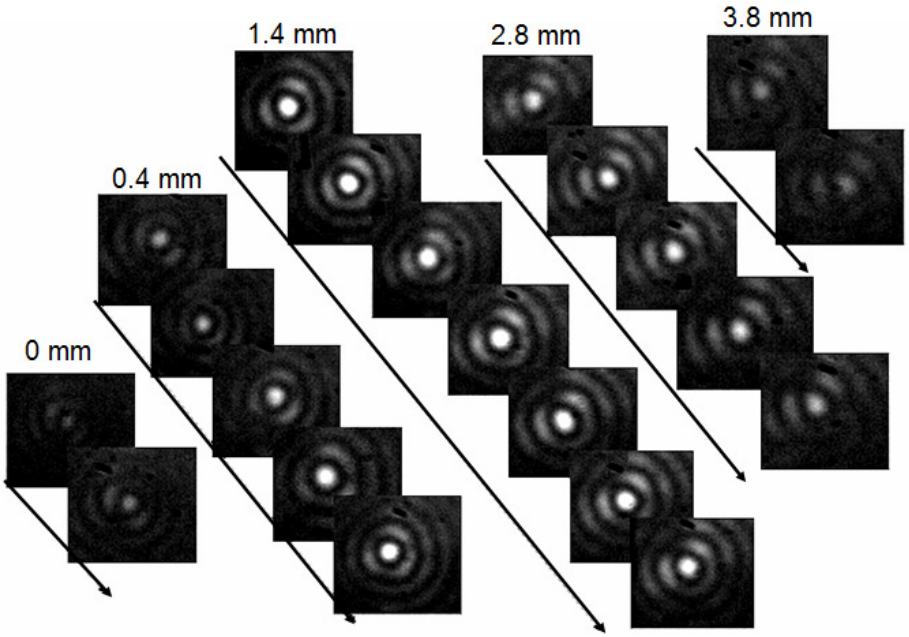

Figure 5.9 CCD images of a Bessel-Gaussian laser beam along the laser propagation direction and through the laser focus.

along the laser propagation direction, the spatial profile remains fairly constant with only the intensity reducing.

Figure 5.10 (a) shows an experimental image of a Bessel-Gaussian beam from the attosecond streak camera. The plot shown in figure (b) is a lineout through the center of the spatial profile. It is known that the electric field vector changes periodically along the transverse direction. This is expressed as the sign change of the Bessel function between adjacent rings. This change can in principle be measured indirectly with interferometric methods [99] since the reversal is equivalent to a phase shift of the light wave. For full characterization however, a direct measurement of the field is required.

There are other benefits to using a Bessel-Gaussian beam as the streaking beam in pulse measurements. Figure 5.11(a) shows a calculated plot using equation 5.2 of Bessel beams generated from different size apertures. The inner mirror in the streak camera has a radius of 9.35 mm. The outer diameter can be controlled by clipping more of the beam with an iris

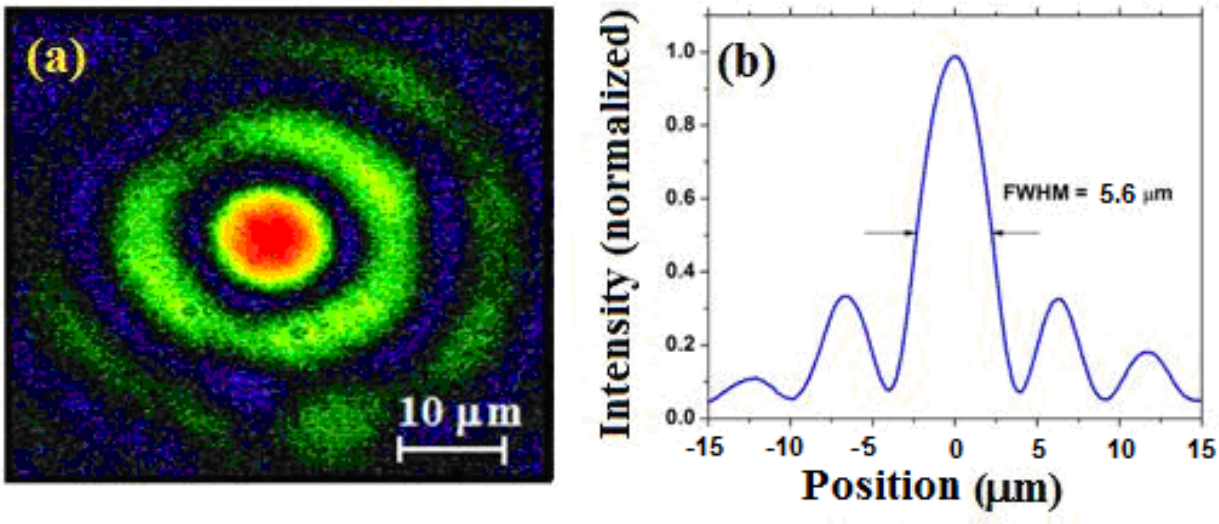

Figure 5.10 (a) Image of a Bessel-Gaussian intensity profile. (b) A lineout plot through the center of (a).

from outside the system. When the aperture is open wide, the focused spot size is smaller than when the aperture is closed. Also, the location of the first ring shifts away from the center spot as the more of the beam is clipped. All of the plots are normalized so that differences in the widths can be seen. Figure 5.11 (b) shows the plots without normalization indicating the relative

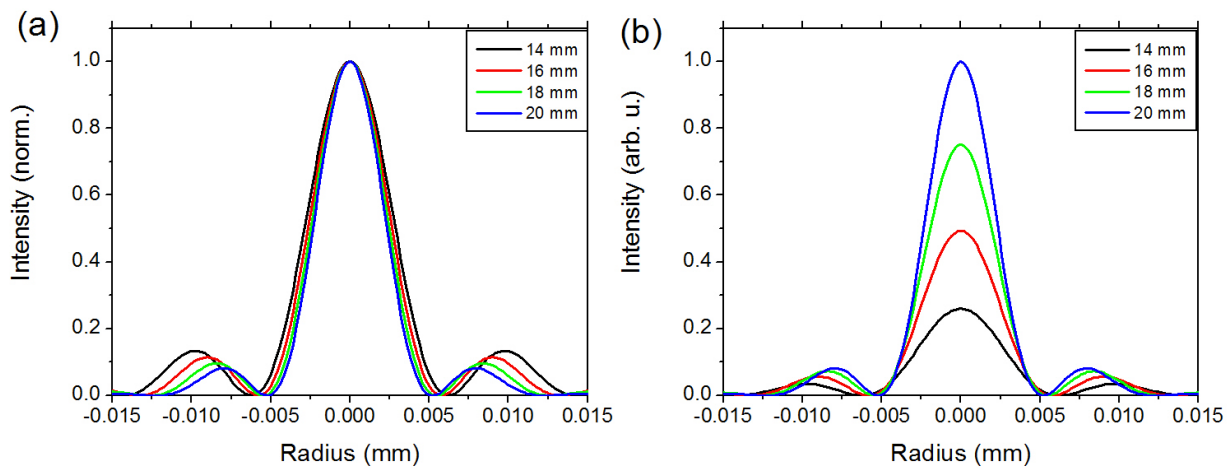

Figure 5.11 (a) Calculated profiles for different outer radii of the input beam (normalized). (b) The same plots in (a) but not normalized.

intensity of each case. Figure 5.12 (a) shows the calculated peak intensities on axis along the laser propagation direction for different aperture sizes assuming an initial spot size of 8 mm and (b) shows the corresponding experimentally obtained values. In this case, clipping the beam increases the Rayleigh range. Since a high quality streaked image requires a uniform streaking field in both the longitudinal and transverse directions, clipping the beam should yield a better result. The losses in power can be compensated by increasing the input laser power. As another benefit of clipping the beam, a longer Rayleigh range reduces the Gouy phase shift variation. Since the streaking momentum shift depends of the magnitude and sign of the field, a slower variation in the Gouy phase will also improve the streaking quality. For these reasons alone, a way to characterize the spatial profile of the focused streaking beam would be beneficial.

To find the strength of the field at every spatial point, the force exerted on a point charge must be calculated. This can be accomplished experimentally only if the point charge is placed in the field within a time interval much less than the period of the laser. Luckily the attosecond pulses already demonstrated in previous chapters have durations (~200 as) that are a small fraction of a single cycle of the streaking laser (~2.5 fs).

From Newton's second law, the time derivative of the momentum of the electron is the force. From equation 3.1, we already know how the momentum shift is related to the field

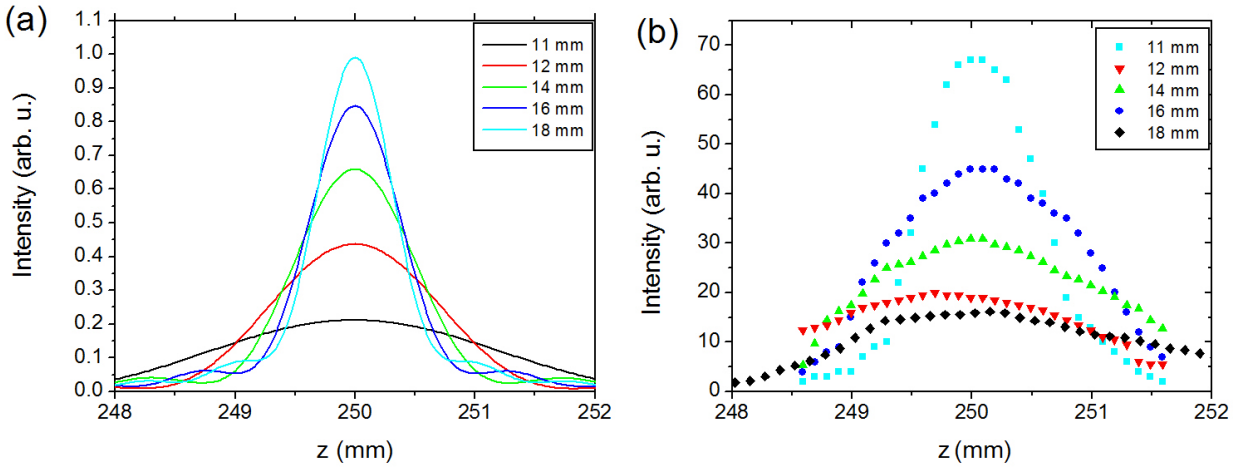

Figure 5.12 (a) Calculated on axis intensity for different outer radii of the input beam. (b) Experimental results for the same conditions as the calculation in (a).

strength. Plugging the field for a Bessel-Gaussian beam yields:

$$\Delta p = \frac{e}{m_e} E_0 J_0(k_\rho r) \int_{t0}^{\infty} E(t') \cos(\omega t') dt' \tag{5.3}$$

where m_e is the electron mass. Carrying out the integration yields:

$$\Delta p = \frac{e}{m_e \omega_0} E_0 J_0(k_\rho r) f(t) \sin(\omega_0 t) \tag{5.4}$$

with f(t) specifying the time varying envelope of the laser pulse; usually a Gaussian function. This equation can be simplified if the momentum shift is measured when f(t)sin(ωt)=1 which is the maximum value of the envelope. Experimentally this is accomplished by first finding the maximum shift in the streaked spectrogram and then locking the temporal delay at this point. Solving equation 5.4 for the spatial field yields a simple relation: $E = \Delta p \omega_0 / e$. This implies that by simply measuring the momentum shift, the field can be determined as long as pulse is at the temporal maximum.

Figure 5.13 shows spatial streaked "spectrograms" [100]. In (a), both the generation gas and detection gas were argon to yield an obvious streaking image although any gas could be used in principle. The experiment was conducted by slowly shifting the 5 axis delay stage under the lens in the streaking arm as the spectrum was recorded. Since this also introduces temporal delay into the streaking arm due to the thickness of the lens, it could only be shifted a

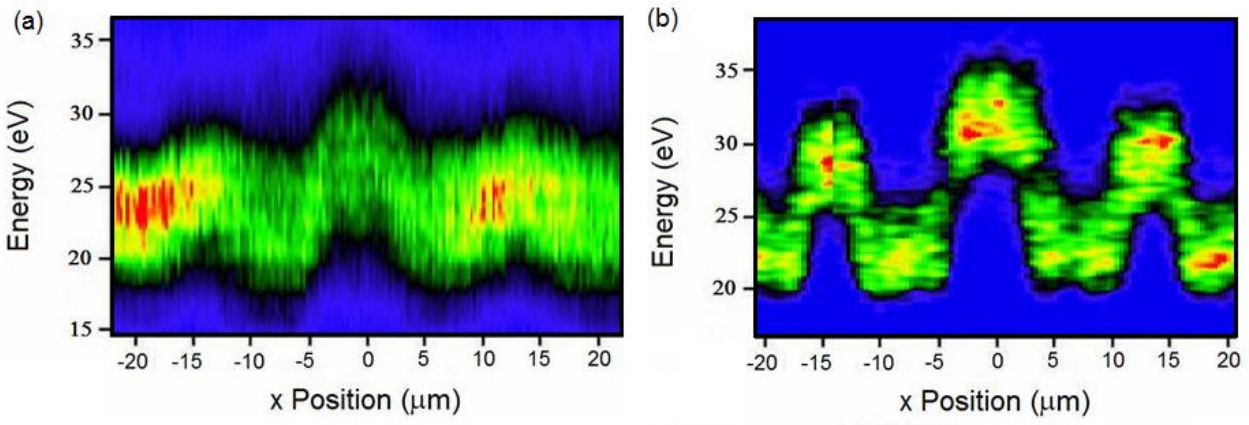

Figure 5.13 (a) Spatial streaking with argon as the detection gas and (b) krypton as the detection gas.

small amount before the interferometer became unlocked. Figure 5.13(b) shows a similar result for the case when the generation gas was argon and the detection gas was krypton. While this result shows a very obvious effect, the streak camera interferometer tripped while the data was being taken (~ -15 μm) and the image is made from two slightly different data sets. Some possible reasons for the differences between the images in (a) and (b) are that (b) may have been closer to the maximum temporal streaking or closer to the center of the spatial profile of the IR beam. In both cases, more streaking could be expected. Also, since (b) used krypton as the detection gas, the streaking will automatically be greater than in (a) but this is probably not the only reason for the differences.

A line connecting the centroid of each spatial slice is shown plotted on top of the image of figure 5.13(a) in figure 5.14(a). This clearly exhibits the Bessel structure that would be expected. Using equation 5.4, the electric field was calculated from the momentum shift at each spatial position. This is shown in figure 5.14(b) as the solid line. This method can be compared to the method used to extract the temporal field as shown in (c) and (d). This is different than the Fourier filtering used in the last chapter as this is a direct measurement of the field strength. Altogether, figure 5.14 shows the full temporal and spatial field of a femtosecond Gaussian laser pulse. Calculating the intensity from the fields in (b) and (d) are shown as the dashed lines in (b) and (d). The comparison of the spatial intensity can be compared to the plot shown in figure

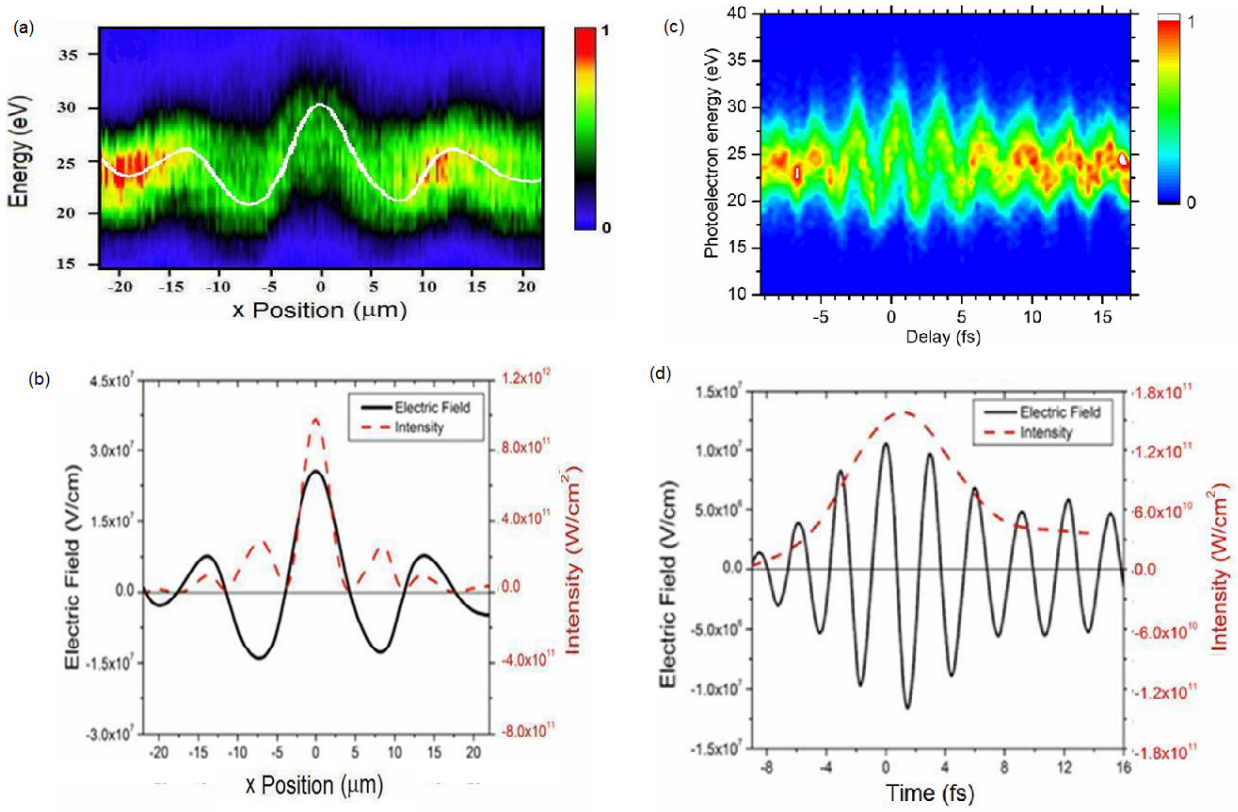

Figure 5.14 (a) Spatial image with centroid indicated (white solid line). (b) Calculated electric field (solid line) and intensity (dashed line) of (a). (c) Temporal profile of pulse used generate (a). (d) Extracted temporal electric field (solid line) and intensity envelope (dashed line).

5.10(b). The image in 5.10 is the actual profile which the spatial streaking was conducted with.

From figure 5.14, the spatial profile of the XUV spot size can also be extracted. Since the IR spot size is well known and can be measured with a CCD camera, a deconvolution of the streaked image can give the XUV spot as well. Since the IR spot was measured to be ~5 μm, the XUV was estimated to also be nearly 5 μm at FWHM. This is much larger than what a calculation would yield assuming the XUV spot is purely Gaussian. The difference is attributed to the surface quality of the Mo/Si reflecting mirror limiting the focused beam from being anywhere near diffraction limited. This shows that a spatial scan of the laser profile allows the XUV spot size to non-intrusively be measured in the experimental setup. Alternate methods for this are knife-edge scans which are difficult with purely photoelectron measurements.

5.2 Attosecond / Femtosecond Pump Probe Experiments

The main goal of using attosecond pulses is for the observation and control of the fastest dynamics in atomic physics. The cross correlations discussed previously are useful but are not the main goal for all of the work that goes into producing and characterizing attosecond pulses. There are very few experiments that have been conducted as of yet due to the difficulty associated with generating true attosecond pulses [101-104]. The rest of this chapter will be spent showing the results conducted with our attosecond pulses for the first ever temporal measurement of the lifetime of an autoionizing state in helium as well as a demonstration over the control of the dynamics of the electrons themselves. For the first experiment, helium was chosen to probe since it is the first non-trivial atom that theorists can simulate easily [105-109]. This work can, however, be extended to a large variety of targets under many conditions. This work therefore serves mainly as a demonstration of what is possible with attosecond pulses.

5.2.1 Temporal Measurements and Control of Electron Dynamics

When a helium atom in the ground state has incident upon it XUV photons with certain energy, two distinct possibilities for ionization are possible. The first is direct photoionization exactly like what is used to generate the electron replicas of the attosecond pulses used in the streak camera. Here, one electron absorbs the full photon energy and is emitted from the atom. The second and more interesting possibility is for both electrons to absorb the photon and be placed in a doubly excited state. After some lifetime, the states can "autoionize" with one electron returning to the lowest energy and the other electron liberated from the atom. Since there are two pathways to the same outcome, quantum interference can result in unique features in the energy domain (see figure 2.34). These features are seen as a series of peaks (known as the Fano resonances [110]) located at the corresponding energy of the doubly excited state [55, 111, 112]. An energy level diagram for helium is shown in figure 5.15. The ground state ($1s^2$) can absorb an XUV photon and be transferred to the doubly excited state. For the 2s2p state, the required energy is 60.1 eV in photon energy minus the ionization potential of helium (24.6 eV) which is ~35.5 eV. From the doubly excited state, autoionization occurs with the emitted electron carrying off the remaining kinetic energy of 35.5 eV. The other option is direct ionization where a 60.1 eV photon is absorbed by one electron in the ground state which carries

off the energy of the photon minus the ionization potential which is again 35.5 eV. These two pathways give the Fano resonances as seen in ref 55.

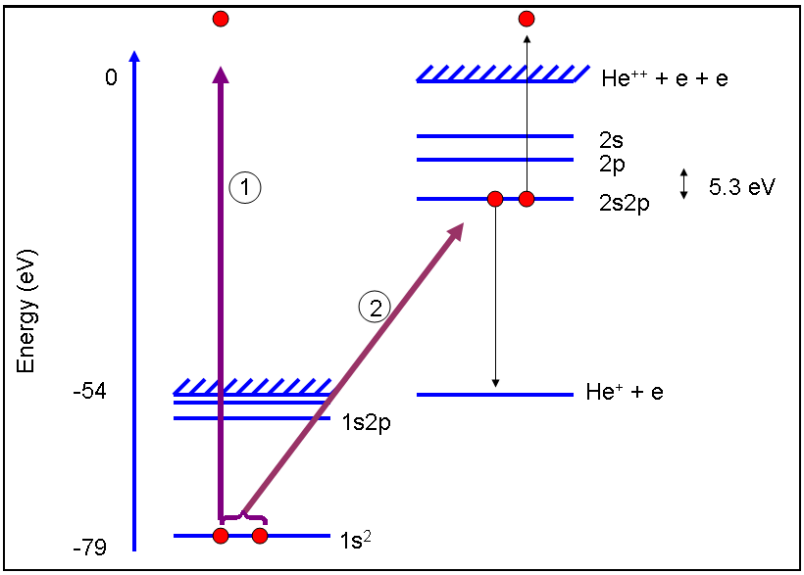

Figure 5.15 Energy level diagram for He. The purple arrows represent XUV photons. Case 1 is direct ionization while case 2 is double excitation followed by autoionization.

From strictly spectral measurements, the lifetime of the autoionization state can be estimated by measuring the width of the resonance in the frequency domain. For the 2s2p autoionization resonance, this is ~17 fs since the width of the peak is ~38 meV [105, 112]. A time domain measurement is not possible with a synchrotron however since the pulse durations are on the order of 100's of picoseconds. Luckily, attosecond pulses can easily probe doubly excited states since the lifetimes are significantly longer than the pulse durations. Figure 5.16(a) shows the physical mechanism for probing the autoionization lifetimes. First, an XUV photon of 60.1 eV populates the 2s2p doubly excited state. Then, before the state autoionizes with its 17 fs lifetime, the state is modified (or destroyed) using an intense IR laser field. Since the coupling of the direct channel with the autoionization channel determines the strength of the Fano resonance, destroying the doubly excited state before it autoionizes will reduce the height of the Fano peak in the energy domain. As the delay between the pump XUV pulse and the probe IR pulse is changed, the population of the state can be plotted thereby mapping the lifetime of the

state. When the IR laser comes first, the helium atom remains unchanged due to its high ionization potential. The XUV photon can then populate the 2s2p doubly excited state which can autoionize resulting in maximum contrast of the Fano resonance. Conversely, when the XUV photon arrives first, the doubly excited state is populated but before autoionization, the IR laser pulse arrives. From the doubly excited state, only an additional ~5.3 eV of photon energy is required to bring the atom into a ionized, excited state, namely the 2s or 2p state. This is indicated in figure 5.16(b). Ionizing such an excited state is easily accomplished with multi-photon ionization from even a moderately intense laser pulse

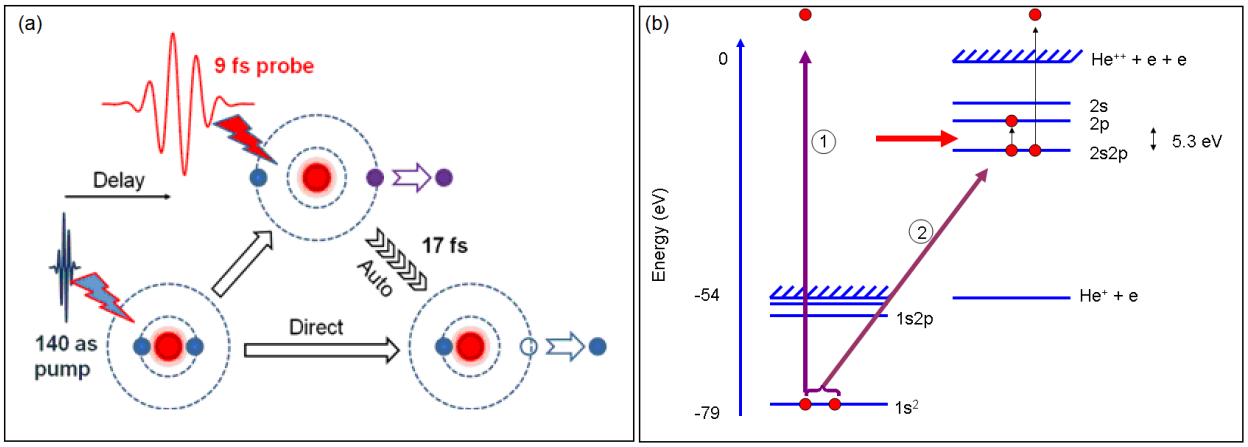

Figure 5.16 (a) Physical mechanism for probing the autoionization lifetime. (b) Energy level diagram for laser disturbed He. The purple arrows represent XUV photons and the red arrow is the IR pulse. Case 1 is direct ionization while case 2 is double excitation.

Determining whether the state can be perturbed by the IR laser field is easy to check experimentally. Figure 5.17 shows the result of the spectrum when the probing IR laser is not (a) and is (b) present. The spectrum was created with the attosecond streak camera by generating a broad continuum from a neon gas target and then letting the formed attosecond pulse impinge on helium gas in the second gas jet. The autoionization resonance is located at ~35.5 eV in (a) as indicated by the blue arrow. The peak almost totally disappears in (b) after the IR laser was added. For this result, the interferometer of the streak camera was unlocked meaning the result is an averaged effect. The result of figure 5.17 can also be used to calibrate the resolution of the

detector. With no retarding potential applied, the width of the peak was measured to be over 650 meV. Since the measured value from synchrotrons is ~38 meV, this gives the resolution of the

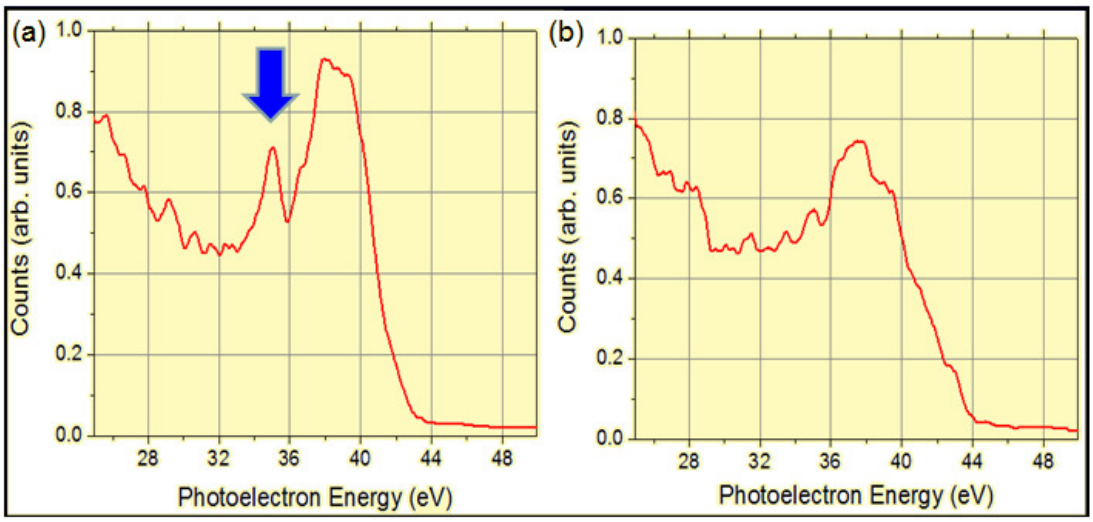

Figure 5.17 (a) Helium photoelectron spectrum. The blue arrow indicates the location of the 2s2p resonance. (b) The same spectrum after an intense IR field was added.

system at 35.5 eV. This agrees fairly closely with the results discussed in figure 3.12.

To conduct a temporal measurement, the streak camera was first locked and the attosecond pulses to be used in the experiment were measured. Neon was chosen as the detection gas for the measurements due to its flat cross section (see figure 3.1) and would therefore result in a more accurate reconstruction. Figure 5.18 shows the attosecond pulse reconstruction during the autoionization experiments. Figure (a) is the experimental spectrogram and (b) is the reconstructed image. Figure (c) shows the temporal profile (black line) and phase (red line) and again the inset shows the pulse is a true isolated pulse. Finally, (d) shows the comparison of the experimental spectrum (black line) and the retrieved spectrum (blue line) and phase (red line). This result proved that the pulse duration was ~140 as and was a single pulse and could be used as a reliable pump pulse in the rest of the experiment.

Once the quality of the attosecond pulses were verified, the detection gas was switched to helium. In order to improve the statistics of the autoionization peak, the integration time per delay slice had to be increased to 3-5 minutes. Also, to improve the resolution, a retarding

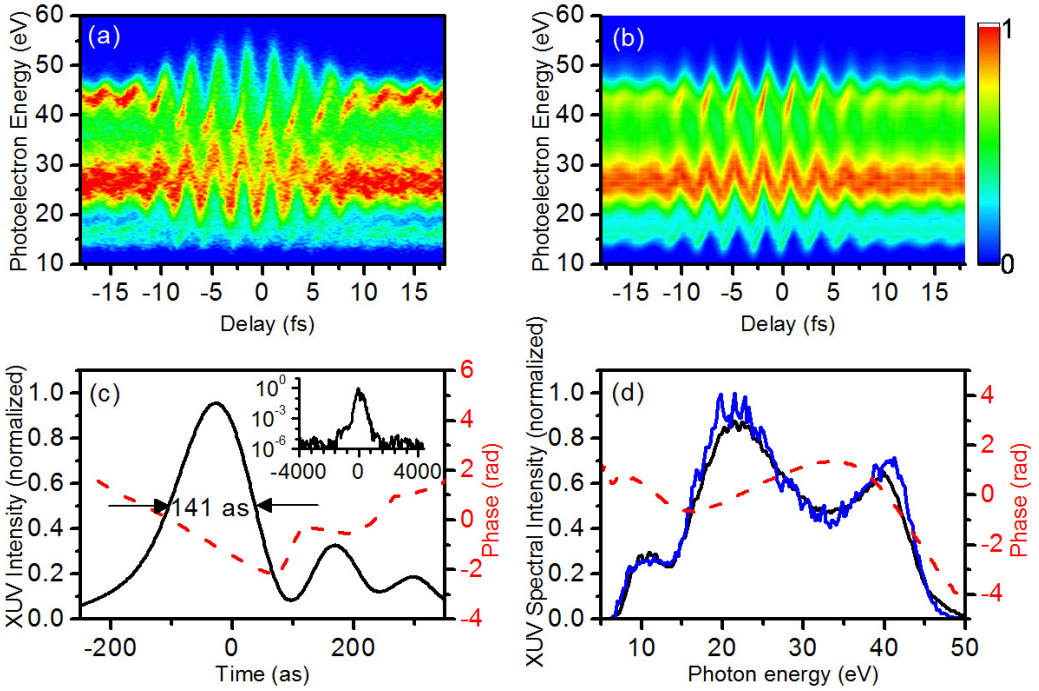

Figure 5.18 (a) Experimental and (b) retrieved streaked spectrograms from a 9 fs laser with neon as the generation gas. (c) The extracted temporal profile (black line) and phase (red dotted line). (d) The unstreaked (blue dotted line) and retrieved spectrum (black line) and phase (red line).

potential was added to shift the photoelectrons to low energy thereby increasing their time of flight. Figure 5.19(a) shows a spectrogram after the spectrum was shifted to lower energy by ~20 eV. The 2s2p autoionization peak was then at 15.5 eV. The resolution was measured to be ~300 meV. On the left side of the figure, the IR comes first and on the right side, the attosecond pulse comes first. The streaking centered around delay = 0 is evidence that the pump pulse is a true isolated attosecond pulse. The differences in the spectral shape between figure 5.18 (a) and figure 5.19 can be attributed to the different detection gas cross sections.

Some interesting features in figure 5.19 are first that the 2s2p autoionization line is clearly evident at 35.5 eV in photoelectron energy (60.1 eV photon energy). It shows a decay when the IR is most intense and then recovers as the delay is increased and the XUV comes first. Second, at ~37 eV and 34 eV, small sidebands appear when the streaking is maximized. This is

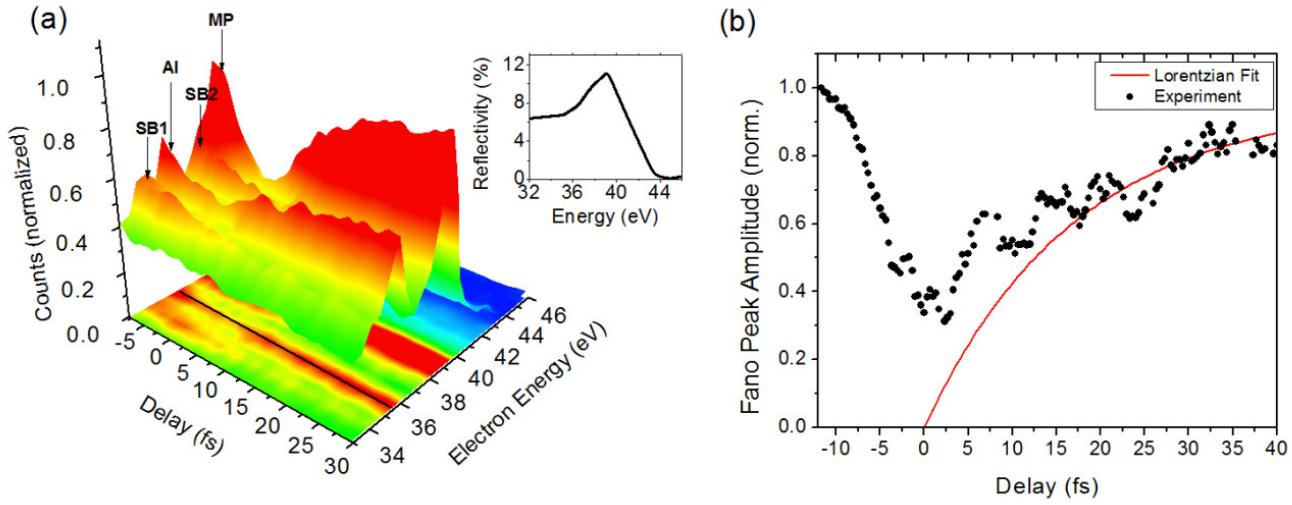

Figure 5.19 (a) Streaked spectrogram with helium as the detection gas. AI = 2s2p resonance, SB1, SB2 = sidebands, MP = mirror peak. (b) Population of the 2s2p autoionization resonance as a function of delay (data points). The red line is a Lorentzian fit added to estimate the lifetime.

attributed to free electrons being liberated from the doubly excited state before autoionization and then being given a single photon (+/- 1.5 eV) energy shift. Finally, the large signal located at ~39 eV comes from the large reflectance of the Mo/Si mirror (see inset of 5.19(a)).

A plot of the region around 35.5 eV is shown in figure 5.19(b). It is evident that as the IR laser increases, the population of the resonance quickly decreases due to depletion of the doubly excited state. Then, as the delay increases, the population eventually recovers. The red line in the plot is a fitting of a Lorentzian line. This gave a lifetime of ~17 fs which agrees well with strictly spectral estimates of the lifetime. This result is the first time domain measurement of the lifetime of the 2s2p autoionization resonance.

To better understand the experimental results, simulations were also conducted to compare with the experimental results. This work can be qualitatively described using the strong-field approximation (SFA) [113, 114]. Also, the SFA calculation was recently extended to describe the formation and decay of an isolated Fano resonance in the presence of a strong NIR laser field [106]. In this model, the XUV attosecond pulse, $E_x(t)$ simultaneously excites ground state electrons to the discrete resonance and to continuum states with momentum, p, through the dipole transition $d(p)$. The resonant state then autoionizes into the continuum with decay

amplitude given by $\frac{\Gamma}{2}(q-i)e^{-iE_r t-\Gamma t/2}$, where E_r is the resonance energy and Γ is the resonance width. The parameter q introduced by Fano [110], indicates the relative probability of excitation to the resonant state and direct photoionization to the continuum. Finally, both the direct photoionized and autoionized electrons propagate in the NIR field. In our approach, the SFA was further modified to take into account the depletion of the population of the autoionizing state by the NIR field.

The amplitude of the continuum electron on the TOF detector with momentum p as $t \to \infty$ is given in atomic units by:

$$b_L(\vec{p},\tau) = .i\int_{-\infty}^{\infty} dt \int_{t}^{\infty} dt' \vec{E}_x(t-\tau)\vec{d}[\vec{p}-\vec{A}(t)]e^{itIp}$$
$$\times\left\{a(t-t')\frac{\Gamma}{2}(q-i)\exp\left[-(iE_r+\frac{\Gamma}{2})(t'-t)\right]+i\delta(t'-t)\right\} \qquad (5.5)$$
$$\times\exp\left(-i\int_{t'}^{\infty}\frac{[\vec{p}-\vec{A}(t'')]^2}{2}dt''\right],$$

where $\vec{A}(t)$ is the vector potential of the NIR laser and τ is the delay between the XUV and NIR pulses.

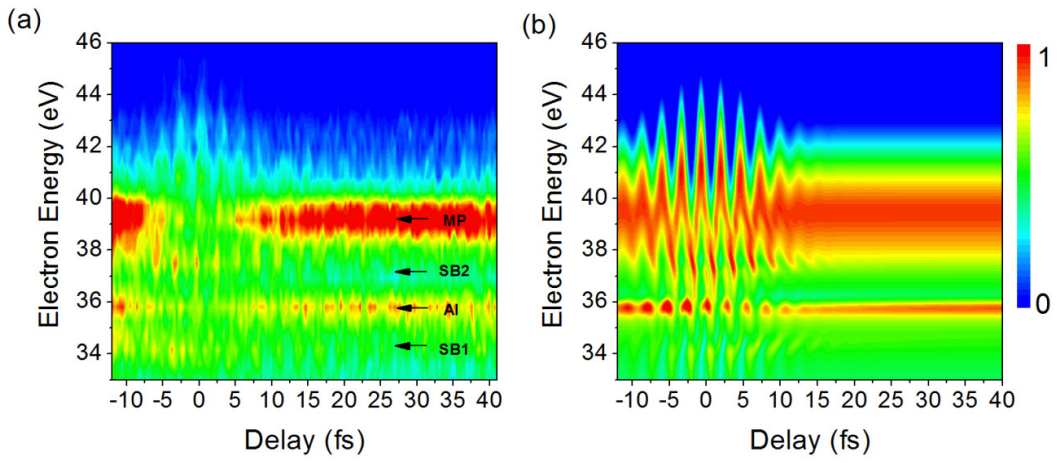

Figure 5.20 (a) Streaked spectrogram with helium as the detection gas. AI = 2s2p resonance, SB1, SB2 = sidebands, MP = mirror peak. (b) Simulation using SFA.

a(t-t') describes the change of the population in the 2s2p state by the NIR laser pulse. To determine the population of the doubly excited state, the PPT model for multi-photon ionization was used [115]. The ionization probability was calculated at each delay and the decay amplitude was inserted into Equation (5.5) in the middle term. The resulting spectrogram was obtained by convolution with the TOF energy resolution for a typical XUV pulse reconstructed in the presence of a NIR field 9 fs in duration and with peak intensity of 7×10^{11} W/cm^2. The actual mirror reflectivity curve (see inset of figure 5.19(a)) was used to generate the spectrum shape. Figure 5.20(b) shows the results of the simulations using this modified version of the SFA.

Figure 5.20(a) shows the experimental spectrogram which is just the projection of figure 5.19(a). It is very similar to the simulation result shown in (b). Again, the weak sideband contributions are slightly evident near 37 eV and 34 eV in the simulation. A plot of the autoionization line from the simulation is shown in figure 5.21. This exhibits a decay and eventual recovery as was seen in the experimental results. One interesting feature not present in the experimental results is the strong modulation in the population near delay 0. This is attributed to direct photoelectrons being streaked into and out of the resonance from different portions of the mirror reflectivity curve. If the mirror had a flat reflectance, the same number of photoelectrons would be streaked into and out of any particular energy for some IR laser field strength. However (as is seen in the inset of 5.19) the mirror used in the experiments has a strong peak near 39 eV. This means more photoelectrons can be streaked into the resonance when the field points one way than when it points the opposite way. This implies a method for controlling the population of the direct photoions as well as the doubly excited ions. By choosing any value of delay and laser intensity, the amount of electrons from either the doubly excited state or direct ionization state which contribute to the strength of the Fano resonance can be selected. In fact, for low delays, the Fano peak can even be increased above the field free case.

In the experimental result, the spectrogram was smoothed to accentuate the decay of the doubly excited channel. However, if we leave it unsmoothed and look near the delay =0 region where the streaking is maximum the shifting is present. Figure 5.22 shows a plot of this oscillatory behavior. The result of figure 5.22 shows the full control of the electron dynamics in the autoionization process. The oscillation shows control over the direct photoionization while

the overall decay shows control over the doubly excited channel through multi-photon ionization with the IR laser field.

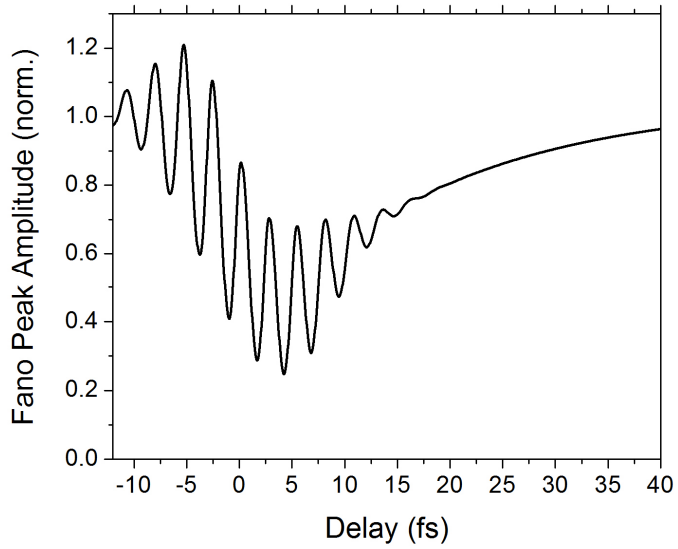

Figure 5.21 Simulated 2s2p Fano resonance population vs. delay.

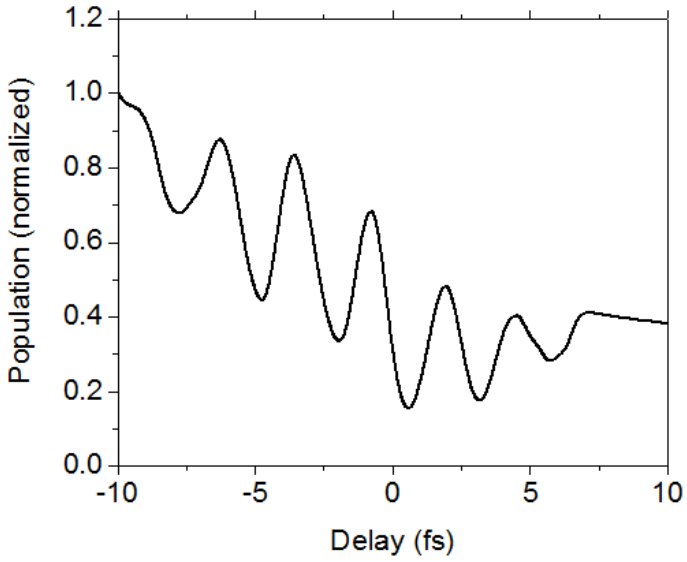

Figure 5.22 Experimental Fano population vs. delay showing control over the direct ionization channel.

Finally, the experiment was repeated for various values of IR laser intensity near the maximum streaking portion. Figure 5.23(a) shows a plot of the minimum population of the Fano resonance for different values of the streaking IR laser intensity. The error bars represent the average values from 3 different datasets. As can be seen by the trend, as the intensity increases, the minimum population decreases. This agrees with the model of depletion of the doubly excited state through multi-photon ionization. The red line indicates the corresponding populations from the PPT model. This is used simply as a test since the PPT model is not necessarily valid for doubly excited states. Like the ADK model, the target atom is assumed to be hydrogen like with a set of effective quantum numbers due to screening of the nuclear core from the ionized electron from the remaining bound electrons. This is too simple for a doubly excited state, however the results do agree well with the experimental results.

Figure 5.23 (b) shows the population as a function of delay around the maximum streaking portion for two different intensities. This shows that when the intensity is large, the modulation depth increases since we can more readily streak direct photoelectrons and the overall population is reduced since we can deplete the doubly excited state easier. Both agree with the model we developed for the electron dynamics control.

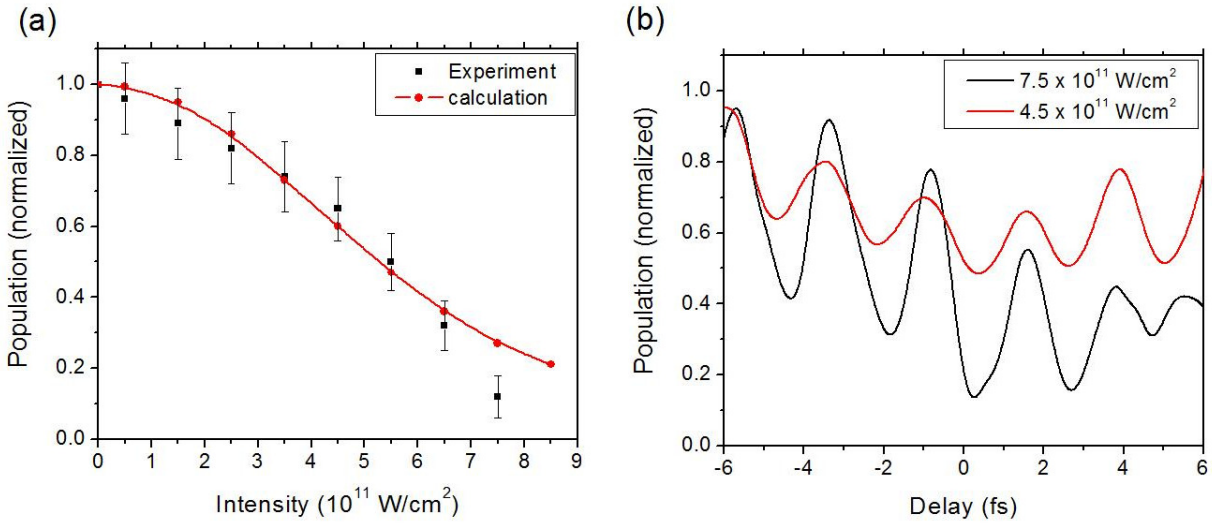

Figure 5.23 (a) Fano resonance population as a function of laser inensity for the experimental (black squares) and calculated (red circles) cases. (b) The Population vs. delay near the center of the streaking laser for two different intensities.

In conclusion, the results of this first experiment using the attosecond pulses as a pump for an atomic process and an IR laser as a probe exhibit observation and control of dynamic processes in atoms. The measurement of the autoionization lifetime of 17 fs agrees well with spectral estimates from the past. This type of experiment was possible only because the attosecond pulse is sufficiently short as compared with the lifetime of the state.

The control of the electron dynamics was demonstrated by modifying the population of the Fano resonance to any value by changing only the delay and intensity of the IR probe laser pulse. Also, the control was total since both the direct and doubly excited populations can be controlled with high accuracy. This work clearly indicates the observation and manipulation of electron dynamics with attosecond pulses and will benefit the theoretical analysis that has been waiting several years for the experimental techniques to reach the current level.

CHAPTER 6 - Conclusions and Outlook

In this work, a robust and efficient method for generating isolated attosecond pulses was developed, tested, and used in a couple of initial experiments. The DOG and GDOG methods greatly reduce the requirements on the driving laser by allowing laser pulses with multiple cycle durations to be used for the first time. The high peak intensity of DOG was used to produce spectra reaching the "water window" and supporting a single isolated attosecond pulse. These pulses have the possibility of being the first sub atomic unit of time pulses ever produced.

The GDOG method further reduces the pulse duration requirement by allowing laser pulses produced directly from an amplifier the ability to generate isolated attosecond pulses for the first time. Finally, attosecond pulses were generated from a CE phase unlocked laser for both DOG and GDOG as well. This will give any lab with the capacity to purchase and operate a commercially available laser amplifier the option to produce attosecond pulses on a daily basis. This does not mean the technologies of CE phase stability and pulse shortening (hollow core fibers, filamentation, etc.) are without use. Instead, either of these technologies will only enhance the results.

The generated pulses were confirmed using the FROG-CRAB method for attosecond pulse characterization. The pulses were measured with a highly stable interferometric attosecond streak camera. This allowed streaked spectrograms to be generated on a near daily basis under a variety of conditions. Using Xe or Ar as the generating medium allowed for high flux pulses to be produced while using Ne allowed broad spectra capable of supporting very short pulses to be produced. The shortest pulses confirmed with DOG so far are ~110 as.

The attosecond pulses were also applied to experiments. Attosecond pulses were used to map complex temporal and spatial profiles of femtosecond laser pulses. This is a direct way to characterize a femtosecond pulse since it does not rely on nonlinear processes like FROG or SPIDER. These experiments were mainly proof of principle experiments however. As a true test of the pulses, electron dynamics in helium were observed and controlled for the first time. A time domain measurement of the lifetime of autoionization in helium was conducted and the interference effect evident by Fano resonances was modified by controlling the coupling of direct photoionization and double excitation and autoionization in the helium atom.

The DOG and GDOG methods can be used for generating ever shorter XUV laser pulses. The main limitations for doing this currently are the resolution of the streak camera. Increasing the TOF tube length or improving the retarding potential are two options if the streak camera is to be used for pulse measurement. The current Mo/Si mirror bandwidth and filter transmission properties also limit the pulses that can be produced, however these are straightforward to correct. The current minimum TL pulses that can be produced are ~80 as meaning correcting the spectral phase could reduce the pulses that can already be produced to sub world record durations. This may be easy to accomplish since the DOG technique can currently generate longer cutoffs than what can be transmitted through our current filters and reflected from the mirror.

As for applications of the attosecond pulses, the helium experiment is only the first of many possibilities for study. Probing dynamics and lifetimes of excited states in the other inert gases is interesting in itself and could provide for many different experiments. Besides this, using molecular targets is the next step beyond atoms. Again, for these types of studies however, the resolution of the system will probably be the main limitation.

Publications

The following list is of papers that were published with the author of this thesis as a contributor. Those in bold pertain to the work in this thesis.

1) **"Isolated attosecond pulse generation without the need to stabilize the carrier-envelope phase of driving lasers", Steve Gilbertson, Sabih Khan, Yi Wu, Michael Chini, and Zenghu Chang, (submitted).**

2) **"Characterizing ultrabroadband attosecond lasers", Michael Chini, Steve Gilbertson, Sabih Khan, and Zenghu Chang, Opt. Exp. 18, 13006 (2010).**

3) **"Observation and control of electron dynamics in helium with attosecond precision", Steve Gilbertson, Michael Chini, Sabih Khan, Yi Wu, and Zenghu Chang, (submitted).**

4) **"Isolated attosecond pulse generation using multi-cycle pulses directly from a laser amplifier", Steve Gilbertson, Yi Wu, Sabih Khan, Michael Chini, Kun Zhao, Ximao Feng, and Zenghu Chang, Phys. Rev A 81, 043810 (2010).**

5) "Advances in carrier-envelope phase stabilization of grating-based chirped-pulse amplifiers", Eric Moon, He Wang, Steve Gilbertson, Hiroki Mashiko, Michael Chini, and Zenghu Chang, *Laser and Photonics Rev.* **4**, 160 (2010).

6) **"Calibration of electron spectrometer resolution in attosecond streak camera", Ximao feng, Steve Gilbertson, Sabih D. Khan, Michael Chini, Yi Wu, Kevin Carnes, and Zenghu Chang, *Opt. Exp.* 18, 1316 (2010).**

7) "Measurement of 1-ps soft-x-ray laser pulses from an injection-seeded plasma amplifier" Y. Wang, M. Berrill, F. Pedaci, M. M. Shakya, S. Gilbertson, Zenghu Chang, E. Granados, B. M. Luther, M. A. Larotonda, J. J. Rocca, Phys. Rev. A 79, 023810 (2009).

8) **"XUV supercontinua supporting pulse durations of sub-one atomic unit of time", Hiroki Mashiko, Steve Gilbertson, Michael Chini, Ximao Feng, Chenxia Yun, He Wang, Sabih D. Khan, Shouyuan Chen, and Zenghu Chang, *Opt. Lett.* 34, 3337 (2009).**

9) **"Delay control in attosecond pump-probe experiments", Michael Chini, Hiroki Mashiko, He Wang, Shouyuan Chen, Chenxia Yun, Shane Scott, Steve Gilbertson, Zenghu Chang, Opt. Express 17, 21459 (2009).**

10) **"Practical issues of retrieving isolated attosecond pulses" He Wang, Michael Chini, Sabih D. Khan, Shouyuan Chen, Steve Gilbertson, Ximao Feng, Hiroki Mashiko and Zenghu Chang, *J. Phys. B* 42, 134007 (2009).**

11) **"Direct measurement of electric field in femtosecond Bessel-Gaussian beams", Steve Gilbertson, Ximao Feng, Sabih Khan, Michael Chini, He Wang, Hiroki Mashiko and Zenghu Chang, , *Opt. Lett.* 34, 2390 (2009).**

12) **"Single Isolated Attosecond Pulses Generation with Double Optical Gating", Ximao Feng, Steve Gilbertson, Hiroki Mashiko, He Wang, Sabih D. Khan, Michael Chini, Yi Wu, and Zenghu Chang, book chapter in *Progress in Ultrafast Intense Laser Science*, Volume VI, Koru Yamanouchi, Andre Bandrauk, Gustav Gerber (Eds), Springer, in press (2009). (invited)**

13) **"Generation of isolated attosecond pulses with 20 to 28 femtosecond lasers", Ximao Feng, Steve Gilbertson, Hiroki Mashiko, He Wang, Sabih D. Khan, Michael Chini, Yi Wu, Kun Zhao, and Zenghu Chang, *Phys. Rev. Lett.* 103, 183901 (2009).**

14) "Generation of 0.5 mJ, few-cycle laser pulses by an adaptive phase modulator", He Wang, Yi Wu, Chengquan Li, Hiroki Mashiko, Steve Gilbertson, Zenghu Chang, Opt. Express 16, 14448 (2008).

15) "Carrier-envelope phase stabilization by controlling compressor grating separation" Chengquan Li, Hiroki Mashiko, He Wang, Eric Moon, Steve Gilbertson, and Zenghu Chang, Appl. Phys. Lett. 92, 191114 (2008).

16) **"Effects of laser pulse duration on extreme ultraviolet spectra from double optical gating", Steve Gilbertson, Hiroki Mashiko, Chengquan Li, Eric Moon, and Zenghu Chang, Appl. Phys. Lett. 93, 1 (2008).**

17) **"Optimizing the photon flux of double optical gated high-order harmonic spectra", Hiroki Mashiko, Steve Gilbertson, Chengquan Li, Eric Moon, and Zenghu Chang, *Phys Rev. A*, 77, 063423 (2008).**

18) **"A low-loss robust setup for double optical gating of high harmonic generation", Steve Gilbertson, Hiroki Mashiko, Chengquan Li, Sabih D. Khan, Mahendra M. Shakya, Eric Moon, and Zenghu Chang, *Appl. Phys. Lett.* 92, 71109 (2008).**

19) **"Double optical gating of high order-harmonic generation with carrier-envelope phase stabilized lasers", Hiroki Mashiko, Steve Gilbertson, Chengquan Li, Sabih D. Khan, Mahendra M. Shakya, Eric Moon, and Zenghu Chang, *Phys. Rev. Lett.,* 100, 10390 (2008).**

20) **"Carrier envelope phase effects on polarization gated attosecond spectra" Mahendra Man Shakya, S. Gilbertson, Hiroki Mashiko, C. Nakamura, C. Li, E. Moon, Z. Duan, Jason Tackett, Zenghu Chang Proc. SPIE Int. Soc. Opt. Eng. 6703, 67030 (2007).**

21) "Pulse duration measurements of grazing-incidence-pumped high repetition rate Ni-like Ag and Cd transient soft x-ray lasers", M. A. Larotonda, Y. Wang, M. Berrill, B. Luther, J.J.

Rocca, M. Shakya, S. Gilbertson, Zenghu Chang, *Opt. Lett.*, **31**, 3043 (2006).

This work was also published at several conferences:

Oral Presentations

1) **"Isolated attosecond pulses generated directly from a femtosecond chirped pulse amplifier", Yi Wu, Steve Gilbertson, Sabih D. Khan, Michael Chini, Kun Zhao, Ximao Feng, and Zenghu Chang, Annual meeting of the Conference on Lasers and Electro-Optics Optics (CLEO), San Jose, CA JThA1 (2010).**

2) **"Control of electron dynamics of doubly excited states from isolated attosecond pulses", Steve Gilbertson, Michael Chini, Sabih D. Khan, Yi Wu, Ximao Feng, and Zenghu Chang, Annual meeting of the Conference on Lasers and Electro-Optics Optics (CLEO), San Jose, CA JThA5 (2010).**

3) **"Temporal Characterization of Isolated Attosecond Pulse Generated with Double Optical Gating", Hiroki Mashiko, Steve Gilbertson, Ximao Feng, He Wang, sabih D. Khan, Michael Chini, Shouyuan Chen, Chenxia Yun, Yi Wu, and Zenghu Chang, Second International Conference on Attosecond Physics, Manhattan, KS, (July-Aug., 2009). (invited oral presentation)**

4) **"Probing Doubly Excited Helium with Isolated Attosecond Pulses", Steve Gilbertson, Ximao Feng, Sabih D. Khan, Michael Chini, He Wang, and Zenghu Chang, Second International Conference on Attosecond Physics, Manhattan, KS, O10 (July-Aug., 2009).**

5) **"Characterization of Isolated Attosecond Pulses from Multi-Cycle Lasers", Steve Gilbertson, Ximao Feng, Hiroki Mashiko, He Wang, Sabih D. Khan, Michael Chini, and Zenghu Chang, Annual meeting of the Conference on Lasers and Electro-Optics Optics (CLEO), Baltimore, MD, JThB3 (June, 2009).**

6) **"XUV Supercontinua Supporting Pulse Durations of Sub-One Atomic Unit of Time", Hiroki Mashiko, Steve Gilbertson, Eric Moon, and Zenghu Chang, Annual meeting of the Conference on Lasers and Electro-Optics Optics (CLEO), Baltimore, MD, JThB2 (June, 2009).**

7) "Generation of 5.1 fs, 0.5 mJ Pulses with an Adaptive Phase Modulator", He Wang, Yi Wu, Hiroki Mashiko, Chengquan Li, Steve Gilbertson, and Zenghu Chang, Annual meeting of the Conference on Lasers and Electro-Optics Optics (CLEO), Baltimore, MD, JFA1 (June, 2009).

8) "Generation of a 1 Picosecond Soft X-Ray Laser Pulses from an Injection-Seeded Plasma Amplifier", Yong Wang, Mark Berrill, Francesco Pedaci, Mahendra Man Shakya, Steve Gilbertson, Zenghu Chang, E. Granados, Brad Luther, M. A. Larontonada, Dave Alessi, and Jorge Rocca, Annual meeting of the Conference on Lasers and Electro-Optics Optics (CLEO),

Baltimore, MD, JWD5 (June, 2009).

9) **"Probing Laser Disturbed Doubly Excited States with Isolated Attosecond Pulses", Steve Gilbertson, Ximao Feng, Sabih D. Khan, Michael Chini, He Wang, Zenghu Chang, Annual meeting of the Conference on Lasers and Electro-Optics Optics (CLEO), Baltimore, MD, IPDA8 (June, 2009). (post-deadline oral presentation)**

10) **"Improving count rate of attosecond streak camera", Ximao Feng, Steve Gilbertson, Hiroki Mashiko, He Wang, Sabih D. Khan, Michael Chini, and Zenghu Chang, Annual meeting of the Division of Atomic, Molecular, and Optical Physics of the American Physical Society (DAMOP), Charletteville, VA, K6.00007 (May, 2009).**

11) **"Attosecond Streak Camera -- Generation and Characterization of Attosecond Pulses with Double Optical Gating", Ximao Feng, Sabih D. Khan, Steve Gilbertson, Hiroki Mashiko, and Zenghu Chang, Annual meeting of the Attosecond Science MURI Workshop, College Station, TX (Aug., 2008).**

12) **"Double Optical Gating of High Harmonic Generation", Hiroki Mashiko, Steve Gilbertson, Chengquan Li, Sabih Khan, Mahendra Shakya, Eric Moon, and Zenghu Chang, CTuO, *Conference on Lasers and Electro-optics*, (CLEO 2008), May 4-9, 2008, San Jose, CA. (invited oral presentation)**

13) **"Phase matching of attosecond XUV supercontinuum," Steve Gilbertson, Hiroki Mashiko, Chengquan Li, Sabih Khan, Mahendra Shakya, Eric Moon, and Zenghu Chang, *The 2008 meeting of the division of atomic, molecular, and optical physics* K6.00003 (DAMOP 2008), May 27-31 2008, State College, PA.**

14) **"Single isolated attosecond pulse generation with multiple-cycle lasers", H. Mashiko, S. Gilbertson, Chengquan Li, M. S. Khan, M. Shakya, E. Moon, and Z. Chang, Attosecond Physics, *International Workshop and Heraeus Seminar on Attosecond Physics*, August 01-05 2007, Dresden, Germany.**

15) **"Generation of Attosecond Pulses by Double Optical Gating" H. Mashiko, S. Gilbertson, C. Li, M. S. Khan, M. Shakya, E. Moon, and Z. Chang, 1st International Conference on Ultrashort Laser Interaction Sciences. ULIS 2007 Oct. 1-5, 2007, Bordeaux France.**

16) **"Attosecond Two-Slit Interference Controlled by Carrier-Envelope Phase", Mahendra M. Shakya, Steve M. Gilbertson, Hiroki Mashiko, Christopher M. Nakamura, Chengquan Li, Eric Moon, Zuoliang Duan, Jason Tackett, Zenghu Chang, JThA2, (CLEO 2007) Presented at CLEO/QELS, May 2007 in Baltimore, MD.**

17) **"Effect of Carrier Envelope Phase on Attosecond Two-Slit Interference", M. M. Shakya, S. Gilbertson, C. Li, E. Moon, C. Nakamura, J. Tackett, H. Mashiko, and Zenghu Chang, *The 2007 meeting of the division of atomic, molecular, and optical physics* N5.00003 (DAMOP 2007), June 5-9 2007, Calgary Canada.**

18) **"Single isolated attosecond pulse generation with multiple-cycle lasers" S. Gilbertson, H. Mashiko, C. Li, M. S. Khan, M. Shakya, E. Moon, and Z. Chang Max Planck Institute for the Physics of Complex Systems, ATTO 07 Aug. 1, 2007, Dresden Germany. (Hot-topic presentation)**

19) **"Effect of carrier-envelope phase on single shot XUV supercontinuum measurements," M. M. Shakya, S. Gilbertson, C. Q. Li, E. Moon, Z. Duan, J. Tackett, S. Ghimire, and Zenghu Chang, *Conference on Lasers and Electro-optics,* JTuE3,(CLEO 2006), May 21-26, 2006, Long Beach, CA. (invited oral presentation)**

20) **"Effect of carrier-envelope phase on single shot XUV supercontinuum measurements," M. M. Shakya, S. Gilbertson, C. Nakamura, C. Q. Li, E. Moon, Z. Duan, J. Tackett, S. Ghimire, and Zenghu Chang, *The 2006 meeting of the division of atomic, molecular, and optical physics* C4-8 (DAMOP 2006), May 16-20, 2006, Knoxville, TN.**

Poster Presentations

1) **"Probing Doubly Excited Helium with Isolated Attosecond Pulses", Steve Gilbertson, Ximao Feng, Sabih D. Khan, Michael Chini, He Wang, and Zenghu Chang, Second International Conference on Attosecond Physics, Manhattan, KS, S22 (July-Aug., 2009).**

2) **"Direct Determination of Spatial Electric Field variations", Steve Gilbertson, Ximao Feng, Sabih D. Khan, Michael Chini, He Wang, and Zenghu Chang, Second International Conference on Attosecond Physics, Manhattan, KS, F45 (July-Aug., 2009).**

3) **"Extending upper limit of laser pulse duration for generating single attosecond pulses", Ximao Feng, Steve Gilbertson, Hiroki Mashiko, He Wang, Sabih D. Khan, Michael Chini, and Zenghu Chang, Second International Conference on Attosecond Physics, Manhattan, KS, F01 (July-Aug., 2009).**

4) **"Strong single attosecond pulses from double optical gating" Steve Gilbertson, Hiroki Mashiko, Chengquan Li, Eric Moon, and Zenghu Chang, Poster, Multi-photon processes Gordon conference (2008), Tilton, NH.**

5) **"High energy 6 fs pulses for generating a single shot XUV supercontinuum", Shambhu Ghimire, Mahendra Shakya, Steve Gilbertson, and Zenghu Chang, International Conference on Multiphoton Processes (ICOMP 2005), Orford, QC, Canada.**

References

1. P.B. Corkum and F. Krausz, Nat. Phys. **3**, 381 (2007).
2. P. B. Corkum and Z. Chang, Optics and Photonics News **19**, 24 (2008).
3. E. Gagnon, P. Ranitovic, X. M. Tong, C. L. Cocke, M. M. Murnane, H. C. Kapteyn, and A. Sandhu, Science **317**, 1374 (2007)
4. O. Geβner, A. M. D. Lee, J. Schaffer, H. Reisler, S. Levchenko, A. I. Krylov, J. Underwood, H. Shi, A. East, D. Wardlaw, E. Chrystom, C. Hayden, and A. Stolow, Science **311**, 219 (2006).
5. M. Yamashita, K. Yamane, and R. Morita, IEEE J. Quantum Electron. **12**, 213 (2006).
6. M. Ferray, A. L'Huillier, X. Li, L. Lompre, G. Mainfray, and C. Manus, J. Phys. B. 21, L31 (1988).
7. A. L'Huiliier, L. Lompre, G. Mainfray, and C. Manus, Phys. Rev. A **27**, 5 (1983).
8. X. Li, A. L'Huillier, M. Ferray, L. Lompre, and G. Mainfray, Phys. Rev. A **39**, 11 (1989).
9. M. Bellini, C. Lynga, A. Tozzi, M. B. Gaarde, T. Hansch, A. L'Huillier, and C. Wahlstrom, Phys. Rev. Lett. **81**, 297 (1998).
10. P. B. Corkum, Phys. Rev. Lett. **71**, 1994 (1993).
11. L. V. Keldysh, Soviet Physics JETP **20**, 1307 (1965).
12. B. H. Bransden and C. J. Joachain, *Physics of Atoms and Molecules*, Pearson Education Limited, Harlow, England, (2003).
13. Z. Chang, Phys. Rev. A **71**, 1 (2005).
14. G. Sansone, E. Bendetti, J. caumes, S. Stagira, C. Vozzi, S. De Silvestri, and M. Nisoli, Phys. Rev. A **73**, 053408 (2006).

15. Y. Mairesse, A. de Bohan, L. Frasinski, H. Merdji, L. Dinu, P. Monchicourt, P. Berger, M. Kovacev, R. Taieb, B. Carre, H. Muller, P. Agostini, and P. Salieres, Science **302**, 1540 (2003).

16. M. B. Gaarde, F. Salin, E. Constant, Ph. Balcou, K. J. Schafer, K. C. Kulander, and A. L'Hiullier, Phys. Rev. A **59**, 1367 (1999).

17. N. Milosevic, A. Scrinzi, and T. Brabec, Phys. Rev. Lett **88**, 093905 (2002).

18. D. Shafir, Y. Mairesse, D. Villeneuve, P. B. Corkum, and N. Dudovich, Nat. Phys. **5**, 412 (2009).

19. O. Smirnova, Y. Mairesse, S. Patchkovskii, N. Dudovich, D. Villeneuve, P. B. Corkum, and M. Y. Ivanov, Nature **460**, 972 (2009).

20. J. Itatani, J. Levesque, D. Zeidler, H. Niikura, H. Pepin, J. Kieffer, P. B. Corkum, and D. Villeneuve, Nature **432**, 867 (2004).

21. M. M. Shakya, S. Gilbertson, H. Mashiko, C. Nakamura, C. Li, E. Moon, Z. Duan, J. Tackett, and Z. Chang, Proc. SPIE Int. Soc. Opt. Eng. **6703**, 67030 (2007).

22. B. L. Henke, E. M. Gullikson, and J. C. Davis, Atomic Data and Nuclear Data Tables **54**, 181 (1993).

23. M. V. Ammosov, N. B. Delone, and V. P. Krainov, Soviet Physics JETP **64**, 1191 (1986).

24. D. G. Lee, J. Kim, K. Hong, and C. H. Nam, Phys. Rev. Lett. 87, 243902 (2001).

25. Z. Chang, A. Rundquist, H. Wang, I. Christov, H. C. Kapteyn, and M. M. Murnane, Phys. Rev. A **58**, R30 (1998).

26. H. Eichmann, A. Egbert, S. Nolte, C. Momma, B. Wellegehausen, W. Becker, S. Long, and J. McIver, Phys. Rev. A **51**, R3414 (1995).

27. S. Watanabe, K. Kondo, Y. Nabekawa, A. Sagisaka, and Y. Kobayashi, Phys. Rev. Lett. **7**3, 2692 (1994).

28. I. J. Kim, C. Kim, H. Kim, G. Lee, J. Park, D. Cho, and C. H. Nam, Phys. Rev. Lett. **94**, 243901 (2004).

29. T. Pfeifer, L. Gallmann, M. Abel, P. Nagel, D. Neumark, and S. Leone, Phys. Rev. Lett. **97**, 163901 (2006).

30. H. Merdji, T. Auguste, W. Boutu, J. Caumes, B. Carre, T. Pfeifer, A. Jullien, D. Neumark, and S. Leone, Opt. Lett. **32**, 3134 (2007).

31. H. Mashiko, C. Nakamura, C. Li, E. Moon, H. Wang, J. Tackett, and Z. Chang, Appl. Phys. Lett. **90**, 161114 (2007).

32. Y. Oishi, M. Kaku, A. Suda, F. Kannari, and K. Midorikawa, Opt. Exp. **14**, 7230 (2006).

33. I. Sola, E. Mevel, L. Elouga, E. Constant, V. Strelkov, L. Poletto, P. Villoresi, E. Benedetti, J. Caumes, C. Vozzi, G. Sansone, and M. Nisoli, Nat. Phys. **2**, 319 (2006).

34. G. Sansone, E. Benedetti, F. Calegari, C. Vozzi, L. Avaldi, R. Flammini, L. Poletto, P. Villoresi, C. Altucci, R. Velotta, S. Stagira, S. De Silvestri, and M. Nisoli, Science **314**, 443 (2006).

35. B. Shan, S. Ghirmire, and Z. Chang, Phys. Rev. A **69**, 021404(R) (2004).

36. C. Lynga, A. L'Huillier, and C. Wahlstrom, J. Phys. B **29**, 3293 (1996).

37. P. Antoine, A. L'Huillier, M. Lewenstein, P. Salieres, and B. Carre, Phys. Rev. A **53**, 1725 (1996).

38. P. B. Corkum, N. Burnett, and M. Ivanov, Opt. Lett. **19**, 1870 (1994).

39. V. Platonenko and V. Strelkov, J. Opt. Soc. Am. B **16**, 030435 (1999).

40. O. Tcherbakoff, E. Mevel, D. Descamps, J. Plumridge, and E. Constant, Phys. Rev. A **68**, 043804 (2003).

41. Z. Chang, Phys. Rev. A **70**, 043802 (2004).

42. B. Shan, S. Ghimire, and Z. Chang, J. Mod. Opt. **52**, 277 (2005).

43. M. Kuchiev and V. Ostrovsky, Phys. Rev. A **60**, 3111 (1999).

44. CVI Melles Griot (http://www.cvimellesgriot.com/Products/Air-Spaced-Achromatic-Waveplates.aspx)

45. SNLO software (www.sandia.gov/imrl/XWEB1128/snloftp.html)

46. H. Mashiko, S. Gilbertson, C. Li, S. Khan, M. Shakya, E. Moon, and Z. Chang, Phys. Rev. Lett. **100**, 103906 (2008).

47. S. Gilbertson, H. Mashiko, C. Li, S. Khan, M. Shakya, E. Moon, and Z. Chang, Appl. Phys. Lett. **92**, 071109 (2008).

48. D. Jones, S. Diddams, J. Ranka, A. Stentz, R. Windeler, J. Hall, S. Cundiff, Science **288**, 635 (2000).

49. E. Moon, C. Li, Z. Duan, J. Tackett, K. Corwin, B. Washburn, and Z. Chang, Opt. Exp. **14**, 9758 (2006).

50. C. Li, E. Moon, and Z. Chang, Opt. Lett. **31**, 3113 (2006).

51. Z. Chang, Appl. Opt. **45**, 8350 (2006).

52. G. Paulus, F. Lindner, H. walther, A. Baltuska, E. Goulielmakis, M. Lezius, and F. Krausz, Phys. Rev. Lett. 91, 253004 (2003).

53. R. W. Boyd, *Nonlinear Optics*, Academic Press, Amsterdam (2003).

54. CVI Melles Griot Sellmeier equations: (http://www.cvimellesgriot.com/products/Documents/Catalog/Dispersion_Equations.pdf)

55. R. Madden and K. Codling, Phys. Rev. Lett. **10**, 516 (1963).

56. S. Gilbertson, Y. Wu, S. Khan, M. Chini, K. Zhao, X. Feng, and Z. Chang, Phys. Rev. A **81**, 043810 (2010).

57. E. Hecht, *Optics 4th Edition*, Addison Wesley, San Francisco (2002).

58. Zenghu Chang, Phys. Rev. A **76**, 051403(R) (2007).

59. E. Takahashi, Y. Nabekawa, and K. Midorikawa, App. Phys. Lett. **84**, 4 (2004).

60. H. Mashiko, S. Gilbertson, C. Li, E. Moon, and Z. Chang, Phys. Rev. A **77**, 063423 (2008).

61. T. Popmintchev, M. Chen, O. Cohen, M. Grisham, J. J. rocca, M. Murnane, and H. Kapteyn, Opt. Lett. **33**, 2128 (2008).

62. A. E. Siegman, *Lasers*, University Science Books, Sausalito, (1986).

63. P. Balcou, A. Dederichs, M. B. Gaarde, and A. L'Huillier, J. Phys. B **32**, 2973 (1999).

64. M. Lewenstein, P. Salieres, and A. L'Huillier, Phys. Rev. A **52**, 4747 (1995).

65. M. Lewenstein, P. Balcou, M. Y. Ivanov, A. L'Huillier, and P. B. Corkum, Phys. Rev. A **49**, 2117 (1994).

66. E. Takahashi, Y. Nabekawa, H. Mashiko, H. Hasegawa, A. Suda, and K. Midorikawa, IEEE J. Quantum Electron. **10**, 1315 (2004).

67. E. Constant, D. Garzella, P. Breger, E. Mevel, C. Dorrer, C. Le Blanc, F. salin, and P. Agostini, Phys. Rev. Lett. **82**, 1668 (1999).

68. Z. Chang, A. Rundquist, J. Zhou, M. M. Murnane, H. C. Kapteyn, X. Liu, B. Shan, J. Liu, L. Niu, M. Gong, and X. Zhang, Appl. Phys. Lett. **69**, 133 (1996).

69. M. Shakya and Z. Chang, Appl. Phys. Lett. **87**, 1 (2005).

70. M. Schelev, M. Richardson, and A. Alcock, Appl. Phys. Lett. **18**, 354 (1971).

71. E. Goulielmakis, M. Uiberacker, R. Kienberger, A. Baltuska, V. Yakovlev, A. Scrizi, T. Weserwalbesloh, U. Kleineberg, U. Heinzmann, M. Drescher, and F. Krausz, Science, **305**, 1267 (2004).

72. M. Drescher, M. Hentschel, R. Kienberger, G. Tempea, C. Spielmann, G. Reider, P. B. Corkum, and F. Krausz, Science **291**, (2001).

73. F. Parpia, W. Johnson, and V. Radojevic, Phys. Rev. A **29**, 3173 (1984).

74. Y. Mairesse and F. Quere, Phys. Rev. A **71**, 011401(R) (2005).

75. D. Kane, IEEE J. Quantum Electron. **35**, 421 (1999).

76. D. Kane and R. Trebino, IEEE J. Quantum Electron. **29**, 571 (1993).

77. H. Wang, M. Chini, S. D. Khan, S. Chen, S. Gilbertson, X. Feng, H. Mashiko, and Z. Chang, J. Phys. B. **42**, 134007 (2009).

78. X. Feng, S. Gilbertson, H. Mashiko, H. Wang, S. Khan, M. Chini, Y. Wu, K. Zhao, and Z. Chang, Phys. Rev. Lett. **103**, 183901 (2009).

79. X. Feng, S. Gilbertson, S. Khan, M. Chini, Y. Wu, K. carnes, and Z. Chang, Opt. Exp. **18**, 1316 (2010).

80. S. Ghimire, *Study on Generation of Attosecond Pulse with Polarization Gating*, PhD Thesis, Kansas State University, Manhattan, Kansas U.S.A. (2007).

81. T. Jahnke, T. Weber, T. Osipov, A. Landers, O. Jagutzki, L. Ph. H. Schmidt, C. L. Cocke, M. Prior, H. Schmidt-Bocking, R. Dorner, J. Elect. Spec. and Related Phenom. **141**, 229 (2004).

82. M. Hentschel, R. Kienberger, C. Spielmann, G. A. Reider, N. Milosevic, T. Brabec, P. Corkum, U. Heinzmann, M. Drescher, and F. Krausz, Nature **414**, 509 (2001).

83. K. Kim, K. Kang, M. Park, T. Imran, G. Umesh, and C. H. Nam, Phys. Rev. Lett. **99**, 223904 (2007).

84. Z. Chang, A. Rundquist, H. Wang, M. M. Murnane, and H. C. Kapteyn, Phys. Rev. Lett. **79**, 2967 (1997).

85. C. Spielmann, N. Burnett, S. Sartania, R. Koppitsch, M. Schnurer, C. Kan, M. Lenzner, P. Wobrauschek, and F. Krausz, Science **278**, 661 (1997).

86. B. Shan and Z. Chang, Phys. Rev. A **65**, 011804(R) (2002).

87. H. Mashiko, S. Gilbertson, M. Chini, X. Feng, C. Yun, H. Wang, S. Khan, S. Chen, and Z. Chang, Opt. Lett. **34**, 3337 (2009).

88. B. Shan, C. Wang, and Zenghu Chang, U. S. Patent No. 7,050,474, issued on May 23, (2006).

89. C. P. J. Barty, G. Korn, F. Raksi, C. Rose-Petruck, J. Squier, A.-C. Tien, K. R. Wilson, V. V. Yakovlev, and K. Yamakawa, Opt. Lett. **21**, 219 (1996).

90. S. Gilbertson, S. Khan, Y. Wu, M. Chini, and Z. Chang, (submitted).

91. M. Chini, S. Gilbertson, S. Khan, and Z. Chang, Opt. Exp. **18**, 13006 (2010).

92. M. Drescher, M. Hentschel, R. Keinberger, M. Uiberacker, V. Yakovlev, A. Scrinzi, T. Westerwalbesloh, U. Kleineberg, U. Heinzmann, and F. Krausz, Nature **419**, 803 (2002).

93. R. Polikar, *Wavelet tutorial*, (http://users.rowan.edu/~polikar/WAVELETS/WTpart1.html).

94. R. Grunwald, M. Bock, V. Kebbel, S. Huferath, U. Neumann, G. Steinmeyer, G. Stibenz, J. Neron, and M. Piche, Opt. Exp. **16**, 1077 (2008).

95. J. Arlt, V. Garces-Chavez, W. Sibbett, and K. Dholakia, Opt. Commun. **197**, 239 (2001).

96. C. G. Durfee, J. Lynch, and H. M. Milchberg, Phys. Rev. E **51**, 2368 (1995).

97. C. Altucci, R. Bruzzese, D. D'Antuoni, C. de Lisio, and S. Solimeno, J. Opt. Soc. Am. B **17**, 34 (2000).

98. A. Averchi, D. Faccio, R. Berlasso, M. Kolesik, J. Moloney, A. Couairon, and P. Di Trapani, Phys. Rev. A **77**, 021802(R) (2008).

99. J. Lu and J. Greenleaf, IEEE Trans. On UFFC **37**, 438 (1990).

100. S. Gilbertson, X. Feng, S. Khan, M. Chini, H. Wang, H. Mashiko, and Z. Chang, Opt. Lett. **34**, 2390 (2009).

101. E. Goulielmakis, V. Yakovlev, A. Cavalieri, M. Uiberacker, V. Pervak, A. Aplonski, R. Keinberger, U. Kleinberg, and F. Krausz, *Science* **317**, 769 (2007).

102. M. Uiberacker, T. Uphues, M. Schultze, A. Verhoef, V. Yakovlev, M. F. Kling, J. Rauschenberger, N. Kabachnik, H. Schroder, M. Lezius, K. Kompa, H. Muller, M. J. J. Vrakking, S. Hendel, U. Kleinberg, U. Heinzmann, M. Drescher, and F. Krausz, *Nature* **446**, 627 (2007).

103. R. Kienberger, E. Goulielmakis, M. Uiberacker, A. Baltuska, V. Yakovlev, F. Bammer, A. Scrinzi, T. Westerwalbesloh, U. Kleinberg, U. Heinzmann, M. Drescher, and F. Krausz, *Nature* **427**, 817 (2004).

104. M. F. Kling *et al*., Conference on Lasers and Electro-Optics (CLEO), paper JFH1 San Jose, California (2008).

105. X. M. Tong, and C. D, Lin, Chu, Phys. Rev. A **71**, 033406 (2005).

106. Z. X. Zhao and C. D. Lin, *Phys. Rev. A* **71**, 060702(R) (2005).

107. T. Morishita, S. Watanabe, C. D. Lin, *Phys. Rev. Lett.* **98**, 083003 (2007).

108. M. Wickenhauser, J. Burgdorfer, F. Krausz, and M. Drescher*, Phys. Rev. Lett.* **94**, 023002 (2005).

109. T. Mercouris, Y. Komninos, and C. A. Nicolaides, *Phys. Rev. A.* **75**, 013407 (2007).

110. U. Fano, *Physical Review* **124**, 1866 (1961).

111. F. J. Wuilleumier and M Meyer, *J. Phys. B: At. Mol. Opt. Phys.* **39**, R425 (2006).

112. M. Domke, K. Schulz, G. remmers, and G. Kaindl*, Phys. Rev. A* **53**, 1424 (1996).

113. M. Kitzler, N. Milosevik, A. Scrinzi, F. Krausz, and T. Brabec*, Phys. Rev. Lett.* **88**, 173904 (2002).

114. J. Itatani, F. Quere, G. Yudin, M. Yu. Ivanov, F. Krausz, and P. B. Corkum*, Phys. Rev. Lett.* **88**, 173903 (2002).

115. A. M. Perelomov, V. S. Popov, and M. V. Terent'ev, *Soviet Physics JETP* **23**, 924, (1966).

116. Eksma Nonlinear Crystals Data: (http://www.eksmaoptics.com/repository/catalogue/pdfai/NLOC/nonlinear%20crystals/BBO.pdf).

117. E. Moon, *Carrier Envelope Phase Stabilization of Grating Based Chirped Pulse Amplifiers*, PhD Thesis, Kansas State University, Manhattan, Kansas U.S.A. (2008).

Appendix A - ADK Calculation

The ionization probability calculations shown in this thesis were conducted with the Ammosov-Delone-Krainov (ADK) theory. For an atom in an intense laser field, the ionization only occurs within a fraction of one optical cycle. The average ionization rate over one cycle is given in atomic units by [23]:

$$W(t) = I_p \left| C_{n^* l^*} \right|^2 G_{lm} \left(\frac{4(2I_p)^{3/2}}{E(t)} \right)^{2n^* - |m| - 1} e^{\frac{-2(2I_p)^{3/2}}{3E(t)}} \tag{A.1}$$

where the coefficients are given by:

$$\left| C_{n^* l^*} \right|^2 = \frac{2^{2n^*}}{n^* \Gamma(n^* + l^* + 1)\Gamma(n^* - l^*)} \tag{A.2}$$

$$G_{lm} = \frac{(2l+1)(l+|m|)!}{2^{|m|}|m|!(1-|m|)!} \tag{A.3}$$

and I_p is the ionization potential of the target atom. The value of n*, which is the effective principle quantum number, is given as:

$$n^* = \frac{Z}{\sqrt{2I_p}}. \tag{A.4}$$

Z in (A.4) is the atomic core charge, which for single ionization is 1. The "m" term is just the projection of the angular momentum, l, on the electric field. l* is the effective angular momentum quantum number and is n*-1. Once the rate is known, the ionization probability is calculated as:

$$P(t) = 1 - \exp\left(\int_{-\infty}^{t} W(t')dt' \right). \tag{A.5}$$

As an example, for the fields given in equations 2.2 and 2.3 the ionization probability of argon is shown in figure A.1. (a) is the driving field, (b) is the gating field, and (c) is the vector sum of the two fields. Figure (d) shows the ionization probability. For the calculations, the pulse duration was 7.9 fs and the delay was 7.5 fs. This gives a 1 optical gate width. The intensity at the center of the gate width was 2.8 x 10^{14} W/cm^2.

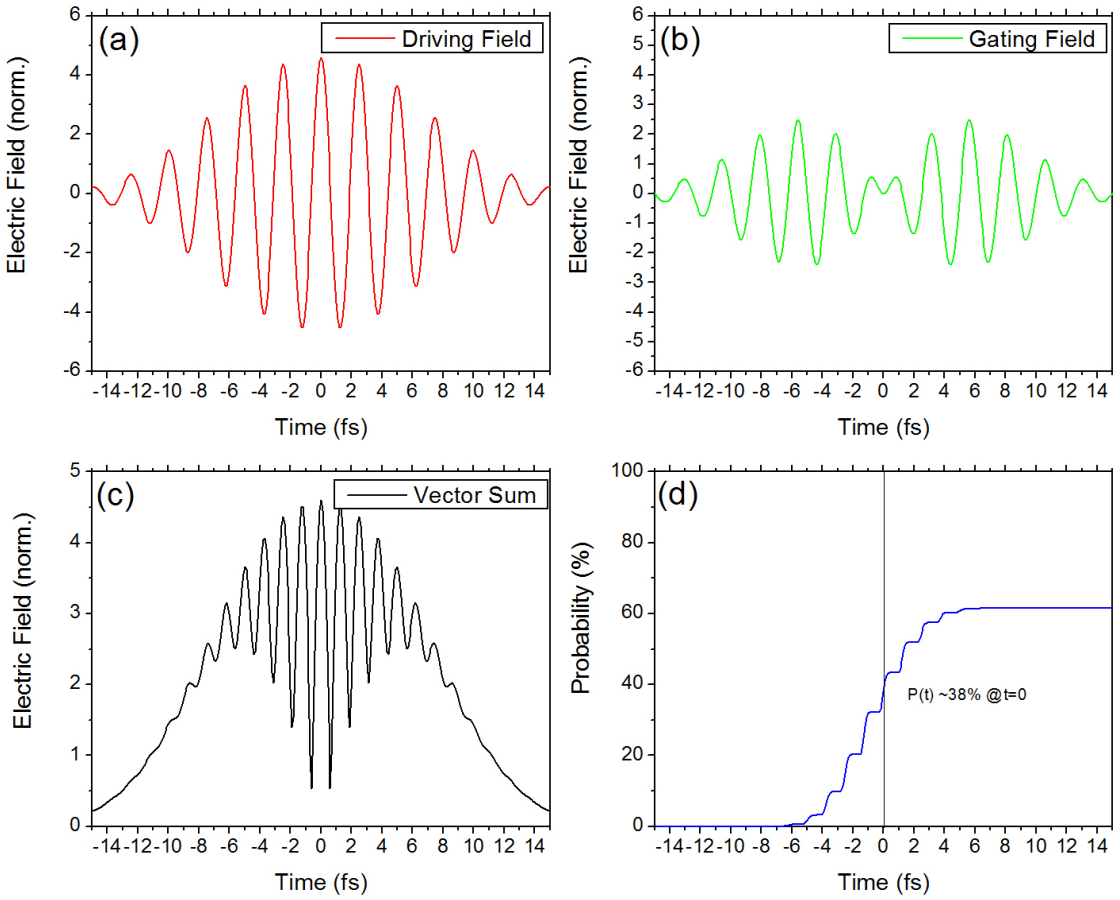

Figure A.1 (a) The driving field, (b) gating field, and (c) vector sum of (a) and (b). The ionization probability is shown in (d).

Appendix B - Quartz Plates Calculations

The principle of DOG and GDOG relies on proper selection of quartz plate and BBO thickness. This appendix will show the calculations used to determine which plates should be used in the experiment.

The most basic requirement for DOG is that the gate width (see eq. 2.15) must be one optical cycle or less. Since the pulse duration can be easily tailored depending on gas pressure and laser intensity in the hollow core fiber, it is a fairly free parameter. The delay introduced by the first quartz plate on the other hand is only dependent on the thickness of the first plate and the material it is made of. Unlike polarization gating, the orientation of the driving and gating field with respect to the input polarization is critical since it they must overlap properly with the second harmonic generated from the BBO.

To ensure the driving field of DOG is parallel to the input polarization, the first quartz plate must be a full order waveplate. This means the phase delay must be an integer number of cycles. The phase is given by:

$$\phi_{delay} = \Delta n(\lambda) L / \lambda_0 \tag{B.1}$$

where $\Delta n(\lambda)$ is the difference in refractive index between the e and o axis of the medium, L is the medium length and the center wavelength is λ_0. Every term in equation B.1 is fixed except the thickness, L. To find the refractive index as a function of the wavelength, Sellmeier equations were used [ref]. The equation is:

$$n^2 = B_1 + B_2\lambda^2 + \frac{B_3}{\lambda^2} + \frac{C_1}{\lambda^4} + \frac{C_2}{\lambda^6} + \frac{C_3}{\lambda^8}. \tag{B.2}$$

This equation depends on a series of constants which are different for the o-ray and the e-ray. They are listed in table B.1.

	B1	B2	B3	C1	C2	C3
n_e	2.3849	-1.259E-2	1.079E-2	1.6518E-4	-1.94741E-6	9.36476E-8
n_o	2.35728	-1.17E-2	1.054E-2	1.34143E-4	-4.45368E-7	5.92362E-8

Table B.1 Sellmeier equation parameters for quartz.

As an example, for λ_0 = 790 nm, n_e = 1.5475 and n_o = 1.53857. This shows that quartz is positive uniaxial since $n_o < n_e$. Using equation B.1 and B.2 with L= 440 μm, and λ_0 = 790 nm gives a total phase delay of 4.97 cycles. This is nearly a full order waveplate. Additional precision is not possible since the medium manufacturers usually have a tolerance of +/- 5 μm.

The phase delay can also be tuned slightly during the experiment since the quartz plate angle of incidence can be tuned. This effectively increases the thickness of the medium which can be calculated from simple geometry. Less intuitively however, the effective refractive index of the e-ray also changes by the equation [53]:

$$n_e(\theta,\lambda) = \frac{n_e(0,\lambda)n_o(\lambda)}{\sqrt{n_o(\lambda)^2 \sin^2(\theta) + n_e(0,\lambda)^2 \cos^2(\theta)}}, \tag{B.3}$$

where the angle θ is the angle between the optical axis and the propagation vector. This can be plotted in polar coordinates and is shown in figure B.1. When the angle is 90 degrees, the refractive index is equal to n_e which is the normal operating angle and is for normal incidence.

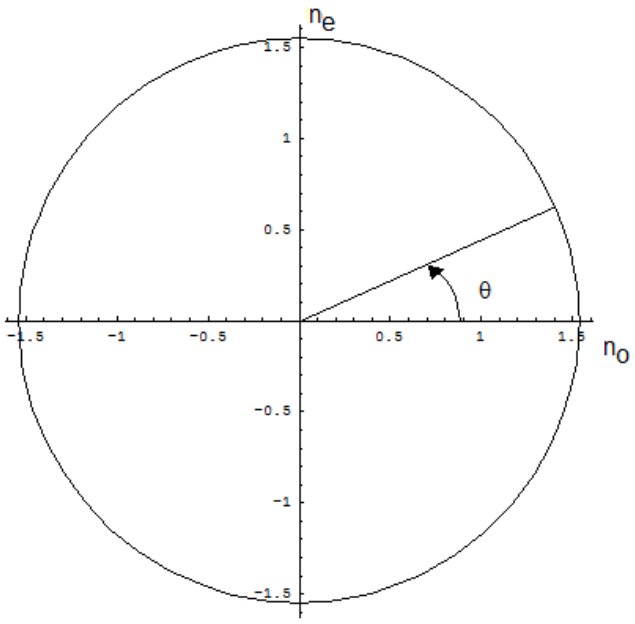

Figure B.1 Polar plot of equation B.3.

Once the refractive index is known, it is used to calculate the phase of the laser pulse after passing through the quartz plate. The procedure is laid out in the next several steps. First, a Gaussian laser pulse is Fourier transformed to get the frequency domain representation:

$$FFT\{f(t)\} = f(\omega)$$

(B.4) The phase, calculated as $\phi_i = 2\pi n_i(\lambda)L/\lambda_0$, is next digitized and included with $f(\omega)$. Finally, an inverse FFT is taken:

$$IFFT\{f(\omega)e^{i\phi}\} = E(t').$$

(B.5)

Figure B.2 shows a plot of the time domain after including the spectral phase for a 10 fs pulse passing through a 440 μm thick quartz plate. The two pulses are orthogonally polarized. Clearly the delay corresponds to an integer number of full cycles. Also, the pulses are not very distorted indicating higher order phase terms do not play too much of a role for such a thin quartz plate.

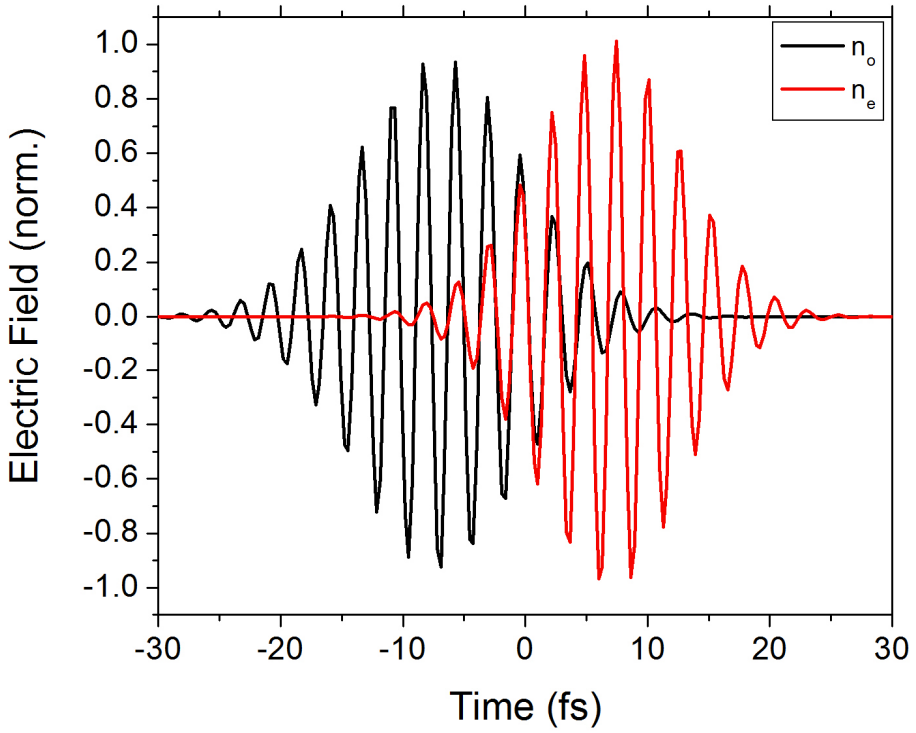

Figure B.2 Field components including spectral phase after 1st quartz plate.

The above procedure is next repeated for the second quartz plate and BBO. The BBO will be discussed in Appendix C but the second quartz plate is also a multi-order waveplate. The results after the laser pulse passes through all of the plates are shown in figure B.3. At the center of the laser pulse, the gating field goes to zero while the driving field is a maximum. This is the basic requirement for DOG. An interesting feature is that the high order phase starts to play a role after all of the plates. The total pulse becomes chirped due to the second order dispersion from the combination of all the plates. In reality, the pulse is negatively chirped to compensate for this dispersion while in this calculation I started with a TL pulse. The actual experimental results will therefore be better than this.

Since the plates are full waveplates, the final DOG pulse has the linear portion pointing parallel to the input polarization.

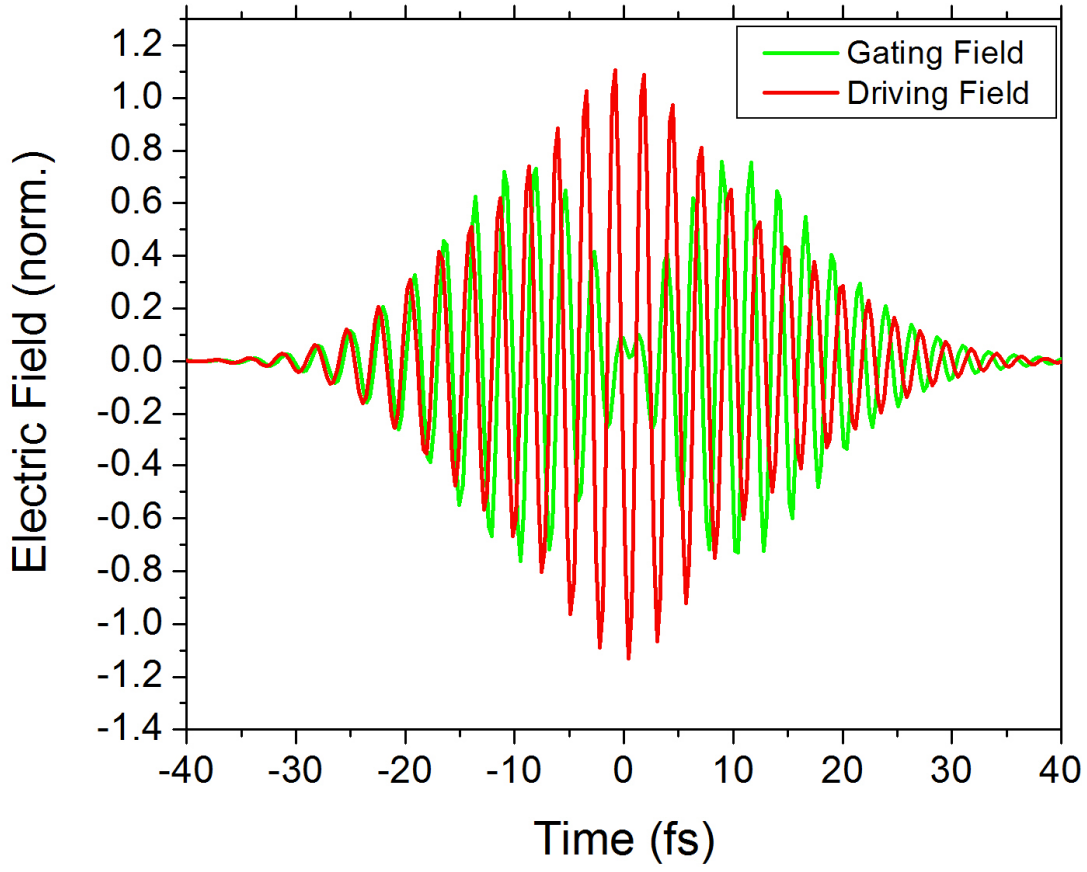

Figure B.3 Field components including spectral phase after both quartz plates and BBO.

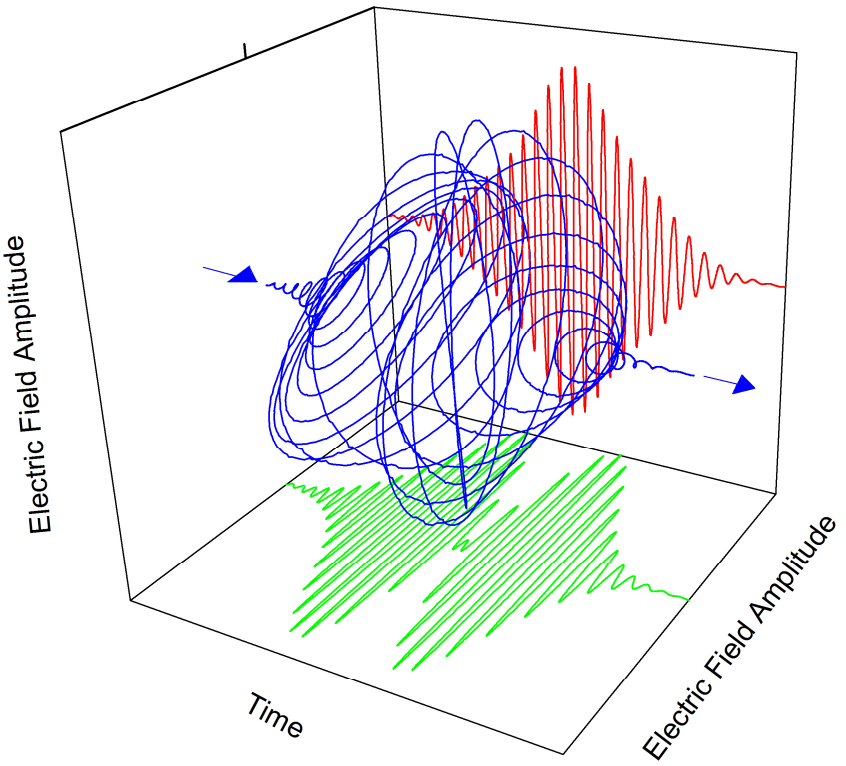

Figure B.4 Vector sum of field component from figure B.3.

As a final comparison, figure B.4 shows the 3-D vector sum of the driving field and gating field after passing through all of the plates. The shape is somewhat distorted as compared with the ideal case shown in figure 2.6 due to material dispersion. However, the linear portion is strong and since the HHG process is strongly dependent on the ellipticity of the generating laser, the final result is the same as the ideal case. Also, since the initial laser pulse can be overcompensated for the additional second order phase distortion introduced by the plates, the result of figure B.4 is the lower limit on the quality of the DOG pulse.

Verification of the thickness of the quartz plates is not easy experimentally. However, the thickness can be estimated by looking at the spectrum of a laser pulse that passes through the plate with polarization 45 degrees away from the optical axis of the plate. This gives the pulses shown in figure B.2. If the laser pulse then passes through a polarizer set to transmit the components parallel to the input polarization and reflect the components perpendicular to the input, two distinct spectra can be seen. In the time domain, the location where the two pulses

overlap in the center creates one pulse parallel to the input polarization. The components perpendicular to this however create two pulses separated in time by the number of cycles of delay the plate introduces. In the spectral domain, that creates a spectrum with a dip in it. The location of the dip as well as its depth depends on the thickness of the plate. If the plate is a true full order plate at the wavelength specified when the plate was ordered, the dip should occur at this wavelength with a strong modulation depth. Figure B.5 shows a schematic of the experimental setup for measuring this. The 1st quartz plate is oriented at 45 degrees to the input polarization. Next, a polarizer is installed a spectrum is taken for both the transmitted and

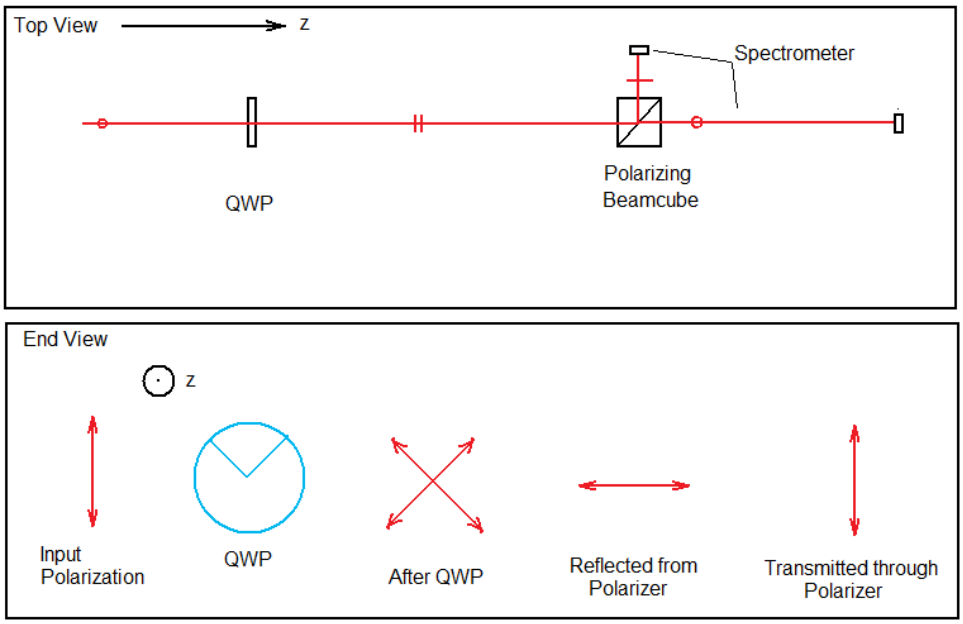

Figure B.5 Experimental setup for measuring quartz thickness.

reflected beams. The results are shown in figure B.6. Clearly the dip occurs at ~785 nm in both cases. Figure (a) shows a broad spectrum passing through a 440 μm quartz plate while (b) shows a narrow spectrum passing through a 1.68 mm quartz plate. In both cases, the incident laser pulse was normal to the surface. The locations of the dips could however be tuned by rotating the plate so as to change the incident angle.

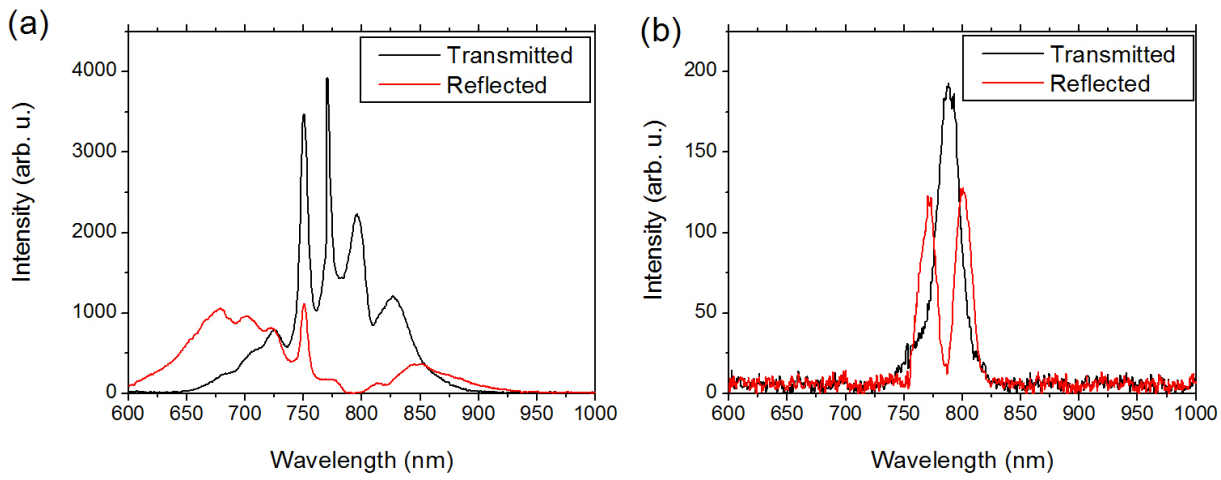

Figure B.6 Spectral dips for (a) a short pulse spectrum passing through a 440 μm plate and (b) a long pulse spectrum passing through a 1.68 mm plate.

Appendix C - BBO Crystal Selection for DOG

The most critical element in the DOG optics arrangement is the BBO crystal. It determines the SHG bandwidth and ensures the final delay of the second quartz plate and BBO is a quarter waveplate. Small changes in the alignment of this single optic can significantly alter the output spectrum.

Like the quartz plate, the thickness of the BBO determines the delay between the two components of the DOG pulse. The Sellmeier equations for BBO are listed below [116]:

$$n^2 = A + \frac{B}{(\lambda^2 - C)} - D\lambda^2 \qquad \text{(C.1)}$$

where the constants depend on whether the o-ray or e-ray is to be calculated. The values for the constants are given in table C.1.

	A	B	C	D
n_e	2.373	0.0128	0.0156	0.0044
n_o	2.7405	0.0184	0.0179	0.0155

Table C.2 Sellmeier equation parameters for BBO.

As an example, for λ = 790 nm, n_e = 1.54638 and n_o = 1.66168. This means BBO is negative uniaxial since $n_o > n_e$. This is the opposite as compared with quartz which is important for proper delay control as will be discussed later.

As with quartz, equation B.3 must be used since the optic axis of BBO is not 90 degrees. However, since the crystal is also used for producing the second harmonic required for DOG, the phase matching condition:

$$n_e(2\omega, \theta) = n_o(\omega) \qquad \text{(C.2)}$$

must be satisfied. This is the case since the crystal is ooe and the fundamental is ordinary and the second harmonic is extraordinary. Plugging this into equation B.3 and solving for $\sin^2\theta$ gives [53]:

$$\sin^2\theta = \frac{\frac{1}{n_o(\omega)^2} - \frac{1}{n_o(2\omega)^2}}{\frac{1}{n_e(2\omega,90)^2} - \frac{1}{n_o(2\omega)^2}}. \qquad \text{(C.3)}$$

Solving equation C.3 for the angle, θ, and plotting it vs. the wavelength gives the proper phase matching angle for any wavelength. This is shown in figure C.1. Clearly the optimal angle for ~800 nm light is around 29 degrees.

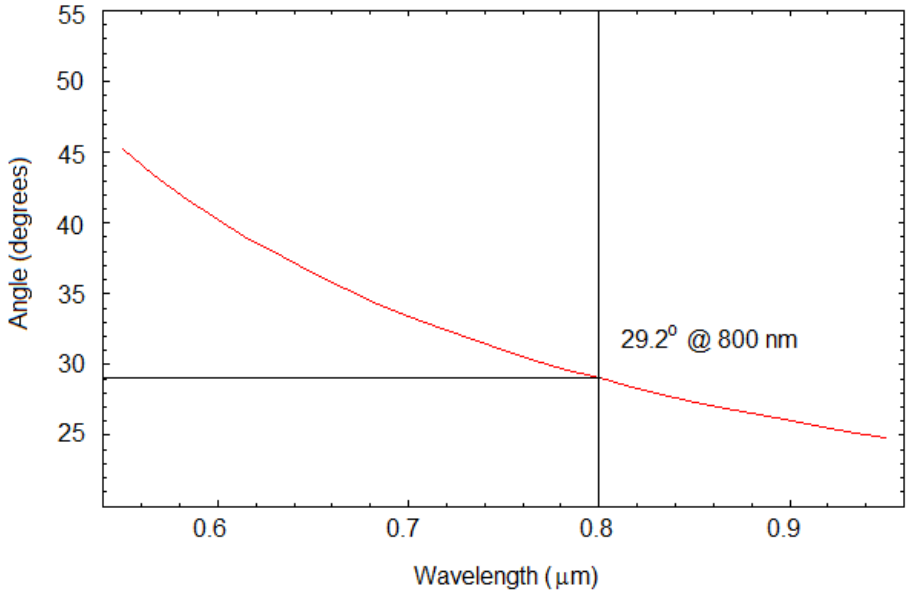

Figure C.1 Phase matching angle vs. wavelength for BBO.

Inserting this angle into equation B.3 gives the ellipse for the BBO. This is plotted in figure C.2. The effect is slightly more elliptical than for quartz since the refractive index difference is greater for BBO than quartz. For normal incidence, the angle read off the ellipse should be for ~29 degrees since this is the angle which the crystal is cut at.

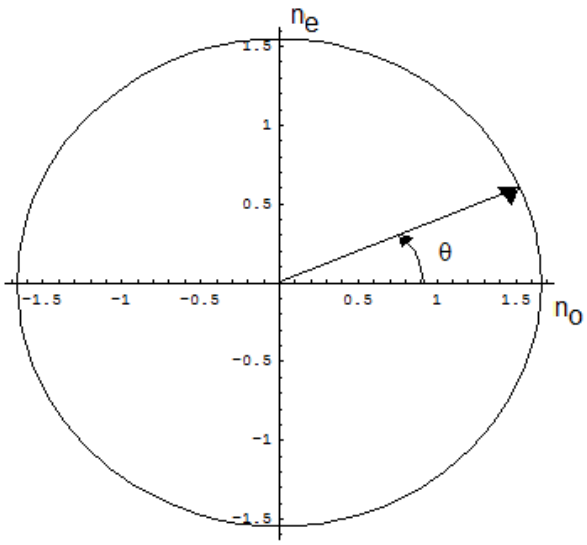

Figure C.2 Polar plot of equation B.3 for BBO.

Next, the phase matching bandwidth must be considered. For thick crystals, the SHG intensity is stronger but the bandwidth is narrower while for thin crystals the opposite is true. For example, in the SHG FROG setup, the BBO is typically 5-10 μm thick to ensure a wide bandwidth can be produced. This is important if an accurate replica of the fundamental pulse is desired. To estimate the phase matching bandwidth, the wave vector mismatch is required. Since the fundamental travels along the ordinary axis and the second harmonic travels along the extraordinary axis:

$$\Delta k = \frac{4\pi}{\lambda}(n_o(\omega) - n_e(2\omega, \theta)). \tag{C.4}$$

With equation C.4, the intensity of the second harmonic plotted versus the fundamental wavelength can be calculated. This is expressed by:

$$I_3 = I_3(\max)\frac{\sin^2(\Delta kL/2)}{(\Delta kL/2)^2} \tag{C.5}$$

where L is the crystal thickness. For θ = 29 degrees, equation C.5 is plotted in figure C.3 for two different thicknesses. In (a), the bandwidth is very large since the crystal is 10 μm thick while in (b) the bandwidth is narrow since the crystal is 141 μm thick. In both cases, the SHG would be expected to peak around the second harmonic of ~800 nm. This makes sense since the phase

matching angle was chosen as 29 degrees. Figure C.4 shows the experimental BBO spectrum (a) and the corresponding fundamental spectrum (b). The fundamental spectrum was from an 8 fs laser pulse. Clearly the SHG bandwidth is limited, however the bandwidth agrees well with the calculation shown in figures C.3(b).

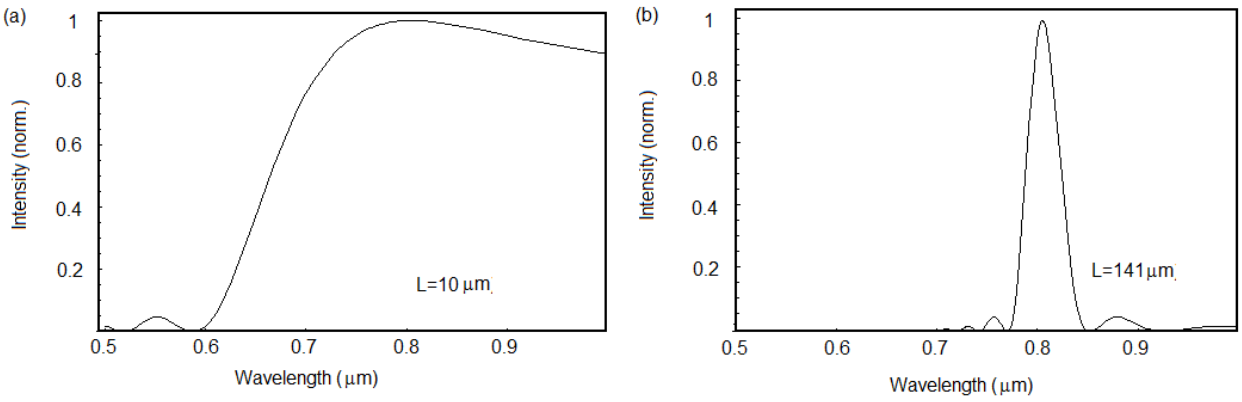

Figure C.3 Phase matching bandwidths for (a) 10 μm and (b) 141 μm thick crystals.

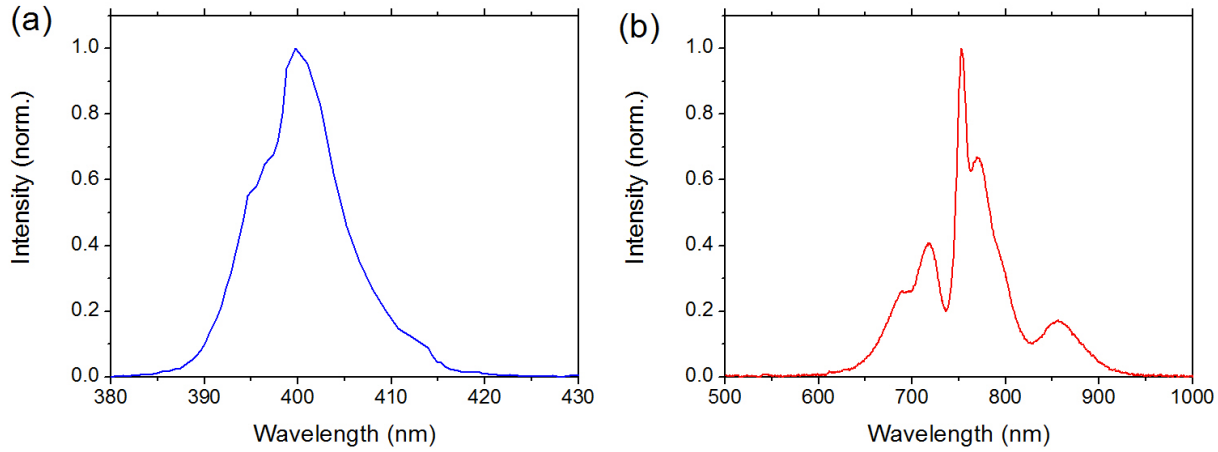

Figure C.4 Experimental spectra for (a) the BBO and (b) the fundamental laser pulse.

Alternatively, equationC.5 can be plotted versus angle assuming the input wavelength is known. For λ=790 nm, figure C.4 shows the so-called Maker fringes for a 141 μm thick BBO.

Again the optimum phase matching angle is shown to be ~ 29 degrees yielding maximum SHG at this angle.

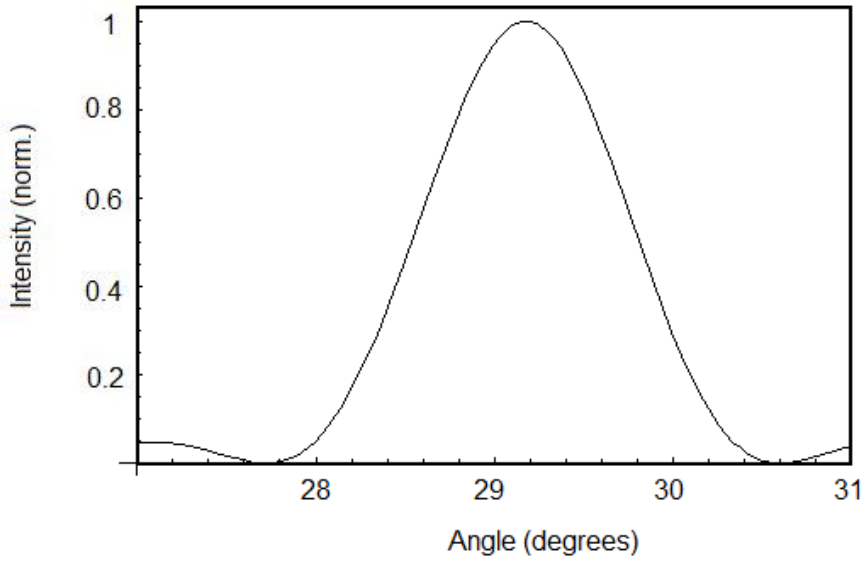

Figure C.5 Maker fringes for a 141 μm thick BBO crystal.

The second criterion for the choice of BBO is how much SHG is expected. This was estimated using software [45] which numerically solves the coupled differential equations associated with SHG. Figure C.6 shows the result for the SHG expected (green line) for an input idler and pump beam (blue and red lines) of equal pulse energy (~ 1 mJ) and spot size on the 141 μm thick crystal of ~4 mm. These are the typical experimental conditions for long pulse streaking with 28 fs laser pulses. The result indicates nearly 20% efficiency of the SHG for a long input pulse. Figure C.7 shows an identical calculation but with 8 fs pulses. This is a typical pulse duration used in DOG. Clearly the output SHG is reduced due to the larger bandwidth of the input laser pulse.

The actual output SHG power is easily measured experimentally since the fundamental and second harmonic beams can be separated. After bouncing the laser pulse off of several dichroic beamsplitters or by separating the two orthogonally polarized beams with a polarizing beamsplitter, the SHG was found to be anywhere from 10-20% efficient, depending on the input laser parameters. This is more than enough for the DOG method to work. Also, as the input

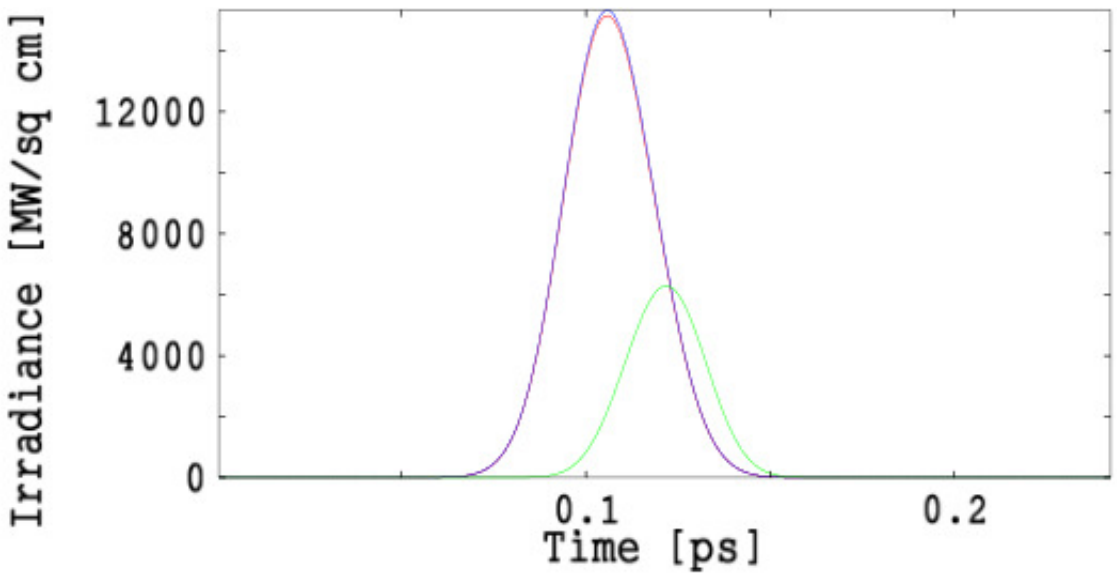

Figure C.6 Calculated SHG for a 141 μm thick crystal with 28 fs pulses from SNLO.

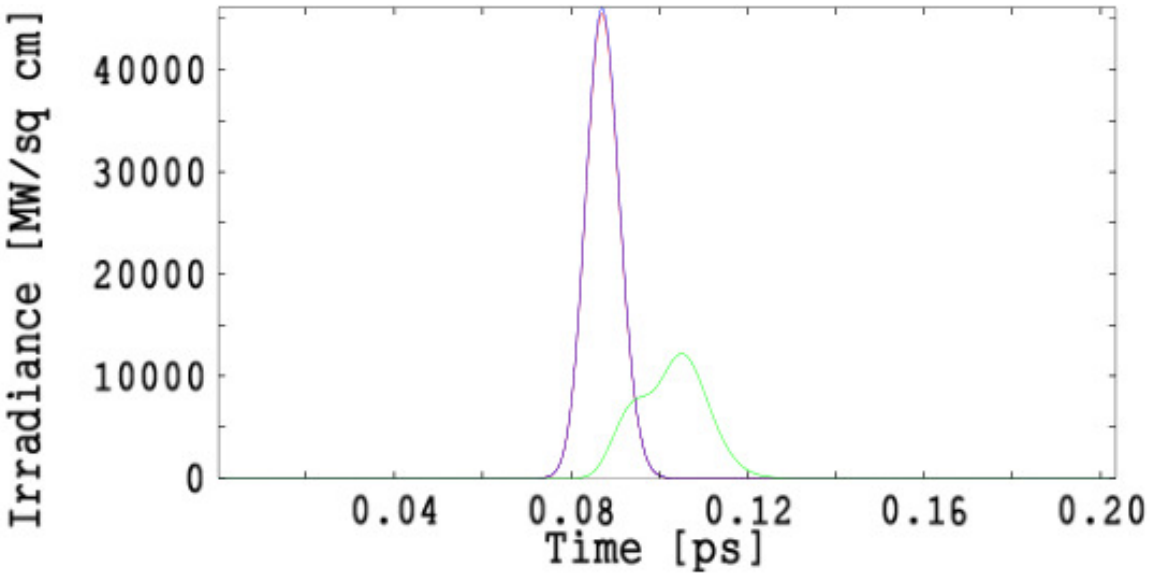

Figure C.7 Calculated SHG for a 141 μm thick crystal with 8 fs pulses from SNLO.

pulse duration increases, the efficiency of SHG also increases meaning GDOG will have no problem generating enough SHG if DOG does not.

The final consideration for the choice of BBO crystal is that it must meet the required amount of delay such that the second quartz plate and the BBO together act as a zero order quarter waveplate. A BBO crystal with length ~150 μm generates sufficient SHG intensity and with a wide enough SHG bandwidth to effectively work with DOG. 150 μm gives -5.6 cycles of delay between the o-ray and e-ray for $\theta = 29$ degrees and wavelength 780 nm. This calculation was done using equations B.1 and C.1. The nearest zero order quarter wave plate configuration would be -5.25 cycles. This corresponds to a thickness of 141 μm. The corresponding quartz plate thickness would be 440 μm which introduces exactly +5 cycles delay (see appendix B).This choice of BBO thickness provides a good compromise between SHG efficiency, dispersion of the input beam and phase matching bandwidth.

Orientation of the crystal in the experimental setup is the next step. Since the input polarization is horizontal (p-polarized) as determined by the direction of the TOF axis in the steak camera, this configuration will be used as an example. After the first plate, the two orthogonal pulses are projected onto the optic axis of the second quartz plate which is set along the original laser polarization. This plate produces the gating field polarized perpendicularly to the input polarization first followed by driving field polarized parallel to the input laser polarization. The driving component is delayed by the number of cycles of delay the second quartz plate introduces, i.e. 5 cycles for a 440 μm thick plate. The driving field must come out second meaning the slow axis is aligned along the input polarization. This is the e-axis since quartz is positive uniaxial. To compensate this delay, the BBO is oriented such that its fast axis (also the e-axis since BBO is negative uniaxial) is aligned parallel to the quartz slow axis. This reduces the delay between the driving and gating field to exactly 0.25 cycles thereby generating the ellipticity varying pulse.

Since the gating field is oriented parallel to the BBO slow axis (the o–axis) and since the BBO is ooe, the second harmonic is generated by the gating field but polarized along the driving field. This gives the field components as shown in figure 2.25(c). The output field components including all the spectral phase distortions is shown in figure B.3 and B.4 for the first and second quartz plates (both 440 μm) and the 141 μm BBO. To ensure the BBO crystal is oriented properly in the experimental setup, the input polarization should generate no SHG if linearly polarized. For the streak camera, the input polarization is horizontal meaning vertical polarization should generate maximum SHG.

Tuning the BBO is a easy way to modify the generated spectrum. However, doing so changes the phase matching bandwidth, the SHG efficiency and the amount of delay introduced between the driving and gating fields simultaneously. This means there is only a very small range of angles through which the BBO can be tuned. Figure C.5 shows that the SHG falls off quickly after the BBO is tuned more than one cycle away from the optimal phase matching angle. Figure C.8(a) shows that if the BBO is tuned more than half a degree, the gating and driving field are no longer a quarter cycle apart meaning the DOG pulse is not constructed properly. Experimentally, there is no longer a strong linear portion in the DOG field and the XUV flux drops off almost completely. The result of figure C.8, combined with the result from figure C.5 indicates that there is less than one degree that is available for tuning the BBO angle.

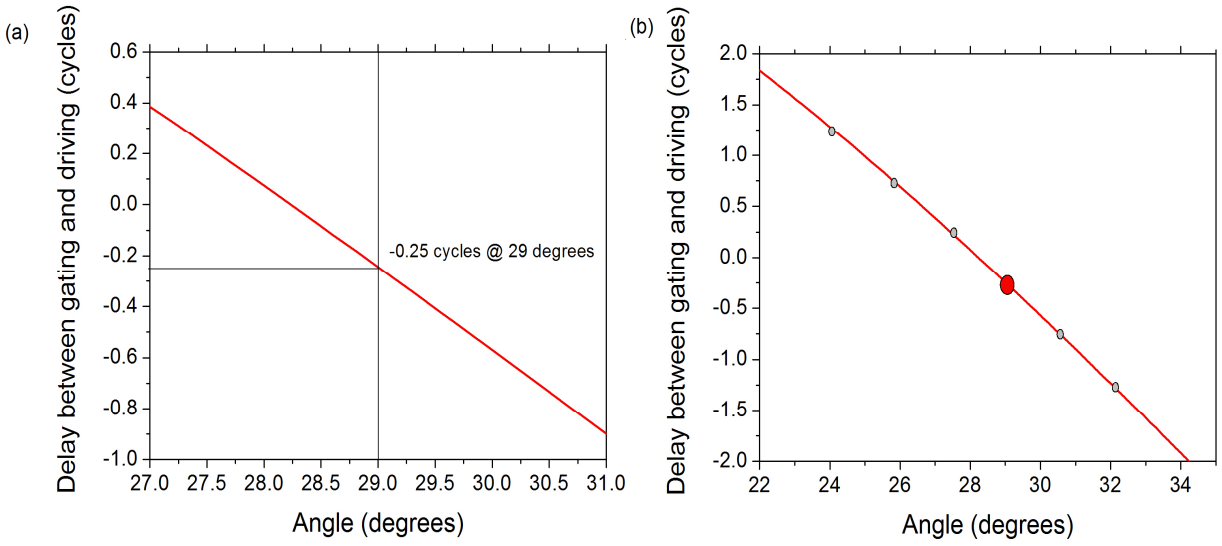

Figure C.8 (a) and (b) Delay between the gating and driving field versus BBO angle.

Interestingly, if the BBO is further tuned, the DOG pulse can be roughly re-made since the delay can come back to +/-0.75 cycles then +/-1.25 cycles, etc. These alternate locations are shown as the gray dots in figure C.8(b) with the large red dot representing the ideal position. Since these are roughly quarter-cycle delays, the linear portion becomes strong again and the XUV signal becomes brighter. This is easily seen experimentally by simply monitoring the spectrum while tuning the BBO. However, since the SHG is no longer efficiently produced at these other angles,

the spectrum becomes very discrete exhibiting only odd order harmonics. This is because the gate width no longer isolates a single attosecond pulse.

Appendix D - Interferometer Locking Method

The two arms of the Mach-Zehnder interferometer needed to be stabilized to time scales smaller than that of the attosecond pulse we wished to measure. This was accomplished by co-propagating a continuous wave (CW) laser with center wavelength of 532 nm through the interferometer, as illustrated in figure D.1. The CW laser entered the interferometer at the first beam splitter but on the opposite side from where the NIR laser entered. The XUV arm of the

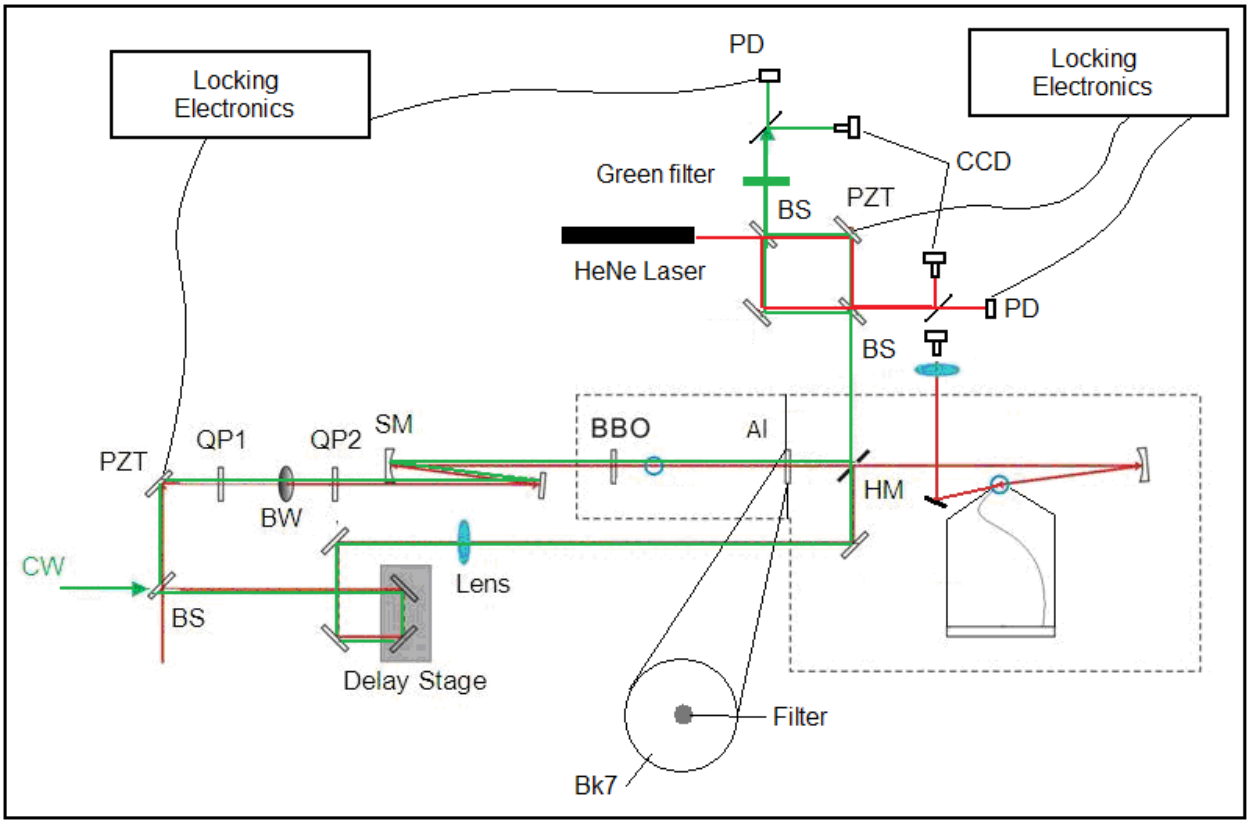

Figure D.1 Experimental setup of the interferometer locking.

interferometer had an aluminum filter used to remove the residual IR. This also had to pass the CW laser however. For this, a Bk7 window had a 1.5 mm hole drilled into it. This was then covered with the 300 nm aluminum filter. The Bk7 allowed the green laser to pass this way. At the hole-drilled mirror the CW beams from both arms of the interferometer were recombined with a second smaller mach-Zhender interferometer to generate interference fringes. The beam

from the XUV arm reflected off the back of the mirror while the beam from the streaking arm passed through the hole in the hole drilled mirror. The fringes were sent through a green filter to remove any IR that may have remained. The fringes were then measured by a photodiode. Changes in the measured intensity indicated shifting of the interference fringes caused by changes in the relative optical path lengths of the two arms of the interferometer, which we wished to minimize. The fringes could also be monitored at the same time by reflecting a small portion of the beam to a CCD camera. From the image, the quality of the locking could be deduced. Since the locking required a secondary interferometer to re-overlap the two green beams, this also had to be stabilized. A CW HeNe laser was passed through the small interferometer to stabilize it as well. The beams were monitored by both a photodiode to collect the intensity signal and a CCD camera to monitor the fringe pattern itself.

The output of the photodiodes was sent to a proportional-integral-derivative (PID) locking system (SRS SIM960 Analog PID Controller) in order to control a single piezoelectric transducer stack (PZT) installed on a mirror in the generating arm of the interferometer. The length of the PZT was varied to ensure that the optical path length difference was stabilized. Figure D.2 shows the stability of the interferometer in the (A) unlocked and (B) locked cases.

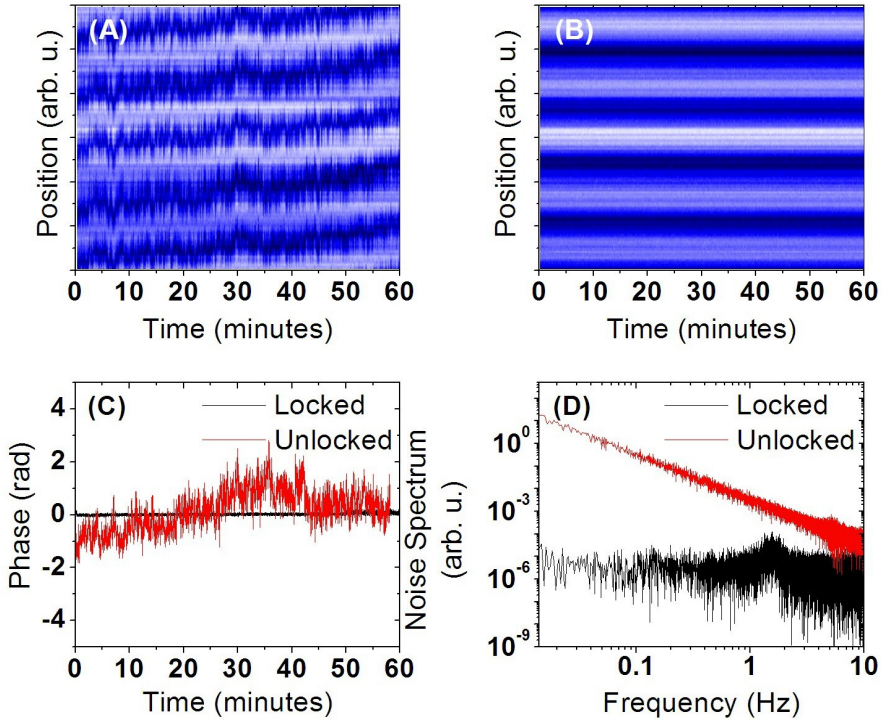

Figure D.2 Stability measurement of the streak camera.

Through our locking technique, we were able to reduce the relative phase fluctuation from ~750 mrad in the unlocked case to less than 30 mrad rms in the locked case as can be seen in Fig. D2(C). This phase jitter translates into about 8 attoseconds of temporal jitter which is much less than the duration of the attosecond pulses we wished to measure. Fig. D2(D) shows the suppression of the low frequency phase noise.

This stability of the interferometer was created by using ultra stable optical mounts (OptoSigma 112-6660) for all mirrors. These were set on heavy, low center of mass bases made of solid steel and were ~3 inches in diameter. Also, the turbos were isolated from the system using Varian vibration dampeners (9699334). This reduced temporal jitter from the turbos which could not be compensated for with the locking electronics. Finally, to reduce sudden shocks to the system, all of the roughing pump hoses were passed through a large box containing ~400 lbs of sand. This damped any shocks that might otherwise have transferred along the hoses themselves. A small tap on the hoses between the sand box and the setup was enough to send the PID controller out of range. However, the hose between the roughing pump itself and the sand box could be violently shaken and the interferometer would remain locked.

Appendix E - Pulse Energy Measurement

To estimate the attosecond pulse energy produced with the DOG method, an XUV photodiode (AXUV 100, IRD instruments) was placed in the beam path after the aluminum filter. The signal from the detector was recorded with an oscilloscope and saved for later analysis.

The photodetector is a silicon p-n junction. When XUV photons with energy greater than 1.12 eV are incident on it, electron-hole pairs are created. The electron-hole pairs are separated by the p-n junction electric field and a current directly proportional to the number of pairs is recorded by the oscilloscope. The current, i, is given in terms of the charge, q, by:

$$i = \frac{dQ}{dt}. \tag{E.1}$$

By Ohm's law, V=iR, the charge can be written in terms of the voltage, V, as:

$$Q = \frac{1}{R}\int V(t)dt\,. \tag{E.2}$$

The resistance in this case is the input impedance of the scope, or 50Ω.

A typical oscilloscope trace is shown in figure E.1. The peak is the decaying charge

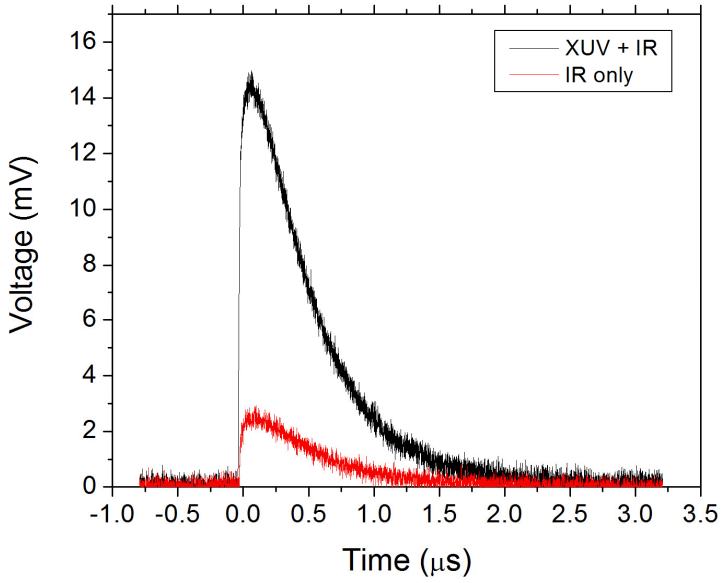

Figure E.1 Photodiode signals for XUV and IR (black line) and IR only (red line).

across the photodetector. The black line is the case when the XUV photons are being generated. If the gas in the first target is turned off, the signal reads the red line. The red line is the background and is because of small pinholes in the filter allowing small amounts of the IR through. The background signal is subtracted from the XUV signal to get only the contribution of the XUV photons.

Once the signal is integrated, the total charge and hence the total number of photons originally generated can be calculated. The number, N, is given as:

$$N = \frac{Q}{e\eta T} \tag{E.3}$$

where e is the elementary charge, η is the quantum efficiency of the detector, and T is the transmission of filters and residual gas in the chamber. The value of the quantum efficiency is provided by the manufacturer and is ~8.38 for our spectrum (~40 eV center energy). The transmission of the filters was independently measured by adding another aluminum filter to the detector. A spectrum was then measured with and without the additional filter in place and the ratio gave the transmission of our typical filter. The transmission vs. energy is plotted in figure E.2. A pure aluminum filter (see figure 3.22) would transmit ~75% of the photons while ours transmits ~10-20%. This is due to thin layers of aluminum oxide present on both sides of the filter. Using T as ~.12, the total number of photons was found to be 1.2 x 10^8. Multiplying by a single photon energy gives a total pulse energy of 6.5 nJ.

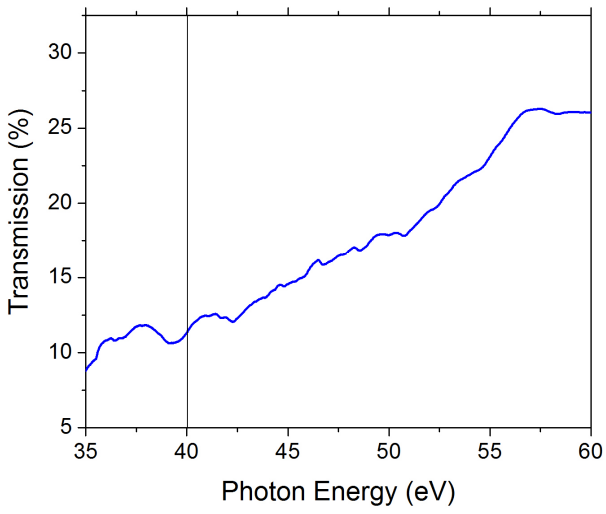

Figure E.2 Measured aluminum filter transmission.

Appendix F - The Kansas Light Source Amplifier

The Kansas Light Source laser system started with a Femtolaser oscillator (Scientific Pro S) as the seed. The oscillator was pumped by 4-5 W of CW 532 nm light from a Verdi 6 pump laser, horizontally polarized and focused into a 2.3 mm long Ti:Sapphire crystal cut at the Brewster angle. The seed beam, after passing through the output coupler, had a repetition rate of ~77 MHz with a pulse to pulse separation of ~13 ns. The pulse energy after the oscillator was on the order of nJ and the individual pulse duration was ~10-12 fs.

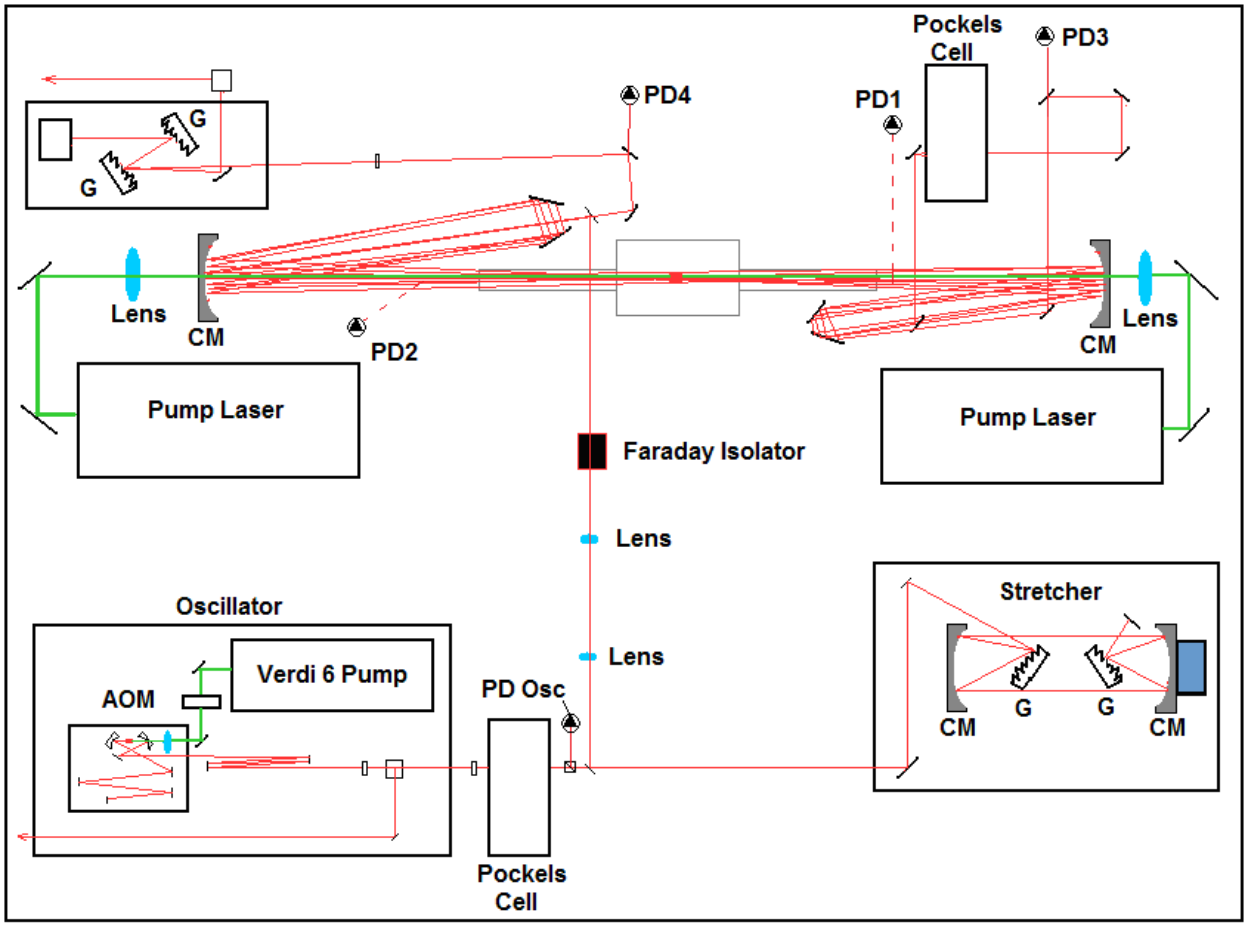

Figure F.1 KLS laser system. G = grating, AOM = accustom-optical modulator, PD = photo diode.

After the oscillator, the pulse train passed through a Pockel's Cell which switched out a 2 kHz train from the ~77 MHz train. This was sent to the double-pass stretcher where the gratings

and focusing mirrors stretched the laser pulses to nearly 80 ps. This allowed the laser pulses to be safely amplified in the 14 pass chirped pulse amplifier. After the stretcher, the ps pulses passed through a telescope and a Faraday isolator. This was used to ensure no back reflections from the amplifier could get back to the oscillator.

From there, the laser pulses entered the amplifier. This consisted of 14 passes through a Ti:Sapphire crystal that was cooled to liquid nitrogen temperatures to avoid thermal lensing effects. After the first 7 passes, the laser pulses were sent through a second Pockel's cell to eliminate any amplified spontaneous emission (ASE) from the amplifier. The beam was also modified with a telescope to change the beam size on the laser crystal. The laser pulse was then sent through the last 7 passes of the amplifier. The final pulse energy is ~4 mJ before the grating compressor which is a total gain on the order of 10^6. The efficiency of the grating compressor is ~50% meaning the output pulse energy is ~2 mJ. After the compressor, the laser pulses had duration of ~25 fs. This is a large increase from the original oscillator pulse duration due to gain narrowing in the amplifier.

To lock the CE phase in the laser system, the oscillator must be first stabilized. This was accomplished by sending a portion of the oscillator through a photonic crystal fiber to generate an octave spanning spectrum. Using an f-2f interferometer, the offset frequency of the oscillator could be detected by beating the 532 nm components from the spectrum with 1064 nm components frequency doubled to 532 nm. The offset frequency drift could be measured and compensated with an accusto-optical modulator (AOM) between the oscillator pump laser and the oscillator cavity. This modulated the intensity of the pump laser thereby changing the Kerr lens effect in the oscillator crystal and tuning the offset frequency. Once the oscillator was stabilized, the slow drift of the CE phase caused by the amplifier could be controlled. Using 10% of the output amplified laser beam, a second f-2f interferometer was used to generate a spectrogram between the 532 nm components and the frequency doubled 1064 nm components produced after the laser was focused into a sapphire plate. The spectrogram could then be controlled by varying the separation between the gratings in the stretcher using a PZT mount. Full details for the CE phase locking system can be found in reference [117].

The daily alignment procedure for the KLS amplifier is listed below.

1. The second 7 passes were blocked after the 2nd pockels cell. This ensured no laser energy could get to the laser crystal after the first 7 passes.

2. The oscillator should be checked to ensure no CW spikes exist in the spectrum and there are no multi-modes in the output train.
3. The seed beam is then checked on PD Osc. The 77 MHz pulse train signal should be visible with the 2 kHz pulses missing.
4. The laser beam should be adjusted so that it passes through the center of the telescope after the first Pockels cell. No adjustments should ever be made within the stretcher box.
5. A flipper mirror for the first pass can be flipped up to send the beam to PD 1. This is used to find the first pass gain. The pump lasers can be turned on and used to optimize the gain using only one pump at a time. The flipper mirror should be flipped down after this point.
6. Next, the second pass gain is checked using a flipper mirror to send the beam to PD 2. Using the first set of roof mirros, the seed beam is adjusted to optimize the signal. The flipper should be flipped down after this.
7. The second set of roof mirrors can be adjusted next to optimize the signal on PD 3. This is the signal for the 3-7 pass.
8. After the 1st 7 passes are optimized, the beam block after the second pockels cell can be removed. The last 7 passes signal can be seen on PD 4 and can be optimized with the mirrors near PD 3. Once the signal is maximized (~ 2 mJ after the compressor), the laser is aligned. Alignment through the compressor can be adjusted easily with the mirror closest to PD 4.